A *hp*-adaptive discontinuous Galerkin finite element method for accurate configurational force brittle crack propagation

Robert E. Bird

Thesis submitted towards the
degree of Doctor of Philosophy

Department of Engineering
Durham University
United Kingdom

September 2019

This thesis is dedicated to
my Parents and Grandparents.

Robert E. Bird

Abstract

Engineers require accurate determination of the configurational force at the crack tip for fracture fatigue analysis and accurate crack propagation. However, obtaining highly accurate crack tip configuration force values is challenging with numerical methods requiring knowledge of the stress field around the crack tip *a priori*. In this thesis, the symmetric interior penalty discontinuous Galerkin finite element method is combined with a residual based *a posteriori* error estimator which drives a *hp*-adaptive mesh refinement scheme to determine accurate solutions of the stress field about about the crack. This facilitates the development of a novel method to calculate the crack tip configurational force that is accurate, requires no *a priori* knowledge of the stress field about the crack tip with, its error bound by an error estimator which is calculated *a posteriori*. Benchmark values of the crack tip configurational force are presented for problems containing multiple mixed mode cracks in both isotropic and anisotropic materials. Additionally, the *hp*-adaptivity is combined with a mathematical analysis of the stress field at the crack tip to critique the convergence and limitations of other methods in the literature to calculate the crack tip configurational force. Two methods for staggered quasi-static crack propagation are also presented. An *rp*-adaptive method which is simple to implement and computationally inexpensive, element edges aligned with the crack propagation path with the exploitation of the discontinuous Galerkin edge stiffness terms existing along element interfaces to propagate a crack. The second method is denoted the *hpr*-adaptive method which combines the accurate computation of the crack tip configuration force with *r*-adaptivity to produce a computationally expensive but accurate method to propagate multiple cracks simultaneously. Further, for indeterminate systems, an average boundary condition that restrains rigid body motion and rotation is introduced to make the system determinate.

Declaration

The work in this thesis is based on research carried out in the Computational Mechanics Group, School of Engineering and Computing Sciences, Durham University. No part of this report has been submitted elsewhere for any other degree or qualification and it is all my own work unless referenced to the contrary in the text. Parts of this work have been published in the following:

Conferences

R. Bird, W.M. Coombs, S. Giani, A discontinuous Galerkin *hp*-adaptive finite element method for brittle crack propagation. *in Proceedings of the 25th UKACM Conference on Computational Mechanics*, 12 - 13 April 2017, University of Birmingham, Birmingham., pp. 138-141, Birmingham: University of Birmingham, April 2017.

R. Bird, W.M. Coombs, S. Giani, Two dimensional configurational-force-driven crack propagation using the discontinuous Galerkin method with *rp*-adaptivity. *in Proceedings of the 24th UK Conference of the Association for Computational Mechanics in Engineering*, 31 March - 01 April 2016, Cardiff University, Cardiff., pp. 137-140, Cardiff: Cardiff University, April 2016.

Articles

First author publications towards this thesis:

R. Bird, W.M. Coombs, S. Giani. Accurate Configuration Force Evaluation via *hp*-adaptive Discontinuous Galerkin Finite Element Analysis. *Engineering Fracture Mechanics*, 216:106370, 2019.

R. Bird, W.M. Coombs, S. Giani. A posteriori discontinuous Galerkin error estimator for linear elasticity. *Applied Mathematics and Computation*, 344:78 - 96, 2019.

R. Bird, W.M. Coombs, S. Giani. A quasi-static discontinuous Galerkin configurational force crack propagation method for brittle materials. *International Journal for Numerical Methods in Engineering*, 113(7):1061 - 1080, 2018.

First author publication separate to this thesis:

R. Bird, W.M. Coombs, S. Giani. Fast native-MATLAB stiffness assembly for SIPG linear elasticity. *Computers & Mathematics with Applications*, 74(12):3209 - 3230, 2017.

Contributions to the following publication:

W. Ai, R. Bird, W.M. Coombs, C.E. Augarde. A configurational force driven cracking particle method for modelling crack propagation in 2D. *Engineering Analysis with Boundary Elements*, 104:197 - 208, 2019.

S. O'Sullivan, R. Bird, W.M. Coombs, S. Giani. Rapid non-linear finite element analysis of continuous and discontinuous Galerkin methods in MATLAB. *Computers and Mathematics with Applications*, In Press, 2019

S. Guarin-Marthe and S. Nielsen and R.E Bird and S. Giani and G. Di Toro. Earthquake Nucleation Size: Evidence of Loading Rate Dependence in Laboratory Faults. *Journal of Geophysical Research: Solid Earth*, 124(1):689 - 708, 2019.

The following research would not have been possible without generous funding from the Engineering and Physical Sciences Research Council[1], School of Engineering, Durham University, and the European Commission-funded RISE-project BESTOFRAC[2].

I have had assistance from many people throughout my time in Durham. Firstly I thank my supervisors Dr William M. Coombs and Dr Stefano Giani, they both invested a significant portion of their time during my studies to make me into the research who I am today, their input was invaluable. They were always available to listen and discuss my research ideas, give me guidance, correct my writing and mathematics, as well as being inspiring researchers to work with. I must also thank my peers at Durham, Lei Fan, Dom, Tom, Tim and El made my time here at Durham particularly enjoyable, I hope my office antics did not distract you too much! Additionally Phil, my housemate, thank you for putting up with me. I am also very grateful to my friends outside of Durham, Jen, Al, Skinny, Tim, Ellen, Chloe, Jenny and Helen, and in particular my brothers, James and Thomas; all supported me throughout my PhD.

I was also very lucky to have the opportunity to perform research in Padova, Italy. This position would not have been possible without Professor Charles Augarde, and Professor Francesco Pesavento who I thank for his expertise and guidance. Also, Giovanna and Nico, who were incredibly welcoming and made my time in Italy a very enjoyable experience - I do miss the Italian sun and coffee.

Last, it would not have been possible to write this thesis without my pals, Chris and Sophie.

Robert E. Bird
Durham, September 2019

[1]EPSRC grant number EP/M507854/1
[2]European grant number 734370

Contents

List of Figures

List of Tables

List of Algorithms

Nomenclature

Abbreviations

BC	boundary condition
BEM	boundary element method
CF	configurational force
CG	continuous Galerkin
CZM	cohesive zone model
DG	discontinuous Galerkin
DOF	degrees of freedom
DG-XFEM	discontinuous Galerkin eXtended finite element method
FE	finite element
FAA	Federal Aviation Administration
FEA	finite element analysis
FEM	finite element method
Lagrange multipliers	LM
LHS	left hand side
LEFM	linear elastic fracture mechanics
MCSC	maximum circumferential stress criterion
MSEDC	minimum strain energy density criterion
MSERRC	maximum strain energy release rate criterion
NDOF	number of degrees of freedom
RHS	right hand side
SEN	single edge notched
SIF	stress intensity factor
SIPG	symmetric interior penalty discontinuous Galerkin
XFEM	eXtended finite element method

Identifiers

$(\cdot)\bar{}$	applied BC
$(\cdot)^h$	approximation of variable
$(\cdot)_q$, $(\cdot)_g$	Gauss point indices
$(\cdot)_{\text{start}}$	first value in a series of hp mesh refinements
$(\cdot)_{\text{end}}$	last value in a series of hp mesh refinements
$\widehat{(\cdot)}$	local element parameter
$(\cdot)^I$	mode I component
$(\cdot)^{II}$	mode II component
$(\cdot)_{xx}$	plane component in x
$(\cdot)_{yy}$	plane component in y
$p_{(\cdot)}$, $p^{(\cdot)}$	polynomial order of $(\cdot)$
$(\cdot)_{xy}$	shear component in xy
$(\cdot)^E$	variable for element edge E
$(\cdot)^V$	variable for element vertex V
$(\cdot)^F$, $(\cdot)_F$	variable of edge F
$(\cdot)^{\widehat{K}}$, $(\cdot)_{\widehat{K}}$	variable of element $\widehat{K}$
$(\cdot)^{K+}$, $(\cdot)_{K+}$	variable of element K^+
$(\cdot)^{K-}$, $(\cdot)_{K-}$	variable of element K^+
$(\cdot)^K$, $(\cdot)_K$	variable of element K
$(\cdot)'$	variable of local system

Scalers

$a_{(\cdot)}$	Gauss point weight for axes α
A^+, A^-, C^+, C^-	crack tip asymptotic expansion coefficients for singular terms
$b_{(\cdot)}$	Gauss point weight for axes μ
B_n^+, B_n^-, D_n^+, D_n^-	crack tip asymptotic expansion coefficients for regular n terms
b H L W	domain dimensions

C	hidden and unknown constant
$C(i,j)$	material compliance constant in position (i,j) of $[C]$
c_η	efficiency constant
C_η	reliability constant
C_Σ	CF error estimator unknown constant
$D_{\max}$	maximum value of $\lvert D_{ijlm}\rvert$
d_l	Measure of element distortion
$d(i,j)$	material stiffness constant in position (i,j) of $[d]$
$D(i,j)$	material stiffness constant in position (i,j) of $[D]$
$\mathscr{D}$	Power dissipation
E_Y	Young's modulus
$E_{Y,1}$, $E_{Y,2}$	Young's moduli of principal orthotropic material directions 1 and 2
E^+, E^-, F^+, F^-, G^+, G^-	crack tip asymptotic expansion coefficients
F	user defined propagation length
$F(x,y)$	Stress function
g_c	Griffith failure criteria
G_{12}	Shear modulus between directions 1 and 2
h_{cF}	characteristic mesh size at the crack tip
h_F	length of edge F
h_{cF}	length of refined elements edge around the crack tip
h_K	diameter of element K
$h_{\max}$	maximum element size in mesh
h_o	increase in crack length
K_c	element with number c
K_I	mode I SIF
K_{II}	mode II SIF
$\lvert K\rvert$	area of K
l	length of ignored region R
n	node number
p	polynomial order of a function
$p_(\cdot)$	polynomial order of K
$p_{\bar{K}}$	polynomial order of $\bar{K}$
$p_{\min}$	minimum element polynomial order in mesh
$\mathscr{P}$	Power applied to a body
q	virtual work function
q_{hp}	hp-adaptivity count
r	radius
r_A, r_B	Westergaard radii
r_d	radius of CF domain integral
r_h	radius about the crack tip with refined element size
R_K	element refinement flag
r_p	radius about the crack tip with elements fo refined polynomial order
s	Sobolev regularity
S	Generation of the mesh
t	time
u	Displacement in x
u_r^+, u_r^-	radial displacement on Γ^+ and Γ^-
v	Displacement in y
(x,y)	Cartesian coordinate system
α	a positive unknown constant
α_{11}, α_{12}, α_{22}	anisotropic mode I coefficients
(α,μ)	Cartesian coordinate system for $\widehat{Q}$
β_{11}, β_{12}, β_{22}	anisotropic mode II coefficients
β_F	Total penalty constant for edge F
γ_F	young's constant for the edge F
$\Delta\mathscr{D}$	Discrete power dissipation

$\Delta\gamma_I$	Karush-Kuhn-Tucker variable
δ_2, δ_1	refinement criteria constants
ϵ	unknown small value
ζ	local Gauss quadrature coordinates
η	residual based *a posteriori* error estimate
η_c	error estimate computed over subdomain of $\mathcal{T}$
$\eta^2_{F,K}$	residual based *a posteriori* error estimate for jumps in stress
$\eta^2_{J,K}$	residual based *a posteriori* error estimate for jumps in displacement
$\eta_{\max}$	maximum element error
$\eta^2_{R,K}$	residual based *a posteriori* error estimate for interior error of K
$\eta_{\lvert R\rvert}$	error of $g_i^{\Gamma\setminus R}$ from ignored region R on the crack edges
η_Γ	error measure of the edge integral of $g_i^{h,\Gamma\setminus R}$
θ	angle
θ_A, θ_B	Westergaard angles
κ	isotropic SIPG penalty parameter
κ_F	anisotropic penalty parameter for F
$\varkappa$	defined crack propagation length
μ	shear modulus
μ μ_1, μ_2, μ_3, μ_4	roots of biharmonic equation
$\bar{\mu}_1$, $\bar{\mu}_2$	complex conjugate of roots μ_1 and μ_2
ν	Poisson's ratio
ν_{12} ν_{21}	Poisson's ratio between orthotropic material directions 1 and 2
σ	uniaxial tensile stress
σ_∞, τ_∞	Plane and shear stress an infinite boundary
Ψ	Total internal energy of a body
$\hat{\psi}$	free energy function
$\psi^E_{p_e}$	edge functions of K where $E \in \{e1, e2, e3\}$ and $2 \leq p_e \leq p_K$
$\psi^B_{p_b}$	bubble functions of K where $3 \leq p_b \leq p_K$
ψ^V	vertex shape functions of $\widehat{K}$ where $V \in \{v1, v2, v3\}$
$\omega_{\cdot,\cdot}$	anisotropic mode II parameter

Tensors

$\dot{a}_i^t$	velocity of crack tip
$\dot{u}(\cdot)_i^t$	spacial velocity
C_{ijlm}	material compliance tensor
D_{ijlm}	material stiffness
d_{ijlm}	square root of D_{ijlm}
f_i	body force
g_i	crack tip CF
G_i	nodal CF
g_i^D	applied Dirichlet function
g_i^N	applied Neumann function
g_i^T	applied Roller function
$g_i^{h,D}$	domain CF calculation
$g_i^{h,t}$	tip CF calculation
$G_i^{V,K}$	nodal CF of vertex V for K
$g_i^{h,\Gamma}$	domain with edges CF calculation
$g_i^{h,\Gamma\setminus R}$	domain with partial crack edges CF calculation
H_{ijpq}	Jacobian tensor
J_{ij}	Jacobian matrix
m_i	element edge tangent
n_i	normal to an edge
n_x	normal in x direction
n_y	normal in y direction
$n^{\parallel}$	tangent to boundary

s_i	velocity function
$t_i(\cdot)$	traction on the edge F
u_i	Displacement
$U^{B,K}_{i,p_b}$	bubble function coefficient for K
$U^{E,K}_{i,p_e}$	edge function coefficient for K
$U^{V,K}_{i}$	vertex shape function coefficient for K
v_i	total spacial velocity
V_i	total material velocity
$V_i^{\partial\Gamma}$	crack tip node material velocity
w_i	test function
x_i^a x_i^b	edge nodes
$x_i^{e\prime}$	updated edge node
x_i^c	new crack position
X_i^c	current crack position
x_i^m	coordinate of node n_m
δ_{ij}	Kronica delta idenity
Δo_i	Discrete crack propagation length
ϵ	Levi-Civita tensor
ε	small strain
(η, ξ)	Cartesian coordinate system of $\widehat{K}$
θ_i	reference coordinate system
σ_{ij}	Cauchy stress
Σ_{ij}	Eshelby stress

Vectors

$\{f\}$	body force
$\{F\}$	right hand side to SIPG equation
$\{G\}$	nodal CF
$\{g^D\}$	Dirichlet function
$\{g^{h,D}\}$	domain CF calculation
$\{g^{h,t}\}$	tip CF calculation
$\{G^{\mathcal{T}_K}\}$	CF values for all nodes in $\mathcal{T}_K$
$\{g^{h,\Gamma}\}$	domain with edges CF calculation
$\{g^{h,\Gamma\setminus R}\}$	domain with partial crack edges CF calculation
$\{g^N\}$	Neumann function
$\{g^T\}$	roller boundary function
$\{h\} = \{\nabla u\}$	displacement spacial derivatives
$\{n\}$	normal vector
$\{sigma(\cdot)\}$	stress
$\{t(\cdot)\}$	traction
$\{U^K\}$	trial function coefficients for all DOF of K
$\{U^{\mathcal{T}}\}$	trial function coefficients for all DOF in the mesh $\mathcal{T}$
$\{V\}$	material velocity
$\{V^K\}$	material velocity shape function coefficients
$\{\nabla V\}$	gradient of material velocity
$\{W^{\mathcal{T}}\}$	test function coefficients for all DOF in the mesh $\mathcal{T}$
$\{W^K\}$	test function coefficients for all DOF of K
$\{\alpha\}$	arbitrary average BC values
$\{\Sigma(\cdot)\}$	Eshelby stress
$\{\varepsilon(\cdot)\}$	small strain
$\{\partial V\}$	crack tip node material velocity

Matrices

$[B^K]$	basis function derivatives for K
$[B^V]$	Vertex shape function derivatives
$[BB^K]$	second order derivatives of basis functions for K

$[C]$	material compliance matrix
$[C^K]$	shape function derivates for average rotation BC
$[D]$	material stiffness matrix
$[D_2]$	reorder material stiffness matrix
$[h]$	displacement spacial derivatives
$[H^K]$	all shape function derivates for K
$[K]$	global stiffness matrix
$[K_u]$	average BC matrix for u
$[K_v]$	average BC matrix for v
$[K_R]$	average BC matrix for rotations
$[n]$	normal matrix
$[N]$	basis function matrix
$[N^K]$	basis functions for K
$[n^\Sigma]$	normal matrix for CF calculation
$[R]$	rotation matrix
$[S]$	tensor to engineering strain conversation matrix
$[q]$	virtual work function matrix

Spaces

$L^2(\cdot)$	L^2 norm
$H(\cdot)^s$	Hilbert space to regularity s over the domain $(\cdot)$
$\mathbb{R}$	Set of real numbers
$W_{\underline{p}}(\cdot)$	hp-discontinuous Galerkin finite element space

Elements and Sets

A	Area around the crack tip
$\mathscr{B}$	Reference domain
C	parth around the crack tip
C_A, $C1$, $C2$, $C3$, $C4$	integral paths around the crack tip
$C(K)$	Set of four children elements crate by the homogeneous h-refinement of K
$\{e1, e2, e3\}$	Edges of triangular element
E_r, E_p	change to $\mathfrak{T}_r$ and $\mathfrak{T}_p$
F	edge of the mesh skeleton
$F_{(\cdot)}$	edge with number
F_c	most align edge with CF
$\mathcal{F}(\cdot)$	set of edges
$\mathcal{F}_B(\cdot)$	set of external edges
$\mathcal{F}_D(\cdot)$	set of Dirichlet edges
$\mathcal{F}_I(\cdot)$	set of internal edges
$\mathcal{F}_K$	set of edges of example mesh
$\mathcal{F}_N(\cdot)$	set of Neumann edges
$\mathcal{F}_T(\cdot)$	set of traction edges
K	Triangular element
$\widehat{K}$	Reference element
$\bar{K}$	Element of $\bar{\mathfrak{T}}$
$K_{(\cdot)}$	Triangular element with number
K_a	element which contains the new crack tip position in its interior
$K^{(c,p)}$	element which has a parent p and is given the child number c
$\widehat{L}$	Reference Gauss quadrature domain
N_E	set of all nodes connected to node n_a by a single face
n_b	set of nodes within A
n_c	current crack tip node
n'_c	new crack tip node
n_e	node connected to n_a by a single face
n_m	nearest node of K_a to x_i^c
n_p	set of nodes corresponding to elements of high polynomial order

n_t	nodes at the crack tip
$\underline{p}$	polynomial order of all elements in mesh $\mathcal{T}$
$\mathcal{P}_{p_{p_K}}(\cdot)$	linear independent set of polynomial functions with maximum degree (p_K)
Q	domain along the crack edges $(\Gamma^+ \cup \Gamma^-) \setminus R$
$\widehat{Q}$	Reference Square
R	ignored integral region of $\{g_i^{h,\Gamma\setminus R}\}$
$\underline{\mathrm{R}}$	vector of elements h-refinement flags
S	Polynomial approximation space of total spacial and material velocity
$\mathcal{T}$	Mesh of elements
$\mathcal{T}'$	new propagation mesh
$\bar{\mathcal{T}}$	Future mesh
$\mathcal{T}_a$	set of elements which contain to node n_a
$\mathcal{T}_c$	subset of mesh $\mathcal{T}$
$\mathcal{T}_H$	Set of elements of $\mathcal{T}$ marked for h-refinement
$\mathcal{T}_K$	set of elements of example mesh
$\mathcal{T}_p$	Set of elements of $\mathcal{T}$ marked for p-refinement
$\mathcal{T}_r$	Set of elements of $\mathcal{T}$ marked for r-refinement
$\mathcal{T}_S$	Mesh of generation S
$\mathcal{T}_\Gamma$	propagation mesh to determine $g_i^{h,\Gamma\setminus R}$
$\{v1, v2, v3\}$	Vertices of trianglular element
Γ	continuous cracked edge
$\Gamma^+ \cup \Gamma^-$	seperated crack edges
$\bar{\eta}_c$	set of domain error estimator values
Ω	continous cracked domain
Ω_Γ	Problem domain
∂K	Element boundary
$\partial\Gamma$	crack tip
$\partial\Omega_D$	Dirichlet boundary
$\partial\Omega_N$	Neumann boundary
$\partial\Omega_{NO}$	homogeneous Neumann boundary
$\partial\Omega_T$	Traction boundary
$\partial\Omega_\Gamma$	Problem domain boundary

Operators

$a(\cdot,\cdot)$	SIPG bilinear form
$\mathrm{d}s$	integrand over an edge
$\mathrm{d}v$	integrand over an area
$\det(\cdot)$	determinant
F_K	affine transformation
$\lvert\cdot\rvert$	scaler normal
Ξ	Degenerate square to triangle mapping
Π_i^t	Reference to material mapping at time t
∇_i	Differential operator
$\cup$	Union of sets
$\cap$	Intersection of sets
$\forall$	for all
$l(\cdot)$	right hand side of bilinear form
$[\![\cdot]\!]$	jump operator
$\langle\cdot\rangle$	specialised jump operator
$\{\cdot\}$	Average operator
$(\cdot)^\top$	transpose operator
$\Theta_{\widehat{F}}$	line to $\widehat{F}$ of triangle operator
$(\cdot)\circ(*)$	function $(\cdot)$ dependent on function $(*)$
$\lVert\cdot\rVert_{0,(\cdot)}$	L^2 norm over $(\cdot)$
$\lVert\cdot\rVert_{s,(\cdot)}$	$H^s(\cdot)$ norm
$\lVert\cdot\rVert_{\mathcal{T}}$	DG energy norm over $\mathcal{T}$

$\|\cdot\|_{\mathrm{DG}}$	extended DG energy norm over $\mathcal{T}$
$\|\|\|\cdot\|\|\|_{\mathcal{T}}$	SIPG energy norm over $\mathcal{T}$

Chapter 1

Introduction

The study of fracture mechanics is critical to ensuring the safe design and maintenance of engineering structures. Prior to World War II, the subject of fracture was not of particular interest to engineers. Hence, during WWII numerous, and at the time inexplicable, critical fracture failures occurred. A notable example was the use of liberty ships in the north sea which experienced total failure from fracture. A particularly famous example was the ship SS Schenectady [8]. After North Sea trials she was moored at Swan Island, when suddenly the hull cracked in half. This was not a singular occurrence and by 1946, 362 ships of the Liberty ship fleet had suffered at least one major fracture; of these 103 sustained fractures which threatened the structural integrity of the ship. It was concluded that poor welds, produced either by awkward designs or rushed manufacture, and low-grade cold steel components were the source of imperfection that caused *brittle fracture*. Fracture mechanics in brittle materials at this time was poorly understood however, even after interest in the subject gained traction and interest, catastrophic failure through fracture mechanisms still occurred. For instance, the civil aviation industry is particularly vulnerable to *cyclic fatigue fracture* brought about the pressurisation and de-pressurisation of the cabin. Famously in the 1950's, the de Havilland Comet aircraft, the first civil aviation aircraft to be powered by jet engines, experienced three fatal crashes, brought about by *cyclic fatigue* crack growth of the fuselage skin [9]. It was concluded that the crack initiated from the corners of the aircrafts' square windows. Similarly, in 1988 the Boeing 737 of Aloha Airlines Flight 243 experienced a catastrophe failure through fatigue fracture, the plane survived but suffered one fatality. The plane experienced an explosive decompression with approximately 18 feet of cabin skin and structure above the floorline was immediately removed from the plane, leaving an open cabin during flight. It was concluded in the FAA report that the aircraft failed due to *"multiple site fatigue cracking of the fuselage lap joints"*. However, total failure of structures from fatigue fracture, and subsequent propagation, is not unique to aircraft. In 1980 the Alexander L. Kielland oil platform capsized, of the 212 people on board 123 were were killed. It was concluded that a crack initiating from a poor fillet weld which attached a hydrophone to the structure was the cause of the failure. The poor weld, cold weather and cyclical loading conditions induced on the structure from the North Sea waves caused crack growth through fatigue fracture [10]. More recently fractures have been developing in the graphite core of ageing fission reactors induced by irradiation. As continuously monitored, it is unlikely to lead

to catastrophic failure but, there are significant finical implications to shutting a reactor down. An example is Hunterston B reactor, owned by EDF, which was shutdown in 2018 and reopened in 2019 [11]. Demonstrating the core was still safe, and will continue to be safe until 2023, cost EDF £125 million [12]. This does not include the loses incurred from the reactor not producing and selling power.

Crack growth can be predicted through the use of numerical analysis, there are numerous techniques all with their own advantages and disadvantages which are well suited to some problems and less well suited to others. However, before discussing the various techniques available and why I chose my direction of research it is necessary to comment on several pieces of ground breaking analytical work without which, the various numerical methods for fracture prediction would not exist. Arguably, the first significant study on understanding the stress field in a linear elastic plate was performed in 1939 by Westergaard [13]. He considered an infinite plate containing a double ended crack with a uniform plane, or shear, stress traction applied at an infinite boundary. The solution was developed using a method originally presented by Muskhelishvili [14], in essence describing the stress field with a complex variable function and solving a biharmonic description of stress in a isotropic homogeneous material. Since the problem was of infinite size the solution was not necessarily useful for engineering problems however, for the first time a description of a stress field about a crack tip had been produced. Later in 1952, Williams [15] visited the problem and developed the Westergaard solution further by solving an eigenvalue problem of a single crack in a finite domain with arbitrary loading conditions. Unlike the Westergaard solution, the Williams solution was not in closed form. However, if an infinite boundary with a uniform stress field is considered, the Westergaard solution can regained. Even more critically, in the limit of a point becoming close to the crack tip, the Williams solution demonstrated that for an arbitrary boundary condition (BC) the local crack tip stress field always exhibited the same singular stress function, a result *essential* for many numerical techniques. In 1957 Irwin [16] took the form of the Westergaard and Williams solution and produced a local crack tip stress solution. Irwin coined the term stress intensity factor (SIF), a series of coefficients that described the strength of the singular stress field at the crack tip when an arbitrary boundary condition is applied to a domain. It was considered that a crack either acts in a pure opening mode, mode I, a shear mode, mode II, or combination of the two known as mixed mode. The two modes have a respective SIF. Tangential to these publications was the work of Eshelby [17, 18] and Rice [19], both derived analytical expressions to describe how a crack propagates through a material given a particular failure criterion such as, the Griffith [20] or Paris Law [21]. Their approaches to deriving an expression were different however, for a planar propagating crack they arrived at the same conclusion. Eshelby considered a global postulate of energy being dissipated away from a body by a moving crack front, this forms the basis for using Configurational Forces (CF) as a technique for crack propagation [18]. Whereas, Rice examined a local crack tip expression for the dissipation of energy of a crack moving in a planar fashion [19], which is known as the J-integral. Given that the local stress field at the crack tip is understood and that there are analytical techniques for describing how a crack propagates through a material, it is now possible to consider numerical techniques which approximate, to a

lesser or greater degree, both of these aspects.

1.1 Numerical analysis

For problems with arbitrary domain shapes, BCs, number and shape of cracks, numerical analysis is used to determine how and when a crack will propagate. Using the theories of [13, 15, 16, 19] numerous methodologies, which can be applied to a range of numerical schemes, are available to determine the stress field local to the crack tip and the strength of the crack tip stress singularity. A comprehensive literature review of combined numerical schemes and methodologies to determine the local stress field about the crack tip is presented in Chapter 3. Here the state-of-the-art methodologies to determine the stress field local to the crack tip, and the corresponding SIFs, are summarised:

- The J-integral can be used directly as a path independent line integral around the crack, or its equivalent domain integral form, to determine directly the SIF for a pure mode I problem [22]. However, if the near tip stress solution is known *a priori* the J-integral can be used in conjunction with an auxiliary stress and displacement field to determine the mode II SIF. This is known as the M-integral, or interaction integral, technique [23].

- The displacement basis functions, and therefore stress field, can be enriched directly with the crack tip displacement solution. Additionally, the jump in displacement across the crack edges can be approximated with a Heaviside function [24]. Including enrichment basis functions allows for the singular stress fields at the crack tip to be captured, therefore optimal convergence of the stress solution, which was limited by the singular stress behaviour, can be restored. Enriched methods allow for the evaluation of the SIFs directly, or can be used with the M-integral post-processing technique.

- The stress field can be evaluated using a CF approach which determines the crack propagation driving force directly. The CF can be expressed using SIFs [1, 4]. There is no necessity for the stress field to be known *a priori* unlike the previous methods mentioned however, the numerical formulation could be enriched with the local crack tip solution to improve the convergence rate and crack tip stress field.

An extension to LEFM is the use of a cohesive zone model (CZM). The main purpose of the CZM is two-fold:

1. In LEFM the stress field asymptotically close to the crack tip tends to infinity, $\sigma \to \infty$, the CZM argues that no material, however brittle, can withstand such a high stress [25, 26]. A cohesive zone is therefore considered along the crack edges, also known as a plasticisation / process zone at the crack tip. As the crack edges separate the cohesion between them becomes weaker until, the cohesive force no longer exists. The energy required to fully separate the edges is the energy dissipated by the crack propagating. The coupled traction condition is implemented with a material dependent stress-relative displacement law [27]. This forms a non-linear material problem localised at the crack tip [28].

2. The inclusion of a CZM zone model removes the stress singularity from the problem. The impact numerically is that the solution is smooth, and as such numerical difficulties associated with modelling the crack tip singularity are avoided.

The introduction of the CZM creates two tips. The first tip is the physical tip, it is defined as the position along the crack edge where tractions vanish. The second tip is a fictitious tip were the relative jump in displacements across the crack edges is zero. The non-linear material behaviour around the crack tip can be confined to the fracture process zone on the crack edges. The CZM model introduces non-linearity into the model with extra parameters necessary to describe material behaviour. There does not exist a singular stress-strain law which describes the process zone around the crack tip. A comprehensive review of CZMs can be found in [29, 30].

As mentioned above, analytical stress solutions for problems with specific loading conditions, domain shapes and crack topologies have been derived by Williams and Westergaard. Since the materials considered are small strain linear elastic, it is possible to use the principle of superposition to combine solutions; such as generating a mixed mode solution by combining the mode I and II Westergaard solutions. Engineering handbooks where empirical expressions are provided for common shaped domains and cracks experienced during engineering design, [31]. However, for the general LEFM problem a general method to determine the solution is required. Engineers therefore consider numerical methods for solving problems containing cracks. A review of numerical methods for fracturing problems can be found in [32]. The introduction now proceeds to examine and discuss the various numerical methods which are used throughout the literature to model problems containing static and propagation cracks.

XFEM

The eXtended Finite Element Method (XFEM) is an enriched form of the Finite Element Method (FEM) used for crack propagation [24]. The element basis of the FEM is enriched with two functions

1. A Heaviside function that estimates the jump in displacement that exists because of a crack edge (or surface). This removes the necessity for the crack path to coincide with element edges as the function enables jumps in displacements on the interior of elements. This removes the need for remeshing since the crack path is described by a function and not the mesh skeleton. This has been applied to modelling discontinuities in

2. The elements local to the crack tip are enriched with the near crack tip displacement solution, [15]. As the mesh contains the singular solution at the crack tip, optimal convergence of the global is restored [33] because the polynomial basis functions within the mesh are only considering a regular problem. Additionally, it was shown with a coarse mesh that accurate stress solutions can be obtained [24].

The SIFs, or CF, at the crack tip are found by either using the M-integral [24] or by making the SIFs a coefficient of the linear system to be solved for [34]. However, the singular stress and Heaviside function make the system of equations inherently difficult to solve, [33], the local crack tip stress solution has to be known *a priori*. XFEM is also notoriously for being difficult to implement in 3D. An excellent review of XFEM methods can be found in [35].

XBEM

As the name suggests the eXtended boundary element method (XBEM) discretises the problem domain on the boundary, rather than the interior like FEM. With respect to the problem domain the mesh is a dimension less [36]. The boundary element method (BEM) is therefore economical in terms of the problem's number of degree of freedom (NDOF). However, the linear system involves a fully populated non-symmetric stiffness matrix. This is computational expensive to solve, techniques are derived specifically to help solve the system of equations [37]. The BEM formulation naturally requires the evaluation of weakly singular, strongly singular and hypersingular (for the fracture case), functions which have to be carefully treated [38, 39].

The techniques available to BEM to determine the SIFs for cracks are the same as FEM. However, when discretising the crack edges elements which are coincident in space will exist, one for each crack edge, and wrong solutions will be obtained [40]. Hence, the dual-BEM method is required [41]. The first author to form an XBEM for fracture problems was Simpson *et al.* [42], who subsequently published a thesis in which a comprehensive review of the BEM and the corresponding implementation is provided [43].

Phase field

Generally, a phase field model in numerical analysis is a mathematical tool for solving problems containing interfaces. The phase field is used to differentiate between multiple physical phases. The first work to consider phase field and fracture was by Bourdin *et al.* [44]; for fracture mechanics problems the phase field is a variable that interpolates between the fully broken and unbroken states (physical phases) of the fracturing material, [45]. A *thermodynamically consistent* phase field model, preventing crack repair, was derived by Miehe *et al.* [46, 47]. The phase field and linear elastic models are coupled, the irreversible development of the phase field is dictated by tensile strain energy, with consideration to the Griffith failure criteria. This results in damaged material. The coupled equations can be either be solved in a monolithic or staggered algorithm.

The Phase field model can capture crack initiation, crack branching and fracture instability. However it has a few drawbacks

- It can produce unrealistic results such that the entire domain becomes damaged simultaneously with no representation of a crack.
- It is numerically expensive since significant refinement needs to occur around the crack edges and tip where the phase field, and therefore transition from an unbroken to broken state, has high gradient values [47]. However, techniques to reduce the computational cost of damage-like models have been presented, see [48] who introduce an adaptive model order reduction (MOR) technique for non-linear fracture which reduces computational effort.
- It is further computationally expensive as the couple problem adds DOF from the phase field model. Additionally if a monolithic solver is used the problem is non-linear.
- The phase field model contains a parameter l, which dictates the distance over which phase transitions occur. The geometry of the crack is therefore approximated and considered

smeared. As the crack is smeared the width of the crack separation cannot be defined exactly further, pure traction free edges can also not be defined [49].

A thorough review of the use and implementation of phase field fracture can be found in [45].

Meshless methods

Unlike finite element and boundary element methods, meshless methods do not discretise the problem space with elements which contain interpolation functions. Instead of using an element mesh to approximate the weak formulation, meshless methods utilise an interpolation scheme with shape functions. In elasticity this method was first considered by Belytschko *et al.* [50], otherwise known as the element free Galerkin method. The nodes in the domain act as a nodal support for the shape functions.

The first use of meshless methods for crack propagation was performed by Belytschko *et al.* [51]. The key novelty of meshless methods over the standard FEM for crack propagation is that there is no need to remesh during propagation. Meshless methods can account for the crack edge discontinuity by simply truncating a node's domain of influence, this is known as the visibility criterion, Belytschko *et al.* [51]. There are also other methods to model a crack, such as the diffraction criterion [52]. Like all numerical methods, the solution at the crack tip can be improved with the near tip displacement field, a methodology for enriching the crack tip for is provided in [53]. When a meshless method is combined with a methodology to model crack edges and a tip it is more commonly referred to as a cracked particle method. For a thorough description and comprehensive literature review see the works and the references therein of [54–57].

The tools for evaluating the stress field, the CF and the SIFs are the same as those for FEM and BEM. In conclusion, meshless methods in terms of crack tip evaluation have the same issues as the FEM and BEM however, the crack propagation is easier to facilitate since the numerical method is meshless.

Peridynamics

One of the more recent methods developed for modelling fracture problems is called peridynamics, designed specifically for problems containing evolving discontinuities, such as fracture problems [58]. The numerical analysis is not based on a weak formulation of the governing equations for solid mechanics, a partial differential equation. Instead, it is based on integral equation form of internal elastic energy. Internal forces are expressed through non-local interactions between pairs of material points within a continuous body with damage forming part of their constitutive model. An interaction between particles is known as a bond, analogous to a spring, with the area of influence that particles interact called the horizon. Failure, and subsequently fracture, is introduced in the material model by the breaking of the bonds connecting particles. Breaking occurs once a stretching of the bond between the two particles reaches a limit; once a bond fails it does not reconnect.

Using a peridynamic formulation, cracks can be initiated and branched through the breaking of bonds. Since the set of strong form governing partial differential equations is replaced by bonds, which are described in terms of displacement, the necessity to evaluate stress singular-

ities for fracture propagation is removed. The solution is dependent on the horizon value but it is suggested the horizon could be undiscovered material parameter [59]. Further, the peridynamic solution requires significant computational power due to the non-local nature of the method hence a solving the linear system of equations is expensive. Additionally, the continuum equations for solid mechanics are not modelled rather they are approximated through bond interaction and, the Neumann BC can only be implemented by virtue of a body force, as discussed in the review [32].

1.2 Thesis overview and scope

This thesis is concerned with the accurate modelling of the stress field about the crack tip to enable very accurate calculations of the crack tip CF for fracture propagation and fatigue analysis. A thorough literature review of the use of CFs in FEMs for fracture mechanics problems is presented in Chapter 3 with a comparison to the aforementioned numerical analysis schemes and fracture mechanics methods presented in the previous section. The most notable publications for the use of CFs in crack propagation by Miehe *et al.* [1, 4]. Here, an r-adaptive method for crack propagation driven by a nodal CF calculation was presented. It was argued that the crack tip CF vector could be used to determine the direction of crack propagation. The nodal CF calculation with r-adaptivity presents itself as a particularly convenient method to determine the crack propagation direction and fatigue life of a crack since:

- Unlike methods that use SIFs, there is no need to decompose the stress field at the crack to determine the CF.
- The CF calculation is a post-processing technique however, no new numerical mechanics is required to determine the CF when using a FEM.
- The CF calculation does not require any knowledge *a priori* for its calculation.
- r-adaptivity makes the crack propagation path less mesh dependent, and there is no need to remesh after each propagation step.

The use of a CF approach for crack propagation and fatigue life analysis therefore presents itself as an effective and simple method to use. But, the simplicity perhaps comes at a cost. Firstly, the maximum accuracy obtainable in literature using the tip CF method is $\approx 3\%$ [1] with higher accuracies of 0.01% achieved by [60] for a *very* specific set of BCs with quarter point elements [61]. The discrete formulation for the CF presented by Miehe for crack propagation disagrees with the formulations presented by other authors [2, 62–64]. Further, although the r-adaptive method requires no remeshing, it does require a degree of manipulation of the data structure to split element edge / faces and propagate a crack.

The work presented here introduces the concept of crack tip CFs to the symmetric interior penalty discontinuous Galerkin (SIPG) FEM. The SIPG FEM, as discussed in Chapters 2 and 4, is FEM that, due to its formulation, is particularly favourable to h- and p-adaptivity which when driven by an error estimator. It is therefore very effective at achieving highly accurate stress fields. This is used to accurately calculate the crack tip CF without having to resort to

enrichment functions to improve the solution. Additionally, error estimators are introduced to estimate the overall accuracy of the crack tip CF. The error estimates for the CF are therefore used as a criteria for crack propagation. By using CFs and *hp*-adaptivity, no *a priori* knowledge is used to required. This presents the possibility of a single method which can be used to determine the crack tip CF for a range of homogeneous material types. The analysis is limited to LEFM. This thesis consists of seven chapters, a short summary of the structure and the content of the chapters is provided:

- **Chapter 2**

  The second chapter in the thesis is concerned with the numerical framework in which all problems are cast; it forms the basis for all further numerical analysis. Here, the strong form statement for small-strain elasticity in two-dimensions is introduced with the continuous problem domain in which it is cast. The SIPG weak formulation with all weakly imposed BCs, and the corresponding weak SIPG space and discretised domain, is then introduced. This is followed by a description of the SIPG matrix form which is implemented in MATLAB. A series of convergence verification studies finalise the chapter, this includes all boundary conditions and, problems with smooth and non-smooth solutions.

- **Chapter 3**

  The aim of this chapter is to investigate the use of CFs as a method for fracture. The crack tip CF in the continuous domain is derived here from a global power minimisation postulate. From the literature, several different forms of the discretised form of the CF are presented. A discussion is provided as to where the difference in discrete formulations arises. This is then followed by the implications and limitations of each of the forms. Each form is subsequently implemented to support the discussion, a geometry driven *p*-adaptive scheme is also introduced and investigated.

- **Chapter 4**

  In order to obtain highly accurate stresses around the crack tip for the CF calculation, it is possible to *hp*-adaptive scheme driven by a residual based *a posteriori* error estimator. In this chapter such an error estimator is introduced and its implementation and ability to estimate the approximation error is verified. Then, an algorithm for error driven *hp*-adaptive scheme is presented with a description of the associated data structure. The error estimate, with *hp*-adaptive, is finally shown numerically to bound the SIPG approximation error from above and below for a smooth and non-smooth problem.

- **Chapter 5**

  Using the error estimator from the previous chapter a series of problems containing cracks, with and without analytical solutions, are solved to a high accuracy. From the results of these problems stronger conclusions are made to the arguments that were originally presented in Chapter 3; this is only made possible by the error driven *hp*-adaptivity. Subsequently, a novel algorithm for calculating the crack tip CF is derived. The proposed

method is highly accurate, domain independent, and requires no *a priori* knowledge of the local crack tip displacement and stress field. Further, error estimators which bound the error in the CF calculation from above are derived. Last, the proposed method for calculating the crack tip CF is validated using a set of mixed mode static crack problems containing multiple cracks in isotropic homogeneous materials. New benchmarks results for the CF are set for these problems.

- **Chapter 6**

  This chapter extends the analysis from the previous chapter to problems containing cracks in homogeneous anisotropic materials. First, however, an improvement is made to the penalty term for SIPG to make the weak formulation more robust to high levels of anisotropic material behaviour. Next, the proposed method to calculate the crack tip CF, presented in Chapter 5, is tested, with new benchmarks presented, for problems containing multiple mixed mode cracks in orthotropic and fully anisotropic homogeneous materials. The method is shown to be robust, but possible improvements are highlighted.

- **Chapter 7**

  The last results chapter is concerned with crack propagation. Two methods are presented: a *rp*-adaptive crack propagation method which is computational cheap but with limited accuracy and, a *hpr*-adaptive crack propagation method which is more expensive but highly accurate. The results of the two methods are compared against each other, and against results obtained in literature for isotropic homogeneous materials.

- **Chapter 8** In the last chapter conclusions are drawn from the observations of all previous Chapters. Ideas for future work and unexplored ideas that the author would have liked to perform are also provided.

1.3 Novel contribution

In this section the novel contribution to the literature from the thesis, and the associated papers generated during the PhD, is individually summarised by their subject.

1.3.1 Average boundary conditions

The average BCs are introduced, verified and validated in Chapter 2 alongside the introduction of the SIPG formulation. When the essential Dirichlet boundary conditions are missing in a simulation, the system of equations is indeterminate. The linear solver will probably be able to, dependent on the solver, *give a* solution to the problem however, for linear elasticity there is likely to exist an associated non-unique rigid body motion: translation, rotation, or both. The result of such a system, with any rigid motion, correctly satisfies the problem but, it does not represent the true solution to a problem. When only Neumann BCs are applied to a problem, authors in the literature either: apply a point Dirichlet BC condition in a position that is *likely* to be close to 0 m displacement or, apply no Dirichlet BC. As discussed thoroughly in Chapter 2, either approach will give the incorrect solution. Through the definition of rigid motion the

average BCs were defined. They are Lagrange multipliers (LM) for rigid translation and for rotation. The LMs are global quantities such that for an average BC a single LM exists. The average BCs are added to the linear system of equations and set to equal 0 m. This makes the system determinate such that a unique solution exists that is also the true solution to the problem.

1.3.2 *hp*-adaptivity and error estimation of the SIPG norm

The error estimator and *hp*-adaptive technique used throughout this thesis are described in Chapter 4 where:

1. The error estimator is numerically shown to be reliable and efficient for the error in the SIPG norm.

2. A *hp*-adaptive algorithm is presented with its implementation verified. Its ability to achieve exponential convergence for smooth and non-smooth problems is demonstrated.

The residual based *a posteriori* error estimator for the error in the SIPG norm was derived in [65] and was outside the scope of this thesis. The author's contribution to this paper was the numerical validation of the efficiency of the error estimator for the error in the SIPG as well as *all* numerical implementations of the *hp*-adaptive scheme, the linear system and the error estimator. The combination of using a residual based error estimator and a *hp*-adaptive scheme to improve the solution of an elliptic problem is not novel. However, the error driven *hp*-adaptive scheme facilitated the production of novel algorithms to directly calculate the crack tip CF. No *a priori* knowledge of the stress field at the crack tip is required to produce an accuracy as good as, and arguably higher, than methods that required information about the local crack tip stress field *a priori*. The residual based *a posterori* error estimator is also used, for the first time, to bound from above all calculated components of the proposed CF calculation. This is useful since it states how the error of the CF is converging and can be used to estimate the error of the CF computation. Further, this can be used as an accuracy criteria for crack propagation as shown in Chapter 7.

1.3.3 Accurate configurational force static crack evaluation

The key contribution to the literature from this thesis was an investigation into, the current state of the art methodologies for directly determining the crack tip CF and subsequently proposing a novel algorithm which overcomes the flaws of existing methods. This contribution is spread over Chapters 3, 4 and 5. The proposed method is subsequently used for crack propagation in Chapter 7.

In Chapter 3, three discrete crack tip CF calculations were cast within the SIPG formulation and investigated:

- A *tip* CF calculation which only considered the nodal CF value at the crack tip.
- A *domain* CF calculation which used an area integral around the crack tip.
- A *domain and edge* CF calculation which used an area integral around the crack tip with an edge integral along the crack edges.

All three methods used to calculate the crack tip CF were unable to do so accurately: the tip method was unable to produce accurate or achieve optimal, or consistent, convergence results for any problem, the domain method could achieve optimal and consistent convergence for the Westergaard problem however, was also shown to be domain dependent when the energy solution was not continuous across the crack edges. The domain method with the crack edges was unable to achieve convergence for the Westergaard problem but, for the inclined crack problem its formulation was shown to be domain independent. For all methods one way or another, directly determining the CF at the crack tip without using *a priori* knowledge of the crack tip stress field produced a flawed methodology. Hence, a new method for achieving accurate values for the crack tip CF was developed using the *hp*-adaptive scheme and error estimator, and is presented in Chapter 4.

In Chapter 5 a new technique to calculate the crack tip CF which is accurate, domain independent and requires no knowledge of the local crack tip stress field *a priori* is presented. Fundamental to the method is the error estimator and *hp*-adaptive scheme presented in Chapter 4. In order to develop a new method, it was necessary to understand and discuss, using nodal CFs, why the methodologies were domain dependent. Additionally, it was necessary to compare the SIPG solution space at the crack edges, next to the crack tip, with the functional space of the known local crack tip stress solution. This mathematical analysis was supported by the *hp*-adaptive algorithm producing a thorough numerical investigation. As well as producing an accurate method for determining the crack tip CF, the chapter goes further by developing numerical error estimators, based on the residual based error estimator in Chapter 4, for all components of the proposed crack tip CF calculation. The error estimators estimate the maximum error of the CF calculation, also to verify the convergence of the CF calculation with *hp*-adaptivity for problems with unknown solutions.

The algorithm for computing the crack tip CF from Chapter 5 is then used in Chapter 6 for anisotropic materials. The algorithm was used successfully, with no changes required to achieve accurate and exponentially converging results for components of the CF calculation. The penalty term for the SIPG formulation was also improved by considering the coercive proof for homogeneous anisotropic linear elasticity; the new penalty term was validated for very high levels of anisotropic material behaviour. However, the chapter does highlight issues with the algorithm for the proposed crack tip CF technique. In particular it is shown that the algorithm could be made more robust to the *hp*-adaptive refinement parameters δ_2 and δ_1. This could be achieved by using the error estimates of $\{g^{h,\Gamma\setminus R}\}$ $\eta_{|R|}$, the error introduced by ignoring a region of the crack edge, and η_Γ, the error in the crack edge computation, to control how $|R|$ was reduced with *hp*-adaptivity. However, it must also be noted that these observations and conclusions were only possible due to the newly proposed error estimates $\eta_{|R|}$ and η_Γ. However, very good agreement between the crack tip CF values from the calculation proposed here and those in the literature was achieved, with all associated error estimates for the CF calculation converging exponentially.

1.3.4 Crack propagation

From the conclusions of the previous chapters, which evaluated different methodologies for determining the CF at static crack tips, two novel algorithms for brittle crack propagation are proposed, each with their own advantages and disadvantages.

1. A less accurate but faster and simpler algorithm denoted an *rp*-adaptive algorithm. This algorithm agrees well with the results obtained in the literature, computational cheap and relatively simple to implement especially using SIPG. However it was less accurate and precise compared to the *hpr*-adaptive method. It was also sensitive to the discretisation of the domain.

2. A more expensive but accurate and precise method denoted the *hpr*-adaptive algorithm. The algorithm was presented in Algorithm 7.2 and is too complex to be summarised here but, the crack tip CF is calculated using the proposed algorithm in Chapter 5, with propagation only occurring once a predefined level of CF accuracy was achieved. Further, the *hpr*-algorithm includes a mesh quality sub-algorithm that prevents the elements in the mesh becoming distorted when propagation occurs. The algorithm was computational expensive because of the *hp*-adaptivity required to compute the crack tip CF.

1.4 Notation

This thesis uses both tensor and matrix notation throughout, however it is clearly expressed in the text which notation is used for an equation. All numerical analysis tools presented in this thesis were written by the author in MATLAB. MATLAB is used due to the simplicity in implementation and available debugging tools. No run times are presented in this thesis as this was not the focus of the research however, the complexity of algorithms is commented on and in Chapter 7 there is a qualitative comment on the run time for different techniques. Last, the thesis adopts a tension positive convention as is common within the solid mechanics community.

Chapter 2

Discontinuous Galerkin finite elements

2.1 Introduction

Finite element analysis (FEA) is a commonly used technique by engineers to find an approximate solution to difficult problems modelled by elliptic partial differential equations, such as linear elastic or Poisson problems [66]. This thesis is concerned with achieving high fidelity approximations of the stress solution at crack tips, the energy release rate of propagating cracks [20], highly accurate crack propagation paths and accurate crack fatigue life predictions. However before discussing the details of fracture mechanics and casting the associated theory into a numerical method, it is necessary to describe the numerical scheme in which fracture mechanics problems are cast.

Although difficult to accredit a single person, or group of scientists, to the development of the theory and methodology of the finite element method (FEM), its development can be dated as far back as the 1940's, [33]. Currently, there are many variations of the FEM, the method considered to be the most common for modelling linear elastic problems is the continuous Galerkin (CG) FEM, [66]. However relatively recently a group of finite element (FE) techniques known as the discontinuous Galerkin (DG) FEMs has become increasing more common, see [67] for a unification on DG theory for elliptic problems. A defining feature of DG methods used to model elliptic problems is that adjacent elements in the mesh are coupled weakly, this is not the case for CG. The weak coupling allows adjacent elements in a mesh to vary in polynomial order. Additionally, hanging nodes are naturally incorporated into the formulation such that the mesh is non-conforming. This makes DG methods very adept at easily incorporating *hp*-adaptivity strategies to achieve highly accurate solutions for linear elastic problems [65]. Alternative to a polynomial basis for *hp*-adaptivity a NURBS (Non Uniform Rational B-splines) basis could be used, this basis type was shown to be suitable for coupling patches using Nitsche's method, and therefore a possibly application in DG methods, [68].

In this thesis the *hp* symmetric interior penalty discontinuous Galerkin (SIPG) method is used. The aim of this chapter is to introduce the SIPG method, the arbitrary high order basis functions and the arbitrary high order Gauss point integration. Further the SIPG implementa-

tion is verified against regular and non-regular problems with known solutions, since the author implemented all the code presented in this thesis. The chapter begins by outlining the linear elastic strong formulation and all corresponding boundary conditions (BCs), the strong form is subsequently cast into the SIPG bilinear form, written in tensor notation. The hierarchical basis function formulation, and derivatives, for the reference triangular element is presented in Section 2.3. In Section 2.4 the SIPG bilinear form is recast as a matrix equation, the form of which is solved numerically to give the displacement solution in the problem domain. Section 2.4 also includes the Gauss point integration scheme used to integrate over element areas and edges, and a discussion of the average BC implementation. Finally since all numerical methods are implemented by the author, Section 2.5 demonstrates correct implementation of the SIPG FEM. This is achieved by considering the convergence rate of regular and non-regular problems with known solutions against the expected convergence rate from the *hp-a priori* error estimate [69].

2.2 Symmetric Interior Penalty Method

This section is split into two further sections. Section 2.2.1 provides the strong form statement of equilibrium for linear elastic with corresponding boundary conditions. This is followed by Section 2.2.2 where the strong form statement of equilibrium is cast into the bilinear SIPG weak form with its associated mesh.

2.2.1 Linear elasticity

All numerical analysis is performed in a two dimensional small strain linear elastic setting. The problems are modelled in the domain Ω_Γ, a bounded polygonal domain in $\mathbb{R}^2$ with the boundary $\partial\Omega_\Gamma = \partial\Omega_D \cup \partial\Omega_N \cup \partial\Omega_T$, where the intersection between any of these is an empty set. The strong form statement of equilibrium for linear elasticity and the associated boundary conditions are defined as,

$$\begin{aligned} \nabla_j \sigma_{ij} &= f_i && \text{in} \quad \Omega_\Gamma, \\ u_i &= g_i^D && \text{on} \quad \partial\Omega_D, \\ \sigma_{ij} n_j &= {g_i}^N && \text{on} \quad \partial\Omega_N, \\ \sigma_{ij} n_j n_i^{\parallel} &= 0 && \text{on} \quad \partial\Omega_T, \\ u_i n_i &= {g_i}^T n_i && \text{on} \quad \partial\Omega_T, \end{aligned} \tag{2.1}$$

where i and j are tensor indices for a two dimensional space, $\sigma_{ij} \in \mathbb{R}^{2\times 2}$ is the Cauchy stress tensor, $u_i = (u, v) \in \mathbb{R}^{2\times 1}$ is displacement, the Dirichlet boundary condition is applied on $\partial\Omega_D$, the Neumann boundary condition is applied on $\partial\Omega_N$ and the mixed Neumann/Dirichlet boundary condition is applied on $\partial\Omega_T$ (more commonly referred to as a roller, or slip [70], boundary condition). On the set of all boundaries $\partial\Omega_\Gamma$ there exists the outward normal $n_i = (n_x, n_y)$ and corresponding tangent $n_j^{\parallel}$. g_i^D and g_i^T are the applied displacements on $\partial\Omega_D$ and $\partial\Omega_T$ respectively; g_i^N is the applied traction on $\partial\Omega_N$. Last f_i is a body force applied on the interior of the domain Ω_Γ. A schematic of the domain and the diagrammatic notation for the different types of boundary conditions used throughout the thesis is provided by Figure 2.1. When no traction is applied to a Neumann part of the boundary it is referred to as a homogeneous

boundary, shown in Figure 2.1 by the region of $\partial\Omega_\Gamma$ containing no symbol. The Cauchy stress

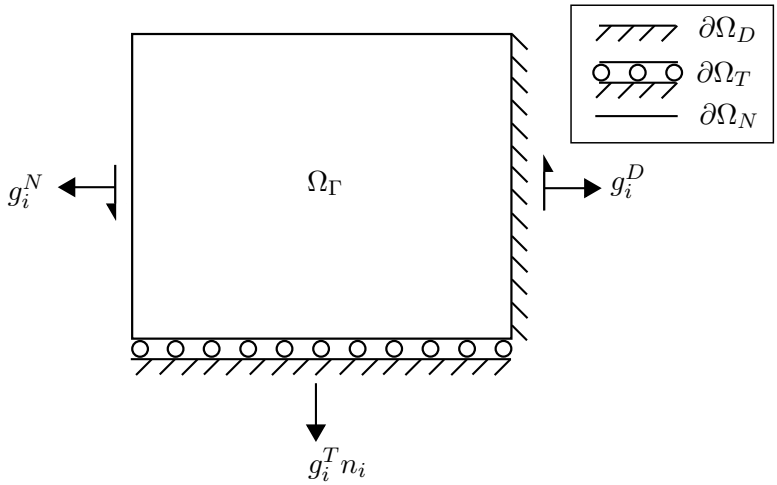

Figure 2.1: A schematic displaying the different types of boundary condition described in (2.1) and their corresponding diagrammatic notation.

tensor for linear elasticity as a function of strain is $\sigma_{ij} = D_{ijlm} : \varepsilon_{lm}$, where $D_{ijlm} \in \mathbb{R}^{2\times2\times2\times2}$ is the fourth order material stiffness tensor and the small strain tensor $\varepsilon_{lm} \in \mathbb{R}^{2\times2}$ is

$$\varepsilon_{ij} = \frac{1}{2}(\nabla_j u_i + \nabla_i u_j) = \begin{bmatrix} \frac{\partial u}{\partial x} & \frac{1}{2}(\frac{\partial v}{\partial x} + \frac{\partial u}{\partial y}) \\ \frac{1}{2}(\frac{\partial v}{\partial x} + \frac{\partial u}{\partial y}) & \frac{\partial v}{\partial y} \end{bmatrix}, \tag{2.2}$$

where (x, y) is the Cartesian coordinate system describing Ω_Γ. Alternatively the Cauchy stress tensor can be described using the matrix notation

$$\begin{aligned} \{\sigma\} &= [D]\{\varepsilon\} \\ \begin{Bmatrix} \sigma_{xx} \\ \sigma_{yy} \\ \sigma_{xy} \end{Bmatrix} &= \begin{bmatrix} D_{11} & D_{12} & D_{13} \\ D_{21} & D_{22} & D_{23} \\ D_{31} & D_{32} & D_{33} \end{bmatrix} \begin{Bmatrix} \frac{\partial u_1}{\partial x} \\ \frac{\partial u_2}{\partial y} \\ \frac{\partial u_2}{\partial x} + \frac{\partial u_1}{\partial y} \end{Bmatrix}, \end{aligned} \tag{2.3}$$

where $\{\sigma\}$ is the Cauchy stress vector, $\{\varepsilon\}$ is the engineering small strain vector and $[D]$ is the symmetric material stiffness matrix for a problem acting in plane strain or stress. Describing Cauchy stress as vector makes the material tensor D_{ijlm} simpler to visualise and describe, additionally it makes the FE implementation easier. For the homogeneous isotropic linear elastic case acting in plane stress $[D]$ has the form

$$[D] = \frac{E_Y}{1-\nu^2} \begin{bmatrix} 1 & \nu & 0 \\ \nu & 1 & 0 \\ 0 & 0 & \frac{1-\nu}{2} \end{bmatrix} \tag{2.4}$$

and for plane strain has the form

$$[D] = \frac{E_Y}{(1+\nu)(1-2\nu)} \begin{bmatrix} 1-\nu & \nu & 0 \\ \nu & 1-\nu & 0 \\ 0 & 0 & \frac{1-2\nu}{2} \end{bmatrix}. \tag{2.5}$$

Several different types of homogeneous anisotropic materials acting in plane stress are also considered in this thesis and are also described using $[D]$. The material matrix for these materials is given when the materials are used for analysis in Chapter 6, this is due to the range of anisotropic materials available.

2.2.2 Bilinear form of SIPG

To solve linear elastic problems, the strong form statement of equilibrium (2.1) is cast into SIPG finite element weak form. The SIPG method considers the problem domain Ω_Γ subdivided by the mesh $\mathcal{T}$, where $\mathcal{T}$ consists of elements K. The mesh $\mathcal{T}$ is in general irregular, there is no requirement for the element distribution in the mesh to be structured. This chapter considers only considers meshes with no hanging nodes but, in later chapters meshes with a maximum of one hanging node per element face are considered. The SIPG method requires integrals on the interior of all elements in the mesh and the edges existing between elements, [67]. It is therefore necessary, as well as defining the interior of elements within the mesh, to define the edges existing between elements. The set of the elemental edges for an element K is defined as $\mathcal{F}(K)$. If the

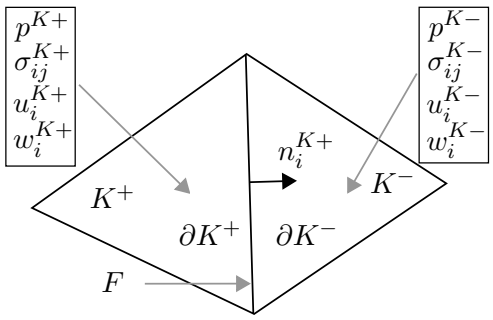

Figure 2.2: A sample mesh consisting of elements K^+ and K^-, internal face $F = \partial K^+ \cap \partial K^-$ and corresponding variables, and properties, for K^+ and K^-.

intersection $F = \partial K^+ \cap \partial K^-$ exists, between two adjacent elements K^+ and K^-, then F is an interior edge of $\mathcal{T}$ with the set of all interior edges denoted by $\mathcal{F}_I(\mathcal{T})$. Further on the boundary of the domain, a natural consequence of SIPG method is the weak application of the essential Dirichlet boundary condition appearing depending on the DG method in the same, or similar, form to that of Nitsche's method [71]. Analogously, if the intersection $F = \partial K \cap \partial\Omega_\Gamma$ of an element $K \in \mathcal{T}$ and $\partial\Omega_\Gamma$ is a segment, we call F a boundary edge of $\mathcal{T}$. The set of all boundary edges of $\mathcal{T}$ is denoted by $\mathcal{F}_B(\mathcal{T})$ and it is the union of the three sets $\mathcal{F}_N(\mathcal{T})$, $\mathcal{F}_D(\mathcal{T})$ and $\mathcal{F}_T(\mathcal{T})$ of edges on the three boundaries $\partial\Omega_N$, $\partial\Omega_D$ and $\partial\Omega_T$ respectively. Since two elements share an interior edge it is necessary to define the elements sharing that edge, denoted arbitrarily K^+ and K^-. Additionally, the variables, basis functions and properties for K^+ and K^- are given respectively the superscripts $K+$ or $K-$, Figure 2.2. Given this notation, jumps and averages

across element boundaries are defined as

$$[\![w]\!]_{ij} = \begin{cases} n_j^{K+} w_i^{K+} - n_j^{K+} w_i^{K-}, & \text{if on the internal edges,} \quad F = \partial K^+ \cap \partial K^- \in \mathcal{F}_I(\mathcal{T}), \\ \\ n_j^K w_i^K, & \text{if on the external edges,} \quad F = \partial K \cap \partial \Omega_\Gamma \in \mathcal{F}_B, \end{cases} \tag{2.6}$$

and

$$\{\sigma\}_{ij} = \begin{cases} \frac{1}{2}\left(\sigma_{ij}^{K+} + \sigma_{ij}^{K-}\right), & \text{if on the internal edges,} \quad F = \partial K^+ \cap \partial K^- \in \mathcal{F}_I(\mathcal{T}), \\ \\ \sigma_{ij}^K, & \text{if on the external edges,} \quad F = \partial K \cap \partial \Omega_\Gamma \in \mathcal{F}_B. \end{cases} \tag{2.7}$$

For each element $K \in \mathcal{T}$ the polynomial order is defined as p_K. The vector function $\underline{p} = \{\, p_K \,:\, K \in \mathcal{T} \,\}$ is also defined, containing the polynomial order for every element in the mesh. For any mesh $\mathcal{T}$ of Ω_Γ with the degree vector $\underline{p}$, the *hp*-version discontinuous Galerkin finite element space is defined by,

$$W_{\underline{p}}(\mathcal{T}) = \{\, w_i \in [L^2(\Omega_\Gamma)]^2 \,:\, w_i|_K \in [\mathcal{P}_{p_K}(K)]^2,\ K \in \mathcal{T} \,\}. \tag{2.8}$$

Given the strong form statement of equilibrium (2.1), the SIPG solution space (2.8), the mesh $\mathcal{T}$, elements K, the set of all faces $\mathcal{F}_I(\mathcal{T}) \cup \mathcal{F}_B(\mathcal{T})$, and various boundary types it is possible to introduce the SIPG bilinear formulation to find the displacement solution ${u_i}^h \in W_{\underline{p}}(\mathcal{T})$ such that,

$$a(u_i^h, w_i) = l(w_i), \quad \forall w_i \in W_{\underline{p}}(\mathcal{T}), \tag{2.9}$$

were $a(u_i^h, w_i)$ is function of u_i^h and w_i, and $l(w_i)$ is a function of w_i. The bilinear forms for (2.9) are

$$\begin{aligned} a(u_i, w_i) := & \sum_{K \in \mathcal{T}} \int_K \tilde{\varepsilon}_{ij} \sigma_{ij} \, dc \\ & - \sum_{F \in \mathcal{F}_I(\mathcal{T}) \cup \mathcal{F}_D(\mathcal{T})} \int_F \underbrace{\{\sigma\}_{ij} [\![w]\!]_{ij}}_{(1)} + \underbrace{\{\tilde{\sigma}\}_{ij} [\![u]\!]_{ij}}_{(2)} \, ds \\ & + \sum_{F \in \mathcal{F}_I(\mathcal{T}) \cup \mathcal{F}_D(\mathcal{T})} \frac{\kappa p_F^2}{h_F} \int_F \underbrace{[\![u]\!]_{ij} [\![w]\!]_{ij}}_{(3)} \, ds \\ & - \sum_{F \in \mathcal{F}_T(\mathcal{T})} \int_F \underbrace{(t_i n_i)(w_j n_j)}_{(4)} + \underbrace{(\tilde{t}_i n_i)(u_j n_j)}_{(5)} \, ds \\ & + \sum_{F \in \mathcal{F}_\mathrm{T}(\mathcal{T})} \frac{\kappa p_F^2}{h_F} \int_F \underbrace{(u_i n_i)(w_j n_j)}_{(6)} \, ds \ , \end{aligned} \tag{2.10}$$

$$
\begin{aligned}
l(w_i) := & \sum_{K\in\mathfrak{T}} \int_K \underbrace{f_i w_i}_{(1)} \, \mathrm{d}v \\
& + \sum_{F\in\mathcal{F}_D(\mathfrak{T})} \frac{\kappa p_F^2}{h_F} \int_F \underbrace{g_i{}^D w_i}_{(2)} \, ds - \sum_{F\in\mathcal{F}_D(\mathfrak{T})} \int_F \underbrace{g_i^D \tilde{t}_i}_{(3)} \, ds \\
& + \sum_{F\in\mathcal{F}_N(\mathfrak{T})} \int_F \underbrace{g_i^N w_i}_{(4)} \, ds \\
& - \sum_{F\in\mathcal{F}_T(\mathfrak{T})} \int_F \underbrace{(g_j^T n_j)(\tilde{t}_i n_i)}_{(5)} \, ds + \sum_{F\in\mathcal{F}_T(\mathfrak{T})} \frac{\kappa p_F^2}{h_F} \int_F \underbrace{(g_i^T n_i)(w_j n_j)}_{(6)} \, ds,
\end{aligned}
\tag{2.11}
$$

where $\tilde{(\cdot)}$ shows a function to be a function of w_i rather than u_i, and κ is the SIPG penalty constant and is chosen here to have a value of $10 \times \max(|D_{ijlm}|)$. $t_i = \sigma_{ij} n_j$ is a general description of a traction, the edge polynomial, p_F, for an edge F is

$$
p_F = \begin{cases} \max\left(p^{K+}, p^{K-}\right), & \text{if on the internal edges,} \quad F = \partial K^+ \cap \partial K^- \in \mathcal{F}_I(\mathfrak{T}), \\ p_K, & \text{if on the external edges,} \quad F = \partial K \cap \partial \Omega_\Gamma \in \mathcal{F}_B, \end{cases}
\tag{2.12}
$$

and h_F is the length of the segment F.

By the definition of the SIPG space (2.8), all degrees of freedom (DOF) in the mesh are element specific and as such discontinuities in displacement exist between adjacent elements. This is contrary to CG methods where the displacement solution is continuous throughout the solution domain. For the SIPG method continuity in displacement is enforced weakly between elements through edge integrals. Although developed independently [67], the integrals appear in a form similar to Nitsche's method [71], which is more conventionally used to apply Dirichlet BCs. In (2.10) the weak interaction between adjacent elements occurs through edge integrals (1), (2) and (3). (1) of (2.10) averages the tractions acting between elements, (3) penalises the displacement across the element interface stabilising the SIPG method and (2) is a symmetrisation term, the transpose of (1), which is necessary to ensure that for a regular problem the convergence rate increases consistently with increasing polynomial order, [72]. Together terms (1), (2) and (3) ensure optimal convergence and increasing convergence rates with polynomial order. However other DG methods for elliptic problems, which possess a similar form to SIPG, such as the non-symmetric and incomplete interior penalty DG method, do not necessarily converge optimally and do not possess optimal convergence rates which increase consistently with polynomial order [72].

To be consistent with the weakly enforced continuity in displacement across adjacent elements, the Dirichlet boundary condition on the edge of the domain is also applied weakly. For SIPG this takes the same form as Nitsche's method. For a Dirichlet BC the variants of (1) and (3) of (2.10) for the edge of the domain $\partial\Omega_D$ are computed along with terms (2) and (3) of (2.11). The slip, or roller boundary condition, along $\partial\Omega_T$ is a variant of Nitsche's method but isolated to the components of u_i that act normal to the edge of $\partial\Omega_T$, with a homogeneous

Neumann boundary acting tangential to the boundary $\partial\Omega_T$. This boundary condition is implemented using terms (4) and (6) of (2.10) and terms (5) and (6) of (2.11). The slip BC was found by the author in [70] for the Stoke's flow problem and was modified here for linear elasticity. Last the body force and Neumann BCs are applied respectively with terms (1) and (4) of (2.11), these BCs are known as the natural BCs from the strong form statement of elasticity (2.1).

2.3 Hierarchical basis

Only triangular elements are used to discretise (2.10). The elements K in the mesh $\mathcal{T}$ are formed by the affine transformation $F_K : \widehat{K} \to K$ from a reference element $\widehat{K}$, see Figure 2.3, defined

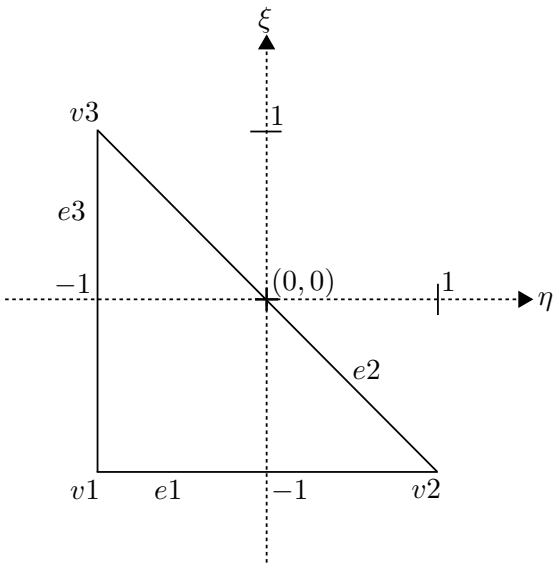

Figure 2.3: The coordinate system of the reference triangular element $(\eta, \xi) \in \widehat{K}$, with vertex numbers ($v1$,$v2$,$v3$) and edge numbers ($e1$,$e2$,$e3$).

as

$$\widehat{K} = \{(\eta, \xi) \in \mathbb{R}^2; -1 < \eta, \xi; \eta + \xi < 0\}, \tag{2.13}$$

with local Cartesian coordinates (η, ξ), to an element K in the global problem domain with global Cartesian coordinates (x, y). The basis used throughout this are defined in [73] for $\widehat{K}$, it is an arbitrarily high order hierarchical polynomial basis that can be constructed numerically. Depending on the order of the basis, and therefore the order of $\widehat{K}$, the basis is formed by summing three different sets of shape function type: (*i*) vertex, (*ii*) edge and (*iii*) bubble. Vertex functions are always included in the basis whereas the edge and bubble functions are only included if $2 \leq p_{\widehat{K}}$ and $3 \leq p_{\widehat{K}}$ respectively. The inclusion of a shape function type and the respective number of functions is summarised in Table 2.1. The vertex shape functions are the first set to be defined, these are all first order polynomials and are

$$\begin{aligned} \widehat{\psi}^{v1} &= -(\eta + \xi)/2, \\ \widehat{\psi}^{v2} &= (\eta + 1)/2, \\ \widehat{\psi}^{v3} &= (\xi + 1)/2. \end{aligned} \tag{2.14}$$

Shape function type	Inclusion in basis	Number of shape function
Vertex	always	3
Edge	$2 \leq p_K$	$3(p_K - 1)$
Bubble	$3 \leq p_K$	$(p_K - 1)(p_K - 2)/2$

Table 2.1: Construction table for the number of vertex, edge and bubble shape functions required to construct the basis for a triangular element of order p_K.

The second set of shape functions to be defined are the hierarchical edge shape functions. Three hierarchical edge shape function exist, one for each edge of $\widehat{K}$. For an element of order $p_{\widehat{K}}$, each hierarchical edge function contributes to the basis the sum of polynomial functions in the range $2 \leq p_e \leq p_{\widehat{K}}$, where p_e is the polynomial order of an edge function. For DG methods there is no requirement, whereas there is for CG methods, for adjacent elements sharing an edge to have the same order polynomial functions along the edge, therefore all edges of an element K are of order p_K. The three edge hierarchical functions are

$$\begin{array}{rcll} \widehat{\psi}^{e1}_{p_e} & = & -(\eta+\xi)(\xi+1)/4 \quad \phi_{p_e-2}((2\xi+\eta+1)/2), & 2 \leq p_e \leq p_K, \\ \widehat{\psi}^{e2}_{p_e} & = & (\eta+1)(\xi+1)/4 \quad \phi_{p_e-2}((\eta-\xi)/2), & 2 \leq p_e \leq p_K, \\ \widehat{\psi}^{e3}_{p_e} & = & -(\eta+\xi)(\eta+1)/4 \quad \phi_{p_e-2}(-(2\eta+\xi+1)/2), & 2 \leq p_e \leq p_K, \end{array} \tag{2.15}$$

where the Lobatto kernel $\phi_p(\cdot)$, of order p_e, is a function of the Cartesian coordinates (η, ξ) and is calculated using the algorithm presented in [73]. The last hierarchical shape function required to complete the basis is the hierarchical bubble function $\psi^B_{p_b}$

$$\widehat{\psi}^B_{b_n} = -(\eta+1)(\eta+\xi)(\xi+1)/8 \; \phi_{b_n-1}((2\xi+\eta+1)/2)\phi_{b_n-1}(-(2\eta+\xi+1)/2), \tag{2.16}$$

where

$$1 < b_n \quad \text{and} \quad 2b_n < p_K - 1$$

which, similar to the edge shape functions (2.15), contributes to the basis the sum of polynomial functions in the range $3 \leq p_b \leq p_K$. For (2.14), (2.15) and (2.16) to be used for $K \in \mathfrak{T}$ the affine mapping $F_K : \widehat{K} \to K$ is required, this allows the following definitions between basis functions of the elements $K \in \mathfrak{T}$ and of $\widehat{K}$ to exist

$$\begin{array}{rcll} \psi^V & := & \widehat{\psi}^V(F_K^{-1}(x,y)) & \text{for } V \in \{v1, v2, v3\}, \\ \psi^E_{p_e} & := & \widehat{\psi}^E_{p_e}(F_K^{-1}(x,y)) & \text{for } E \in \{e1, e2, e3\} \text{ and } 2 \leq p_e \leq p_K, \\ \psi^B_{p_b} & := & \widehat{\psi}^B_{p_b}(F_K^{-1}(x,y)) & \text{for } 3 \leq p_b \leq p_K. \end{array} \tag{2.17}$$

It therefore also follows that the equivalence relation of the derivatives of (2.17) between elements can be given as

$$\begin{array}{rcll} \nabla_i \psi^V & = & J^{-1}_{ij} \widehat{\nabla}_j \widehat{\psi}^V(F_K^{-1}(x,y)) & \text{for } V \in \{v1, v2, v3\}, \\ \nabla_i \psi^E_{p_e} & = & J^{-1}_{ij} \widehat{\nabla}_j \widehat{\psi}^E_{p_e}(F_K^{-1}(x,y)) & \text{for } E \in \{e1, e2, e3\} \text{ and } 2 \leq p_e \leq p_K, \\ \nabla_i \psi^B_{p_b} & = & J^{-1}_{ij} \widehat{\nabla}_j \widehat{\psi}^B_{p_b}(F_K^{-1}(x,y)) & \text{for } 3 \leq p_b \leq p_K, \end{array} \tag{2.18}$$

where $\widehat{\nabla} = [\partial/\partial\eta \;\; \partial/\partial\xi]^\top$, and J_{ij} is the Jacobian matrix,

$$J_{ij} = \begin{bmatrix} \frac{\partial\eta}{\partial x} & \frac{\partial\eta}{\partial y} \\ \frac{\partial\xi}{\partial x} & \frac{\partial\xi}{\partial y} \end{bmatrix} \tag{2.19}$$

which is constant for an element K since F_K is affine. The combination of (2.14), (2.15) and (2.16) form the hierarchical basis which exists in $\widehat{K}$. Given definition (2.17) the displacement solution within K for a given coordinate $(x, y) \in \Omega$ is

$$u_i^{h,K} = \sum_{V\in\{v1,v2,v3\}} U_i^{V,K}\psi^V + \sum_{2\le p_e\le p_K}\sum_{E\in\{e1,e2,e3\}} U_{p_e,i}^{E,K}\psi_{p_e}^E + \sum_{3\le p_b\le p_K} U_{p_b,i}^{B,K}\psi_{p_b}^B, \tag{2.20}$$

where the tensoral index i refers to the displacement in the x and y direction, and $U_i^{V,K}$, $U_{p_e,i}^{E,K}$ and $U_{p_b,i}^{B,K}$ are the vertex V, edge E and bubble B shape function coefficients respectively for the element K. The stress state over an element K is described by the derivative of (2.20), with the Hookian stiffness tensor,

$$\sigma_{ij}^{h,K} = D_{ijlm}\left(\nabla_l u_m^{h,K} + \nabla_m u_l^{h,K}\right)/2 \tag{2.21}$$

where, given (2.18), the derivative of the displacement for a given global coordinate (x, y), is

$$\nabla_j u_i^{h,K} = \sum_{V\in\{v1,v2,v3\}} U_i^{V,K}\nabla_j\psi^V + \sum_{2\le p_e\le p_K}\sum_{E\in\{e1,e2,e3\}} U_{p_e,i}^{E,K}\nabla_j\psi_{p_e}^E + \sum_{3\le p_b\le p_K} U_{p_b,i}^{B,K}\nabla_j\psi_{p_b}^B. \tag{2.22}$$

2.4 Formulating the global stiffness matrix

In order to solve (2.9) and find u_h, it is necessary to formulate (2.10) as a FE stiffness matrix equation which can be solved. The first step in formulating the global stiffness matrix is substituting the basis representations (2.20) and (2.21), in terms of u_i^h and w_i, into (2.10). However numerically it is more convenient to express $u_i^{h,K}$, $w_i^{h,K}$, $\sigma_{ij}^{h,K}$ and $\tilde{\sigma}_{ij}^{h,K}$ as a set of matrices. The full matrix forms are given by (A.0.2), (A.0.4), (A.0.6) and (A.0.7) respectively. (2.10) can

therefore be rewritten in a more convenient matrix form,

$$
\begin{aligned}
a(u_i, w_i) :=& \{W^{\mathcal{T}}\}^{\top} \sum_{K\in\mathcal{T}} \int_K \left([B^K]^{\top}[D][B^K]\right)\, \mathrm{d}v\ \{U^{\mathcal{T}}\} \\
&- \{W^{\mathcal{T}}\}^{\top} \sum_{F\in\mathcal{F}_I(\mathcal{T})\cup\mathcal{F}_D(\mathcal{T})} \frac{1}{2}\int_F \left([N^{K+}]^{\top}[n][D][B^{K+}] + [B^{K+}]^{\top}[D][n]^{\top}[N^{K+}]\right)\, \mathrm{d}s\ \{U^{\mathcal{T}}\} \\
&+ \{W^{\mathcal{T}}\}^{\top} \sum_{F\in\mathcal{F}_I(\mathcal{T})\cup\mathcal{F}_D(\mathcal{T})} \frac{1}{2}\int_F \left([N^{K-}]^{\top}[n][D][B^{K+}] - [B^{K-}]^{\top}[D][n]^{\top}[N^{K+}]\right)\, \mathrm{d}s\ \{U^{\mathcal{T}}\} \\
&- \{W^{\mathcal{T}}\}^{\top} \sum_{F\in\mathcal{F}_I(\mathcal{T})\cup\mathcal{F}_D(\mathcal{T})} \frac{1}{2}\int_F \left([N^{K+}]^{\top}[n][D][B^{K-}] - [B^{K+}]^{\top}[D][n]^{\top}[N^{K-}]\right)\, \mathrm{d}s\ \{U^{\mathcal{T}}\} \\
&+ \{W^{\mathcal{T}}\}^{\top} \sum_{F\in\mathcal{F}_I(\mathcal{T})\cup\mathcal{F}_D(\mathcal{T})} \frac{1}{2}\int_F \left([N^{K-}]^{\top}[n][D][B^{K-}] + [B^{K-}]^{\top}[D][n]^{\top}[N^{K-}]\right)\, \mathrm{d}s\ \{U^{\mathcal{T}}\} \\
&+ \{W^{\mathcal{T}}\}^{\top} \sum_{F\in\mathcal{F}_I(\mathcal{T})\cup\mathcal{F}_D(\mathcal{T})} \frac{\kappa p_F^2}{h_F}\int_F \left([N^{K+}]^{\top}[N^{K+}]\right)\, \mathrm{d}s\ \{U^{\mathcal{T}}\} \\
&- \{W^{\mathcal{T}}\}^{\top} \sum_{F\in\mathcal{F}_I(\mathcal{T})\cup\mathcal{F}_D(\mathcal{T})} \frac{\kappa p_F^2}{h_F}\int_F \left([N^{K+}]^{\top}[N^{K-}]\right)\, \mathrm{d}s\ \{U^{\mathcal{T}}\} \\
&- \{W^{\mathcal{T}}\}^{\top} \sum_{F\in\mathcal{F}_I(\mathcal{T})\cup\mathcal{F}_D(\mathcal{T})} \frac{\kappa p_F^2}{h_F}\int_F \left([N^{K-}]^{\top}[N^{K+}]\right)\, \mathrm{d}s\ \{U^{\mathcal{T}}\} \\
&+ \{W^{\mathcal{T}}\}^{\top} \sum_{F\in\mathcal{F}_I(\mathcal{T})\cup\mathcal{F}_D(\mathcal{T})} \frac{\kappa p_F^2}{h_F}\int_F \left([N^{K-}]^{\top}[N^{K-}]\right)\, \mathrm{d}s\ \{U^{\mathcal{T}}\} \\
&- \{W^{K}\}^{\top} \sum_{F\in\mathcal{F}_T(\mathcal{T})} \int_F \left([N^{K}]^{\top}\{n\}^{\top}\{n\}[n][D][B^{K}] + [B^{K}]^{\top}[D][n]^{\top}\{n\}\{n\}^{\top}[N^{K}]\right)\, \mathrm{d}s\ \{U^{\mathcal{T}}\} \\
&+ \{W^{\mathcal{T}}\}^{\top} \sum_{F\in\mathcal{F}_T(\mathcal{T})} \frac{\kappa p_F^2}{h_F}\int_F \left([N^{K}]\{n\}\{n\}^{\top}[N^{K}]\right)\, \mathrm{d}s\ \{U^{\mathcal{T}}\}, \\
a(u_i, w_i) =& \{W^{\mathcal{T}}\}^{\top}[K]\{U^{\mathcal{T}}\},
\end{aligned}
\tag{2.23}
$$

and

$$
\begin{aligned}
l(w_i) :=& \{W^{\mathcal{T}}\}^{\top} \sum_{K\in\mathcal{T}} \int_K \left([N^K]^{\top}\{f\}\right)\, \mathrm{d}v \\
&+ \{W^{\mathcal{T}}\}^{\top} \sum_{F\in\mathcal{F}_D(\mathcal{T})} \int_F \left([N^K]^{\top} - [B^K]^{\top}[D][n]^{\top}\right)\{g^D\}\, \mathrm{d}s \\
&+ \{W^{\mathcal{T}}\}^{\top} \sum_{F\in\mathcal{F}_N(\mathcal{T})} \int_F \left([N^K]^{\top}\{g^N\}\right)\, \mathrm{d}s \\
&+ \{W^{\mathcal{T}}\}^{\top} \sum_{F\in\mathcal{F}_T(\mathcal{T})} \int_F \left(\frac{\kappa p_F^2}{h_F}[N^K]^{\top}\{n\} - [B^K]^{\top}[D][n]^{\top}\{n\}\right)\{n\}^{\top}\{g^T\}\mathrm{d}s, \\
l(w_i) =& \left\{W^{\mathcal{T}}\right\}^{\top}\{F\}.
\end{aligned}
\tag{2.24}
$$

where

$$\{W^{\mathcal{T}}\} = \sum_{K\in\mathcal{T}} \{W^K\}, \quad \{U^{\mathcal{T}}\} = \sum_{K\in\mathcal{T}} \{U^K\}, \quad [n] = \begin{bmatrix} n_x & 0 & n_y \\ 0 & n_y & n_x \end{bmatrix} \quad \text{and} \quad \{n\} = \begin{Bmatrix} n_x \\ n_y \end{Bmatrix}. \tag{2.25}$$

It is important to note that the summation operators in (2.23), (2.24) and (2.25) are the typical finite element summation operators which sum with respect to the DOF to form the global stiffness matrix $[K]$, [66]. (2.23) can therefore be expressed as

$$\left\{W^{\mathcal{T}}\right\}^{\top} [K] \left\{U^{\mathcal{T}}\right\} = \left\{W^{\mathcal{T}}\right\}^{\top} \{F\} \tag{2.26}$$

where as $\left\{W^{\mathcal{T}}\right\}^{\top}$ is arbitrary vector of constants can be removed to give

$$[K] \left\{U^{\mathcal{T}}\right\} = \{F\} \tag{2.27}$$

from which $\left\{U^{\mathcal{T}}\right\}$ can be found, providing the solution $u_i^h \in W_{\underline{p}}(\mathcal{T})$.

2.4.1 Element area integration

In order to formulate the SIPG stiffness matrix $[K]$ (2.23) it is necessary to integrate polynomial functions over the area of triangular elements $K \in \mathcal{T}$. Since the polynomial functions can be of an arbitrarily high order, for exact integration it is necessary to also have an arbitrary high Gauss quadrature over the area of the triangle K. Arbitrarily high economical Gauss quadrature schemes exist, such as that presented by Dunavant *et al.*. However, $[K]$ and $\{F\}$ require integrals over both the edges and areas of triangles, therefore from a implementation perspective, it is convenient for the area and edge integral schemes to originate from the same integration scheme. This is equally robust and is the methodology chosen here.

To generate the Gauss quadrature for the triangle $\widehat{K}$ several steps need to occur:

1. The Gauss quadrature for the line $\widehat{L}$ is defined.

2. The integration scheme over the line $\widehat{L}$ is used to define the Gauss quadrature over the quadrilateral $\widehat{Q}$.

3. The degenerate mapping function $\Xi : \widehat{Q} \to \widehat{K}$ is used map the Gauss points locations from $\widehat{Q}$ to $\widehat{K}$, and define the corresponding weights for $\widehat{K}$ from $\widehat{Q}$.

The exact Gauss quadrature scheme for a polynomial function $h(\zeta)$ of order p over the line $\zeta \in [-1, 1]$ is

$$\int_{-1}^{1} h(\zeta)\ \mathrm{d}s = \sum_{q=1}^{\lceil (p+1)/2 \rceil} h(\zeta_q)\ a_q \tag{2.28}$$

where ζ_q is the Gauss point position on $\widehat{L}$, a_q is the Gauss point weight and q is the Gauss point number. The Gauss points and their associated weights for the line ζ is generated here using the classical Golub-Welsch method [74]. The Gauss quadrature for a line can now be extended

to the quadrilateral $\widehat{Q}$

$$\widehat{Q} = \{(\alpha, \mu) \in \mathbb{R}^2; -1 < \alpha < 1, -1 < \mu < 1\} \tag{2.29}$$

where α and μ are Cartesian coordinates. The polynomial function $h(\alpha, \mu)$ is of order p in the directions α and μ, it is integrated over $\widehat{Q}$ by using the appropriate over Gauss quadrature scheme [73] for each integral such that,

$$\int_{-1}^{1}\int_{-1}^{1} h(\alpha, \mu)\ \mathrm{d}v = \sum_{g=1}^{\lceil (p+1)/2 \rceil} \sum_{q=1}^{\lceil (p+1)/2 \rceil} h(\alpha_q, \mu_g)\ a_q\ b_g, \tag{2.30}$$

where α_q and a_q are the Gauss point positions and weights over $\alpha \in [-1, 1]$, μ_g and b_g are the Gauss point positions and weights over $\mu \in [-1, 1]$; both quadratures are generated directly from the integration scheme for $\widehat{L}$, (2.28). To map the Gauss points from $\widehat{Q}$ to $\widehat{K}$ the mapping function Ξ [73], Figure 2.4, is defined

$$\Xi(\alpha, \mu) : (\alpha, \mu) \rightarrow (\eta, \xi) = \begin{pmatrix} -1 + (1 - \mu)(\alpha + 1)/2 \\ \mu \end{pmatrix} \tag{2.31}$$

with the corresponding Jacobian

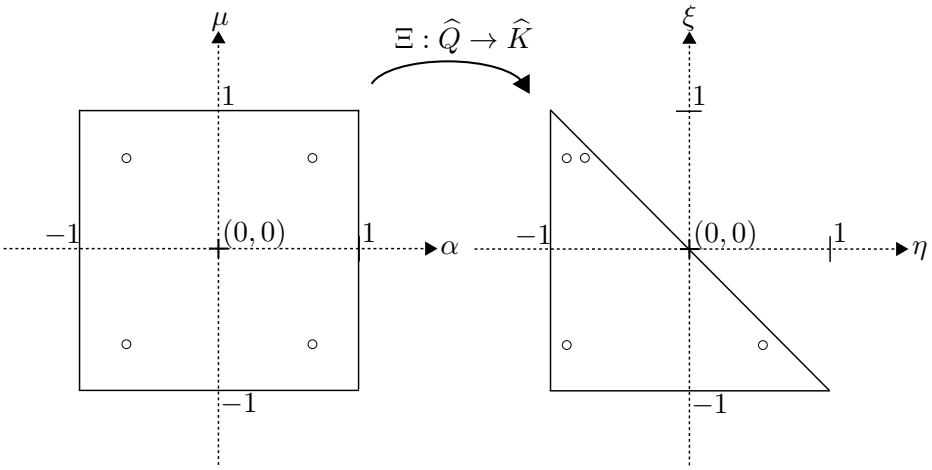

Figure 2.4: A diagram showing the mapping of four example Gauss points, indicated by the circles, from the reference quadrilateral element $(\alpha, \mu) \in \widehat{Q}$ to the reference triangle element $(\eta, \xi) \in \widehat{K}$ by the mapping function $\Xi(\alpha, \mu)$.

$$\det\left(\frac{\mathrm{d}\,\Xi(\alpha, \mu)}{\mathrm{d}(\eta, \xi)}\right) = \frac{1 - \mu}{2} = \frac{1 - \xi}{2}. \tag{2.32}$$

The integral of the polynomial function $h(\eta, \xi) \in \widehat{K}$ is of order p in both the η and ξ direction can therefore be represented as an integral over $\widehat{Q}$ by considering (2.31) and (2.32),

$$\int_{\widehat{K}} h(\eta, \xi)\ \mathrm{d}v = \int_{-1}^{1}\int_{-1}^{1} \left(\frac{1 - \mu}{2}\right) h(-1 + (1 - \mu)(\alpha + 1)/2, \mu)\ \mathrm{d}v. \tag{2.33}$$

With a numerical integration scheme over $\widehat{Q}$, (2.33) becomes

$$\int_{\widehat{K}} h(\eta,\xi)\ \mathrm{d}v = \sum_{g=1}^{\lceil (p+2)/2 \rceil} \sum_{q=1}^{\lceil (p+1)/2 \rceil} \left(\frac{1-\mu_g}{2}\right) h(-1+(1-\mu_g)(\alpha_q+1)/2, \mu_g)\ a_q b_g \tag{2.34}$$

It is important to note that the Jacobian term in the right hand side of (2.33) increases the polynomial order in the μ direction by 1, it is therefore necessary to also increase the Gauss quadrature order in the μ direction, see the first sum operator of (2.34).

To formulate the area term of the global stiffness matrix $[K]$ (2.23) and the body force term in $\{F\}$ (2.24), area integrals over the elements K are required. The area integral terms for $[K]$ and $\{F\}$ respectively integrate the basis function matrix $[N^K]$ (A.0.2) and the basis function derivative matrix $[B^K]$ (A.0.6). Using the basis function identity (2.17), $[N^K]$ can be equivalently expressed as

$$[N^K(\psi(x,y))] = [\widehat{N}^K(\widehat{\psi}(\eta,\xi))], \quad \text{where} \quad (\eta,\xi) = F_K^{-1}(x,y) \tag{2.35}$$

where ψ and $\widehat{\psi}$ are generic shape functions of K and $\widehat{K}$. Similarly since the basis function derivatives of the element K can be written in terms of $\widehat{K}$ using (2.18), the basis function derivative matrix for the element K can be expressed in terms of the shape function derivatives of $\widehat{K}$ such that

$$[B^K(\nabla_j \psi(x,y))] = [\widehat{B}^K(J_{ij}^{-1}\widehat{\nabla}_j \widehat{\psi}(\eta,\xi))], \quad \text{where} \quad (\eta,\xi) = F_K^{-1}(x,y) \tag{2.36}$$

is true, with J_{ij} as the Jacobian of the mapping F_K. (2.35) and (2.36) allow the area integral over elements $K \in \Im$ for terms in $[K]$ and $\{F\}$ to written in terms of an integral over the reference element $\widehat{K}$,

$$\int_K [B^K]^\top [D][B^K]\ \mathrm{d}v = \int_{\widehat{K}} [\widehat{B}^K]^\top [D][\widehat{B}^K] \det(J_{ij})\ \mathrm{d}v \tag{2.37}$$

which means Gaussian integration over the triangle $\widehat{K}$ can be used to determine (2.37),

$$\int_{\widehat{K}} [\widehat{B}^K]^\top [D][\widehat{B}^K] \det(J_{ij})\ \mathrm{d}v = \sum_{q=1}^{\lceil (2p_K+2)/2 \rceil} \sum_{g=1}^{\lceil (2p_K+1)/2 \rceil} \left(\frac{1-\xi_q}{2}\right) [\widehat{B}^K]^\top [D][\widehat{B}^K] \det(J_{ij})\ a_q b_g. \tag{2.38}$$

Since F_K is affine $\det(J_{ij})$ is a constant, g and q are the Gauss point numbers corresponding to the directions η and ξ respectively, η_g and ξ_q are the Gauss point locates on $\widehat{K}$ generated by the mapping Ξ (2.31).

2.4.2 External element face integration

Both the force vector $\{F\}$ (2.24) and the stiffness matrix $[K]$ (2.23) require integrals over element edges which are on the boundary of the domain $\partial\Omega_\Gamma$. To integrate over an element edge a second affine transformation, $\Theta_{\widehat{F}} : \widehat{L} \to \widehat{K}$, is required which maps points from the line $\widehat{L}$ to an edge of the reference element $\widehat{K}$, see Figure 2.5. Consider the integral of the polynomial function

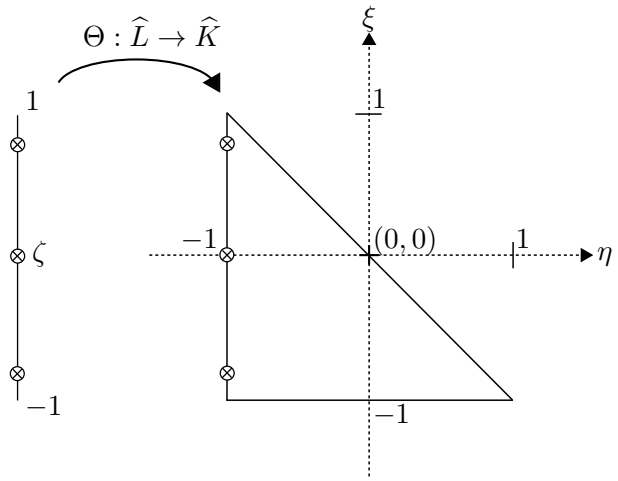

Figure 2.5: A diagram showing the mapping of three example Gauss points, indicated by the circles with crosses, from the reference line element $\zeta \in \widehat{L}$ to the reference triangle element $(\eta, \xi) \in \widehat{K}$ by the mapping function $\Theta(\alpha, \mu)$.

$h(\eta, \xi)$, of order p in the directions η and ξ, over $\widehat{F}$ of $\widehat{K}$ and its equivalent integral over the line $\widehat{L}$,

$$\int_{\widehat{F}} h(\eta,\xi)\mathrm{d}s = \int_{\widehat{L}} h(\Theta_{\widehat{F}}(\zeta))\frac{|\widehat{F}|}{|\widehat{L}|}\mathrm{d}s \quad \text{where} \quad (\eta,\xi) = \Theta_{\widehat{F}}(\zeta) \tag{2.39}$$

where $\widehat{F}/\widehat{L}$ is the Jacobian of $\Theta_{\widehat{F}}$, and is a constant. On the right hand side of (2.39) the integral of h is now over $\widehat{L}$, Gauss quadrature for a line (2.28) can simply be applied such that (2.39) can be expressed as

$$\int_{\widehat{L}} h(\Theta_{\widehat{F}}(\zeta))\frac{\widehat{F}}{\widehat{L}}\mathrm{d}s = \sum_{q}^{\lceil (p+1)/2 \rceil} h(\Theta_{\widehat{F}}(\zeta_q))\frac{|\widehat{F}|}{|\widehat{L}|}a_q. \tag{2.40}$$

As stated respectively by (2.35) and (2.36), the matrices $[N^K]$ and $[B^K]$ for the element K can be equivalently stated in terms of basis functions and their derivatives for the element $\widehat{K}$. These expressions can be extended further to be described with coordinates ζ of the line $\widehat{L}$ and the transformation $\Theta_{\widehat{F}}$, respectively

$$[\widehat{N}^K(\widehat{\psi}(\eta,\xi))] = [\widehat{N}^K](\widehat{\psi}(\Theta_{\widehat{F}}(\zeta)))], \quad \text{where} \quad (\eta,\xi) = \Theta_{\widehat{F}}(\zeta) \tag{2.41}$$

and

$$[\widehat{B}^K(\widehat{\psi}(\eta,\xi))] = [\widehat{B}^K(\widehat{\psi}(\Theta_{\widehat{F}}(\zeta)))], \quad \text{where} \quad (\eta,\xi) = \Theta_{\widehat{F}}(\zeta). \tag{2.42}$$

Therefore, using the first edge integral term in $\{F\}$ as an example, the expression (2.35) and (2.36) allow the integral over the face F of $K \in \mathcal{T}$ to be performed by an integral over the equivalent face $\widehat{F}$ of $\in \widehat{K}$

$$\int_F \left([B^K]^\top[D][n]^\top + [N^K]^\top\right)\{g^D\}\,\mathrm{d}s = \int_{\widehat{F}} \left([\widehat{B}^K]^\top[D][n]^\top + [\widehat{N}^K]^\top\right)\{g^D\}\frac{|F|}{|\widehat{F}|}\,\mathrm{d}s, \tag{2.43}$$

where $|F|/|\widehat{F}|$ is the constant Jacobian of the mapping from $F \to \widehat{F}$. Subsequently using the relations (2.41) and (2.42) the integral over $\widehat{F}$ can then be performed over $\widehat{L}$,

$$\int_{\widehat{F}} \left([\widehat{B}^K]^\top [D][n]^\top + [\widehat{N}^K]^\top \right) \{g^D\} \frac{|F|}{|\widehat{F}|} \, \mathrm{d}s = \int_{\widehat{L}} \left([\widehat{B}^K]^\top [D][n]^\top + [\widehat{N}^K]^\top \right) \{g^D\} \frac{|F|}{|\widehat{L}|} \, \mathrm{d}s, \quad (2.44)$$

The Gauss quadrature for the line integral (2.28) can now be used to determine the right hand side of (2.44) numerically,

$$\int_{\widehat{L}} \left([\widehat{B}^K]^\top [D][n]^\top + [\widehat{N}^K]^\top \right) \{g^D\} \frac{|F|}{|\widehat{L}|} \, \mathrm{d}s = \sum_{q=1}^{\lceil (2p_K+1)/2 \rceil} \left([\widehat{B}^K]^\top [D][n]^\top + [\widehat{N}^K]^\top \right) \{g^D\} \frac{|F|}{|\widehat{L}|} a_q, \quad (2.45)$$

where q is the Gauss point number, a_q is the Gauss point weight, and $[\widehat{B}^K]$ and $[\widehat{N}^K]$ are determined from the Gauss point locations ζ_q on the line $\widehat{L}$. $\{g_D\}$ is normally expressed in terms of the problem domain coordinate system $(x, y) \in \Omega_\Gamma$, as well as $\{g_D\}$ and $\{g_T\}$ of (2.24). Therefore when integrating these terms over the line $\widehat{L}$, such as in the case of (2.44), the following compound mapping is necessary

$$(x, y) = F_K(\eta, \xi) \circ \Theta_{\widehat{F}}(\zeta). \quad (2.46)$$

2.4.3 Internal element face integration

The process of numerical integrating components of $[K]$ that require integrals over internal elements edges $F \in \mathcal{F}_I(\mathcal{T})$ is more complex than integrating over edges on the boundary of the domain. Internal edge components of $[K]$ require basis functions from both K^+ and K^- of $F = \partial K^+ \cap \partial K^-$. For the face F, the portion of the edge ∂K^+ which intersects with ∂K^- is denoted F^+, similarly the portion of the ∂K^- which intersects with ∂K^+ is denoted F^-. The internal face integration occurs over the reference line $\widehat{L}$. Therefore when integrating on the line $\widehat{L}$ it is necessary that the local Gauss points positions ζ_p map to the same global coordinate for the face F^+ of K^+ and the face F^- of K^-. Hence the compound mapping to determine the Gauss point positions for the integral of functions on K^- is introduced

$$\Theta_{\widehat{F}-} = F_{K-}^{-1} \circ F_{K+} \circ \Theta_{\widehat{F}+} \quad (2.47)$$

$\Theta_{\widehat{F}-}$ firstly maps Gauss points from the reference line $\widehat{L}$ to the reference element edge $\widehat{F}^+$, with the + indicating the edge on $\widehat{K}$ which corresponds to the same edge of F^+ of K^+. The Gauss point positions are then mapped from the coordinates of $\widehat{K}$ to (x, y) with F_{K+} and then back to the reference element with F_{K-}^{-1}. This ensures that a Gauss point on $\widehat{K}$ for functions of K^+ and K^- correspond to the same position in the global domain. The basis function matrix and the basis function derivative matrix can therefore be written in terms of $\Theta_{\widehat{F}+}$ and $\Theta_{\widehat{F}-}$,

$$\begin{array}{rcll} [\widehat{N}^{K+}(\widehat{\psi}(\eta, \xi))] & = & [\widehat{N}^{K+}(\widehat{\psi}(\Theta_{\widehat{F}}(\zeta)))], & \text{where} \quad (\eta, \xi) = \Theta_{\widehat{F}+}(\zeta) \\ [\widehat{N}^{K-}(\widehat{\psi}(\eta, \xi))] & = & [\widehat{N}^{K-}(\widehat{\psi}(\Theta_{\widehat{F}}(\zeta)))], & \text{where} \quad (\eta, \xi) = \Theta_{\widehat{F}-}(\zeta) \end{array} \quad (2.48)$$

and

$$\begin{array}{rcll} [\widehat{B}^{K+}(\widehat{\psi}(\eta,\xi))] & = & [\widehat{B}^{K+}(\widehat{\psi}(\Theta_{\widehat{F}}(\zeta)))], & \text{where} \quad (\eta,\xi) = \Theta_{\widehat{F}+}(\zeta) \\ [\widehat{B}^{K-}(\widehat{\psi}(\eta,\xi))] & = & [\widehat{B}^{K-}(\widehat{\psi}(\Theta_{\widehat{F}}(\zeta)))], & \text{where} \quad (\eta,\xi) = \Theta_{\widehat{F}-}(\zeta) \end{array} \tag{2.49}$$

When integrating over an internal edge, for example the second edge integral term of $[K]$, the procedure for Gaussian integration is the same as the external face integration but with the inclusion of the relations (2.48) and (2.49). Starting with the integral over the face F and using (2.35) and (2.36) expresses the integral over the reference face $\widehat{F}$,

$$\int_F [N^{K-}]^\top [n][D][B^{K+}]^\top \mathrm{d}s = \int_{\widehat{F}} [\widehat{N}^{K-}]^\top [n][D][\widehat{B}^{K+}]^\top \frac{|F|}{|\widehat{F}|} \mathrm{d}s \tag{2.50}$$

Using the expressions (2.48) and (2.49) transforms the integral (2.50) over $\widehat{F}$ to a Gauss point integral over $\widehat{L}$

$$\begin{array}{rcl} \displaystyle\int_{\widehat{F}} [\widehat{N}^{K-}][n][D][\widehat{B}^{K+}]^\top \frac{|F|}{|\widehat{F}|}\, ds & = & \displaystyle\int_{\widehat{L}} [\widehat{N}^{K-}][n][D][\widehat{B}^{K+}]^\top \frac{|F|}{|\widehat{L}|} \mathrm{d}s \\ & & \displaystyle\sum_{q=1}^{\lceil((p_{K+}+p_{K-})+1)/2)\rceil} [\widehat{N}^{K-}][n][D][\widehat{B}^{K+}]^\top \frac{|F|}{|\widehat{L}|} a_q. \end{array} \tag{2.51}$$

where q is the Gauss point number with associated weights a_q and Gauss point locations ζ_q on $\widehat{L}$.

2.4.4 Average boundary conditions

By definition the Dirichlet boundary conditions, whether strongly or weakly applied, are essential to find a unique solution to a finite element problem. However often in literature many problems are described with only Neumann boundaries, such as a crack in a plate acting in plane stress with a uniaxial tension applied [1]. Often the chosen solution is to include a point homogeneous Dirichlet boundary condition on an element vertex. This has several problems:

1. The displacement solution is unknown, and so therefore it is uncertain whether the point chosen to have a homogeneous Dirichlet boundary condition should have zero displacement;

2. If the displacement solution for the chosen point is actually non-zero, the point will have the wrong displacement and stress solution.

3. Often when reading literature and comparing results it was difficult to locate, or often not mentioned, where the point boundary condition was applied.

The author therefore introduces an average boundary condition, detailed in [75], which to the author's knowledge is the first of its kind implemented for a linear elastic problem. This boundary condition sets the sum of displacement in both directions of u_i, and the total rotation of the problem, to be 0

$$0 = \int_{\Omega_\Gamma} u_1 \ \mathrm{d}v \approx \sum_{K\in\mathfrak{T}} \int_K [{N_u}^K]\{U^K\}\mathrm{d}v = \sum_{K\in\mathfrak{T}} \int_K [{N_u}^K]\mathrm{d}v\{U^\mathfrak{T}\} = [K_u]\{U^\mathfrak{T}\} \tag{2.52}$$

$$0 = \int_{\Omega_\Gamma} u_2 \ \mathrm{d}v \approx \sum_{K\in\mathcal{T}} \int_K [{N_v}^K]\{U^K\}\mathrm{d}v = \sum_{K\in\mathcal{T}} \int_K [{N_v}^K]\mathrm{d}v\{U^\mathcal{T}\} = [K_v]\{U^\mathcal{T}\} \tag{2.53}$$

and

$$0 = \int_{\Omega_\Gamma} \left(\frac{\partial u_2}{v} - \frac{\partial u_1}{\partial y}\right) \mathrm{d}v \approx \sum_{\Omega_\Gamma} \int_K [C^K]\{U^K\}\mathrm{d}v = \sum_{\Omega_\Gamma} \int_K [C^K]\mathrm{d}v\{U^\mathcal{T}\} = [K_R]\{U^\mathcal{T}\}, \tag{2.54}$$

with the full form of $[C^K]$, $[{N_u}^K]$ and $[{N_v}^K]$ are given by (B.0.6), (B.0.5) and (B.0.4) respectively. Setting the sum of displacement in the system to zero prevents rigid body translation whilst setting the sum of the rotation to zero prevents the body from rotating. However care must be taken when including (2.52), (2.53) and (2.54) in the linear system, (2.27), as it is possible to over constrain the problem. If a Dirichlet BC exists to constrain the problem in u (2.52) and (2.54) are not considered in the system, similarly for a Dirichlet BC restricting motion in v (2.53) and (2.54) are not included. If a Dirichlet BC exists to constrain the problem in u and v, the linear system does not include any average BCs.

For instance the problem described by Figure 2.6a, two Neumann BCs exist of equal value acting on a plate to impose a uniaxial tensile load. Since the directional load of the two BCs sum to zero, no rigid body displacement should occur. The loads are also acting such that there is no global rotation, therefore (2.52), (2.53) and (2.54) are applied. However Figure 2.6a has

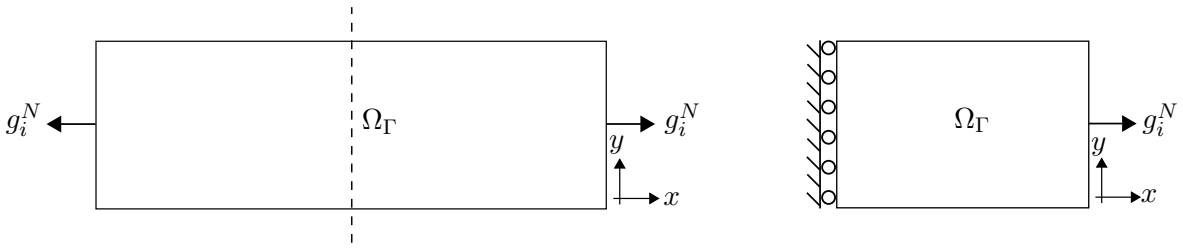

(a) (b)

an axis of symmetry, marked by the dashed line. The problem can therefore be reformulated as Figure 2.6b, the original problem is divided in half with a roller BC applied through the axis of symmetry. In Figure 2.6b a Dirichlet boundary condition exists to restrain rigid body motion in the x-direction. In this instance only the average displacement BC in y, (2.53), is applied since the sum of the displacement in x is not zero. Last, it is possible to manufacture problems which have an applied body force and with only Neumann boundary conditions such that the sum of displacement over the domain in x and y is not zero. The result is that (2.6a) is not true and the average BC cannot be applied.

To include (2.52), (2.53) and (2.54) into the linear system of equations, (2.23), they are incorporated into the global stiffness matrix and thus form part of the solution,

$$\begin{Bmatrix}\{F\}\\ \{0\}\end{Bmatrix} = \begin{bmatrix}[K] & [K_{BC}]^\top\\ [K_{BC}] & [0]\end{bmatrix} \begin{Bmatrix}\{U^\mathcal{T}\}\\ \{\alpha_{BC}\}\end{Bmatrix}, \quad [K_{BC}] = \begin{bmatrix}[K_u]\\ [K_v]\\ [K_R]\end{bmatrix}, \tag{2.55}$$

where if all three average BCs are included [0] is a 3×3 matrix of zeros, $\{0\}$ is a vector of size

3×1 and $\{\alpha_{BC}\}$ is a 3×1 set of arbitrary values that form part of the solution vector. The dimension of all three terms are defined by the number of average BCs included in the system.

2.5 Verification and numerical examples

All numerical methods implemented for this thesis were written in MATLAB entirely by the author. Therefore before continuing it is necessary to verify the implementation. For verification four examples with manufactured solutions are considered, shown in Figures 2.7a, 2.7b, 2.7c and 2.7d. For each of the four problems the displacement solution is known, it is therefore possible

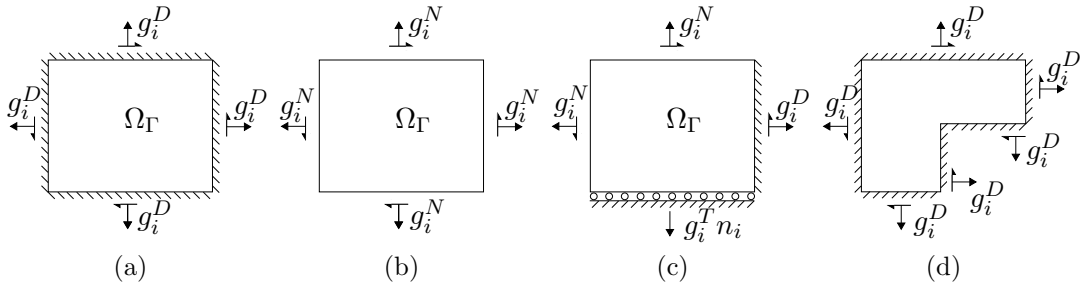

Figure 2.7: Three square domains for verifying the implementations of: (a) the homogeneous and heterogeneous Dirichlet BC, (b) heterogeneous Neumann and all average BCs, and (c) the roller BC. Last, (d) is used to further verify the SIPG implementation by verifying the convergence rate of a problem containing a singularity against the *a priori* error convergence measure (2.56).

to determine the displacement error in the L^2 norm and consequently using the *a priori* error estimate, stated for SIPG in [69],

$$\|u_i^h - u_i\|_{0,K} \leq C \frac{h_K^\mu}{p_K^s} \|u_i\|_{s,K}, \tag{2.56}$$

where $\mu = \min(p_K + 1, s)$ and s is the Sobolev regularity of $u \in [H(\Omega_\Gamma)^s]^2$, determine for a given polynomial order and solution regularity whether the displacement solution is converging at the correct rate and therefore whether the method has been implemented correctly. The four tests are designed for the range of boundary conditions that can be implemented as well verify if the method corresponds correctly to the changes in solution regularity. All four problems are linear elastic acting in plane stress (2.4), with a Young's modulus $E_Y = 10$ Pa and a Poisson's ratio of 0.3. To test a problem a coarse mesh is generated with a uniform polynomial order, the mesh is uniformly refined in h and the error in the L^2 norm is measured for each mesh refinement. The convergence rate for a polynomial order is then measured and compared to the expected convergence rate provided by (2.56).

2.5.1 Smooth numerical example - Dirichlet boundary test

The problem considered here is described by Figure 2.7a, a unit square that has the domain $(x, y) \in \Omega_\Gamma = (0, 1)^2$, with units of metres (m), and with Dirichlet boundary on all outer edges of the domain such that $\partial\Omega_D = \partial\Omega_\Gamma$. The manufactured displacement solution of the problem is,

$$u_i = \begin{Bmatrix} \sin(\frac{15}{2}\pi x)\sin(\frac{15}{2}\pi y) \\ \sin(\frac{15}{2}\pi x)\sin(\frac{15}{2}\pi y) \end{Bmatrix}, \tag{2.57}$$

with $g_D = u_i$ of (2.57) on $\partial\Omega_D$. For this problem u_i is continuously differentiable and as such $u_i = [H(\Omega_\Gamma)^\infty]^2$ and therefore with homogeneous refinement and uniform polynomial within the mesh a convergence rate of $p_K + 1$ is expected. This problem is primarily verifying that the Dirichlet boundary terms in the stiffness matrix $[K]$ and the force vector $\{F\}$ have been implemented correctly, as well the surface and volumetric integral terms of $[K]$ which are not associated with the boundary. The problems was tested with elements ranging from polynomial orders 1 to 9. Elements with $p_K > 2$ require all shape functions in the construction of their basis, see Table 2.1. A maximum mesh polynomial order of $p_K = 9\ \forall K \in \mathcal{T}$ was chosen as:

1. Performing uniform h-refinements with elements of high polynomial order begins to take a large time to solve as the stiffness matrix becomes more densely populated.

2. For a smooth problem a mesh with uniformly high polynomial order may already be sufficiently close to computational accuracy such that optimal convergence may not be achieved due to being limited by computational accuracy.

3. Last, $p_K = 9$ is considered suitable high enough to test the hierarchical generation of the shape functions as well as the generation Gauss point quadrature and the associated Gauss point integral rule.

A plot of the error in the L^2 norm of displacement against the square root of the number of degrees of freedom (NDOF) is shown in Figure 2.8 for meshes of uniform polynomial order $p_K = [1, 9]$. The corresponding values for the first 6 refinement steps are shown in Table 2.2 and the rate of convergence is given in Table 2.3. For all 9 polynomial orders the expected convergence rate $p_K + 1$ was achieved. For the meshes with a polynomial order 1 to 7 the convergence rate was determined using the last refinement step. However for polynomial orders 8 and 9 the last refinement step yielded results that were influenced by computational accuracy, this is demonstrated by the gradients exhibiting optimal convergence followed slightly less than optimal convergence on the final refinement step. Hence the convergence rate of the penultimate refinement step was used to demonstrate optimal convergence.

	$\|u_i - u_i^h\|_{0,\Omega_\Gamma}$					
h (m)	4	5	6	7	8	9
0.5	1.49×10^{1}	7.56×10^{0}	3.85×10^{0}	1.57×10^{0}	8.05×10^{-1}	5.41×10^{-1}
0.25	6.60×10^{-1}	3.01×10^{-1}	1.33×10^{-1}	5.62×10^{-2}	1.89×10^{-2}	6.20×10^{-3}
0.125	4.53×10^{-2}	1.16×10^{-2}	2.40×10^{-3}	4.56×10^{-4}	7.31×10^{-5}	1.11×10^{-5}
0.0625	1.92×10^{-3}	2.24×10^{-4}	2.38×10^{-5}	2.12×10^{-6}	1.74×10^{-7}	1.25×10^{-8}
0.0313	6.39×10^{-5}	3.82×10^{-6}	1.96×10^{-7}	8.84×10^{-9}	3.56×10^{-10}	1.37×10^{-11}
0.0156	2.05×10^{-6}	6.12×10^{-8}	1.56×10^{-9}	3.58×10^{-11}	5.32×10^{-12}	9.63×10^{-12}

Table 2.2: A square domain with heterogeneous and homogeneous Dirichlet BCs, for problem see Figure 2.7a: A table of the displacement error in the L^2 norm for polynomial orders 4 to 9 corresponding to the plot, Figure 2.8.

p_K	1	2	3	4	5	6	7	8	9
Convergence rate	1.988	2.992	3.990	4.964	5.966	6.973	-7.949	-8.935	-9.831

Table 2.3: A square domain with heterogeneous and homogeneous Dirichlet BCs, for problem see Figure 2.7a: A table of the convergence rates of the displacement error in the L^2 norm for polynomial orders 1 to 9 corresponding to the plot, Figure 2.8.

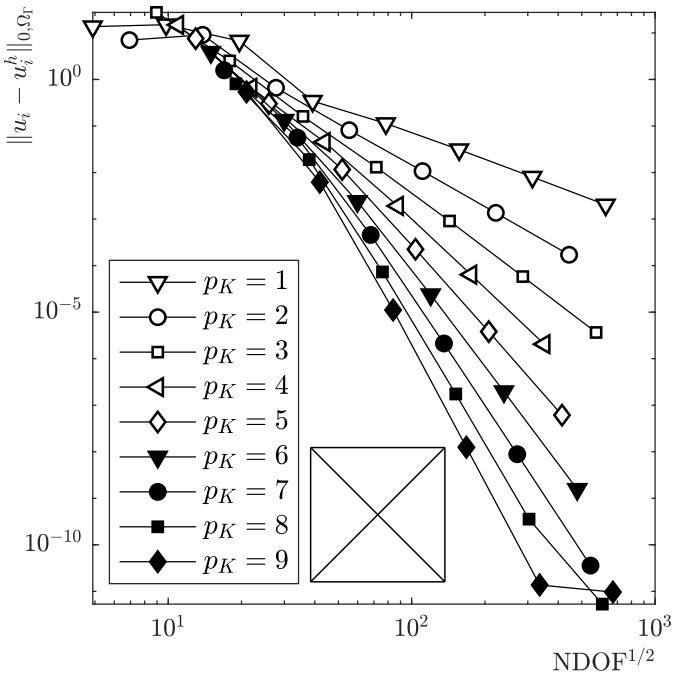

Figure 2.8: A square domain with homogeneous and heterogeneous Dirichlet BCs, for problem see Figure 2.7a: A plot of the L^2 displacement error against NDOF$^{1/2}$, for different uniform mesh polynomial orders, with uniform refinement in h. The initial mesh is included as an inset Figure.

2.5.2 Smooth numerical example - Average and Neumann boundary test

This problem is a unit square which exists in the domain $(x, y) \in \Omega_\Gamma = (0, 1)^2$ m. Neumann boundary conditions are applied on all the edges of the domain so that $\partial\Omega_N = \partial\Omega_\Gamma$. This problems therefore verifies that the Neumann boundary conditions have implemented correctly, but since no Dirichlet boundary condition has been applied the average boundary condition is applied to make the linear system determinate. Hence, the efficacy and implementation of the average boundary conditions is also tested. The manufactured displacement solution for this problem is

$$u_i = \begin{Bmatrix} \sin(10\pi x)\sin(10\pi y) \\ \sin(10\pi x)\sin(10\pi y) \end{Bmatrix}. \tag{2.58}$$

This solution differs slightly from the displacement solution (2.57) from the previous section. Although the average BCs restrict rigid body motion, they are limited by the fact that the solution must be symmetric in u_i and the global rotation is zero; (2.52), (2.53) and (2.54) must

be true. The graph showing the convergence rate of the displacement error in the L^2 norm against the square root in the NDOF is shown in Figure 2.9, again noting that for meshes with

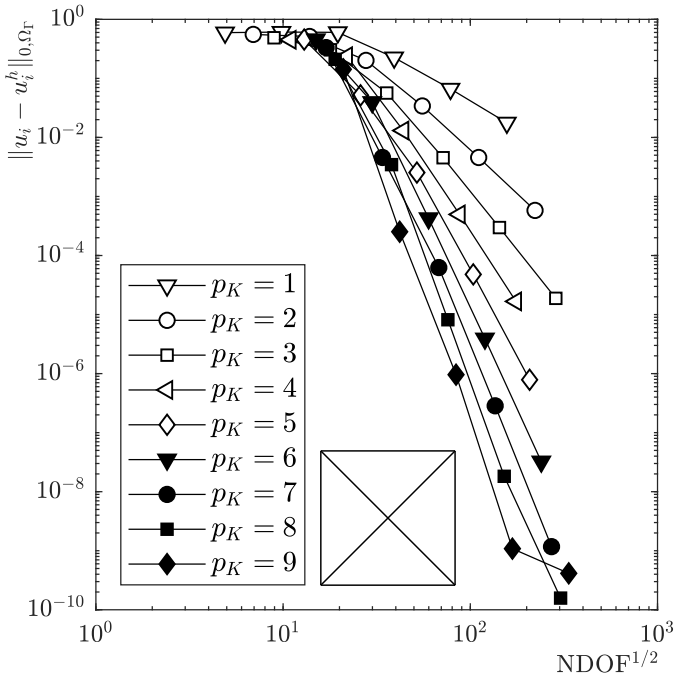

Figure 2.9: A square domain with heterogeneous Neumann BCs, for problem see Figure 2.7b: A plot of the L^2 displacement error against NDOF$^{1/2}$, for different uniform mesh polynomial orders, with uniform refinement in h. The initial mesh is included as an inset figure.

polynomial orders 8 and 9 that the final refinement step leads to a error in the L^2 norm that is limited in computational accuracy. The initial mesh of the problem is inset in Figure 2.9. The values of the displacement error are provided in Table 2.4, with the associated convergence

	$\|u_i - u_i^h\|_{0,\Omega_\Gamma}$					
h (m)	4	5	6	7	8	9
0.5	4.51×10^{-1}	4.55×10^{-1}	4.57×10^{-1}	3.32×10^{-1}	2.10×10^{-1}	1.42×10^{-1}
0.25	2.37×10^{-1}	5.16×10^{-2}	3.95×10^{-2}	4.58×10^{-3}	3.46×10^{-3}	2.53×10^{-4}
0.125	1.31×10^{-2}	2.54×10^{-4}	4.26×10^{-4}	6.25×10^{-5}	8.17×10^{-6}	9.59×10^{-7}
0.0625	4.97×10^{-4}	4.79×10^{-5}	3.91×10^{-6}	2.85×10^{-7}	1.82×10^{-8}	1.08×10^{-9}
0.0313	1.67×10^{-5}	7.86×10^{-7}	3.23×10^{-8}	1.17×10^{-9}	1.58×10^{-10}	4.14×10^{-10}

Table 2.4: A square domain with heterogeneous Neumann BCs, for problem see Figure 2.7b: A table of the displacement error in the L^2 norm for polynomial orders 4 to 9 corresponding to the plot, Figure 2.9.

rates for all polynomial orders given in Table 2.5. The displacement solution of this problem is smooth, hence optimal convergence with respect to the *a priori* error estimate is expected. Table 2.5 demonstrates near optimal convergence for all polynomial orders. As well concluding correct implementation of the Neumann boundary condition, it is also concluded using the numerical

p_K	1	2	3	4	5	6	7	8	9
Convergence rate	1.906	2.977	3.981	4.893	5.928	6.919	7.923	8.808	9.889

Table 2.5: A square domain with heterogeneous Neumann BCs, for problem see Figure 2.7b: A table of the convergence rates of the displacement error in the L^2 norm for polynomial orders 1 to 9 corresponding to the plot, Figure 2.9.

evidence of Table 2.5 that the average boundary condition does not inhibit optimal convergence of the displacement error measured in the L^2 norm.

2.5.3 Smooth numerical example - All boundary condition test

The last verification test of a smooth problem considers all BCs such that $\partial\Omega_\Gamma = \partial\Omega_D \cup \partial\Omega_N \cup \partial\Omega_T$, apart from the average boundary condition, with the location of the BCs provided by Figure 2.7c. Again, similar to the previous two smooth verification tests, the problem domain is $(x, y) \in \Omega_\Gamma = (0, 1)^2$ m with the displacement solution

$$u = \begin{Bmatrix} y^2 \cos(10\pi y) \exp(x^5 y^5) \\ y^2 \cos(10\pi y) \exp(x^5 y^5) \end{Bmatrix}. \tag{2.59}$$

The Neumann and Dirichlet boundary conditions for a problem with a manufactured solution can be determined directly from the solution, in this case (2.59). However for the roller boundary condition on $\partial\Omega_T$ the manufactured solution must satisfy the zero tangential traction condition, such that $n_j^{\parallel}\sigma_{ij} = 0_i$. The convergence of the displacement error in the L^2 against the NDOF is shown for polynomial orders 1 to 9 in Figure 2.10. The displacement error in the L^2 norm is given in Table 2.6, with the corresponding convergence rates provided by Table 2.7. Given the

	$\|u_i - u_i^h\|_{0,\Omega_\Gamma}$					
h (m)	4	5	6	7	8	9
0.5	3.64×10^{-1}	3.50×10^{-1}	3.41×10^{-1}	3.18×10^{-1}	3.02×10^{-1}	2.79×10^{-1}
0.25	3.27×10^{-1}	1.91×10^{-1}	1.62×10^{-1}	6.68×10^{-2}	3.49×10^{-3}	1.39×10^{-2}
0.125	5.78×10^{-2}	1.07×10^{-2}	4.19×10^{-3}	8.06×10^{-4}	1.55×10^{-4}	3.39×10^{-5}
0.0625	1.37×10^{-3}	3.73×10^{-4}	3.07×10^{-5}	4.29×10^{-6}	4.17×10^{-7}	2.83×10^{-8}
0.0313	7.33×10^{-5}	5.22×10^{-6}	3.09×10^{-7}	1.72×10^{-8}	8.44×10^{-10}	2.56×10^{-10}

Table 2.6: A square domain with all edge boundary conditions applied, for problem see Figure 2.7c: A table of the displacement error in the L^2 norm for polynomial orders 4 to 9 corresponding to the plot, Figure 2.10.

solution u_i is in $[H^\infty(\Omega_\Gamma)]^2$ the optimal convergence rate from (2.56) is $p_K + 1$, inspecting Table 2.7 shows that for all polynomial orders optimal convergence is achieved. This demonstrates that the roller BC has been implemented correctly, but also the algorithm for implementing a range of boundary conditions on $\partial\Omega_\Gamma$ is correct.

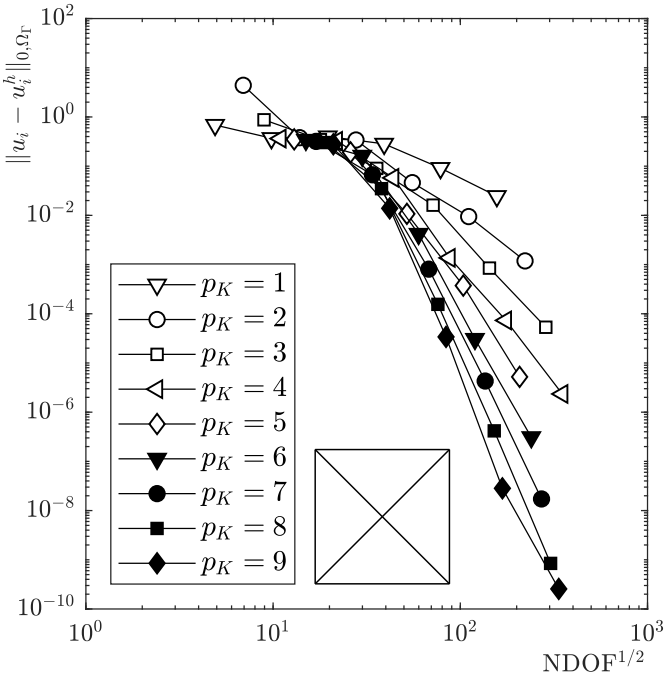

Figure 2.10: A square domain with all edge boundary conditions applied, for problem see Figure 2.7c: A plot of the L^2 displacement error against NDOF$^{1/2}$, for different uniform mesh polynomial orders, with uniform refinement in h. The initial mesh is included as an inset Figure.

p_K	1	2	3	4	5	6	7	8	9
Convergence rate	1.895	2.993	3.993	4.966	6.161	6.834	7.961	8.947	10.223

Table 2.7: A square domain with all edge boundary conditions applied, for problem see Figure 2.7c: A table of the convergence rates of the displacement error in the L^2 norm for polynomial orders 1 to 9 corresponding to the plot, Figure 2.10.

2.5.4 Non-smooth numerical example

The last verification problem considers an L-shaped domain, $(x, y) \in \Omega_\Gamma(-0.5, 0.5)^2/([0, 0.5] \times [-0.5, 0])$ m, with only Dirichlet BCs applied, see Figure 2.7d. Unlike the previous verification problems, the manufactured solution for this problem is not regular. The manufactured displacement solution is,

$$u_i = \begin{Bmatrix} r^{1/2}(1 - r^2\cos(\theta)^2)(1 - r^2\sin(\theta)^2) \\ r^{1/2}(1 - r^2\cos(\theta)^2)(1 - r^2\sin(\theta)^2) \end{Bmatrix}, \quad \text{where} \quad \theta = \arctan(y/x),\ r = |x_i|, \tag{2.60}$$

where $u_i \in [H^{3/2-\epsilon}(\Omega_\Gamma)]^2$ [33], with a stress singularity existing at the point $(0, 0)$. Inspecting (2.56) shows that from $\mu = \min(p_K + 1, s)$ for all polynomial orders the expected convergence rate of the displacement error in the L^2 norm with respect to the NDOF$^{1/2}$ is 3/2. The achieved displacement errors, with uniform refinement, against the NDOF$^{1/2}$ for meshes of uniform different polynomial orders is shown in Figure 2.11, with the corresponding displacement error for polynomial orders 4 to 9 provided by Table 2.8 and the convergence rate for meshes of polyno-

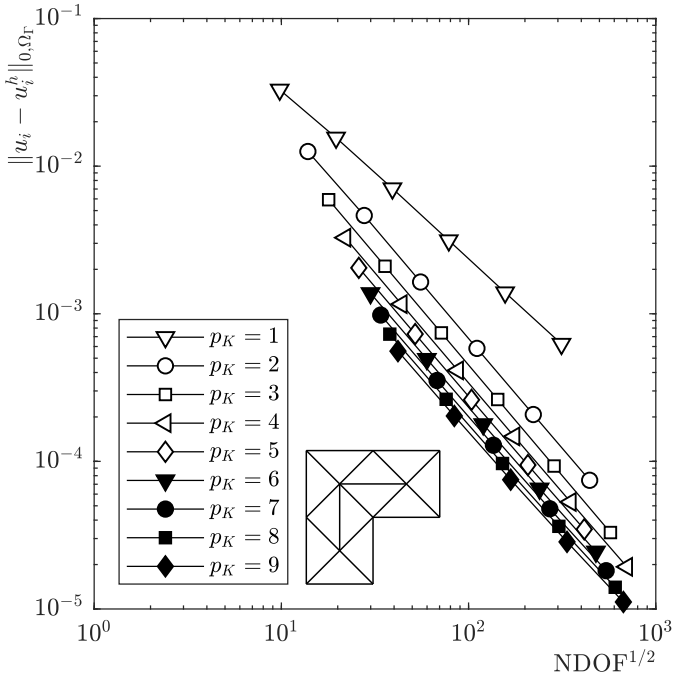

Figure 2.11: A L-shaped domain with heterogeneous and homogeneous Dirichlet BCs applied, for problem see Figure 2.7d: A plot of the L^2 displacement error against NDOF$^{1/2}$, for different uniform mesh polynomial orders, with uniform refinement in h. The initial mesh is included as an inset Figure.

mial orders 1 to 9 given in Table 2.9. Table 2.9 demonstrates that for this non regular problem

	$\|u_i - u_i^h\|_{0,\Omega_\Gamma}$					
h (m)	4	5	6	7	8	9
0.25	3.28×10^{-3}	2.04×10^{-3}	1.37×10^{-3}	9.78×10^{-4}	7.25×10^{-4}	5.56×10^{-4}
0.125	1.16×10^{-3}	7.27×10^{-4}	4.92×10^{-4}	3.52×10^{-4}	2.62×10^{-4}	2.02×10^{-4}
0.0625	4.13×10^{-4}	2.60×10^{-4}	1.77×10^{-4}	1.28×10^{-4}	9.60×10^{-5}	7.45×10^{-5}
0.0313	1.47×10^{-4}	9.40×10^{-5}	6.49×10^{-5}	4.73×10^{-5}	3.59×10^{-5}	2.81×10^{-5}
0.0156	5.31×10^{-5}	3.46×10^{-5}	2.44×10^{-5}	1.82×10^{-5}	1.40×10^{-5}	1.12×10^{-5}

Table 2.8: A L-shaped domain with heterogeneous and homogeneous Dirichlet BCs applied, for problem see Figure 2.7d: A table of the displacement error in the L^2 norm for polynomial orders 4 to 9 corresponding to the plot, Figure 2.11.

polynomial orders 2 to 9 converge near to the expected rate of 3/2. However for the mesh $p_K = 1$

p_K	1	2	3	4	5	6	7	8	9
Convergence rate	1.169	1.490	1.498	1.495	1.490	1.482	1.475	1.468	1.462

Table 2.9: A L-shaped domain with heterogeneous and homogeneous Dirichlet BCs applied, for problem see Figure 2.7d: A table of the convergence rates of the displacement error in the L^2 norm for polynomial orders 1 to 9 corresponding to the plot, Figure 2.11.

the convergence rate is significantly below that which is expected. Given the previous results for the regular problem this is due to the SIPG approximation being the pre-asymptomatic stage of convergence, however further uniformly refinement in h requires considerable computation effort and given this, the previous results, and the results obtained by the higher polynomial orders, further investigation is not continued.

2.6 Observations

The following observations are drawn from this chapter:

- A description of the SIPG bilinear form, hierarchical basis, and methodology for the arbitrary high Gauss point integration for both area and face integrals is provided.
- The SIPG method for linear elasticity has been implemented correctly as all convergence rates for regular and non-regular problems are consistent with the theoretical *a priori* error estimate.
- The numerical framework for modelling linear elastic problems has been defined, the next step in analysing techniques used for solving brittle fracture problems can commence.

Now that the SIPG form for modelling linear elastic problems has been introduced, verified and validated it is now possible to cast configuration force (CF) fracture within the SIPG framework. In the next chapter the notation of a CF acting a crack tip is defined in a continuous setting, this is followed by the derivation and testing of the various discrete formulations which are available in the literature.

Chapter 3

Configurational force static crack evaluation

3.1 Introduction

This chapter presents an investigation into the different methodologies, presented in the literature, for determining the crack tip configurational force (CF). The different methods are critiqued by evaluating their respective accuracy and limitations; the ultimate aim of the chapter is to take one methodology forward which can be used to compute highly accurate CF values.

Arguably, the earliest work presented to evaluate the stress field at a crack tip was in 1939 by Westergaard, he developed a solution for the stress field of a double-ended crack in an infinite plate [13]. The Westergaard solution was generated using the complex function method, developed by Muskhelishvili to solve linear elastic problems analytically [14]. The Westergaard solution is in closed form and simpler than the local stress solution provided by Williams [15] which is considered more general, albeit not in closed form. The Williams solution includes additionally higher order analytic terms which are able to describe different boundary conditions on a finite plate. These solutions are useful for validating numerical techniques however, the Westergaard and Williams solutions are most useful when considering the stress solution in vicinity of the crack tip.

In 1957 Irwin [16] took the form of the Westergaard solution and produced a stress solution local to the crack tip. In the same paper Irwin coined the term stress intensity factor (SIF) which, with the near solution, enabled the separated of the stress and displacement solution at the crack tip into two different modes, for two dimensions. A third out of plane shear can also be defined for three dimensions. The first mode, known as a mode I fracture, is shown in Figure 3.1a and is a crack under going a pure opening. The second mode, a mode II fracture, is shown in Figure 3.1b and represents a crack undergoing a pure shear. Irwin's crack tip stress and displacement solution, and the associated SIFs, are particularly useful in the numerical analysis of propagating cracks, be it with with a brittle crack propagation laws such as the Griffith brittle crack failure criterion [20], or with fatigue crack growth laws such as the Paris Law [21]. In particular, Irwin's local stress solution is essential for determining numerically the crack tip SIFs. Whether this is though enriching the basis of elements at the crack tip with

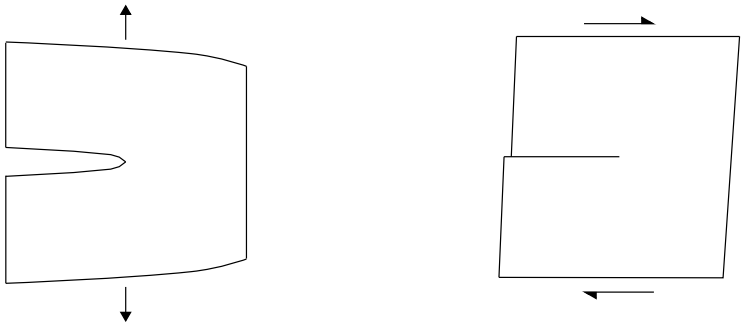

Figure 3.1: Diagrams of crack undergoing mode I and mode II fracture in (a) and (b) respectively.

Irwin's solution directly, such as the eXtended finite element method (XFEM) [24], or by using an auxiliary stress and displacement field, such as the interaction integral method in conjunction with Rice's J-integral [23].

Given that the local stress field for a straight crack in a linear elastic homogeneous isotropic medium is known, the next issue is in determining the energy released when a crack propagates, the associated force (the CF) and the displacement of the crack tip. Some of the earliest work in determining the energy released when a crack propagates can be related to Eshelby's 1951 paper where expressions were derived for the CF acting on point singularities moving through a three dimensional body [17]. Later, in 1956, he revisited his work and extended it to cracks by considering an ellipsoidal inclusion, which represents a crack when the radius of the inclusion is taken to the limit of zero with an associated Young's modulus of also zero [18]. The derivation of the CF acting on a crack tip singularity by Eshelby was produced from a global postulate of energy being dissipated by a body by an advancing crack tip. In 1975 the term *Eshelby stress* was born, otherwise known as *elastic energy-momentum tensor*. The Eshelby stress is the stress term which is integrated over a path around the crack tip to determine the CF [76]. At a similar time, Rice [19] came to the same conclusion as Eshelby, and developed a domain independent integral for the first component of the CF, the J-integral. However, the derivation by Rice considered a local formulation of a crack tip advancing in a planar fashion through a domain.

As mentioned in the introduction to this thesis, a significant contribution to the subject of CFs acting within a material domain has been been provided by Maugin. In terms of CFs acting at a crack tip the work by Maugin in [77, 78] is particularly important. In that work local variational inequalities were used to describe CFs acting to propagate a crack, such power was dissipated from an elastic body an advancing crack tip. Maugin also concluded that the first component of the CF was the same as the J-integral. Gurtin was also made important contributions to the work of propagating cracks with CFs, in particular the works [79, 80] where a framework for dynamic fracture was generated by considering the crack tip CF to have its own force balance with a fracture propagation law, Griffith's law for example, similar to that of classical continuum mechanics. In the works of Steinmann *et al.* [81, 82] the concept of CF mechanics, discussed by Maugin [78], was a recast into a weak formulation and coupled

with classical nonlinear elastic equations to be solved using a FEM for a static crack. However it should be noted that only validation of mode I cracks was considered; there was no mixed mode evaluation. From a numerical perspective the use of the CF to describe a moving fracture front was initially attempted by Mueller and Maugin [83] within the conventional finite-element context and Larsson and Fagerström [84, 85] in XFEM, with an optimally convergent DG-XFEM achieved by [86]. However an enrichment technique requires the near crack tip solution to be known *a priori* which is difficult, but is possible linear elastic, for anisotropic [7], graded heterogeneous [87] and discontinuous heterogeneous [88] materials. Singularities are introduced in the linear system making it more difficult to solve [33]. For SIPG the penalty term is currently only defined for a polynomial basis, the authors of [86] simply choose a polynomial order that is high enough. The CF approach is attractive over these methods since it presents itself as method to propagate a crack without enrichment or with a requirement to knowing the stress solution *a priori*. This makes it a highly robust and attractive method to propagate a crack tip for a range of material types and problems with no requirement for adjustment to the algorithm, or further information, for a new problem.

To propagate a crack the r-adaptive technique [1] was defined by Miehe *et al.* [1, 4, 89] for propagating cracks which was also taken to three dimensions by [90]. Furthermore, Miehe's framework was recently applied to materials with non-linear behaviour, see for example the works of Runesson *et al.* [91] and Tillberg and Larsson [92] on elasto-plasticity and Näser *et al.* [93, 94] on time-dependent materials and the review by Özenç *et al.* [95].

This chapter takes contributions from the author's work in [75, 96]. After the introduction the chapter continues with Section 3.2; following the work of Miehe [1, 4] a summary of the derivation of the CF acting at the crack tip is provided. Firstly the CF in the continuous setting is considered in Section 3.2.1, followed by the discrete setting in Section 3.2.2. The velocity at which the crack propagates is known as the crack tip velocity, or otherwise the material, or configuration, velocity. Different interpretations of the crack tip velocity lead to a number of ways of determining the CF in a numerical setting, this is discussed in Section 3.3. Next, the various discrete formulations described in the literature for determining the CF at the crack validated against empirical data, and numerical results, for a mode I crack in Section 3.4.1. This is followed by a simple mixed mode problem with an analytical solution in Section 3.4.2, and lastly a more complex mixed mode problem in Section 3.4.4 with a numerical solution obtained using knowledge of the local stress field at the crack tip *a priori*. Finally, observations are drawn in Section 3.5.

3.2 Configurational force fracture

In Chapter 2 the SIPG weak form was introduced and verified, presenting a framework for modelling linear elastic problems. This section firstly focuses on the derivation of the CF acting on a crack in a continuous setting, followed by its equivalent formulation in a discretised finite setting, and then finally the form implemented using SIPG.

[1] The r-adaptive technique is simple and robust method for modelling crack propagation. Rather than remeshing each time a crack propagates element edges and node and aligned with the crack path and subsequently split; the benefit is little adjustment is required to the data structure to propagate a crack.

3.2.1 Continuous formulation in time and space

To derive the continuous formulation of a CF acting at a crack tip for small strain elasticity, two domains are considered: (i) a reference domain $\mathscr{B} \subset \mathbb{R}^2$ and (ii) an evolving time-dependent material domain $\Omega \subset \mathbb{R}^2$, which contains crack edges Γ and a crack tip $\partial\Gamma$. The crack edges and the crack tip represent a discontinuity; a material point on a crack edge therefore corresponds to both crack edges, as such it two displacement values. The displacement cannot be defined therefore, a subset of Ω is defined as $\Omega_\Gamma = \Omega \setminus (\Gamma \cup \partial\Gamma)$, where the material points and a displacement field can be defined. The crack edges and tip on Ω_Γ are represented by the limit of $\Gamma^+ \to \Gamma$, $\Gamma^- \to \Gamma$ and $C \to \partial\Gamma$, where Γ^+ and Γ^- are crack edges and C is a line encircling the crack tip, as shown in Figure 3.2. The time dependent mapping $\Pi_i^t : \mathscr{B} \to \Omega_\Gamma$ exists at time t. Π_i^t represents a map of the reference configuration onto itself with a change of material structure in the form of a propagating crack. The material domain Ω_Γ is the same domain as the domain defined for the strong form statement of equilibrium in Section 2.2.1. Therefore the material domain has the same corresponding boundary $\partial\Omega_\Gamma = \partial\Omega_D \cup \partial\Omega_N \cup \partial\Omega_T$, with the additional definition of the crack edges and tip as a subset of the homogeneous (traction free) Neumann boundary, $(\Gamma^+ \cup \Gamma^- \cup C) \subset \partial\Omega_\Gamma$.

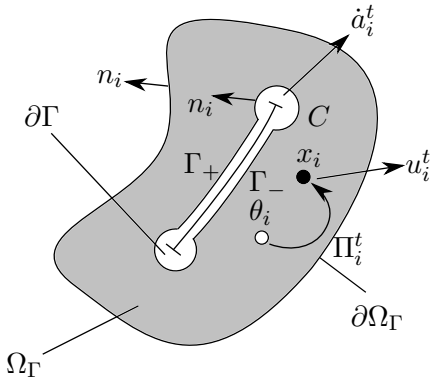

Figure 3.2: CF quantities defined on the material domain Ω_Γ (adapted from [1]).

Now that the domain Ω_Γ containing evolving crack geometry has been described, it is now possible to develop a description of how the crack will propagate within the domain. First, the material points are defined $x_i \in \Omega_\Gamma$, where i is a tensor index, the same as those given by the strong formulation in Section 2.2.1. They evolve from a set of reference coordinates $\theta_i \in \Omega$ using the time dependent mapping Π_i^t, Figure 3.2 demonstrates the time dependent mappings. The displacement at time $t \in \mathbb{R}^+$ is defined as

$$u_i^t = \begin{cases} \Omega_\Gamma \to \mathbb{R}^2 \\ x_i \to u_i^t. \end{cases} \tag{3.1}$$

Next the global power postulate of the mechanical form of the second law of thermodynamics for power dissipation $\mathscr{D}$ is defined, as

$$\mathscr{D} := \mathscr{P} - \frac{\mathrm{d}}{\mathrm{dt}}\Psi \geq 0, \quad \mathscr{P} = \int_{\partial\Omega_\Gamma} t_i \dot{u}_i \mathrm{d}s \quad \text{and} \quad \Psi = \int_{\Omega_\Gamma} \hat{\psi} \mathrm{d}v. \tag{3.2}$$

$\mathscr{P}$ is the power applied to the boundary $\partial\Omega_\Gamma$ by a traction t_i and $\hat{\psi} = \frac{1}{2}D_{ijlm}\varepsilon_{ij}\varepsilon_{lm}$ is the free energy function. Following the work by Miehe *et al.* [1], four terms are substituted in (3.2) to define the dissipation of power in terms of material and spacial displacements.

1. The definition of hyperelasticity, $\hat{\psi} = \frac{1}{2}D_{ijlm}\varepsilon_{ij}\varepsilon_{lm}$.

2. The partial differential of spacial displacement with respect to time

$$\frac{\partial u_i}{\partial t} = \dot{u}_i = v_i - (\nabla_j u_i)V_j. \tag{3.3}$$

3. The partial differential of the gradient of displacement with respect to time

$$\frac{\partial(\nabla_j u_i)}{\partial t} = \nabla_j \dot{u}_i = \nabla_j v_i - (\nabla_l u_i)\nabla_l V_j. \tag{3.4}$$

4. The rate of change of a small area with respect to time

$$\frac{\partial(\mathrm{d}v)}{\partial t} = (\delta_{ij}\nabla_j V_i)\mathrm{d}v. \tag{3.5}$$

Using the aforementioned four terms, (3.2) becomes

$$\mathscr{D} = \mathscr{P} - \int_{\Omega_\Gamma} (\sigma_{ij}\nabla_j v_i + \Sigma_{ij}\nabla_j V_i)\mathrm{d}v \geq 0. \tag{3.6}$$

where

$$\Sigma_{ij} = \hat{\psi}\delta_{ij} - \nabla_l u_i \sigma_{lj} \tag{3.7}$$

is the Eshelby stress, δ_{ij} is an identity tensor, v_i is the spatial velocity field on Ω_Γ and V_i is the material, or configurational, velocity field on Ω_Γ. The spatial velocity field v_i has the boundary conditions,

$$\dot{u}_i \in \{\dot{u}_i | \dot{u}_i = \bar{\dot{u}}_i \text{ on } \partial\Omega_D\}, \tag{3.8}$$

which has a prescribed value $\bar{v}_i$ on the Dirichlet boundary $\partial\Omega_D$. The boundary conditions for the material velocity V_i are

$$V_i \in \{V_i | V_i \cdot n_i = 0 \text{ on } \partial\Omega_\Gamma \cup \Gamma^+ \cup \Gamma^-,\ V_i = \dot{a}_i \text{ on } C\}, \tag{3.9}$$

with a material velocity $\dot{a}_i$ at the crack tip which represents the rate a crack will propagate. Given that V_i is arbitrary in Ω_Γ, has boundary conditions (3.9) and no body force is applied to Ω_Γ [2], the following conditions are added to the statement of equilibrium (2.1),

$$\sigma_{ij}n_j = 0 \text{ on } \Gamma^+ \cup \Gamma^- \cup C \quad \text{and} \quad \nabla_j \Sigma_{ij} = 0 \text{ in } \Omega_\Gamma. \tag{3.10}$$

Finally, using Gauss-Green's theorem with the boundary terms Γ^+, Γ^- and $\partial\Gamma$ defined explicitly, the boundary conditions (3.8) and (3.9), and the strong statements of equilibrium, (2.1) and

(3.10), results in the power dissipated by a propagating crack to be described as

$$\mathscr{D} = V_i^{\partial\Gamma} \left(\lim_{|C|\to 0} \int_C \Sigma_{ij} n_j \mathrm{d}s \right), \tag{3.11}$$

where $V_i^{\partial\Gamma}$ is the crack tip material velocity. The CF at the crack tip is expressed as,

$$g_i = \lim_{|C|\to 0} \int_C \Sigma_{ij} n_j \mathrm{d}s. \tag{3.12}$$

(3.12) is the final form of the CF acting the crack tip in a continuous setting. The component of (3.12) which acts parallel to the crack edges is the same as the path independent J-integral. The second component of the CF which acts perpendicular to the crack face is path dependent and since the limit is undefinable in discretised setting, numerous ways of interpreting this limit exist. Now that the CF acting at the crack tip has been defined in a continuous setting, following the ideas of [1, 4, 81, 82, 90] a discussion of configurational forces acting on element nodes within a mesh discretisation is provided.

3.2.2 Discrete formulation of the power equation in space

The mesh $\mathcal{T}$ generated for the SIPG discretisation is the same mesh used to evaluate the power dissipated by a propagating crack (3.6). To discretise (3.6) the spatial and material velocity have to be defined on the mesh $\mathcal{T}$ with the space

$$S = \{\, s_i \in [H^1(\Omega_\Gamma)]^2 \,:\, s_i|_K \in [\mathcal{P}_1(K)]^2,\ K \in \mathcal{T} \,\}. \tag{3.13}$$

The spatial velocity on the mesh $\mathcal{T}$ is therefore $v_i^h \in S$ and the material velocity is $V_i^h \in S$.

A more usual form of (3.6) for FE discretisation can be generated by substituting the definition of the spatial velocity (3.3) into (3.6). It should be noted the type of power applied to the boundary, $\mathscr{P}$, is deliberately being left unspecified as it includes both the traction applied externally on a Neumann boundary type condition and the reaction loads experienced by parts of the boundary where a Dirichlet boundary condition exists. Starting with the continuous statement of dissipated power from the domain Ω_Γ,

$$\mathscr{D} = \int_{\partial\Omega_\Gamma} t_i \dot{u}_i \mathrm{d}s - \int_{\Omega_\Gamma} (\sigma_{ij} \nabla_j v_i + \Sigma_{ij} \nabla_j V_i) \mathrm{d}v \geq 0,$$

and substituting (3.6), $\dot{u}_i = v_i - (\nabla_j u_i) V_j$, gives

$$\mathscr{D} = \int_{\partial\Omega_\Gamma} t_i (v_i - (\nabla_j u_i) V_j) \mathrm{d}s - \int_{\Omega_\Gamma} (\sigma_{ij} \nabla_j v_i + \Sigma_{ij} \nabla_j V_i) \mathrm{d}v \geq 0.$$

Further, since the material velocity cannot act perpendicular to the domain boundary, otherwise the shape of the domain would change, $V_j n_j = 0$ on $\partial\Omega_\Gamma$ (3.9). This results in

$$\mathscr{D} = \int_{\partial\Omega_\Gamma} t_i v_i \mathrm{d}s - \int_{\Omega_\Gamma} \sigma_{ij} \nabla_j v_i \mathrm{d}v - \int_{\Omega_\Gamma} \Sigma_{ij} \nabla_j V_i \mathrm{d}v \geq 0. \tag{3.14}$$

The continuous form (3.14) over the domain Ω_Γ can now be subdivided by the mesh $K \in \mathcal{T}$. This is achieved by firstly considering (3.14) over an element K to give

$$\mathscr{D} = \int_{F \in \mathcal{F}_B} t_i v_i \mathrm{d}s - \int_{K \in \mathcal{T}} \sigma_{ij} \nabla_j v_i \mathrm{d}v - \int_{K \in \mathcal{T}} \Sigma_{ij} \nabla_j V_i \mathrm{d}v \geq 0, \tag{3.15}$$

which when summed over all elements in the mesh $\mathcal{T}$, and substituting $t_i = \sigma_{ij} n_j$, becomes

$$\begin{aligned} \mathscr{D} = &\sum_{F \in \mathcal{F}_B} \int_F \sigma_{ij}^h n_j v_i \mathrm{d}s + \sum_{F \in \mathcal{F}_I} \int_F (\sigma_{ij}^{h,K+} - \sigma_{ij}^{h,K-}) v_i n_j^+ \mathrm{d}s \\ &- \sum_{K \in \mathcal{T}} \int_K \sigma_{ij}^h \nabla_j v_i \mathrm{d}v - \sum_{K \in \mathcal{T}} \int_K \Sigma_{ij}^h \nabla_j V_i \mathrm{d}v \geq 0, \end{aligned} \tag{3.16}$$

The superscripts + and − correspond to variables of elements K^+ and K^- which have the same internal edge $F = \partial K^+ \cap \partial K^-$. The weak formulation of the power dissipated by the mesh $\mathcal{T}$ is (3.16) where it should be noted that all finite element methods approximate the first three terms to be zero. In the limit of the displacement and stress solution becoming continuous, the second term of (3.16) is zero and the first and third term sum to give zero. This is the same assumption made for CG methods by the authors in [1, 4, 90]. Therefore, the dissipation of power by a propagating crack over the discretised domain Ω_Γ is

$$\mathscr{D} = -\sum_{K \in \mathcal{T}} \int_K \Sigma_{ij} \nabla_j V_i \mathrm{d}v \geq 0. \tag{3.17}$$

The crack propagates in the direction which maximises (3.17). For a unit length extension of the crack tip this is shown in Chapter 7 to be when the crack tip material velocity is colinear with the CF.

3.2.3 Computing the dissipated power

To compute the power dissipated by the entire mesh $\mathcal{T}$, not just at the crack tip, it is convenient to write (3.17) as a matrix equation,

$$\mathscr{D} = -\sum_{K \in \mathcal{T}} \int_K \{\nabla V\}^\top \{\Sigma(u_l^h)\} \mathrm{d}v \geq 0, \tag{3.18}$$

where

$$\{\nabla V\} = \begin{Bmatrix} \frac{\partial V_1}{\partial x} \\ \frac{\partial V_2}{\partial y} \\ \frac{\partial V_1}{\partial y} \\ \frac{\partial V_2}{\partial x} \end{Bmatrix} \quad \text{and} \quad \{\Sigma^{h,K}\} = \begin{Bmatrix} \Sigma_{xx}^{h,K} \\ \Sigma_{yy}^{h,K} \\ \Sigma_{xy}^{h,K} \\ \Sigma_{yx}^{h,K} \end{Bmatrix}. \tag{3.19}$$

$\{\Sigma^{h,K}\}$ is the Eshelby stress vector and is calculated from the SIPG stress solution. It is calculated numerically using the Cauchy stress matrix

$$[\sigma(u_l^{h,K})] = \begin{bmatrix} \sigma_{xx}(u_l^{h,K}) & \sigma_{xy}(u_l^{h,K}) \\ \sigma_{yx}(u_l^{h,K}) & \sigma_{yy}(u_l^{h,K}) \end{bmatrix} \quad \text{where} \quad \begin{Bmatrix} \sigma_{xx}(u_l^{h,K}) \\ \sigma_{yy}(u_l^{h,K}) \\ \sigma_{xy}(u_l^{h,K}) \end{Bmatrix} = \{\sigma(u_l^{h,K})\} = [D][B_{p_K}^K]\{U^K\}, \tag{3.20}$$

where $\sigma_{xy}(u_l^{h,K}) = \sigma_{yx}(u_l^{h,K})$ and the strain vector is defined as $\{\varepsilon(u_l^{h,K})\} = [B^K]\{U^K\}$. The displacement gradient term of the Eshelby stress is also determined from SIPG displacement solution $\{U^K\}$. Its required form is a displacement gradient matrix, however it is computationally convenient to calculate the terms of the matrix using a vector calculation, respectively

$$[h] = \begin{bmatrix} \frac{\partial u_1^{h,K}}{\partial x} & \frac{\partial u_1^{h,K}}{\partial y} \\ \frac{\partial u_2^{h,K}}{\partial x} & \frac{\partial u_2^{h,K}}{\partial y} \end{bmatrix} \quad \text{where} \quad \{h\} = \begin{Bmatrix} \frac{\partial u_1^{h,K}}{\partial x} \\ \frac{\partial u_2^{h,K}}{\partial y} \\ \frac{\partial u_1^{h,K}}{\partial y} \\ \frac{\partial u_2^{h,K}}{\partial x} \end{Bmatrix} = [H_{p_K}^K]\{U^K\}. \tag{3.21}$$

The basis function derivative matrix $[H_{p_K}^K]$ is defined in Appendix (C.0.2). The Eshelby stress vector $\{\Sigma^{h,K}\}$ can therefore be determined from its matrix equivalent form via

$$\begin{aligned} [\Sigma(u_l^{h,K})] &= \begin{bmatrix} \Sigma_{xx}(u_l^{h,K}) & \Sigma_{xy}(u_l^{h,K}) \\ \Sigma_{yx}(u_l^{h,K}) & \Sigma_{yy}(u_l^{h,K}) \end{bmatrix} \\ &= \frac{1}{2}\begin{bmatrix} 1 & 0 \\ 0 & 1 \end{bmatrix}\left(\{\sigma(u_l^{h,K})\}\{\varepsilon(u_l^{h,K})\}^\top\right) - [h]^\top[\sigma]. \end{aligned} \tag{3.22}$$

The crack tip material velocity is not calculated in this thesis since it adds another layer of mathematical complexity through the coupling of the equilibrium statements for linear elasticity and configurational mechanics, where as this thesis will explore, there are already a number of issues in using the crack tip CF as a method for propagating a crack accurately. However, it is recognised that efforts have been made in literature to solve for the material velocity using a non-linear analysis [90]. For an element K, the term $\{\nabla V\}$ is determined from only the vertex

shape functions such that

$$\{\nabla V\} = \begin{bmatrix} \frac{\partial}{\partial x} & 0 \\ 0 & \frac{\partial}{\partial x} \\ \frac{\partial}{\partial y} & 0 \\ 0 & \frac{\partial}{\partial y} \end{bmatrix} \begin{Bmatrix} V_1 \\ V_2 \end{Bmatrix}$$

$$= \underbrace{\begin{bmatrix} \frac{\partial}{\partial x} & 0 \\ 0 & \frac{\partial}{\partial x} \\ \frac{\partial}{\partial y} & 0 \\ 0 & \frac{\partial}{\partial y} \end{bmatrix} \begin{bmatrix} \psi^{v1} & 0 & \psi^{v2} & 0 & \psi^{v3} & 0 \\ 0 & \psi^{v1} & 0 & \psi^{v2} & 0 & \psi^{v3} \end{bmatrix}}_{[B^V]} \begin{Bmatrix} V_1^{v1,K} \\ V_1^{v1,K} \\ V_2^{v2,K} \\ V_2^{v2,K} \\ V_3^{v3,K} \\ V_3^{v3,K} \end{Bmatrix} = [B^V]\{V^K\} \,. \tag{3.23}$$

The full matrix form of (3.18) therefore becomes,

$$\mathscr{D} = -\sum_{K\in\mathcal{T}} \int_K \{V^K\}^\top [B^V]^\top \{\Sigma^{h,K}\} \mathrm{d}v \geq 0. \tag{3.24}$$

3.3 The material velocity

In this thesis only the material velocity at the crack tip is considered, but it is noted that material velocities in the domain are relevant for mesh optimisation techniques, see for example [97]. The finite element form of the power dissipated from a body through a change in its geometry in the material domain Ω_Γ is given by (3.24). The Eshelby stress component $\{\Sigma^{h,K}\}$ is determined directly from the SIPG displacement solution, however, the material velocity component is chosen to maximise the energy dissipated by an increase in the crack length. Kaczmarczyk *et al.* [90] attempt to calculate the crack tip material velocity using a non-linear solver which considers a balance of the CF with a Griffith failure criterion in the same notion as Gurtin [79, 80]. For this thesis, a change in configuration is describing an extension to the crack length and a dissipation of power away from the body. However, the precise definition of the material velocity at the crack leads to three different methods for calculating the CF at the crack tip. These methods are described and discussed in the following sections.

3.3.1 Tip calculation of the configuration force

The first method considered for calculating the CF comes directly from [1, 4] and the discretised definition of the power released from a body (3.18). In this approach it is assumed that when determining the power dissipated by an advancing crack, only the crack tip is considered to have a material velocity. For a mesh $\mathcal{T}$ this equates to only the node which is coincident with the crack tip having a material velocity; hence, only the CF value at the crack tip needs to be

evaluated. The power dissipated from the body by the node at the tip is described as,

$$\begin{aligned}\mathscr{D} &= -\{\partial V\}^\top \sum_{n\in n_t}\sum_{K\in A}\int_K [B^V]^\top \{\Sigma^{h,K}\}\mathrm{d}v \geq 0 \\ &= \{\partial V\}^\top \{g^{h,t}\}\end{aligned} \tag{3.25}$$

where $\{\partial V\}$ is the crack tip node material velocity and $\{g^{h,t}\}$ is the crack tip CF on the mesh $\mathcal{T}$. The set A is defined by all elements K that contain a node n that it is coincident with the crack tip node n_t. The second summation operator sums together an element's CF contribution to each node with respect to the element's degrees of freedom. The first summation operator sums together all the nodal CF values $n \in n_t$.

3.3.2 Domain calculation of the configurational force

The crack tip domain CF method, [60], is an evolution of (3.25) and is considered to be more accurate [4, 60, 75, 98]. Here, and also stated in [81, 82], the CF values at nodes other than those at the crack are considered to be a numerical feature developed from the elements with a polynomial basis around the crack tip. These elements are unable to capture the stress singularity at the crack tip. Therefore, it was concluded that by summing together the nodal CF values within a domain a more accurate approximation for the CF at the crack tip could be obtained; with the material velocity still being considered to only have a value at the crack tip node. This method for calculating the CF takes the form,

$$\mathscr{D} = -V_i^{\partial\Gamma}\left(\int_A \Sigma_{ij}\nabla_j q \ \mathrm{d}v\right) \tag{3.26}$$

where the function q continuously varies from a value of 1 at the crack tip to 0 at the edge of the domain A [60, 62]. When (3.26) is written for the mesh $K \in \mathcal{T}$ it becomes

$$\begin{aligned}&= -\{\partial V\}^\top \sum_{K\in A}\int_K [q]^\top [B^V]^\top \{\Sigma_{ij}^{h,K}\} \ \mathrm{d}v \\ &= \{\partial V\}^\top \{g^{h,D}\}.\end{aligned} \tag{3.27}$$

The set A is defined as all the elements K which contain a node within the radius r_d about the crack tip and $[q]$ is the matrix form of the function q. In this thesis the variation of q is defined here to be the same as [60], such that at all nodes $q = 1$ other than those on the boundary of A, where $q = 0$. Therefore for an element K, $[q]$ is a matrix of constants on the vertices of the element K,

$$[q]^\top = \begin{bmatrix} q^{v1,K} & 0 & q^{v2,K} & 0 & q^{v3,K} & 0 \\ 0 & q^{v1,K} & 0 & q^{v2,K} & 0 & q^{v3,K} \end{bmatrix}, \tag{3.28}$$

and has the corresponding matrix for the shape function vertices,

$$[N] = \begin{bmatrix} \psi^{v1} & 0 & \psi^{v2} & 0 & \psi^{v3} & 0 \\ 0 & \psi^{v1} & 0 & \psi^{v2} & 0 & \psi^{v3} \end{bmatrix} \tag{3.29}$$

where $\{v1, v2, v3\}$ are the vertex numbers of the element K. This is equivalent to summing together the CF values from all nodes on the interior of A. The nodes considered within the domain A are defined from a topological perspective, and an illustration of $K \in A$, the radius r_d, and the set of interior nodes n_b (highlighted in white), is depicted in Figure 3.3. Investigations

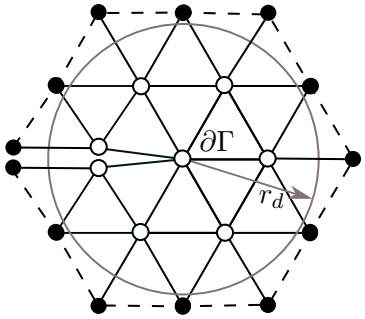

Figure 3.3: The mesh around the crack tip $\partial\Gamma$ showing the nodes which are considered in the CF domain calculation.

are also performed into the number of rings of elements which are of a higher order about the crack tip, an illustration of elements in ring 0 and ring 1 are highlighted in grey in Figure 3.4. Additionally the number of elements, and the associated nodes in the sets n_b and n_t, are also considered in terms of rings. Nodes in these sets are highlighted in white for ring 0 and ring 1 of Figure 3.4.

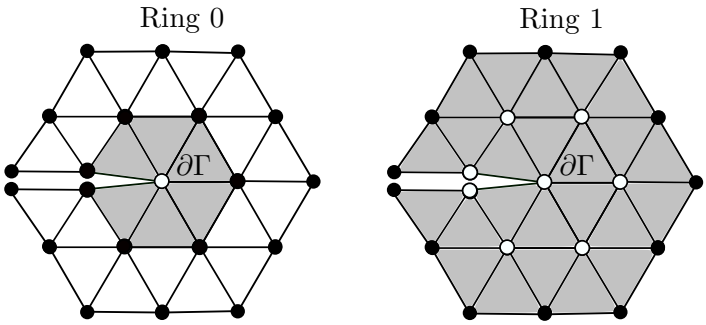

Figure 3.4: An illustration of rings of elements about the crack tip. The left figure highlights in grey the elements which are considered in ring 0, and right figure highlights the elements in ring 1.

3.3.3 Domain with crack edges calculation of the configurational force

The final method for calculating the CF acting at the crack tip begins, unlike the previous two formulations, from the continuous form of the CF (3.12). This formulation is achieved through the definition of the material velocity in the domain Ω_Γ. Following the work of [62, 63] and a similar derivation from [64], the material velocity around the crack tip is stated to have the form

$$V_i = \begin{cases} V_i^{\partial\Gamma} & \text{on } \partial\Gamma = \lim_{|C1|\to 0}(C1) \\ 0_i & \text{on } C4 \end{cases} \tag{3.30}$$

where $C1$ and $C4$ are the edges in Figure 3.5. The value of $V_i^{\partial\Gamma}$ varies continuously from a value

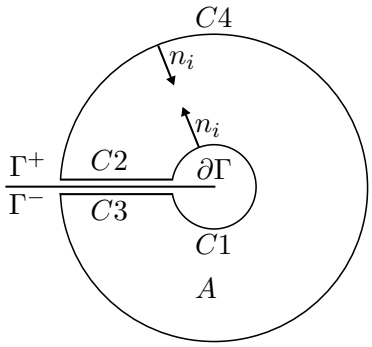

Figure 3.5: Integral path $C_A = C1 + C2 + C3 + C4$ around the crack tip $\partial\Gamma$.

of $V_i^{\partial\Gamma}$ on $C1$, to zero on $C4$. $V_i^{\partial\Gamma}$ can therefore described by the function $V_i = qV_i^{\partial\Gamma}$, where $q = 1$ on $C1$ and $q = 0$ on $C4$. It is important to note that q is dimensionless. Substituting this statement of the material velocity into (3.12) and using the terminology defined in Figure 3.5 gives the following dissipation equation

$$\mathscr{D} = V_i^{\partial\Gamma} \lim_{|C1|\to 0} \int_{C1} q\Sigma_{ij} n_j \mathrm{d}s. \tag{3.31}$$

Using divergence theorem, the strong statement of configurational force equilibrium for a homogeneous material with no body force $\nabla_j \Sigma_{ij} = 0_i$, and the definition of the path $C1 = C_A - C2 - C3 - C4$, (3.31) can be rewritten into the form,

$$\mathscr{D} = V_i^{\partial\Gamma} \left(\int_{C_A} q\Sigma_{ij} n_j \mathrm{d}s - \int_{C2+C3+C4} q\Sigma_{ij} n_j \mathrm{d}s \right). \tag{3.32}$$

$q = 0$ on $C4$ and so (3.32) becomes

$$\mathscr{D} = V_i^{\partial\Gamma} \left(\int_{C_A} q\Sigma_{ij} n_j \mathrm{d}s - \int_{C2+C3} q\Sigma_{ij} n_j \mathrm{d}s \right). \tag{3.33}$$

Applying the divergence theorem to the first term on the RHS of (3.33) gives

$$\mathscr{D} = V_i^{\partial\Gamma} \left(\int_{C_A} \nabla_j (q\Sigma_{ij}) \mathrm{d}s - \int_{C2+C3} q\Sigma_{ij} n_j \mathrm{d}s \right), \tag{3.34}$$

which when integrated by parts, and using $\nabla_j \Sigma_{ij} = 0_i$, becomes

$$\mathscr{D} = -V_i^{\partial\Gamma} \left(\int_{A} (\nabla_j q) \Sigma_{ij} \mathrm{d}v - \int_{C2+C3} q\Sigma_{ij} n_j \mathrm{d}s \right). \tag{3.35}$$

(3.35) is the final form of the power dissipated by a propagating crack achieved by [64]. With a finite element formulation (3.35) becomes,

$$\begin{aligned}\mathscr{D} &= -\{\partial V\}^\top \left(\sum_{K\in A} \int_K [q]^\top [B^V]^\top \{\Sigma_{ij}^{h,K}\} \, \mathrm{d}v + \sum_{F\in(C2+C3)} \int_F [q]^\top [N]^T [n^\Sigma] \{\Sigma^{h,K}\} \mathrm{d}s \right) \\ \mathscr{D} &= \{\partial V\}^\top \{g^{h,\Gamma}\}.\end{aligned} \tag{3.36}$$

Lastly the normal matrix is also defined,

$$[n^\Sigma] = \begin{bmatrix} n_x & 0 & n_y & 0 \\ 0 & n_y & 0 & n_x \end{bmatrix}. \tag{3.37}$$

[60] performed a similar analysis to [62, 63] and [64] to generate $\{g^{h,D}\}$. However, the conclusive statement of the domain CF calculation was different as it was believed the crack edge terms in (3.35) were deemed unnecessary and only the area integral of (3.35) was required.

It is now necessary to validate, compare and contrast the three different discretisation to compute the crack tip CF. This is performed in the next section.

3.4 Validation of the configurational force calculation

The methods to calculate the three different discrete CF calculations

- the tip $\{g^{h,t}\}$ (3.25),
- the domain $\{g^{D,t}\}$ (3.27), and
- the domain with edge integrals $\{g^{h,\Gamma}\}$ (3.36),

are validated and critiqued against three problems in Sections 3.4.1, 3.4.2 and 3.4.4. The problems either have an empirical, numerical or analytical solution. The first problem is the single edge notched (SEN) problem; it is used to evaluate which topological features of the mesh influence the accuracy of the first component of the CF. The second problem is Westergaard's double crack tip solution in an infinite plate [13]. It is used to investigate the convergence of the second component of the CF calculated using the three different methods. The last problem is the inclined crack problem, first presented by [2]; it is used to investigate the necessity of including the edge integral terms in (3.36).

When performing the validation tests the CF is calculated on a series of meshes that have undergone uniform refinement in element size, otherwise known as h-refinement. To uniformly refine the $\mathcal{T}$, every element in the mesh is refined by being split into four similar triangles, as shown in Figure 3.6.

3.4.1 Single edge notched static tensile test

This single edge notched (SEN) test is used to show that SIPG method produces CF values within the range of accuracy obtained in literature, [1, 60]. The value of the CF is dependent on:

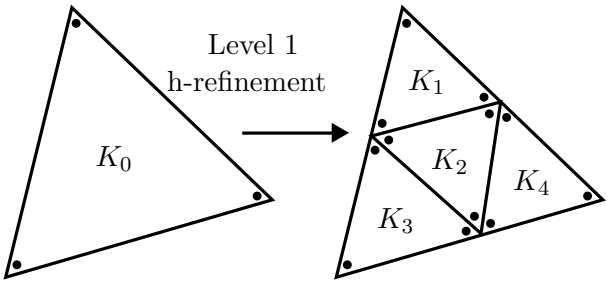

Figure 3.6: A level 1 homogeneous mesh refinement of a triangular element K_0 into four new elements. The nodes of the new elements either lie on the middle of the edges, or nodes, of K_0.

- the characteristic mesh size at the crack tip h_{cF};
- the domain around the crack tip where elements have $p_K > 1$ to increase the accuracy of stress solution about the crack tip to also increase the CF stress solution, as demonstrated in [60]. This is defined by the radius r_p; and
- the domain size A, defined by the radius r_d Figure 3.3, used in the area integral component of the CF in $\{g^{h,D}\}$ (3.27) and $\{g^{h,\Gamma}\}$ (3.25).

Additionally, r_h defines the region around the crack tip where elements are of a different length scale to the rest of the mesh. These variables are also shown graphically in Figure 3.7a. The

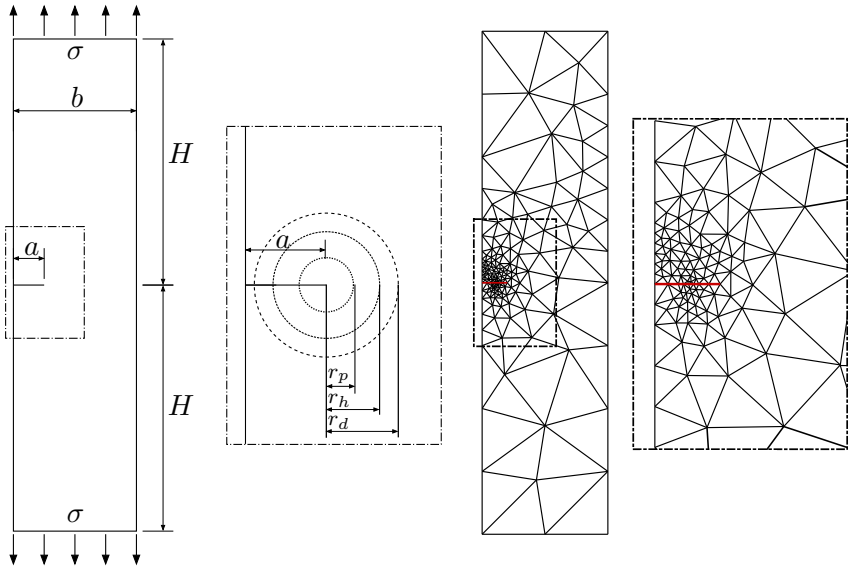

(a) (b)

Figure 3.7: SEN example: (a) geometry and loading conditions of single edge notched specimen. (b) mesh of single edge notched specimen with the crack edges highlighted in red.

geometry of the test is taken from the benchmark provided by [85] and is shown in Figure 3.7a. Here the crack length $a = 0.1$ m, the width of the plate $b = 0.5$ m, the half height of the plate $H = 1.0$ m and the uniaxial tensile stress applied is $\sigma = 10$ MPa. The plate has a Poisson's ratio of $\nu = 0.3$ and a shear modulus $\mu = 80$ GPa. Zero average displacement and rotations boundary conditions were applied using (2.52), (2.53) and (2.54). Lastly, the mesh was generated using

the unstructured mesh triangle generator, Triangle [99], and is shown in Figure 3.7b. All h-refinement occurred in a homogeneous manner uniformly across the entire mesh, as in Figure 3.6. This first investigation was conducted to validate that using SIPG it was possible to obtain accuracies within the range obtained in literature ($\approx 2\%$ see Table 3.1 for a full breakdown) for CF using continuous Galerkin methods, see Table 3.1 for a pure mode I problem. This problem is also used as investigation into how the area integral, necessary for $\{g^{h,D}\}$ (3.27) and $\{g^{h,\Gamma}\}$ (3.25), is affected by the mesh features mentioned above. Therefore for this section *only*, and unless stated otherwise, the domain integral is referring only to the area integral components of the domain calculations $\{g^{h,D}\}$ (3.27) and $\{g^{h,\Gamma}\}$ (3.25).

The first component of the CF at the crack tip can be calculated directly from the mode I SIF and is stated as

$$g_1 = \frac{K_I^2(1-\nu)}{2\mu}, \tag{3.38}$$

with a full discussion of the relation between the CF and SIFs provided in Section 3.4.2. The empirically corrected stress intensity factor, K_I, can be determined from the multiple empirical equations provided by [31]. In an effort not to be biased towards one set of experimental data, a range in the empirical stress intensity factor is defined and therefore also the CF acting at the crack tip. The range is provided by the empirical equations which give the smallest and largest K_I values in [31], respectively:

$$\frac{K_I}{K_o} = 0.265\left(1-\frac{a}{b}\right)^4 + \frac{0.857+0.265\frac{a}{b}}{(1-\frac{a}{b})^{\frac{3}{2}}}, \tag{3.39}$$

and

$$\frac{K_I}{K_o} = \sqrt{\frac{2b}{\pi a}\tan\frac{\pi a}{2b}}\cdot\frac{0.752+0.202\frac{a}{b}+0.37(1-\sin\frac{\pi a}{2b})^3}{\cos\frac{\pi a}{2b}}. \tag{3.40}$$

Using the stress intensity factor $K_o = \sigma\sqrt{\pi a}$ for an infinite plate with a crack length of $2a$, [16], the first component of the CF for the mode I SEN problem can be calculated to be in the range $g_1 = [256.7, 261.8]$ N. As the finite element solutions converge from below for h and p refinements, $g_i = [261.8\ 0]^\top$ N is considered as the reference solution with all percentage differences compared against this value, unless stated otherwise.

Given that the most accurate results obtained in both [1, 60] were obtained with the domain method, this method was used to compute the CF for the problem described in Figure 3.7a. Since r_d is defined purely on a topological basis it was investigated how varying r_d around the crack tip affected the accuracy of the CF. For this test $r_h = 0.1$ m and $p_K = 1$ for all elements. The initial element length within r_h was set to 0.04 m and graded to 0.34 m outside r_h. The mesh was refined homogeneously as in Figure 3.6. Figure 3.8 shows how $|g^{h,F}|$ changes when considering different numbers of element rings about the crack tip, the results are consistent with the works of [60, 100–103]. The CF domain integral, [60], is poorly represented by all refinement levels when only considering elements at the tip; $|g^{h,t}|$ (3.25) is equivalent to ring 0. This is followed by a large increase in accuracy, $\approx 20\%$ for all refinements. After this initial jump an overall average $\approx 1\%$ increase in accuracy between 1 and 4 rings of elements occurs, however it

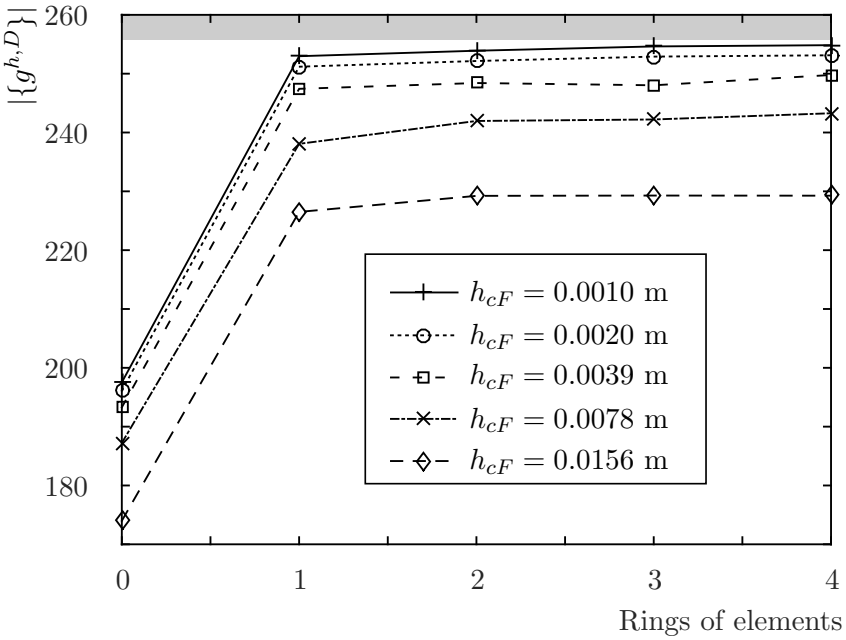

Figure 3.8: CF magnitude, for different mesh refinements at the crack tip, the range in the empirical solution of g_i is marked in grey.

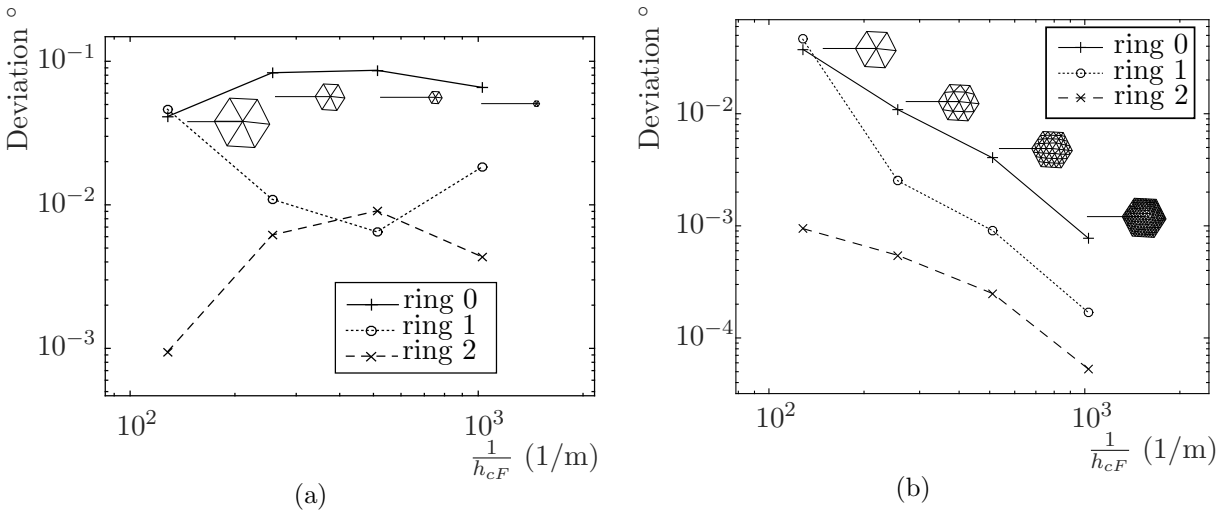

Figure 3.9: SEN: (a) How the CF deviation angle changes with element size at the crack tip and when considering different rings of elements around the crack tip when computing (3.27). (b) How CF deviation angle varies when considering the same area of elements, dictated by the element ring area on the coarsest mesh, when computing (3.27) for different mesh refinements. Example meshes of the elements considered for the computation of the CF are shown for ring 0 in both (a) and (b).

is noted that increasing the ring size in this region does not guarantee an improvement. Indeed even with refinement an improvement for an element ring size is not guaranteed. If increase in the number of element rings includes a section of poor mesh, the domain calculation could consider a region of the mesh were the stress solution is poor. The result is that the CF calculation could be perturbed leading to a less accurate result.

Since this is a pure mode I crack problem, the correct predicted crack path propagation direction is parallel with the crack edges, otherwise known as planar propagation. Therefore, the first component of the crack CF, g_1, which acts parallel to the crack edges, should have a finite value. The second CF component, g_2, which acts perpendicular to the crack edges, should be 0N. If the second CF component has a value other than 0, the predicted crack path will deviate from the correct planar propagation. The deviation is measured as the angle, $\tan^{-1}(g_2/g_1)$, with a value of 0° for planar propagation. Figure 3.9a shows how the CF deviation changes when the number of rings about the crack tip for the domain computation is kept constant but the mesh is uniformly refined. The figure shows a lack of CF angle convergence, both when increasing the number of element rings and refining the mesh for a ring size in the CF domain calculation. However, when considering a fixed area dictated by a number of element rings about the crack tip on the coarsest mesh, Figure 3.9b, monotonic convergence is achieved with uniform homogeneous mesh refinement. In the finite element formulation if the area for computing the domain evaluated CF is fixed, and homogeneous refinement occurs, the stress solution will improve in this area. Therefore the domain integral, represented here as the summation of CF nodal values, will improve monotonically.

The next investigation demonstrates how varying element polynomial order around the crack tip affected the accuracy of the CF magnitude with homogeneous mesh refinement. The initial mesh is displayed in Figure 3.7b. In Figure 3.10a $r_d = 0.08$ m, the radius of the domain integral

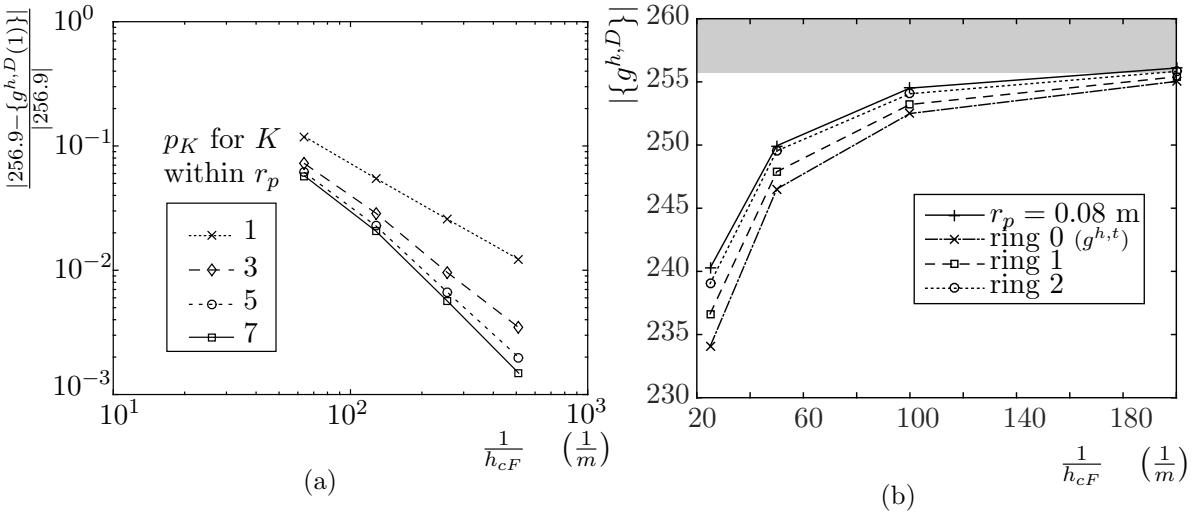

Figure 3.10: SEN: (a) varying polynomial order, p_K, of elements within $r_p = 0.05$ m, (b) varying the number of $p_K = 5$ elements modelling the stress field around the crack tip for different mesh refinements. The range in the empirical solution of g is marked in grey.

about the crack tip, and $r_p = 0.05$ m, the radius about the crack tip within which elements have an increased polynomial order, both are kept constant. The polynomial order p_K of elements within r_p at the crack tip was varied. In order to demonstrate convergence rates for this problem, a value $g_i = [256.9\ 0]^\top$ N for the CF was obtained using a structured mesh with greater than 10^6 DOF with $h_{cF} = 9.8 \times 10^{-5}$ m. This value is within the range presented by equations (3.39) and (3.40). Figure 3.10a demonstrates that refinement in either h or p converges to a CF value of

$g_i = [256.9\ 0]^\top$ N. For all polynomial orders monotonic convergence was achieved with uniform h-refinement, Figure 3.6. h-refinement converges more efficiently than p-refinement as the stress is singular at the crack tip [16]. This agrees with the analytical convergence studies obtained in [104, 105] where it was shown for problems with a singularity that h-refinement is more efficient than p-refinement. Overall a minimal error of 1.1% for $p_K = 7$ against the upper bound of the first component of the CF, 261.8 N.

Last, in Figure 3.10b, the number of rings of elements around the crack tip where $p_K = 5$ is varied whilst r_d remains constant at 0.08 m. The figure demonstrates that the accuracy of the CF is more dependent on the number of rings of elements around the crack tip which have $p_K = 5$, rather than specifying a radius r_p within which elements are a higher order. Between the first and last mesh in the series of refinements, the CF error for 2 rings of higher order elements reduces by 7.32% whilst the radius corresponding to these 2 rings decreases by 8.75 times. To be consistent the error values in Table 3.1 which have been obtained using the same

Author	Type of CF evaluation	Element type (at crack tip)	Minimum error (CF magnitude)	Mesh size at tip (m), or # of $p_K = 1$ elements
Miehe *et al.* [1, 4]	tip	1^{st}	$2 - 16\%$	17,230
Miehe *et al.* [1, 4]	domain	1^{st}	$2 - 8\%$	17,230
Bird	tip $\{g_h^t\}$	1^{st}	2.9%	1.9×10^{-3}
Bird	domain $\{g_h^D\}$	1^{st}	2.1%	1.9×10^{-3}
Bird	domain $\{g_h^D\}$	3^{rd}	1.6%	1.9×10^{-3}

Table 3.1: Comparison of error results for calculating the CF at the crack tip for the static SEN problem against methods using a CG framework.

empirical solution for this problem found in [1, 4], here $g_1 = 259.1$ N. SIPG obtains results in the range found in literature for CF values.

3.4.2 Mixed mode Westergaard solution

The Westergaard mixed mode stress solution is used in this section to validate the tip $\{g^{h,t}\}$ (3.25), the domain $\{g^{h,D}\}$ (3.27), and the domain with edge terms formulation $\{g^{h,\Gamma}\}$ (3.36). Westergaard's solution considers a double tipped crack in an infinite plate, see Figure 3.11, either acting as a pure mode I, pure mode II, or a mixed mode problem. The Westergaard stress solution was initially presented in a complex number form in [13], but can be rewritten in terms of the polar coordinates, with three different origins, as found in [106, 107]. The Westergaard stress solution for the pure mode I crack case is,

$$\begin{aligned}
\sigma_{xx}^I &= \frac{\sigma_\infty r}{\sqrt{r_A r_B}} \left(\cos\left(\theta - \frac{\theta_A}{2} - \frac{\theta_B}{2}\right) - \frac{a^2}{r_A r_B} \sin(\theta) \sin\left(\frac{3}{2}(\theta_A + \theta_B)\right)\right), \\
\sigma_{yy}^I &= \frac{\sigma_\infty r}{\sqrt{r_A r_B}} \left(\cos\left(\theta - \frac{\theta_A}{2} - \frac{\theta_B}{2}\right) + \frac{a^2}{r_A r_B} \sin(\theta) \sin\left(\frac{3}{2}(\theta_A + \theta_B)\right)\right) \text{ and} \\
\sigma_{xy}^I &= \frac{\sigma_\infty r}{\sqrt{r_A r_B}} \left(\frac{a^2}{r_A r_B} \sin(\theta) \cos\left(\frac{3}{2}(\theta_A + \theta_B)\right)\right).
\end{aligned} \tag{3.41}$$

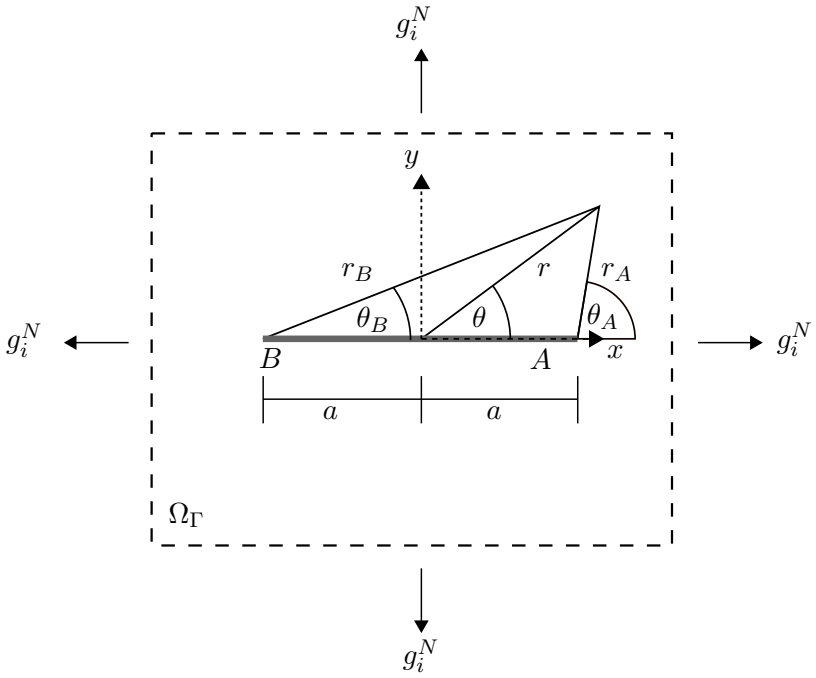

Figure 3.11: A double edge crack with the crack edges given by the grey line, the two crack tips denoted A and B. The double crack exists in an infinite domain, given by the dashed line, with a uniform inhomogeneous Neumann boundary condition existing along each edge.

The stress solution for the pure mode II case is,

$$\begin{aligned}
\sigma_{xx}^{II} &= \frac{\tau_\infty r}{\sqrt{r_A r_B}}\left(2\sin\left(\theta-\frac{\theta_A}{2}-\frac{\theta_B}{2}\right)-\frac{a^2}{r_A r_B}\sin(\theta)\cos\left(\frac{3}{2}(\theta_A+\theta_B)\right)\right)\\
\sigma_{yy}^{II} &= \frac{\tau_\infty a^2 r}{(r_A r_B)^{3/2}}\sin(\theta)\cos\left(\frac{3}{2}(\theta_A+\theta_2)\right) \text{ and}\\
\sigma_{xy}^{II} &= \frac{\tau_\infty r}{\sqrt{r_A r_B}}\left(\cos\left(\theta-\frac{\theta_A}{2}-\frac{\theta_B}{2}\right)-\frac{a^2}{r_A r_B}\sin(\theta)\sin\left(\frac{3}{2}(\theta_A+\theta_B)\right)\right)
\end{aligned} \tag{3.42}$$

r, r_A and r_B are radii shown in Figure 3.11, additionally θ, θ_A and θ_B are angles also shown in Figure 3.11. σ_∞ and τ_∞ are the far field plane and shear stress for the mode I and mode II crack problem respectively. The construction of the mixed mode problem is achieved by summing together (3.41) and (3.42) to give

$$\sigma_{xx}^M = \sigma_{xx}^I + \sigma_{xx}^{II}, \quad \sigma_{yy}^M = \sigma_{yy}^I + \sigma_{yy}^{II} \quad \text{and} \quad \sigma_{xy}^M = \sigma_{xy}^I + \sigma_{xy}^{II}. \tag{3.43}$$

To determine the value of the CF for the mode I, mode II or mixed problem it is more convenient to express the stress solutions (3.41), (3.42) and (3.43) as local forms about the crack tip. Consider crack (A), of Figure 3.11, and take $r_A \to 0$, $r \to a$ and $r_B \to 2a$ where $\theta_2 \approx \theta \approx 0$

such that (3.41) becomes

$$\begin{aligned}
\sigma_{xx}^{I} &= \frac{\sigma_\infty\sqrt{\pi a}}{\sqrt{2\pi r_A}}\cos\left(\frac{\theta_A}{2}\right)\left(1-\sin\left(\frac{\theta_A}{2}\right)\sin\left(\frac{3\theta_A}{2}\right)\right)\\
\sigma_{yy}^{I} &= \frac{\sigma_\infty\sqrt{\pi a}}{\sqrt{2\pi r_A}}\cos\left(\frac{\theta_A}{2}\right)\left(1+\sin\left(\frac{\theta_A}{2}\right)\sin\left(\frac{3\theta_A}{2}\right)\right)\\
\sigma_{xy}^{I} &= \frac{\sigma_\infty\sqrt{\pi a}}{\sqrt{2\pi r_A}}\sin\left(\frac{\theta_A}{2}\right)\cos\left(\frac{\theta_A}{2}\right)\cos\left(\frac{3\theta_A}{2}\right)
\end{aligned} \tag{3.44}$$

where the mode I stress intensity factor (SIF) is defined as $K_I = \sigma_\infty\sqrt{2\pi a}$ [16]. The same procedure can be applied to the mode II stress solution about the crack tip to give a local stress solution,

$$\begin{aligned}
\sigma_{xx}^{II} &= -\frac{\tau_\infty\sqrt{\pi a}}{\sqrt{2\pi r_A}}\sin\left(\frac{\theta_A}{2}\right)\left(2+\cos\left(\frac{\theta_A}{2}\right)\cos\left(\frac{3\theta_A}{2}\right)\right)\\
\sigma_{yy}^{II} &= \frac{\tau_\infty\sqrt{\pi a}}{\sqrt{2\pi r_A}}\sin\left(\frac{\theta_A}{2}\right)\cos\left(\frac{\theta_A}{2}\right)\cos\left(\frac{3\theta_A}{2}\right)\\
\sigma_{xy}^{II} &= \frac{\tau_\infty\sqrt{\pi a}}{\sqrt{2\pi r_A}}\cos\left(\frac{\theta_A}{2}\right)\left(1-\sin\left(\frac{\theta_A}{2}\right)\sin\left(\frac{3\theta_A}{2}\right)\right)
\end{aligned} \tag{3.45}$$

where the mode II SIF is defined as $K_{II} = \tau_\infty\sqrt{2\pi a}$. An alternative, and more general description, of the stress field local to a crack tip was developed by Williams [15]. However, importantly, both solutions at the limit $r_A \to 0$ have the same dominant terms singular terms. The continuous definition of the CF is also in the limit of an integral line path $|C| \to 0$ (3.12), which has a radius in the limit of $r \to 0$. In the limit of $r \to 0$ the stress solutions (3.44) and (3.45) and displacement solutions can be used to write the CF in terms of SIFs

$$g = \left\{ \begin{array}{l} (K_I^2 + K_{II}^2)/E_Y^* \\ -2(K_I K_{II})/E_Y^* \end{array} \right\}, \tag{3.46}$$

where the value of E_Y^* changes depending on whether the two dimensional problem is acting in plane stress or strain,

$$E_Y^* = \begin{cases} E_Y & \text{plane stress} \\ \frac{E_Y}{1-\nu^2} & \text{plane strain.} \end{cases} \tag{3.47}$$

3.4.3 Westergaard mixed mode problem validation

The Westergaard stress solution and the CF solution (3.46) are used to validate, and inspect the efficacy, of the tip (3.25), domain (3.27), and domain with edge integral terms (3.36) formulations of the CF with uniform refinement for a mixed mode crack problem with an analytical solution. A linear elastic problem solved using the SIPG formulation (2.9) is used to model the Westergaard problem. The Westergaard problem has an infinite domain. In order to be solved using the FEM the domain is truncated to a finite size, see Figure 3.12a, with $H = 1$ m, $W = 1$ m and crack length $a = 0.5$ m. The mixed mode stress solution (3.43) is applied as an inhomogeneous Neumann boundary condition on $\partial\Omega_N = \partial\Omega \setminus (\Gamma^+ \cup \Gamma^-)$ such that the stress solution on

the interior of the truncated domain will converge to the mixed mode Westergaard solution (3.46). The material is isotropic homogeneous linear elastic acting in plane stress with a Young's modulus $E = 1$ Pa and a Poisson's ratio $\nu = 0.3$. The SIFs define the Neumann boundary

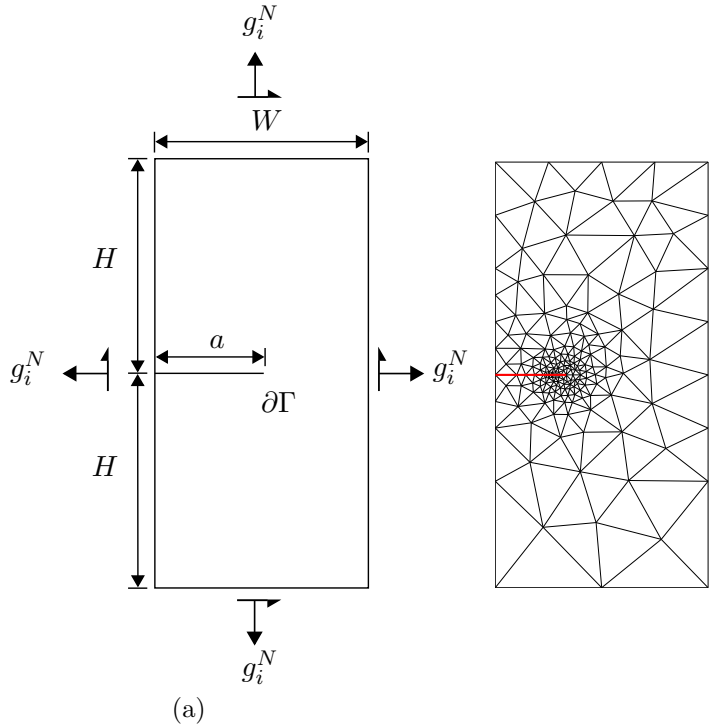

Figure 3.12: The mixed mode Westergaard problem: (a) a geometric description of the truncated domain used for the analysis and (b) the initial mesh used for the analysis for the crack edges highlighted in red.

conditions (3.44) and (3.45), and are chosen here to have a value $K_I = K_{II} = \sqrt{\pi}$ N/m. Not only does this define the stress solution on the interior of the domain, but the value of the CF at crack tip can also be defined using (3.46) and has a value

$$g = \left\{ \begin{array}{c} 2\pi \\ 2\pi \end{array} \right\} \text{ N}. \tag{3.48}$$

The initial mesh is shown in Figure 3.12b, similarly to Section 3.4.1, outside a radius $r_h = 0.1$ m about the crack tip the elements have a length 0.34 m, inside r_h the elements have a length 0.03 m. The polynomial of the elements at the crack tip are also increased. Outside the radius $r_p = 0.05$ m, about the crack tip, the elements are $p_K = 1$. Inside r_p the element order is varied to investigate how the polynomial order effects the accuracy and convergence of both components of the CF for this mixed mode problem. Last, the integral radius $r_d = 0.05$ m is defined to give the domain size A, required for the ares integrals for the CF calculations (3.27) and (3.36).

The initial mesh is uniformly refined three times. For each mesh the polynomial order within r_p is uniformly set to values in the set $r_p \in \{1, 3, 5, 7\}$. A plot of the error in the CF calculated using either $\{g^{h,t}\}$, $\{g^{h,D}\}$ or $\{g^{h,\Gamma}\}$ against the number of degrees of freedom is provided by

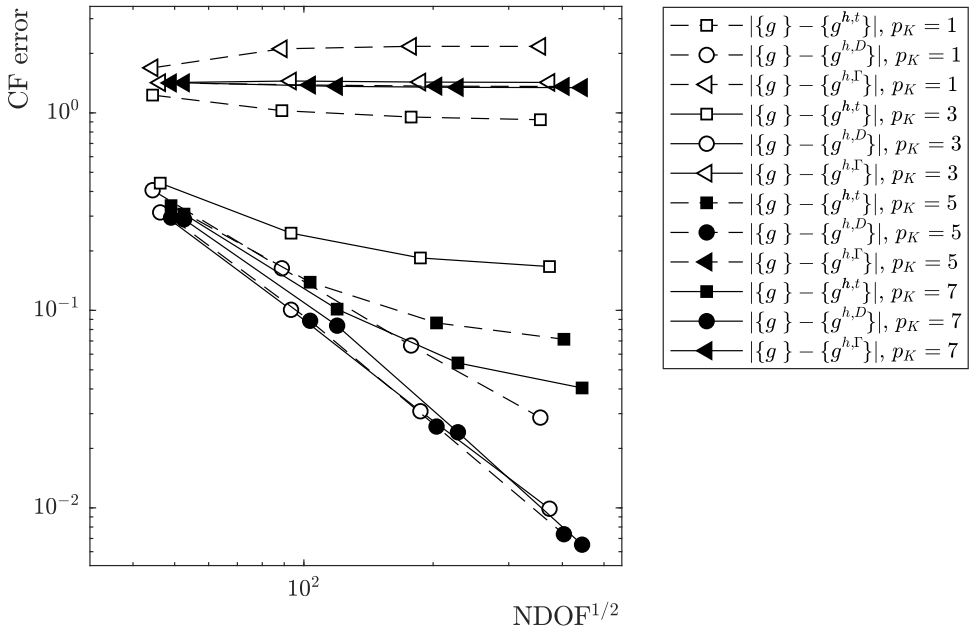

Figure 3.13: Westergaard mixed mode problem: A Convergence plot of the error in the norm of the CF calculated using the tip (3.25), domain (3.27), and domain with crack edge terms (3.36) against the Westergaard CF solution (3.46).

Figure 3.13. The Westergaard problem is a useful problem to validate that the solution of the domain components of the CF converge. Inspecting the results and assessing the convergence of the various methods of calculating the crack tip CF show firstly, when considering the domain integral and the edge integral terms, $g^{h,\Gamma}$, no convergence is achieved and the error is large, $> 100\%$. Better accuracies are achieved by the tip evaluation of the CF $\{g^{h,t}\}$, however the convergence with uniform refinement is not consistent as the rate of convergence decreases with each refinement step. When considering the domain CF calculation $g^{h,D}$, the most accurate results are achieved of $\approx 0.6\%$, the convergence rate is also consistent with refinement. However, as shown in the next section, $\{g^{h,D}\}$ can only be applied to a specific problem type.

3.4.4 Inclined crack validation

The last validation problem is the inclined crack problem shown in Figure 3.14a. It is a mixed mode problem that does not have an analytical solution for the CF at the crack tip. The problem was initially examined by [2], the results of which for the CF were computed using knowledge of the local stress field at the crack tip. The results for the CF obtained here use the tip and the two domain formulations of the CF calculation, all of which directly evaluate the CF with no knowledge of the local stress field. Since [2] does use knowledge of the local stress field to obtain a value of the CF, the results of which are used as a benchmark from which to draw conclusions.

The geometry of the inclined crack problem is shown in Figure 3.14a with dimensions $H = W = 1$ m and $a = \sqrt{0.32}$ m. The crack tip is located at $\partial\Gamma$ and the crack edges have an angle of $\theta = 45°$ to the vertical. A inhomogeneous Neumann BC is applied on the top most edge

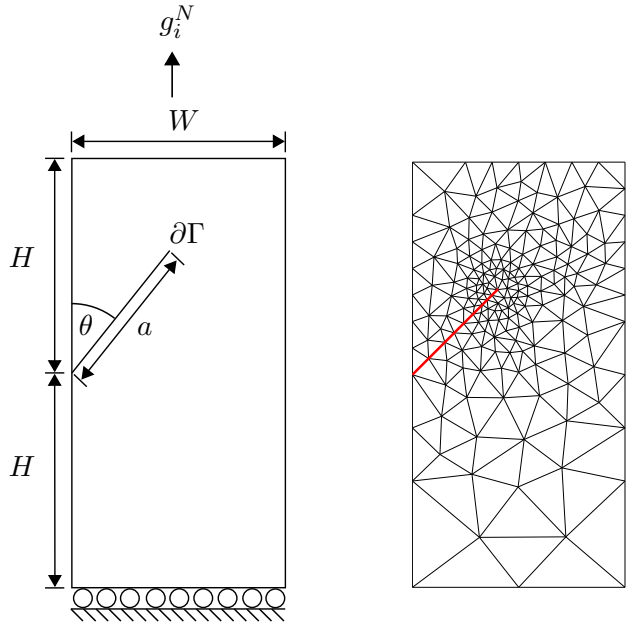

(a) (b)

Figure 3.14: Inclined crack problem: (a) the geometry of the inclined crack problem with crack tip $\partial\Gamma$ with the initial mesh shown in (b).

with a value of $g_i^N = [0\ 1]^\top$, on the bottom most edge a roller boundary condition is imposed. The roller boundary condition has a Dirichlet boundary component such that the problem is restrained in the y-axis, however no restraint exists in the x-direction. Therefore the average displacement BC in the x direction is applied, 2.52, making the system determinate.

The initial mesh is shown in Figure 3.14b, similar to the Westergaard problem in the previous section, the element sizes and polynomial order are defined by the radii r_h and r_p about the crack tip. For this problem $r_h = 0.1$ m, elements inside r_h have a side length of 0.04 m whilst elements outside of r_h are set to have a side length of 0.34 m. Elements have a polynomial order of 1 outside of $r_p = 0.05$ m, whilst elements inside of r_p have a polynomial order of 3. To validate the methods for determining the CF, the mesh is refined three times generating four sets of results for each method of evaluating the CF.

The inclined crack problem is considered to be a more general problem for analysis of the crack tip CF, since the energy solution is not continuous across the crack edges. The domain method to calculate the CF without the crack edge terms (3.27) achieved consistent convergence for the Westergaard problem, hence the domain components of both (3.27) and (3.36) are converging optimally. The Westergaard problem has a continuous energy solution across the crack edges, and hence the edge integral term of (3.36) should be zero. However, Figure 3.13 shows there is an issue with evaluating the edge term of $\{g^{h,\Gamma}\}$ along the crack edges. Further, since the energy solution is continuous across the crack edges it is not possible to determine whether the edge term of (3.36) is necessary, and if it is necessary what effect does this have on evaluating the CF when considering the CF domain formulation with the crack edge terms, (3.27).

One of the key characteristics of the first component of the CF, otherwise known as the J-

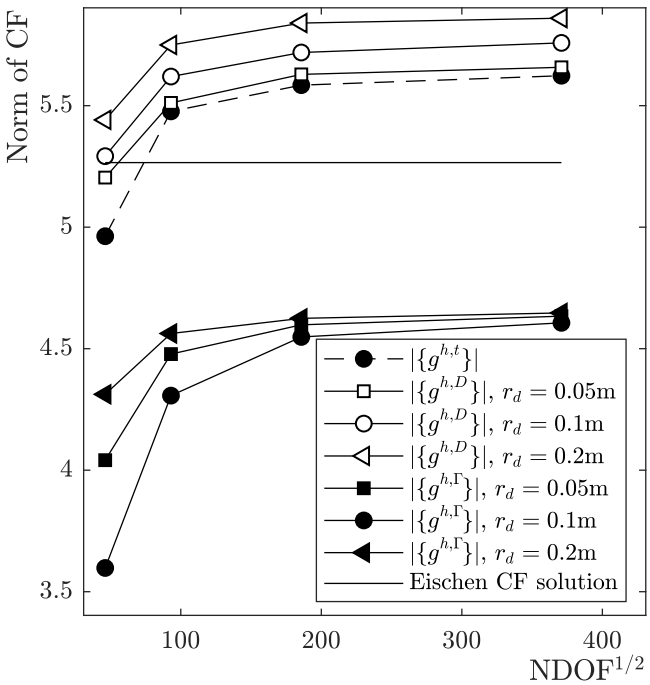

Figure 3.15: Inclined crack problem: CF with uniform mesh refinement for the tip (3.25), domain (3.27) and domain with edges (3.36) methods for calculating the CF. The solution generated by [2] is also shown.

integral [22], is that it is path independent, in its edge integral form, and domain independent in its domain integral form. Additionally it contains no edge integrals along the crack edges, which are known to be difficult to compute. Clearly there is debate in the literature about the second component of the CF, since [1, 4, 60] consider there to be no edge term, whereas following the derivations from [62–64], and observations in [108], state that there is. [108] suggested that not including the edge term will make the value of the CF from the domain computation (3.27) dependent on the domain size, however no analysis on the effect on considering different domain size on the second component of the CF was performed. Here when running the inclined crack problem, the domain radius r_d, defining the domain area A, is varied between the values in the set $r_d \in \{0.05, 0.1, 0.2\}$ for the calculation of both $\{g^{h,D}\}$ (3.27) and $\{g^{h,\Gamma}\}$ (3.36).

The norm of the CF obtained for the inclined crack problem using $\{g^{h,t}\}$ (3.25), $\{g^{h,D}\}$ (3.27) and $\{g^{h,\Gamma}\}$ (3.36) are shown in Figure 3.15. The norm of the result obtained by [2] is also included as the horizontal black line. By inspecting Figure 3.15 it is observed that:

- All of the methods for calculating the CF do not converge to that obtained by [2], and as such the three methods are inadequate at directly evaluating the CF at the crack tip. The most similar is that obtained using the tip CF method (3.25), however even this method is different by 4.7% and further was shown in the previous section to be limited in accuracy by its inconsistent convergence rate.

- For all values of r_d the domain method with the edge integrals, $\{g^{h,\Gamma}\}$(3.36), demonstrated

convergence to similar results. Compared to the largest value obtained by (3.36), a variance of 1.08% between the three different domain sizes was achieved for the final value in the series of refinements. However the value obtained for all domain sizes was at least $\approx 12\%$ away from the value obtained by [2].

- All three domain sizes considered by (3.27) converged to a different value. A correlation also exists, the smaller the domain size the closer the converged value to that achieved by [2].

In summary (3.27) converges to a value dependent on the domain, therefore the observation from [108] that the crack edges terms are required for domain independence is true. (3.36) demonstrates convergence to the same value irregardless of the domain size, however the value is inaccurate. Finally the tip evaluation of the CF (3.25) converges to a value similar to that of the smallest domain size by (3.27).

Determining whether the tip formulation is correct and, or, its inaccuracy is a numerical feature is not trivial. The near tip stress solution has a singularity proportional to $r^{-1/2}$, where r is the distance away from the crack tip. An element with a polynomial basis will be unable to capture this component of the stress solution, as the span of the derivative of the polynomial basis will not include functions which are non-analytic, such as $r^{-1/2}$. If the elements at the crack tip contained in their basis functions which could model $r^{-1/2}$ singularities, such as with XFEM methods [24], then the tip CF method would still be integrating over a domain, albeit only one element deep. It would therefore suffer from the same domain dependence issues as (3.27). Only by taking elements to the limit of $|K| \to 0$, will the tip solution converge to the correct value.

3.5 Observations

Several observations can be carried through by considering the analysis in this chapter. All three methods used to calculate the crack tip CF were unacceptable. The tip method (3.25) is unable to produce accurate results, with a minimal error of $\approx 4\%$, when the elements at the crack tip only have a polynomial basis, with consistent convergence to a value unobtainable as shown in Figure 3.13. It is suggested, but not fully investigated, accurate results would only be achieved if an enrichment function which contains the crack tip stress solution was included in elements at the crack tip and these elements were taken to the limit of $|K| \to 0$. The domain method (3.27) produced consistent convergence for the Westergaard problem and the SEN problem. However when considering the inclined crack the calculated CF was domain dependent. Last, the domain method with the crack edges, (3.36), was unable to achieve convergence for the Westergaard problem, however for the inclined crack problem its formulation was shown to be domain independent. As suggested by [2, 64, 98] the crack edge terms are difficult to evaluate close to the crack tip due to the crack tip singularity. This suggests that the formulation could be correct, but since the elements at the crack tip only have a polynomial basis the edge term is not evaluated correctly.

The second observation derives from the analysis conducted in Section 3.4.1. Other authors, such as [60, 90] performed a similar analysis (however less thorough and less conclusive),

considering rings of elements and local refinement in polynomial of elements around the crack tip. However, Section 3.4.1 demonstrated that a limited accuracy and convergence rate can be achieved. As such the efficacy of improving the accuracy by locally increasing the polynomial order about the crack top and homogeneously refining in element size is both limited and unknown, depending on the problem. This is a particularly important issue when highly accurate values of the CF, and the associated SIFs, are needed for the crack propagation direction and crack propagation rate when considering fatigue laws, such as the Paris Law [21], as discussed in [106]. In the next chapter a residual based *a posteriori* error estimate and *hp*-adaptive scheme is introduced. These new numerical tools are used to investigate further the conclusions and discussion in this chapter. Ultimately this leads to a new method which is capable of achieving highly accurate values for the crack tip CF which can be applied to a range of material types.

Chapter 4

hp-adaptivity with an *a posteriori* residual-based error estimator

4.1 Introduction

In Chapter 3 a study into the various methods to determine the CF at the crack tip was performed. During the investigation the Westergaard problem was used as a verification technique, in which an absolute error of $\approx 5 \times 10^{-3}$ was achieved for the CF, corresponding to a percentage error of $\approx 0.14\%$. This accuracy as achieved by locally refining in polynomial order around the crack tip and uniformly refining the entire mesh; the number of refinements was limited by computational power available. The accuracy of the CF is important for both the propagation direction and also for the propagation rate using fatigue measures such as the Paris law [21], which is governed by the SIFs of the CF taken to a power. The CF is shown in the previous chapter to be of a higher accuracy than those achieved in the literature however, the Westergaard problem only has one crack, smooth data is applied at the boundaries and the simulation is only in two dimensions. Clearly, achieving the same accuracy for a larger problem, considering more cracks, still in two dimensions is going to be unachievable with the same computer, let alone a three dimension problem. Therefore, a more effective and efficient method of achieving high accuracy computations of the CF at the crack tip is required.

The methodology and theory in this section provides the grounding for achieving highly accurate solutions for problems containing cracks. One of the results of the SIPG FE space, which is an advantage over conventional CG FEs, is that there is no requirement for the mesh to be conforming, and jumps in polynomial order can exist between elements. As such, implementation of a mesh containing elements varying in polynomial order and varying significantly in size is possible by employing hanging nodes. This makes SIPG highly suitable to adaptive *hp*-refinement, otherwise known as *hp*-adaptivity, where the elements in the mesh are chosen to be refined in h or p so that an error measure, such as the error in the L^2 norm of displacement, decreases at an exponential rate with respect to the total NDOF. In this thesis the *hp*-adaptivity is an automated process, driven by an error estimator, where no knowledge of a possible distribution of the error is known *a priori*, unlike the previous chapter where elements of a higher polynomial order were included around the crack tip.

Since the solution to most engineering problems is unknown, the approximation error of the FE solution is also unknown and so it cannot be used to drive a *hp*-adaptive method. However, it is possible to estimate the error distribution with the mesh using an error estimator which, up to some arbitrary constants, bounds the approximation error, or some quantity of interest, from above and below. Since the error estimate is reliable since it bounds the approximation error from above. The error estimate is also efficient since it bounds the approximation error from below. An *a posteriori* residual error estimate is used in this thesis to drive the *hp*-adaptive method [109]. The first *a posteriori* residual error estimate for SIPG was originally presented by [110] for the Poisson problem. In this thesis the *a posteriori* residual error estimate for linear elasticity, modelled using *hp*-SIPG is used, [65]. An alternative *a posteriori* error estimate, to the residual-based, is the goal orientated error estimate. Within the context of fracture mechanics [111, 112] made a significant contribution to goal-orientated error estimation in providing an estimation of the J-integral accuracy, and hence which element to flag elements for *h*-refinement. The adaptivity approach of the analysis was further improved upon by [98]. Although arguably easier to develop a reliable and efficient goal error estimate, they are considered expensive since an adjoint, or dual, problem of higher numerical fidelity has to be solved. Whereas the value of a residual-based error estimate is found by using the finite element solution, [113]. Alternatively, [114] used two enriched recovery based techniques to estimate the error in XFEM approximations containing cracks. The authors of [114] show numerically that their error estimate converges to the exact value.

The proceeding section to the introduction is Section 4.2 where the *hp a posteriori* residual based error estimate for linear elasticity is introduced along side the SIPG norm. Each norm of the error estimate and the SIPG norm is presented initially in tensor notation and then expanded out into its full form for clarity. This is followed by a description of how to determine the displacement, gradient of displacement, stress, gradient of stress from the finite element solution. For ease of readability an overview of the numerical integration schemes, presented initially in Chapter 2, is repeated here. Up to this point in the thesis conforming meshes, whereby no element edges have a hanging nod, are considered. However in this chapter and all future chapters, meshes are generated by an *hp*-adaptive method which do contain hanging nodes. The methodology of the *hp*-adaptive method used in the thesis, and the associated data structure, is presented in Section 4.3. Last in Section 4.4, the implementation of the *hp*-SIPG, error estimate and SIPG norm are verified; the efficacy *hp*-adaptive scheme for smooth and non-smooth problems is also discussed. The chapter is concluded with observations drawn in Section 4.5. It is noted that the author's published work contributes to this chapter [65].

4.2 Error Estimation

In this section the *hp a posteriori* residual based error estimator for linear elasticity using the SIPG FEM is introduced. The error estimator is derived in [65] however, the derivation is very complex and beyond the scope of this and therefore not repeated here; only a description of the purpose of each term is provided. The error estimator is denoted η and bounds the error in the

SIPG norm, $|||u_i - u_i^h|||_{\mathcal{T}}$ from above and below

$$c_\eta \eta \leq |||u_i - u_i^h|||_{\mathcal{T}} \leq C_\eta \eta, \tag{4.1}$$

where $|||u_i - u_i^h|||_{\mathcal{T}}$ is the SIPG norm error for the mesh $\mathcal{T}$, where i is a tensor index such that the norm considers all components of displacement in its calculation. In this thesis the terms reliability and efficiency are used to describe the two inequalities in (4.1). Reliability is defined as,

$$|||u_i - u_i^h|||_{\mathcal{T}} \leq C_\eta \eta, \tag{4.2}$$

and efficiency is

$$c_\eta \eta \leq |||u_i - u_i^h|||_{\mathcal{T}}, \tag{4.3}$$

where C_η and c_η are two positive constants independent of the element size and magnitude of the loading applied on the boundary [65]. The term *efficiency* is consistent with the works of [65, 115, 116], it is used here to describe the inequality (4.3) not the value c_η. Another term to describe error estimates is the effectivity index [98, 117], which is the ratio between the true error and the estimated error

$$C_E = \frac{|||u_i - u_i^h|||_{\mathcal{T}}}{\eta}. \tag{4.4}$$

It is important to note that C_E is *not* the same quantity as c_η. This chapter is *only* concerned with showing numerically that (4.3) is true, in other words stating that η is efficient for the error in the SIPG norm and not how well η estimates $|||u_i - u_i^h|||_{\mathcal{T}}$. This is important since it demonstrates that a change in value of η will correspond to a similar change of value in $|||u_i - u_i^h|||_{\mathcal{T}}$. C_η is proved in [65] to be independent of polynomial order, however, c_η is only shown numerically to be independent of p_K, or that c_η has a negligible dependence on p_K.

η is a residual based *a posteriori hp* error estimator and is applicable to where the element size and polynomial order vary within the mesh. η estimates the error of the computed numerical solution by considering the residual of the numerical solution in a suitable norm of the strong form governing differential equation for linear elasticity and the associated boundary conditions [113]. The *suitable* norm in this case is η, in this thesis it is only used as indication of convergence of the error in the SIPG norm with mesh refinement. This is possible since η is reliable and efficient for the error in SIPG norm.

In this section the SIPG norm error measure and η are introduced in a mathematical sense, respectively Section 4.2.1 and 4.2.2. Both the SIPG norm error and η are determined once the SIPG solution has been found, the method to extract the relevant data from the SIPG solution is then described in Section 4.2.3.

4.2.1 The SIPG norm

The SIPG norm error is introduced as

$$
\begin{aligned}
|||u_i - u_i^h|||_{\mathcal{T}} := \Bigg(& \sum_{K\in\mathcal{T}} \|\nabla_j u_i^{h,K} - \nabla_j u_i\|_{0,K}^2 + \sum_{F\in\mathcal{F}_{\mathrm{I}}(\mathcal{T})} \frac{\gamma p_F^2}{h_F} \left\| u_i^{h,K+} n_j^{K+} - u_i^{h,K-} n_j^{K+} \right\|_{0,F}^2 \\
& + \sum_{F\in f\mathcal{F}_{\mathrm{D}}(\mathcal{T})} \frac{\gamma p_F^2}{h_F} \left\| u_i^{h,K} - g_i^D \right\|_{0,F}^2 + \sum_{F\in\mathcal{F}_{\mathrm{T}}(\mathcal{T})} \frac{\gamma p_F^2}{h_F} \left\| u_i^{h,K} n_i - g_i^T n_i \right\|_{0,F}^2 \Bigg)^{1/2},
\end{aligned}
\tag{4.5}
$$

which when writing the norms explicitly becomes

$$
\begin{aligned}
|||u_i - u_i^h|||_{\mathcal{T}} := \Bigg(& \sum_{K\in\mathcal{T}} \int_K \left(\begin{array}{c} \left(\frac{\partial u_1^{h,K+}}{\partial x} - \frac{\partial u_1}{\partial x} \right)^2 + \left(\frac{\partial u_1^{h,K+}}{\partial y} - \frac{\partial u_1}{\partial y} \right)^2 \\ + \left(\frac{\partial u_2^{h,K+}}{\partial x} - \frac{\partial u_2}{\partial x} \right)^2 + \left(\frac{\partial u_2^{h,K+}}{\partial y} - \frac{\partial u_2}{\partial y} \right)^2 \end{array} \right) \mathrm{d}v \\
& + \sum_{F\in\mathcal{F}_{\mathrm{I}}(\mathcal{T})} \frac{\gamma p_F^2}{h_F} \int_F ((u_1^{h,K+} - u_1^{h,K-})^2 + (u_2^{h,K+} - u_2^{h,K-})^2) \mathrm{d}s \\
& + \sum_{F\in\mathcal{F}_{\mathrm{D}}(\mathcal{T})} \frac{\gamma p_F^2}{h_F} \int_F ((u_1^{h,K} - g_1^D)^2 + (u_2^{h,K} - g_2^D)^2) \mathrm{d}s \\
& + \sum_{F\in\mathcal{F}_{\mathrm{T}}(\mathcal{T})} \frac{\gamma p_F^2}{h_F} \int_F (u_1^{h,K} n_1 + u_2^{h,K} n_2 - g_1^D n_1 - g_2^D n_2)^2 \mathrm{d}s \Bigg)^{1/2}.
\end{aligned}
\tag{4.6}
$$

Similar to the L^2 error estimate (2.56), which measures the error in the displacement solution in the mesh $\mathcal{T}$, an *a priori* error estimate exists for the SIPG energy norm,

$$
|||u_i - u_i^h|||_{\mathcal{T}} \lesssim \frac{h_{\max}^{\mu-1}}{p_{\min}^{s-3/2}} \|u_i\|_{s,\Omega} \tag{4.7}
$$

where $s \geq 2$ and $\mu = \min(p_K + 1, s)$. (4.6) is necessary to numerically verify the error estimator for the SIPG norm using problems with known solutions, alongside the *a priori* error estimate (4.7).

4.2.2 The *a posteriori* error estimate

Since η is considered to be both reliable and efficient for the SIPG norm error, the convergence of η for a mesh with uniform polynomial order which is homogeneous refined in elements size is also governed by (4.7). To numerically verify that the statement (4.1) which states that the error estimator is reliable and efficient for the error in the SIPG norm, and that the numerical implementation of η is correct, the rate convergence of η is studied and compared to (4.7). η is defined as

$$
\eta = \sqrt{\sum_{K\in\mathcal{T}} \left(\eta_{R,K}^2 + \eta_{J,K}^2 + \eta_{F,K}^2 \right)} = \sqrt{\sum_{K\in\mathcal{T}} \eta_K^2}, \tag{4.8}
$$

where a single element error estimate squared is $\eta_K^2 = \eta_{R,K}^2 + \eta_{J,K}^2 + \eta_{F,K}^2$. The first component of η_K^2 is an area integral,

$$\begin{aligned}\eta_{R,K}^2 &= \frac{h_K^2}{p_K^2}\left\|\nabla_j \sigma_{ij}^{h,K} - f_i\right\|_{0,K}^2 \\ &= \frac{h_K^2}{p_K^2}\int_K \left(\begin{array}{c} \left(\frac{\partial \sigma_{11}^{h,K}}{\partial x} + \frac{\partial \sigma_{12}^{h,K}}{\partial y} - f_1\right)^2 \\ +\left(\frac{\partial \sigma_{21}^{h,K}}{\partial x} + \frac{\partial \sigma_{22}^{h,K}}{\partial y} - f_2\right)^2 \end{array} \right) \mathrm{d}v \end{aligned} \tag{4.9}$$

where h_K is the diameter of element K and p_K is the polynomial order of K. $\eta_{R,K}^2$ measures how well the strong form statement of equilibrium $\nabla_j \sigma_{ij} = f_i$ (2.1), where f_i is a body force on the interior of K, has been satisfied by the finite element approximation.

As the SIPG finite element space (2.8) allows for jumps in displacement between elements, and as such the solution is mesh dependent. The solution to the SIPG method does not necessarily satisfy $\mathcal{C}^0$ across element edges and therefore displacement jumps exist between adjacent element edges, $F \in \mathcal{F}_I(\mathcal{T})$. The Dirichlet BC on, $\partial\Omega_D$, and the Dirichlet component of the roller BC, $\partial\Omega_T$, are imposed weakly. Jumps in displacement therefore exist pointwise between the solution on the boundary and the boundary condition imposed; this is an error since the true solution on the element edge, that resides on the boundary, should be equal to the imposed Dirichlet BC. The error in the jump in displacement on the segment $F \in \mathcal{F}_I(\mathcal{T})$, the pure Dirichlet boundary $F \in \mathcal{F}_D(\mathcal{T})$ and the roller boundary $F \in \mathcal{F}_T(\mathcal{T})$ are measured as

$$\begin{aligned}\eta_{J,K}^2 = \frac{1}{2}\sum_{F\in\mathcal{F}_I(K)} \frac{\gamma^2 p_F^3}{h_F}\left\|u_i^{h,K+} n_j^{K+} - u_i^{h,K-} n_j^{K+}\right\|_{0,F}^2 + \sum_{F\in\mathcal{F}_D(K)} \frac{\gamma^2 p_F^3}{h_F}\left\|u_i^{h,K} - g_i^D\right\|_{0,F}^2 \\ + \sum_{F\in\mathcal{F}_\mathrm{T}(K)} \frac{\gamma^2 p_F^3}{h_F}\left\|u_i^{h,K} n_i - g_i^T n_i\right\|_{0,F}^2 \end{aligned} \tag{4.10}$$

which when expanded into its full form becomes

$$\begin{aligned}\eta_{J,K}^2 = \frac{1}{2}\sum_{F\in\mathcal{F}_I(K)} \frac{\gamma^2 p_F^3}{h_F}\int_F \left(\begin{array}{c} (u_1^{h,K+} n_1^+ - u_1^{h,K-} n_1^+)^2 + (u_2^{h,K+} n_1^+ - u_2^{h,K-} n_1^+)^2 \\ +(u_1^{h,K+} n_2^+ - u_1^{h,K-} n_2^+)^2 + (u_2^{h,K+} n_2^+ - u_2^{h,K-} n_2^+)^2 \end{array} \right) \mathrm{d}s \\ + \sum_{F\in\mathcal{F}_D(K)} \frac{\gamma^2 p_F^3}{h_F}\int_F \left((u_1^{h,K} - g_1^D)^2 + (u_2^{h,K} - g_2^D)^2\right) \mathrm{d}s \\ + \sum_{F\in\mathcal{F}_\mathrm{T}(K)} \frac{\gamma^2 p_F^3}{h_F}\int_F \left((u_1^{h,K} n_1 - g_1^T n_1)^2 + (u_2^{h,K} n_2 - g_2^T n_2)^2\right) \mathrm{d}s. \end{aligned} \tag{4.11}$$

Like most finite element methods, SIPG does not satisfy $\mathcal{C}^1$ across edges of adjacent elements $F \in \mathcal{F}_I(\mathcal{T})$. For element edges on the Neumann boundary $F \in \mathcal{F}_N(\mathcal{T})$, and for element edges on

the roller boundary, $F \in \mathcal{F}_T(\mathcal{T})$, these errors are respectively measured as

$$\begin{aligned}
\eta_{F,K}^2 &= \frac{1}{2} \sum_{F \in \mathcal{F}_I(K)} \frac{h_F}{p_F} \left\| \sigma_{ij}^{h,K+} n_j^{K+} - \sigma_{ij}^{h,K-} n_j^{K+} \right\|_{0,F}^2 \\
&+ \sum_{F \in \mathcal{F}_N(K)} \frac{h_F}{p_F} \left\| \sigma_{ij}^{h,K} n_j - g_i^N \right\|_{0,F}^2 + \sum_{F \in \mathcal{F}_T(K)} \frac{h_F}{p_F} \left\| t_i n_i^{\parallel} \right\|_{0,F}^2. \\
&= \frac{1}{2} \sum_{F \in \mathcal{F}_I(K)} \frac{h_F}{p_F} \int_F \begin{pmatrix} \left(\sigma_{11}^{h,K+} n_1^+ - \sigma_{11}^{h,K-} n_1^{K+} + \sigma_{12}^{h,K+} n_2^{K+} - \sigma_{12}^{h,K-} n_2^+ \right)^2 \\ \left(\sigma_{21}^{h,K+} n_1^+ - \sigma_{21}^{h,K-} n_1^{K+} + \sigma_{22}^{h,K+} n_2^{K+} - \sigma_{22}^{h,K-} n_2^{K+} \right)^2 \end{pmatrix} \mathrm{d}s \\
&+ \sum_{F \in \mathcal{F}_N(K)} \frac{h_F}{p_F} \int_F \begin{pmatrix} \left(\sigma_{11}^{h,K} n_1 + \sigma_{12}^{h,K} n_2 - g_1^D \right)^2 \\ \left(\sigma_{21}^{h,K} n_1 + \sigma_{22}^{h,K} n_2 - g_2^D \right)^2 \end{pmatrix} \mathrm{d}s \\
&+ \sum_{F \in \mathcal{F}_T(K)} \frac{h_F}{p_F} \int_F \left(t_1^{h,K} n_1 + t_2^{h,K} n_2 \right)^2 \mathrm{d}s
\end{aligned} \tag{4.12}$$

The SIPG error norm and all the terms of η have now been introduced, both of which are computed once the the solution u_i^h has been solved using the SIPG bilinear formulation (2.9). The following section is concerned with calculating each norm from an implementation perspective.

4.2.3 Norm integration schemes

The same integration methodology used to formulate the SIPG global stiffness matrix $[K]$ of (2.27) in Chapter 2 is used here to evaluate the error norms over the interior and edges of elements. For the sake of readability notation is briefly repeated here, but can found in more detail in Section 2.4 of Chapter 2.

The chosen numerical integration exists in the reference element $\widehat{K}$. An affine mapping $F_K : \widehat{K} \to K$ also exists which maps $\widehat{K}$ to an element K in the mesh $\mathcal{T}$. The basis functions and their derivatives can also be mapped from $K \to \widehat{K}$ so that an equivalent integration of the basis functions, and/or their derivatives, over K can be instead be performed over $\widehat{K}$. Therefore using F_K the following definition for the shape function matrix $[N^K]$ and equivalence form for the shape function derivative matrix $[B^K]$ therefore exist for the element $\widehat{K}$,

$$[N^K(\psi(x,y))] = [\widehat{N}^K(\widehat{\psi}(\eta,\xi))] \tag{4.13}$$

and

$$[B^K(\nabla_j \psi(x,y))] = [\widehat{B}^K(J_{ij}^{-1} \widehat{\nabla}_j \widehat{\psi}(\eta,\xi))], \quad \text{where} \quad (\eta,\xi) = F_K^{-1}(x,y). \tag{4.14}$$

J_{ij} is the Jacobian of the mapping function F_K, the full form of which is (2.19) in Chapter 2, and, $\widehat{\psi}(\eta,\xi)$ and $\psi(\eta,\xi)$ are generic basis functions in the element $\widehat{K}$ and K respectively .

The displacement solution at a point within a element is determined using the order of basis functions, p_K, for that element used for the FE analysis, $[N^K]$, and the coefficients of the basis for the element K, $\{U^K\}$, which were found using SIPG. Since the basis functions are defined for $\widehat{K}$, the definition (4.13) is used to determine the displacement for a point $(x,y) \in K \subset \mathcal{T}$

with the mapping $(\eta, \xi) = F_K^{-1}(x, y)$,

$$u_i^{h,K} = [\widehat{N}^K]\{U^K\}. \tag{4.15}$$

Similarly using the equivalence relation (4.14), the stress solution at the a point $(x, y) \in \Omega$ can be found using a matrix of basis derivatives $[\widehat{B}^K]$ with the solved for basis coefficients $\{U^K\}$. Again the order of the basis functions, p_K, for the element K used to generate the global stiffness matrix $[K]$ is used to define $[\widehat{B}^K]$. The stress solution is therefore expressed as

$$\{\sigma(u_i^{h,K})\} = \left\{ \begin{array}{c} \sigma_{xx}^{h,K} \\ \sigma_{yy}^{h,K} \\ \sigma_{xy}^{h,K} \end{array} \right\} = [D][\widehat{B}^K]\{U^K\}. \tag{4.16}$$

From (4.16) the stress tensor $\sigma_{ij}^{h,K}$ can be represented in matrix form,

$$\sigma_{ij}^{h,K} = \left[\begin{array}{cc} \sigma_{xx}^{h,K} & \sigma_{xy}^{h,K} \\ \sigma_{yx}^{h,K} & \sigma_{yy}^{h,K} \end{array} \right] \quad \text{where} \quad \sigma_{yx}^{h,K} = \sigma_{xy}^{h,K}. \tag{4.17}$$

Next, the traction vector $t_i^{h,K}$ that exists on the edge of the element is also expressed in terms of the shape function derivative matrix $[\widehat{B}^K]$, the vector of basis coefficients $\{U^K\}$, and a matrix $[n]$ that contains normal vector components to the edge of an element,

$$\{t^{h,K}\} = \left\{ \begin{array}{c} t_1^{h,K} \\ t_2^{h,K} \end{array} \right\} = [n][D][\widehat{B}^K]\{U^K\} \quad \text{where} \quad [n] = \left[\begin{array}{ccc} n_x & 0 & n_y \\ 0 & n_y & n_x \end{array} \right]. \tag{4.18}$$

Last, the gradient of the displacement, $\nabla_j u_i^{h,K}$, can be found using the matrix of basis derivatives $[\widehat{H}^K]$ and element basis coefficients,

$$\{\nabla u^{h,K}\} = \left\{ \begin{array}{c} \frac{\partial u_1^{h,K}}{\partial x} \\ \frac{\partial u_2^{h,K}}{\partial y} \\ \frac{\partial u_1^{h,K}}{\partial y} \\ \frac{\partial u_2^{h,K}}{\partial x} \end{array} \right\} = [\widehat{H}^K]\{U^K\} \quad \text{where} \quad \nabla_j u_i^{h,K} = \left[\begin{array}{cc} \frac{\partial u_1^{h,K}}{\partial x} & \frac{\partial u_1^{h,K}}{\partial y} \\ \frac{\partial u_2^{h,K}}{\partial x} & \frac{\partial u_2^{h,K}}{\partial y} \end{array} \right], \tag{4.19}$$

where

$$[H^K(\nabla_j \psi(x, y))] = [\widehat{H}^K(J_{ij}^{-1} \widehat{\nabla}_j \widehat{\psi}(\eta, \xi))] \quad \text{and} \quad (\eta, \xi) = F_K^{-1}(x, y). \tag{4.20}$$

The full form of the matrix and vector components of (4.15), (4.16) and (4.19) are described in (A.0.2), (A.0.6) and (C.0.2) respectively.

The numerical integration for the area of a triangle is defined for $\widehat{K}$ however, this is not the case for integrating over the edge $\widehat{F}$ of $\widehat{K}$. Instead, the integration is defined for the line $\widehat{L}$ and mapped to the appropriate edge $\widehat{F}$ with the mapping function $\Theta_{\widehat{F}} : \widehat{L} \to \widehat{F}$, where (ζ) is the local coordinate system for the line $\widehat{L}$. When integrating a norm on an exterior edge the Gauss point positions on $\widehat{L}$ are simply mapped to the appropriate face $\widehat{F}$ of $\widehat{K}$, such that the basis

function matrix and basis function derivative matrix can be respectively described as

$$\{u^{h,K}\} = [\widehat{N}^K(\widehat{\psi}(\eta,\xi))]\{U^K\} = [\widehat{N}^K(\widehat{\psi}(\Theta_{\widehat{F}}(\zeta)))]\{U^K\} \tag{4.21}$$

and

$$\{\sigma^{h,K}\} = [\widehat{B}^K(\widehat{\psi}(\eta,\xi))]\{U^K\} = [\widehat{B}^K(\widehat{\psi}(\Theta_{\widehat{F}}(\zeta)))]\{U^K\}, \tag{4.22}$$

where $(\eta,\xi) = \Theta_{\widehat{F}}(\zeta)$. Whereas for interior edges $F \in \mathcal{F}_I$, which are shared by adjacent elements K^+ and K^-, the mapping function is introduced $\Theta_{\widehat{F}^+} = \Theta_{\widehat{F}}$ for $\widehat{F}^+$, and for $\widehat{F}^-$ where

$$\Theta_{\widehat{F}^-} = F_{K^-}^{-1} \circ F_{K^+} \circ \Theta_{\widehat{F}^+}. \tag{4.23}$$

(4.23) ensures that the Gauss point on $\widehat{F}^+$ for K^+ and the Gauss point on $\widehat{F}^-$ for K^- correspond to the same position in the global domain Ω_Γ. See Section 2.4.3 of Chapter 2 for a full explanation. Therefore the displacement and stress vectors can be written in matrix form with the mapping functions $\Theta_{\widehat{F}^+}$ and $\Theta_{\widehat{F}^-}$,

$$\begin{array}{rcl} \{u^{h,K+}\} = [\widehat{N}^{K+}(\widehat{\psi}(\eta,\xi))]\{U^{K+}\} & = & [\widehat{N}^{K+}(\widehat{\psi}(\Theta_{\widehat{F}^+}(\zeta)))]\{U^{K+}\} \\ \{u^{h,K-}\} = [\widehat{N}^{K-}(\widehat{\psi}(\eta,\xi))]\{U^{K-}\} & = & [\widehat{N}^{K-}(\widehat{\psi}(\Theta_{\widehat{F}^-}(\zeta)))]\{U^{K-}\} \end{array} \tag{4.24}$$

and

$$\begin{array}{rcl} \{\sigma^{h,K+}\} = [\widehat{B}^{K+}(\widehat{\psi}(\eta,\xi))]\{U^{K+}\} & = & [\widehat{B}^{K+}(\widehat{\psi}(\Theta_{\widehat{F}^+}(\zeta)))]\{U^{K+}\} \\ \{\sigma^{h,K+}\} = [\widehat{B}^{K-}(\widehat{\psi}(\eta,\xi))]\{U^{K-}\} & = & [\widehat{B}^{K-}(\widehat{\psi}(\Theta_{\widehat{F}^-}(\zeta)))]\{U^{K-}\}. \end{array} \tag{4.25}$$

The method to extract all the variables from the SIPG solution for the norms that comprise the SIPG norm error and η have now been described. The integral schemes required to compute the SIPG norm error (4.6) and the components of η (4.8), except $\eta^2_{R,K}$, are provided here. The computation of $\eta^2_{R,K}$ is described in the next section. The integration schemes can be split into five groups.

Group 1 can be applied to all terms of the SIPG norm (4.6) and η where the norm of a displacement jump is evaluated on an interior element edge $F \in \mathcal{F}_I$.

$$\begin{array}{l} \|u_i^{h,K+}n_j^{K+} - u_i^{h,K-}n_j^{K+}\|^2_{0,F} = \\ \displaystyle\int_{F\in\mathcal{F}_\jmath} \left(\begin{array}{c} (u_1^{h,K+}n_1^{K+} - u_1^{h,K-}n_1^{K+})^2 + (u_2^{h,K+}n_1^{K+} - u_2^{h,K-}n_1^{K+})^2 \\ +(u_1^{h,K+}n_2^{K+} - u_1^{h,K-}n_2^{K+})^2 + (u_2^{h,K+}n_2^{K+} - u_2^{h,K-}n_2^{K+})^2 \end{array} \right) \mathrm{d}s \\ = \displaystyle\sum_{q=1}^{\lceil((p_{K+}+p_{K-})+1)/2\rceil} \left(\begin{array}{c} (u_1^{h,K+}n_1^{K+} - u_1^{h,K-}n_1^{K+})^2 + (u_2^{h,K+}n_1^{K+} - u_2^{h,K-}n_1^{K+})^2 \\ +(u_1^{h,K+}n_2^{K+} - u_1^{h,K-}n_2^{K+})^2 + (u_2^{h,K+}n_2^{K+} - u_2^{h,K-}n_2^{K+})^2 \end{array} \right) \frac{|F|}{|\widehat{L}|} a_q, \end{array} \tag{4.26}$$

where q is the Gauss point number, a_q is the Gauss point weight with corresponding coordinates $(\xi_q,\eta_q) \in \widehat{K}$ and, $u_i^{h,K+}$ and $u_i^{h,K-}$ are determined by (4.24).

Group 2 evaluates the jumps in stresses for η along an interior element edge. Its form is similar to (4.26), but is repeated for the sake of clarity. The numerical integration of the norm

of the jump in stress is by

$$\begin{aligned}
&\|\sigma_{ij}^{h,K+}n_j^{K+} - \sigma_{ij}^{h,K-}n_j^{K-}\|_{0,F}^2 \\
&= \int_{F\in\mathcal{F}_\jmath} \left(\begin{array}{r} \left(\sigma_{11}^{h,K+}n_1^{K+} - \sigma_{11}^{h,K-}n_1^{K+} + \sigma_{12}^{h,K+}n_2^{K+} - \sigma_{12}^{h,K-}n_2^{K+}\right)^2 \\ +\left(\sigma_{21}^{h,K+}n_1^{K+} - \sigma_{21}^{h,K-}n_1^{K+} + \sigma_{22}^{h,K+}n_2^{K+} - \sigma_{22}^{h,K-}n_2^{K+}\right)^2 \end{array} \right) \mathrm{d}s \\
&= \sum_{q=1}^{\lceil((p_{K+}+p_{K-})+1)/2\rceil} \left(\begin{array}{r} \left(\sigma_{11}^{h,K+}n_1^{K+} - \sigma_{11}^{h,K-}n_1^{K+} + \sigma_{12}^{h,K+}n_2^{K+} \ldots \right. \\ +\left(\sigma_{21}^{h,K+}n_1^{K+} - \sigma_{21}^{h,K-}n_1^{K+} + \sigma_{22}^{h,K+}n_2^{K+} \ldots \right. \\ \left. \ldots - \sigma_{12}^{h,K-}n_2^{K+}\right)^2 \\ \left. \ldots - \sigma_{22}^{h,K-}n_2^{K+}\right)^2 \end{array} \right) \frac{|F|}{|\widehat{L}|}a_q,
\end{aligned} \tag{4.27}$$

where $\sigma_{ij}^{h,K+}$ and $\sigma_{ij}^{h,K-}$ are evaluated for the Gauss point q with (4.25).

Group 3 evaluates the jumps in displacement along exterior element boundaries and the imposed displacement boundary condition. This is used to evaluate the error between the applied Dirichlet BC applied to $\partial\Omega_D$ and $\partial\Omega_T$. Since the BC applied to $\partial\Omega_D$ considers both components of the displacement, whereas the BC on $\partial\Omega_T$ only considers the displacement acting normal to the boundary, the error norm to evaluate the error in displacement along $\partial\Omega_D$ is used as an example. It is noted that the same integration strategy is applied to both norms. The numerical integration of error in the displacement along a Dirichlet boundary is

$$\begin{aligned}
\|u_i^h - g_i^D\|_{0,F}^2 &= \int_{F\in\mathcal{F}_\jmath} \left((u_1^h - g_1^D)^2 + (u_2^h - g_2^D)^2\right) \mathrm{d}s \\
&= \sum_{q=1}^{(P\lceil(2p_K+1)/2\rceil)} \left((u_1^h - g_1^D)^2 + (u_2^h - g_2^D)^2\right) \frac{|F|}{|\widehat{L}|}a_q,
\end{aligned} \tag{4.28}$$

where $P > 0$ is an integer which increases the number of Gauss points. This an integration is being applied to a function which potentially may not be exactly integrable with Gauss quadrature, hence a higher Gauss quadrature is required. u_i^h is evaluated at a Gauss point with (4.21) and the value of function $g_i^D(x,y)$ at the gauss point location (ξ_q, η_q) is found using F_K^{-1}.

Group 4 To evaluate the error between the imposed stress along the boundary and the stress along the element edge, the same integration scheme as (4.28) is used. The integration is scheme is used to evaluate the jumps in stresses along the roller and the Neumann BC, respectively $\partial\Omega_T$ and $\partial\Omega_D$. Evaluation of the error norm in the Neumann boundary is used here as an example, but again a similar integral can be perform to evaluate the stress components of $\partial\Omega_T$. The numerical integration of the error norm of the Neumann BC is,

$$\begin{aligned}
\|\sigma_{ij}^h n_j - g_i^N\|_{0,F}^2 &= \int_{F\in\mathcal{F}_\jmath} \left(\begin{array}{r} \left(\sigma_{11}^{h,K}n_1 + \sigma_{12}^{h,K}n_2 - g_1^N\right)^2 \\ +\left(\sigma_{21}^{h,K}n_1 + \sigma_{22}^{h,K}n_2 - g_2^N\right)^2 \end{array} \right) \mathrm{d}s \\
&= \sum_{q=1}^{(P\lceil(2p_K+1)/2\rceil)} \left(\begin{array}{r} \left(\sigma_{11}^{h,K}n_1 + \sigma_{12}^{h,K}n_2 - g_1^N\right)^2 \\ +\left(\sigma_{21}^{h,K}n_1 + \sigma_{22}^{h,K}n_2 - g_2^N\right)^2 \end{array} \right) \frac{|F|}{|\widehat{L}|}a_q,
\end{aligned} \tag{4.29}$$

where $\sigma_{ij}^{h,K}$ is found at a gauss point by considering (4.22), and the value of function $g_i^N(x,y)$ at the gauss point location (ξ_q, η_q) is found using F_K^{-1}.

Group 5 The last term to consider for numerical integration is the error norm of the displacement gradient from the approximate solution, $\nabla_j u_i^h$, against the true solution, $\nabla_j u_i$. The integral is evaluated in the interior of elements for the SIPG error norm (4.6) and uses the same numerical scheme as the integral of the volumetric components of $[K]$. The norm is evaluated numerically with

$$\|\nabla_j u_i^{h,K} - \nabla_j u_i\|_{0,K}^2 = \int_K \begin{pmatrix} \left(\frac{\partial u_1^{h,K}}{\partial x} - \frac{\partial u_1}{\partial x}\right)^2 + \left(\frac{\partial u_1^{h,K}}{\partial y} - \frac{\partial u_1}{\partial y}\right)^2 \\ + \left(\frac{\partial u_2^{h,K}}{\partial x} - \frac{\partial u_2}{\partial x}\right)^2 + \left(\frac{\partial u_2^{h,K}}{\partial y} - \frac{\partial u_2}{\partial y}\right)^2 \end{pmatrix} \mathrm{d}v$$

$$= \sum_{q=1}^{(P\lceil(2p_K+2)/2\rceil)} \sum_{g=1}^{(P\lceil(2p_K+1)/2\rceil)} \left(\frac{1-\xi_q}{2}\right) \begin{pmatrix} \left(\frac{\partial u_1^{h,K}}{\partial x} - \frac{\partial u_1}{\partial x}\right)^2 + \left(\frac{\partial u_1^{h,K}}{\partial y} - \frac{\partial u_1}{\partial y}\right)^2 \\ + \left(\frac{\partial u_2^{h,K}}{\partial x} - \frac{\partial u_2}{\partial x}\right)^2 + \left(\frac{\partial u_2^{h,K}}{\partial y} - \frac{\partial u_2}{\partial y}\right)^2 \end{pmatrix} \frac{1-\xi_a}{2} \det(J_{ij})\, a_q b_g. \tag{4.30}$$

where $\nabla_j u_i^h$ is determined at a Gauss point location $(\eta_{q,g}, \xi_{q,g})$, with q and g as the Gauss point number *not* tensor indices, using the mapping F_K^{-1}, a_q and b_g are Gauss point weights respectively for Gauss point numbers q and g. Last $\det J_{ij}$ is a constant found using (2.19) in Chapter 2.

4.2.4 $\eta_{R,K}^2$ computation

The numerical integration scheme for $\eta_{R,K}^2$ is the same numerical integration used to evaluate the error norm of the gradient of the displacement (4.30). The numerical integration of the norm in $\eta_{R,K}^2$ can therefore be immediately provided,

$$\|\nabla_j \sigma_{ij}^{h,K} - f_i\|_{0,K}^2 = \int_K \begin{pmatrix} \left(\frac{\partial \sigma(u_l^{h,K})_{11}}{\partial x} + \frac{\partial \sigma(u_l^{h,K})_{12}}{\partial y} - f_1\right)^2 \\ + \left(\frac{\partial \sigma(u_l^{h,K})_{21}}{\partial x} + \frac{\partial \sigma(u_l^{h,K})_{22}}{\partial y} - f_2\right)^2 \end{pmatrix} \mathrm{d}v$$

$$= \sum_{q=1}^{(P\lceil(2p_K)/2\rceil)} \sum_{g=1}^{(P\lceil(2p_K-1)/2\rceil)} \begin{pmatrix} \left(\frac{\partial \sigma(u_l^{h,K})_{11}}{\partial x} + \frac{\partial \sigma(u_l^{h,K})_{12}}{\partial y} - f_1\right)^2 \\ + \left(\frac{\partial \sigma(u_l^{h,K})_{21}}{\partial x} + \frac{\partial \sigma(u_l^{h,K})_{22}}{\partial y} - f_2\right)^2 \end{pmatrix} \left(\frac{1-\xi_a}{2}\right) \det(J_{ij})\, a_q b_g. \tag{4.31}$$

Where q and g are Gauss point numbers with corresponding positions $(\eta_{q,g}, \xi_{q,g}) \in \widehat{K}$ and $f_i(x,y)$ is a body function which is determine at a Gauss point within $\widehat{K}$ using F_K^{-1}. However, since the numerical integration in (4.31) occurs over the reference element $\widehat{K}$ and the terms of $\nabla_j \sigma_{ij}$ contain second order derivatives of displacement, and therefore second order derivatives of the basis functions, a Jacobian fourth order tensor of first order derivative terms squared is introduced. This tensor maps the second order derivatives of the shape functions from the global coordinate system to the local coordinate system. However first, the second order derivative of

displacement is introduced in terms of basis functions and their respective coefficients for the global coordinate system,

$$\nabla_i\nabla_j u_q^{h,K} = \underbrace{\sum_{V\in\{v1,v2,v3\}} U_q^{V,K}(\nabla_i\nabla_j\psi^V)}_{=0_q} + \sum_{2\le p_e\le p_K}\sum_{E\in\{e1,e2,e3\}} U_{p_e,q}^{E,K}\nabla_i\nabla_j\psi_{p_e}^E + \sum_{3\le p_b\le p_K} U_{p_b,q}^{B,K}\nabla_i\nabla_j\psi_{p_b}^B. \tag{4.32}$$

The basis functions of (4.32) can be mapped to the reference element $(\eta,\xi)\in\widehat{K}$. This is achieved with the use of the Jacobian tensor $H_{ijpq}(x,y,\eta,\xi)$ such that, $(\nabla_i\nabla_j\psi(x,y)) = H_{ijpq}^{-1}(\widehat{\nabla}_i\widehat{\nabla}_j\widehat{\psi}(\eta,\xi))\circ F_K^{-1}(x,y)$, to give

$$\underbrace{\begin{bmatrix} \left(\frac{\partial x}{\partial\eta}\right)^2 & 2\left(\frac{\partial x}{\partial\eta}\frac{\partial y}{\partial\eta}\right) & \left(\frac{\partial y}{\partial\eta}\right)^2 \\ \frac{\partial x}{\partial\eta}\frac{\partial x}{\partial\xi} & \left(\frac{\partial x}{\partial\eta}\frac{\partial y}{\partial\xi}+\frac{\partial x}{\partial\xi}\frac{\partial y}{\partial\eta}\right) & \frac{\partial y}{\partial\eta}\frac{\partial y}{\partial\xi} \\ \left(\frac{\partial x}{\partial\xi}\right)^2 & 2\left(\frac{\partial x}{\partial\xi}\frac{\partial y}{\partial\xi}\right) & \left(\frac{\partial y}{\partial\xi}\right)^2 \end{bmatrix}}_{[H]} \underbrace{\begin{Bmatrix} \frac{\partial^2\psi}{\partial x^2} \\ \frac{\partial^2\psi}{\partial yx} \\ \frac{\partial^2\psi}{\partial y^2} \end{Bmatrix}}_{\{\nabla\nabla\psi\}} = \underbrace{\begin{Bmatrix} \frac{\partial^2\widehat{\psi}}{\partial\eta^2} \\ \frac{\partial^2\widehat{\psi}}{\partial\eta\xi} \\ \frac{\partial^2\widehat{\psi}}{\partial\xi^2} \end{Bmatrix}}_{\{\widehat{\nabla}\widehat{\nabla}\hat{\psi}\}}. \tag{4.33}$$

From an implementation point of view, the second order derivatives of the basis functions are known in $\widehat{K}$ and the Gaussian integration scheme exists for $\widehat{K}$. Every term in $[H]$ can be determined directly from J_{ij} (2.19). The tensor $\nabla_j\sigma_{ij}^{h,K}$ can be represented as a matrix vector equation

$$\{\nabla\sigma^{h,K}\} = \begin{Bmatrix} \frac{\partial\sigma_{11}^{h,K}}{\partial x}+\frac{\partial\sigma_{12}^{h,K}}{\partial y} \\ \frac{\partial\sigma_{21}^{h,K}}{\partial x}+\frac{\partial\sigma_{22}^{h,K}}{\partial y} \end{Bmatrix} = [D_2][\widehat{BB}^K(H_{ijpq}^{-1}(\widehat{\nabla}_i\widehat{\nabla}_j\widehat{\psi}(\eta,\xi)))]\{U^K\} \tag{4.34}$$

where $(\eta,\xi) = F_K^{-1}(x,y)$, $[D_2]$ is a matrix of material coefficients, $[\widehat{BB}^K]$ is a matrix of second order derivatives of basis functions for the element $\widehat{K}$, and $\{U^K\}$ is a vector contain the basis function coefficients; the matrices in their expanded form are shown in (D.0.3).

4.3 *hp*-adaptivity and the data structure

When η is combined with a suitable *hp*-adaptive scheme, η will converge exponentially with respect to the $\text{NDOF}^{1/2}$ for problems with a smooth solution, and $\text{NDOF}^{1/3}$ for problems with a non-smooth solution [118]. A smooth solution is considered here to be $u\in[H^s(\Omega_\Gamma)]^2$ where the regularity $s>3/2$. A solution is considered non-smooth when $s<3/2$. Since η is both reliable and efficient for the error in the SIPG norm (4.1), the error in the SIPG norm also convergences exponentially.

In this section the *hp*-adaptive strategy and *hp*-SIPG data structure is outlined. All elements used are arbitrary high order triangles found in [73]. The strategy used here was originally proposed by [119] for BEM, and was shown to be proficient for finite elements in [118]. It is driven by the error estimate value on each element η_K^2 with the aim of reducing η with the smallest possible increase in the NDOF.

4.3.1 *hp*-SIPG data structure

The introduction of the *hp*-SIPG data structure requires the definition of new variables for its description, all of which are summarised in Table 4.1. When *hp*-adaptively refining two meshes

variable	description
S	Generation of the mesh
$\mathcal{T}_S$	Current mesh
$\bar{\mathcal{T}}$	Future mesh, of $\mathcal{T}_S$, to be generated from *hp*-adaptivity
$K \in \mathcal{T}$	Element K of the mesh $\mathcal{T}$
$\bar{K} \in \bar{\mathcal{T}}$	Element $\bar{K}$ of the mesh $\bar{\mathcal{T}}$
$\mathcal{E}$	The set of all meshes generated, such that $\bar{\mathcal{T}} \subset \mathcal{E}$ and $\mathcal{T}_S \subset \mathcal{E}$
$C(K)$	Set of four children elements created by the homogeneous h-refinement of K
c	The element number
p	An element's parent number

Table 4.1: A table of variables introduced to describe the *hp*-SIPG data structure

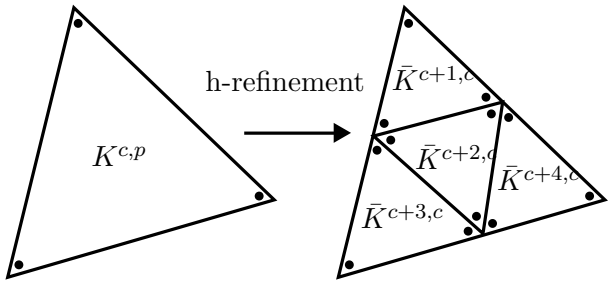

Figure 4.1: A homogeneous mesh refinement of triangular element $K^{c,p}$ into 4 new elements, where the superscripts c, p are respectively the element and element's parent number.

are considered at a time, the current mesh $\mathcal{T}_S$ in the which the SIPG solution has just been found, and the new mesh $\bar{\mathcal{T}}$ which is produced from the *hp*-adaptive method. The meshes $\mathcal{T}_S$ and $\bar{\mathcal{T}}$ respectively have generation numbers S and $S+1$, where the first mesh in series of refinements has $S = 0$. Since $\mathcal{T}_S$ is being refined it is considered to be inactive, the future mesh $\bar{\mathcal{T}}$, and all $\bar{K} \in \bar{\mathcal{T}}$, is considered to be active. When an element in the mesh $\mathcal{T}_S$ is marked for h-refinement it is refined homogeneously, see Figure 4.1. The original element is defined as the parent K, the new smaller elements are known as its children which form a set of four siblings, $\bar{K} \in C(K)$. Every element in $\mathcal{E}$ has two variables which define it, the element number c and the element's parent number p. If an element is not a parent it is considered active such that $\bar{K} \in \bar{\mathcal{T}}$. Last, if an element has no parent $p = 0$. The mesh data structure is stored in a data tree as described by Figure 4.2, where an element K is label's with superscripts c and p, $K^{c,p}$, to illustrate its position in the data tree. When producing the future mesh $\bar{\mathcal{T}}$, two conditions need to be satisfied to ensure that η remains reliable and efficient for the SIPG norm error. In other words, to prevent the constants c_η and C_η of (4.1) becoming a function of the polynomial

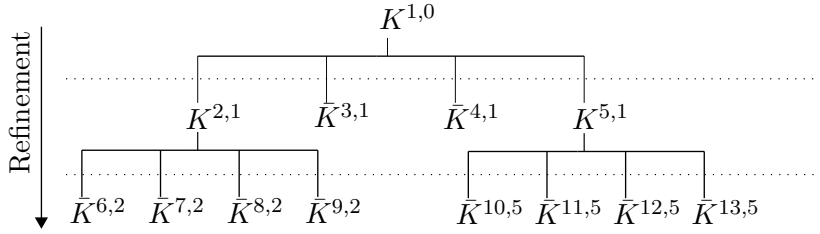

Figure 4.2: An element family tree, where $K^{c,p}$ are inactive elements with element number c and parent p, elements $\bar{K}$ are in the future mesh $\bar{\mathcal{T}}$.

order and/or the diameter of elements with the mesh [65]. This two statements are respectively referred to the p-smoothness and h-smoothness condition. The p-smoothness condition ensures the difference in polynomial order between the elements K^+ and K^- which share the face $F \in \mathcal{F}_I$ cannot have a difference of greater than 1. The h-smoothness condition ensures that only one hanging node exists on any element face. It is important to reiterate here that $K \in \mathcal{T}$ only refers to the geometry of an element, each element has an associated polynomial order p_K. A second variable for K is also defined as R_K, with the vector function $\underline{R} = \{R_K : K \in \mathcal{T}\}$. R_K is a refinement flag used to ensure the h-smoothness condition. At $S = 0$ no refinement steps have occurred and the mesh is conforming such that $R_K = 0 \; \forall K \in \mathcal{T}$.

4.3.2 hp-adaptivity

The hp-adaptive method is driven by the element estimate η_K^2 calculated for all $K \in \mathcal{T}$. The hp-adaptive strategy was originally proposed by [119] for the boundary element method but was shown to be proficient for the FEM when the solution contains singularities [118]. Whether an element K is refined in h or p is governed by two user pre-defined constants, δ_2 and δ_1 such that :

- If $\eta_K^2 > \delta_2 \eta_{\max}^2$ the element K is refined in h;
- Else if $\delta_2 \eta_{\max}^2 \geq \eta_K^2 \geq \delta_1 \eta_{\max}^2$ the element K is refined in p.

Where $\eta_{\max}^2 = \max_{K \in \mathcal{T}}(\eta_K^2)$. Elements with the larger errors in the mesh, $\eta_K^2 > \delta_2 \eta_{\max}^2$, are assumed to be associated with a non-smooth part of the solution and so a h-refinement on the element K will have a faster reduction in η with respect to the NDOF. In the extreme case it could be possible that the solution is sufficiently non-smooth in K that an increase in p will not decrease η. However more generally, an arbitrarily high polynomial function could always have some error associated with modelling a non-smooth function, it is therefore more efficient to refine these elements in h. Elements with errors in the band, $\delta_2 \eta_{\max}^2 \geq \eta_K^2 > \delta_1 \eta_{\max}^2$, are considered to be modelling a smooth part of the solution, but p_K is not high enough to obtain a good solution and so a relatively large value of η_K^2 still exists. Since the solution is assumed to be smooth it is more efficient here to refine in p order than in h. Although refining in h will achieve convergence, it will be slower with respect to the number of degrees of freedom added. The hp-adaptive algorithm is described with Algorithm 4.1 with the use of an example consisting of six elements.

Algorithm 4.1 *hp*-adaptive algorithm.

This algorithm describes the error driven hp-adaptive method. It is explained in conjunction with an example consisting of 6 elements, shown below. Each element has a polynomial order and refinement level, p_K and R_K respectively; these are expressed as a row vector $[R_K, p_K]$ in each element contained in the Algorithm.

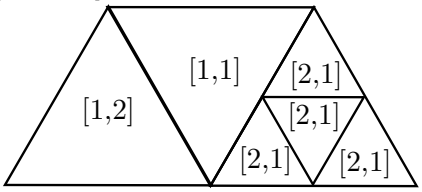

Step 1 Compute the estimated error η_K and determine the maximum element error, $\eta^2_{\max} = \max_{K\in\mathcal{T}}(\eta^2_K)$.

Step 2 Determine the set of elements to refine in p and create $\mathcal{T}_P = \{K \in \mathcal{T} | \delta_2\eta^2_{\max} \geq \eta^2_K > \delta_1\eta^2_{\max}\}$.

Step 3 Identify the set of elements to refine in h and create $\mathcal{T}_H$ of $\mathcal{T}$ such that $\mathcal{T}_H = \{K \in \mathcal{T} | \eta^2_K > \delta_2\eta^2_{\max}\}$.

Step 4 Elements are p-refined by adding 1 to p_K if $K \in \mathcal{T}_P$, and elements are marked for h-refinement by adding 1 to R_K if $K \in \mathcal{T}_H$. This is indicated in the diagram below, the elements marked for p and h refinement are marked with light and dark grey shading respectively.

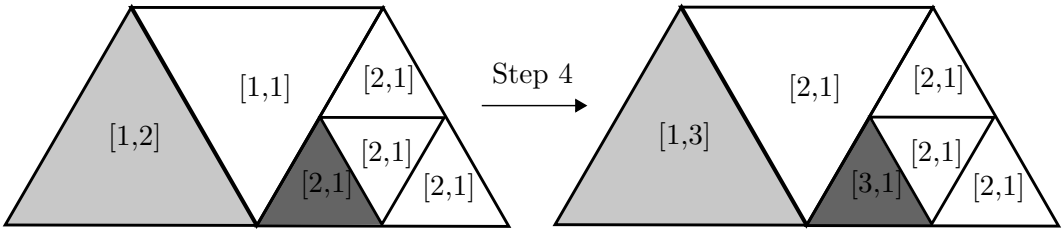

4.4 numerical verification

In this section the same four examples used to verify the correct implementation of the SIPG method by investigating the convergence of the error in the L^2 displacement are used here to verify:

1. That η is efficient and reliable for the SIPG norm error, (4.1), and as such the constants c_η and C_η are independent of polynomial order and diameter of elements in the mesh.

2. The statement of the *a priori* error for the SIPG norm (4.6), and thus also η, is true for problems with a regularity $s = 3/2 - \epsilon$.

3. η has been implemented correctly for all boundary conditions.

The convergence of η is studied for each of the four problems, the geometry and boundary conditions of which are shown in Figures 4.3a, 4.3b, 4.3c and 4.3d. Every problem has a Young's modulus $E_y = 5/2$ Pa and Poisson's ratio $\nu = 0.3$ and is considered to be acting in plane stress. For each problem an initial mesh of homogeneous polynomial order is generated, the mesh is subsequently uniformly refined to generate a series of new meshes. For each mesh the value of η and the NDOF is recorded; the convergence rate of η with respect to $NDOF^{1/2}$ is also

Step 5 To ensure that only one hanging node exists on an element edge, the absolute difference in R_K for two adjacent elements, K^+ and K^-, must be less than or equal to 1, $|R_K^+ - R_K^-| \leq 1$. To facilitate this, all edges in the mesh are looped through. If $|R_K^+ - R_K^-| \leq 1$ is not true for an edge the element with the smaller R_K value is: identified, its value increased by 1 and K is added to the set $\mathfrak{T}_H$. The loop is only exited when a complete run through of all edges in within the mesh is completed with no changes to $R_K \in \underline{R}$. In this example only one new element is identified for h-refinement, indicated by the dark grey shaded element below.

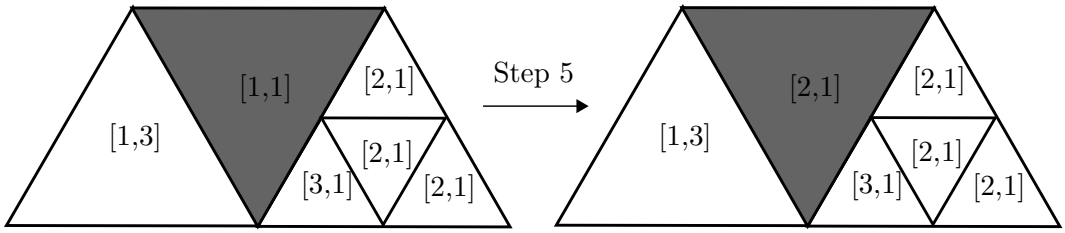

Step 6 h-refine all elements $K \in \mathfrak{T}_H$ to create the new mesh $\bar{\mathfrak{T}}$.

Step 7 Another criteria of to ensure the error estimate is reliable and efficient for the true error is that the difference in polynomial order between two adjacent elements in a mesh must be less than or equal to one. To ensure this is true, all edges in the mesh are looped through. If $|p_K^+ - p_K^-| \leq 1$ is not true for an edge the element with the smaller $p_{\bar{K}}$ value is: identified, its value increased by 1 and $\bar{K}$ is added to the set $\bar{\mathfrak{T}}_P$. The loop is only exited when a complete run through of all edges within the new mesh is completed with no changes to $p_{\bar{K}} \in \underline{\bar{p}}$. In this example two new elements are identified for p-refinement, indicated by the light grey shaded elements below.

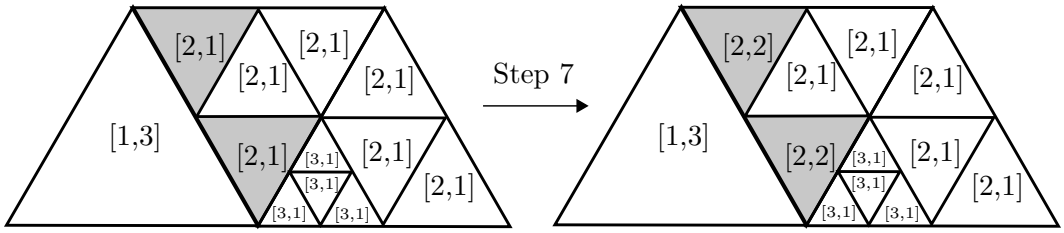

Step 8 Last, as the hp-adaptive algorithm is complete, the mesh number is increased by 1: $S = S + 1$.

recorded. By showing the convergence of η is the same as that of the *a priori* error estimate of the SIPG norm error supports the argument that c_η has a very mild, or no dependence, on the polynomial order and diameter of elements in the mesh. This is also studied more thoroughly in the next section by considering hp-adaptivity. If the convergence rate is correct for all regular problems this will additionally show that the implementation is correct for all boundary conditions, further it will also show that the average boundary condition has no effect on the efficacy of η. If the convergence rate is also correct for the non-smooth problem where $s = 3/2$, it will demonstrate that the condition $s > 2$ for the *a priori* estimate for the SIPG norm can be relaxed. Further, it will provide numerical evidence that the analysis performed in [65] is applicable to problems where $s = 3/2$, therefore concluding that for these problems the statement (4.1) is still true. Lastly, achieving the convergence rate for all smooth problems will

show the correct implementation of η.

Showing that η is both reliable and efficient for the error in the DG norm ensures that the both η and the SIPG norm error converge at very similar rates. If the error estimate is only reliable then it could be possible that the SIPG norm converges at a rate much faster than η, with η therefore providing a poor measure of how the error in the SIPG norm is converging. The result is, although η bounds the SIPG error from above, η may not be a good representation of the distribution of the error in the SIPG norm. Since η is used to drive the *hp*-adaptivity method elements could be incorrectly chosen for h and p refinement resulting in a less effective *hp*-adaptive method.

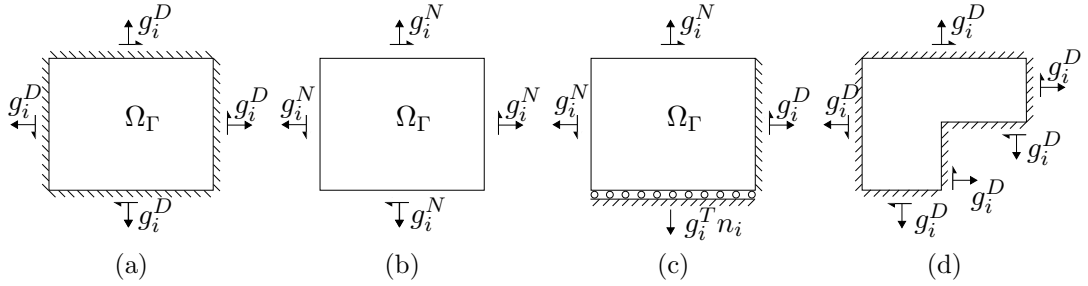

Figure 4.3: Three square domains for verifying the evaluation of η for: (a) the homogeneous and heterogeneous Dirichlet BC, (b) heterogeneous Neumann and all average BCs, and (c) the roller BC. Last, (d) is used to further verify the convergence of η for a problem containing a singularity.

4.4.1 Smooth numerical verification - Dirichlet boundary test

A square of dimensions $(x, y) \in \Omega_\Gamma = (0, 1)^2$, Figure 4.3a, with units of metres (m), has a Dirichlet boundary on all exterior edges such that $\partial\Omega_D = \partial\Omega_\Gamma$. The manufactured displacement solution for this problem is,

$$u_i = \begin{Bmatrix} \sin(\frac{15}{2}\pi x)\sin(\frac{15}{2}\pi y) \\ \sin(\frac{15}{2}\pi x)\sin(\frac{15}{2}\pi y) \end{Bmatrix}. \tag{4.35}$$

A body force f_i is also applied to the interior of the domain. The function that describes the body force is found by directly considering the strong form statement of equilibrium (2.1) and the manufactured displacement solution (4.35). By inspecting the *a priori* statement of convergence for the SIPG norm error (2.56) for a problem with a regular solution, η is expected to have a convergence rate of p_K for a mesh of uniform polynomial order p_K. The initial mesh consists of 4 elements and is shown as an inset figure in Figure 4.4. The error estimate is calculated for each mesh and plotted against $\text{NDOF}^{1/2}$ in Figure 4.4 producing a convergence plot, the value of η for each mesh are shown in Table 4.2. Examining Figure 4.4 and Table 4.3, which provides the convergence rate for each mesh, shows that for meshes of homogeneous polynomial order undergoing uniform h-refinement the error estimate has been implemented correctly for a problem which considers only Dirichlet BCs.

4.4.2 Smooth numerical verification - Average and Neumann boundary test

The next problem considers a square domain where only heterogeneous Neumann BCs are applied to the exterior edge such that $\partial\Omega_\Gamma = \partial\Omega_D$. A body force is applied to the interior,

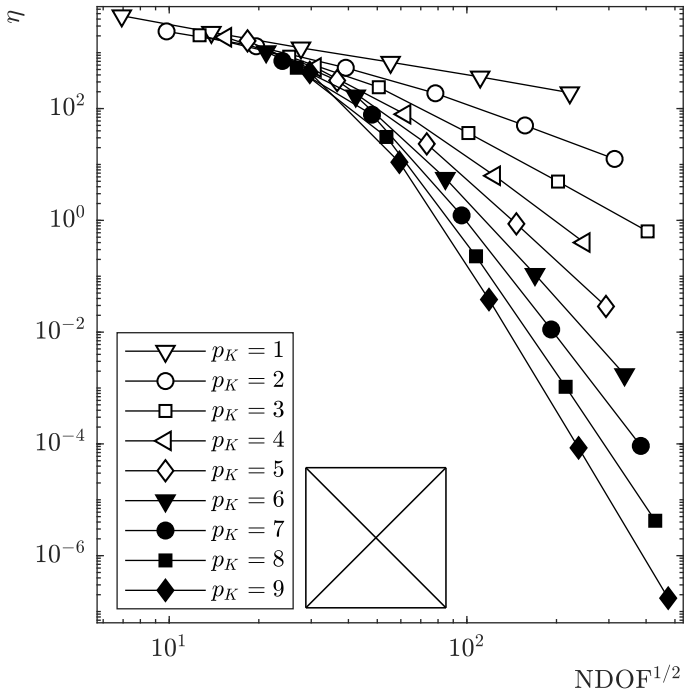

Figure 4.4: A square domain with heterogeneous Dirichlet BCs, for the problem description see Figure 4.3a: A plot of η against NDOF$^{1/2}$, for different uniform mesh polynomial orders, with uniform refinement in h. The initial mesh is included as an inset figure.

	η					
h (m)	4	5	6	7	8	9
0.5	1.88×10^3	1.63×10^3	1.04×10^3	7.11×10^2	5.38×10^2	4.44×10^2
0.25	5.44×10^2	3.18×10^2	1.69×10^2	7.79×10^1	3.11×10^1	1.10×10^1
0.125	7.92×10^1	2.34×10^1	5.67×10^0	1.23×10^0	2.27×10^{-1}	3.83×10^{-2}
0.0625	6.28×10^0	8.66×10^{-1}	1.08×10^{-1}	1.11×10^{-2}	1.05×10^{-3}	8.49×10^{-5}
0.0625	4.01×10^{-1}	2.88×10^{-2}	1.74×10^{-3}	9.20×10^{-5}	4.21×10^{-6}	1.74×10^{-7}

Table 4.2: A square domain with heterogeneous Dirichlet BCs, for problem see Figure 4.3a: A table of η for polynomial orders 4 to 9 corresponding to the plot, Figure 4.4.

p_K	1	2	3	4	5	6	7	8	9
Convergence rate	0.938	1.990	2.961	3.969	4.909	5.958	6.920	7.962	8.93

Table 4.3: A square domain with heterogeneous Dirichlet BCs, for problem see Figure 4.3a: A table of the convergence rate of η for a meshes of polynomial order 1 to 9, corresponding to the plot in Figure 4.4.

and since no Dirichlet BCs are present, the average BCs, (2.52), (2.53) and (2.54), also applied. This problem tests whether the implementation of η is correct for problems containing only heterogeneous Neumann BCs, and also verifies that optimal convergence of the error estimate is achievable when the average BCs are applied. The square domain has dimensions $(x, y) \in \Omega_\Gamma =$

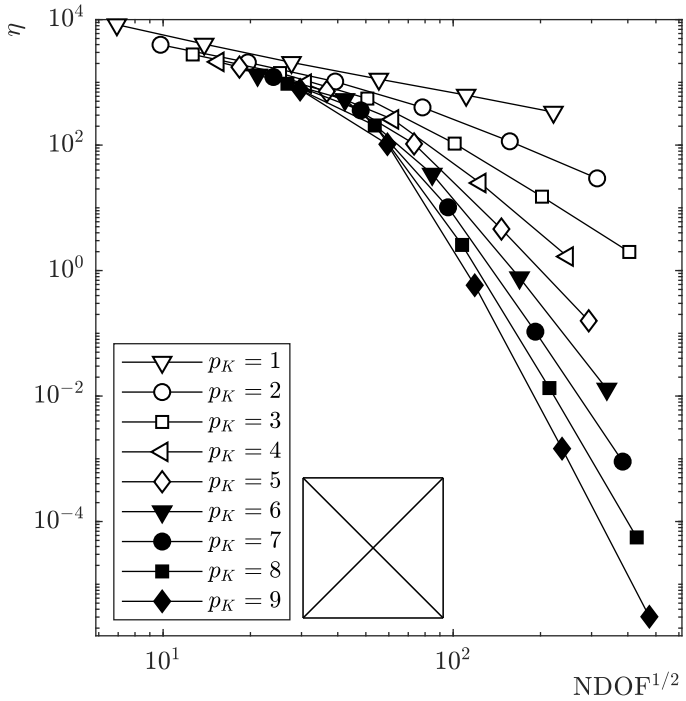

Figure 4.5: A square domain with heterogeneous Neumann and average BCs, for the problem description see Figure 4.3b: A plot of η against NDOF$^{1/2}$, for different uniform mesh polynomial orders, with uniform refinement in h. The initial mesh is included as an inset figure.

$(0,1)^2$ and the manufactured displacement solution applied is

$$u_i = \begin{Bmatrix} \sin(10\pi x)\sin(10\pi y) \\ \sin(10\pi x)\sin(10\pi y) \end{Bmatrix}. \tag{4.36}$$

The function applied g_i^D applied on the Neumann BC is determined directly by considering (4.36) and the description of σ_{ij} in terms of u_i (2.3). The displacement solution is smooth, for a mesh of homogeneous polynomial order, $p_k = p \forall K \in \mathfrak{T}$, η is expected to converge at a rate of p with uniform refinement. A plot of η for each mesh of order p uniformly refined in h is also provided in Figure 4.5, the initial mesh for this verification is inset in Figure 4.5. The corresponding values of η for polynomial orders 4 to 9 are provided by Table 4.4 with the convergence rates for polynomial order 1 to 9 provided in Table 4.5. Table 4.5 demonstrates that optimal convergence of η is achieved when considering a problem that contains average BCs, thus for a problem with no Dirichlet BCs applied in the traditional sense η is reliable and efficient for the error in the SIPG norm. Secondly, the convergence results of Figure 4.5 and Table 4.5 show that η has been implemented correctly for problems which consider only heterogeneous Neumann boundary conditions on the boundary.

4.4.3 Smooth numerical verification - All boundary condition test

This is the last verification problem that has a regular manufactured displacement solution on a square domain with dimensions $(x, y) \in \Omega_\Gamma = (0,1)^2$. The manufactured displacement solution

	η					
h (m)	4	5	6	7	8	9
0.5	2.12×10^3	1.74×10^3	1.31×10^3	1.21×10^3	9.50×10^2	7.63×10^2
0.25	9.51×10^2	7.17×10^2	5.33×10^2	3.57×10^2	2.05×10^2	1.03×10^2
0.125	2.56×10^2	1.04×10^2	3.44×10^1	1.01×10^1	2.56×10^0	5.82×10^{-1}
0.0625	2.48×10^1	4.59×10^0	7.70×10^{-1}	1.06×10^{-1}	1.34×10^{-2}	1.45×10^{-3}
0.0313	1.67×10^0	1.58×10^{-1}	1.29×10^{-2}	9.02×10^{-4}	5.57×10^{-5}	3.03×10^{-6}

Table 4.4: A square domain with heterogeneous Neumann BCs, for problem see Figure 4.3b: A table of η for polynomial orders 4 to 9 corresponding to the plot, Figure 4.5.

p_K	1	2	3	4	5	6	7	8	9
Convergence rate	0.900	1.962	2.928	3.894	4.859	5.895	6.879	7.909	8.900

Table 4.5: A square domain with heterogeneous Neumann BCs, for problem see Figure 4.3b: A table of the convergence rate of η for a meshes of polynomial order 1 to 9, corresponding to the plot in Figure 4.5.

is

$$u = \begin{Bmatrix} y^2 \cos(10\pi y) \exp(x^5 y^5) \\ y^2 \cos(10\pi y) \exp(x^5 y^5) \end{Bmatrix}, \tag{4.37}$$

with the appropriate heterogeneous Neumann, Dirichlet, and roller BCs applied on the boundary as in Figure 4.3d. This problem is designed to verify:

- The correct implementation of the error estimator evaluation of the roller BCs;
- and the the correct implementation of η considering multiple BCs.
- Lastly that η does converge at the correct rate with respect to the *a priori* SIPG norm error (4.7) and showing that η is reliable and efficient for the SIPG norm error when considering all boundary conditions.

Similar to the previous two verifications 9 meshes of homogeneous polynomial order, in the range $p_K = p \ \forall K \in \mathcal{T}$ where $p = [1, 9]$, are considered. Each mesh is uniformly refined in h with η, and the NDOF$^{1/2}$, recorded for each mesh. The values of η for a series of uniformly refined meshes of the same homogeneous polynomial order are plotted as a line in Figure 4.6. For polynomial orders 4 to 9 the values of η for all mesh refinements are shown in Table 4.6, with the corresponding convergence rate of η against NDOF$^{1/2}$ for meshes of polynomial orders 1 to 9 displayed in Table 4.7. Table 4.7 shows, supported by the data presented in Table 4.6 and Figure 4.6, that the implementation of η when considering a problem with a range of different types of BC applied to the edge of the domain is correct. The results also support the argument further that the error estimate is efficient for the SIPG norm error. For each mesh of uniform polynomial order η converges at a rate consistent with the SIPG norm *a priori* error (4.7).

4.4.4 Non-smooth verification

The last problem considers a problem on a L-shaped domain with a non-smooth solution. The mathematical analysis in [65] only considered problems with $s \geq 2$ however, the local crack

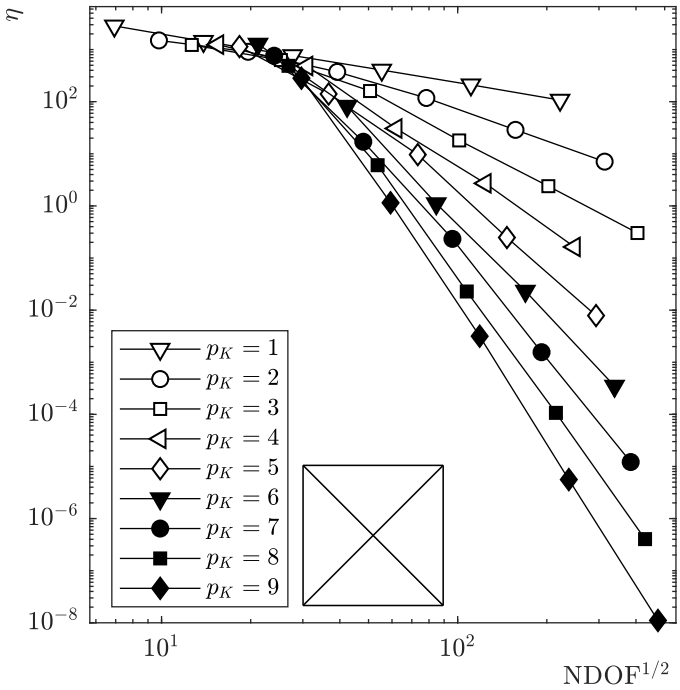

Figure 4.6: A square domain with heterogeneous Neumann, heterogeneous Dirichlet, and homogeneous roller BCs, for the problem description see Figure 4.3c: A plot of η against NDOF$^{1/2}$, for different uniform mesh polynomial orders, with uniform refinement in h. The initial mesh is included as an inset figure.

	η					
h (m)	4	5	6	7	8	9
0.5	1.24×10^3	1.14×10^3	1.28×10^3	7.62×10^2	4.88×10^2	2.83×10^2
0.25	4.85×10^2	1.41×10^2	8.22×10^1	1.70×10^1	6.04×10^0	1.15×10^0
0.125	3.06×10^1	9.64×10^0	1.11×10^0	2.33×10^1	2.2×10^{-2}	3.16×10^{-3}
0.0625	2.71×10^0	2.47×10^{-1}	2.32×10^{-2}	1.55×10^{-3}	1.06×10^{-4}	5.60×10^{-6}
0.0313	1.63×10^{-1}	7.86×10^{-3}	3.50×10^{-4}	1.22×10^{-5}	4.03×10^{-7}	1.11×10^{-8}

Table 4.6: A square domain with all edge boundary conditions applied, for problem see Figure 4.3c: A table showing η for polynomial orders 4 to 9 corresponding to the plot, Figure 4.6.

p_K	1	2	3	4	5	6	7	8	9
Convergence rate	0.975	0.203	0.299	4.06	0.498	0.605	0.700	0.805	0.898

Table 4.7: A square domain with all edge boundary conditions applied, for problem see Figure 4.3c: A table of the convergence rates of η for polynomial orders 1 to 9 corresponding to the plot, Figure 4.6.

displacement solution exists in $u_i \in [H^s(\mathcal{T})]^2$ with $s < 3/2$ [33], a lower order of regularity than the mathematical analysis considered.

The numerical verification in this section investigates a problem with a manufactured displacement solution that exists in $u_i \in [H^{3/2}(\mathcal{T})]^2$. The results presented in this section are of

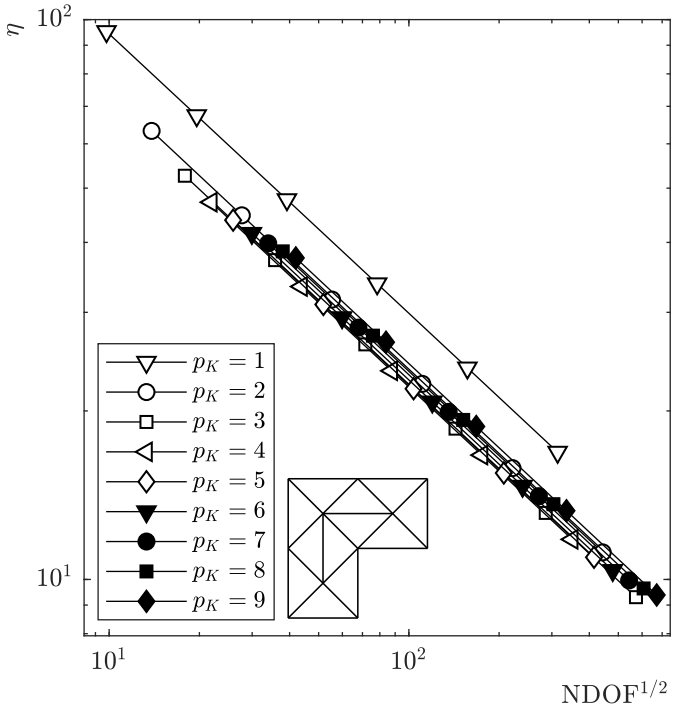

Figure 4.7: A L-shaped domain with heterogeneous and homogeneous Dirichlet BCs applied, for problem see Figure 4.3d: A plot of η against NDOF$^{1/2}$, for different uniform mesh polynomial orders, with uniform refinement in h. The initial mesh is included as an inset Figure.

notable significant as in future chapters η is used to analyse the distribution of errors in the mesh, as well as bound errors in the CF, for problems containing cracks. This numerical verification is therefore used to provide evidence that η is both reliable and efficient for non-regular problems of order $s = 3/2 - \epsilon$, where ϵ is a small number. The manufactured displacement solution for this problem is

$$u_i = \begin{Bmatrix} r^{1/2}(1 - r^2\cos(\theta)^2)(1 - r^2\sin(\theta)^2) \\ r^{1/2}(1 - r^2\cos(\theta)^2)(1 - r^2\sin(\theta)^2) \end{Bmatrix}, \quad \text{where} \quad \theta = \arctan(y/x),\ r = |x_i|, \tag{4.38}$$

with a heterogeneous Dirichlet BC, $g_i^D = u_i$, applied to exterior edge of the domain such that $\partial\Omega_D = \partial\Omega$, see Figure 4.3d, and a body force f_i applied to the interior of the domain. Similar to the verification analysis of the three previous sections, nine meshes of homogeneous polynomial order, in the range $[1, 9]$, are uniformly refined. η and the NDOF$^{1/2}$ recorded for each refinement and plotted in Figure 4.7.

Figure 4.7 shows that for every series of uniformly refined meshes of the same homogeneous polynomial order the rate of convergence is the same. The value of η for every mesh, which has homogeneous polynomial order in the range $[4, 9]$, is shown in Table 4.8 with the corresponding convergence rate, of all meshes, shown in Table 4.9.

Inspecting the SIPG *a priori* error estimate (4.7) shows that the convergence rate, with respect to NDOF$^{1/2}$ for a non-smooth problem with $s = 3/2$ is 0.5 for all polynomial orders.

	η					
h (m)	4	5	6	7	8	9
0.25	4.71×10^1	4.38×10^1	4.15×10^1	3.98×10^1	3.85×10^1	3.75×10^1
0.125	3.33×10^1	3.09×10^1	2.93×10^1	2.81×10^1	2.72×10^1	2.65×10^1
0.0625	2.35×10^1	2.19×10^1	2.07×10^1	1.99×10^1	1.92×10^1	1.87×10^1
0.0313	1.66×10^1	1.54×10^1	1.46×10^1	1.40×10^1	1.36×10^1	1.32×10^1
0.0156	1.17×10^1	1.09×10^1	1.03×10^1	9.95×10^0	9.63×10^0	9.38×10^0

Table 4.8: A L-shaped domain with heterogeneous and homogeneous Dirichlet BCs applied, for problem see Figure 4.3d: A table of η for polynomial orders 4 to 9 corresponding to the plot, Figure 4.7.

This is demonstrated numerically to be true for all polynomial orders, see Table 4.9. This supports the argument that η is reliable and efficient for the SIPG norm error for problems where $s < 2$. Although η is converging at the correct rate, a feature of Figure 4.7 is that the convergence plots for meshes of different polynomial order overlap, however considering Table 4.8 shows that for each mesh size an increase in polynomial results in a decreases of η, albeit relatively small. Inspecting (4.7) shows that when $s = 3/2$ the statement of the SIPG *a priori* error is no longer a function of the polynomial order of the mesh and so there is no expectation for the SIPG norm error to decrease, and hence since η is reliable and efficient for the SIPG norm error there is no reason for η too.

p_K	1	2	3	4	5	6	7	8	9
Convergence rate	0.499	0.500	0.499	0.499	0.499	0.499	0.499	0.499	0.499

Table 4.9: A L-shaped domain with heterogeneous and homogeneous Dirichlet BCs applied, for problem see Figure 4.3d: A table of the convergence rates of η for polynomial orders 1 to 9 corresponding to the plot, Figure 4.7.

4.4.5 *hp*-adaptivity

Previously in this Chapter η was shown to be implemented correctly for problems considering conforming meshes with a homogeneous polynomial order for a range of problems. In this section two problems are *hp*-adaptivity refined using Algorithm 4.1. The first problem is a unit square domain with a smooth solution, the second problem is an L-shaped domain with a non-smooth solution. For both problems η and the error in the SIPG norm are calculated after each *hp*-adaptivity step. The convergence of both error measures are compared the NDOF to demonstrate how this, relatively simple, *hp*-adaptive method is capable of achieving exponential convergence for smooth and non-smooth problems. The error measures are also compared against each for each adaptivity step to support the argument that η is reliable and efficient for the error in the SIPG norm, specifically to show that c_η has no dependency on the polynomial order of elements in the mesh. The convergence plots will also show that the implementation of the *hp*-SIPG method with hanging nodes and jumps in polynomial order is implemented correctly, as well as the calculation of the error in the SIPG norm and η.

The *hp*-adaptive strategy described in Section 4.3.2 has two governing constants δ_2 and

δ_1 which determine whether an element is chosen for either: h-refinement, p-refinement, or no refinement. Three adaptive strategies are considered to investigate the efficacy of the hp-adaptive strategy discussed in this thesis for smooth and non-smooth problem. The three refinement strategies are:

- p-adaptivity with $\delta_1 = 0.07$ and $\delta_2 = 1$.
- h-adaptivity with $\delta_1 = 0.07$ and $\delta_2 = 0.07$.
- hp-adaptivity with $\delta_1 = 0.07$ and $\delta_2 = 0.7$, the same values considered in [118].

The ethos behind an hp-adaptive strategy is to achieve the greatest reduction in error per unit cost in NDOF added. In [118] a study of the different hp-adaptive strategies was performed where it was noted for CG methods, and demonstrated in [115] for SIPG methods, for a two dimensional problem a hp-adaptive strategy should achieve exponential convergence of η with respect to $\text{NDOF}^{1/2}$ and $\text{NDOF}^{1/3}$ for a smooth problem and non-smooth problem respectively.

4.4.6 Smooth problem - hp-adaptivity

The first problem considered for hp-adaptivity has a smooth solution in the unit square domain $(x, y) \in \Omega_\Gamma = (0, 1)^2$. Only Dirichlet BCs are applied to the edge of the domain, see Figure 4.3a, such that $\partial\Omega_D = \partial\Omega_\Gamma$. The manufacture displacement solution for this problem is

$$u_i = \left\{ \begin{array}{c} \sin(15\pi x/2)\sin(15\pi y/2) \\ \sin(15\pi x/2)\sin(15\pi y/2) \end{array} \right\}, \tag{4.39}$$

where on the boundary the Dirichlet BC is set to $g_i^D = u_i$ and a body force f_i, determined from the strong statement of equilibrium 2.1, is applied to the interior of the domain. The initial mesh, shown in Figure 4.9, is conforming and is constructed from 35 elements where initially $p_K = 3\ \forall K \in \mathcal{T}$, shown inset in Figure 6.20.

The SIPG norm error value and η for the three refinement strategies are shown in Figure 4.8a with a plot of the ratio of the error measures against each refinement step provided by Figure 4.8b for the hp-adaptive algorithm. The final mesh after 20 hp-adaptive steps is shown in Figure 4.9. The hp-refinement strategy described in [118] only considers the Poisson problem, Figure 4.8a shows for linear elasticity this hp-adaptive strategy is still capable of producing of exponential convergence, this is demonstrated by the (roughly) straight lines on the log-linear plot. Figure 4.8a also demonstrates that this hp-adaptive strategy is less effective than the p-adaptive strategy. This is the case for regular problems, since the solution is regular over the entire domain and therefore smooth, adaptive p-refinement would produce the greatest reduction in error per unit cost in NDOF. The hp-adaptive strategy employed here will always perform some h-refinement each step. It is recognised that other, more complex, hp-adaptive methods can achieve exponential convergence automatically marking for p-adaptivity only, these adapt by evaluating whether the solution is locally smooth on an element by examining the decay of an element's basis function coefficients [120, 121]. A thorough investigation is presented by [118]. However, for the remainder of the thesis only non-regular problems are considered.

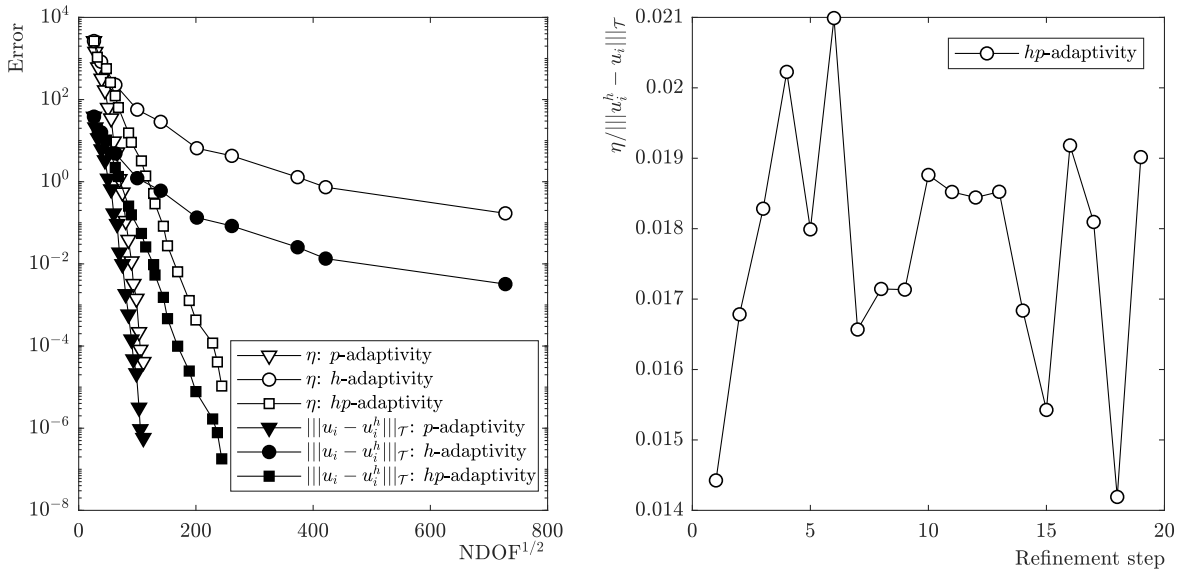

(a) (b)

Figure 4.8: hp-adaptivity of the smooth problem in a square domain: (a) hp-adaptivity of the smooth problem in a square domain: a plot of η and the SIPG norm error against NDOF$^{1/2}$ using a h-, p- and hp-adaptive method. (b) a plot of ratio of the SIPG norm error and η for each hp-adaptive step.

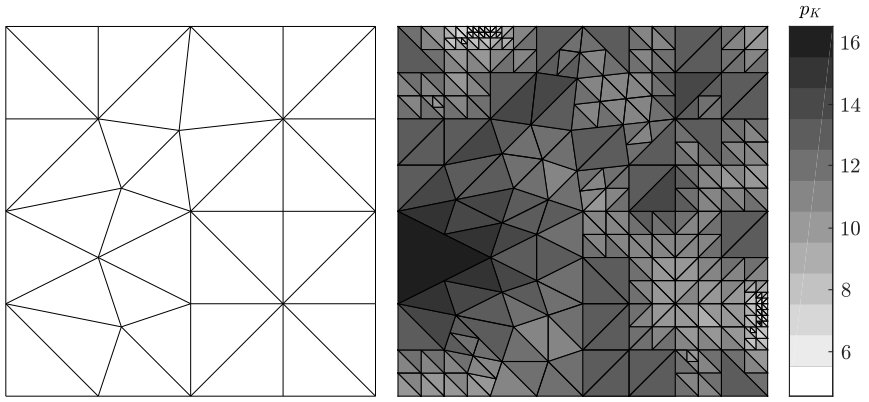

Figure 4.9: hp-adaptivity of the smooth problem in a square domain: Left, the initial mesh with $p_K = 3\ \forall K \in \mathcal{T}$ and on the right is the final mesh after 20 hp-adaptive steps with a colour bar showing the distribution of the polynomial order.

This example shows that even when the adaptive strategy is not optimal, as h-refinements are performed, exponential convergence is achieved with a hp-adaptive strategy.

The plot of the ratio between η and the SIPG norm error is shown in Figure 4.8b for each refinement step. The random nature of the ratio, and therefore lack of a trend, against the number of refinement steps demonstrates that c_η is unaffected by the polynomial order of elements within the mesh. Last, the consistent exponential convergence of both error measures demonstrates that the hp-SIPG method, η and the error in the SIPG norm have all been implemented correctly.

4.4.7 Non-smooth problem - *hp*-adaptivity

The last problem considered is an L-shaped domain with Dirichlet BCs such that $\partial\Omega_D = \partial\Omega_\Gamma$, see Figure 4.3d. The manufactured displacement solution, u_i, has the form (4.38), with the enforced displacement on the Dirichlet BC having the form $g_i^D = u_i$. A body force f_i is also applied to the interior of the domain which corresponds to the displacement solution (4.38). The initial mesh, shown in Figure 4.11, is conforming and is constructed from 84 elements with $p_K = 3\ \forall K \in \mathcal{T}$. For this problem the solution at the convex corner is non-smooth, the error estimate here is therefore likely to be higher here than in the remainder domain. The same δ_2 and δ_1 values are chosen for the *p*-, *h*- and *hp*-adaptive strategies as in Section 4.4.6. In Figure 4.10a the error in the SIPG norm and the error estimate value are plotted against $\text{NDOF}^{1/3}$. $\text{NDOF}^{1/3}$ is chosen as the best known *hp*-strategy for finite element methods achieves an error bound for a singular problem of $|||u_i - u_i^h|||_{H^1(\Omega)} \leq Ce^{-b(\text{NDOF})^{1/3}}$, where C and b are constants, see [122].

For the singular problem the hp-adaptive strategy achieves exponential convergence of the error estimate and the error in the SIPG norm, this is demonstrated by the roughly straight line on the linear-log plot. Additionally, Figure 4.11 shows the *hp*-strategy to refine in h around the singularity and p in regions where the solution is smooth, consistent with [115, 118]. Last the oscillations in the ratio of the error measures, see Figure 4.10b, show the error estimate to be efficient and reliable for singular problems.

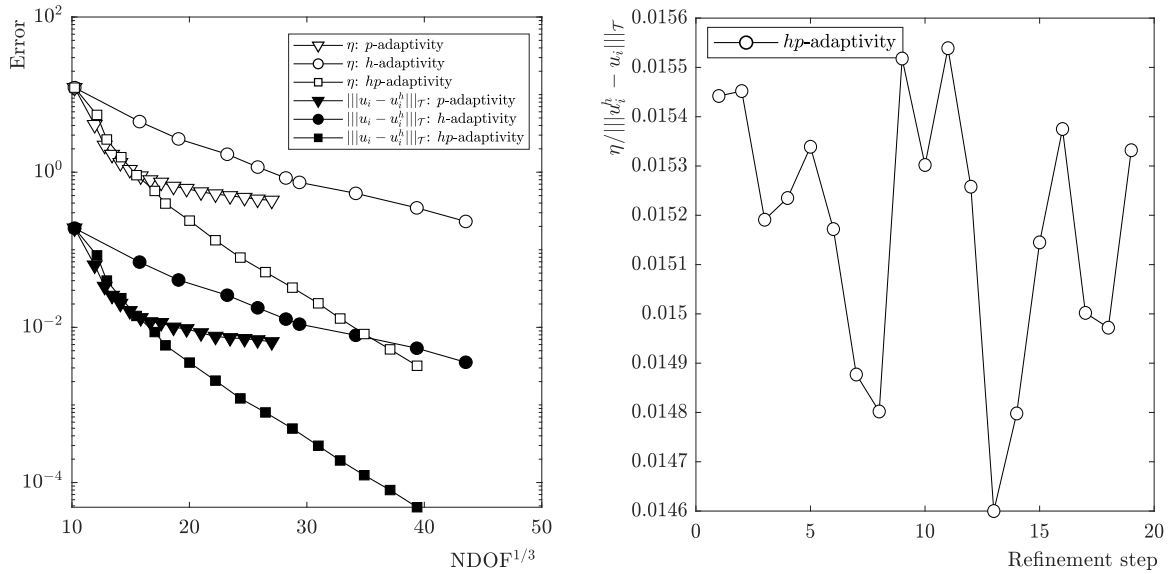

(a) (b)

Figure 4.10: *hp*-adaptivity of the non-smooth problem in a L-shaped domain: (a) a plot of η and the SIPG norm error against $\text{NDOF}^{1/3}$ using a *h*-, *p*- and *hp*-adaptive method. (b) *hp*-adaptivity of the non-smooth problem in a L-shaped domain: a plot of ratio of the SIPG norm error and η for each *hp*-adaptive step.

Figure 4.10a shows the error estimator value for the first five *p*-adaptive steps is less than the corresponding *hp*-adaptive steps. Further, the time taken to achieve the more accurate solutions

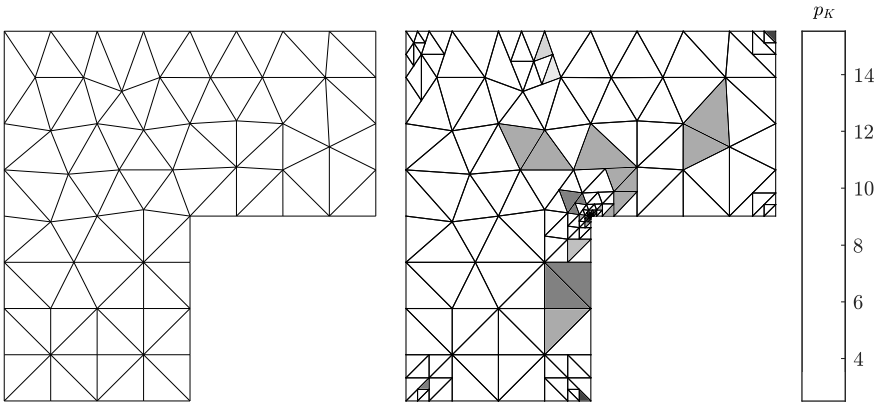

Figure 4.11: *hp*-adaptivity of the smooth problem in a L-shaped domain: Left, the initial mesh with $p_K = 3\ \forall K \in \mathcal{T}$ and on the right is the final mesh after 20 *hp*-adaptive steps with a colour bar showing the distribution of the polynomial order.

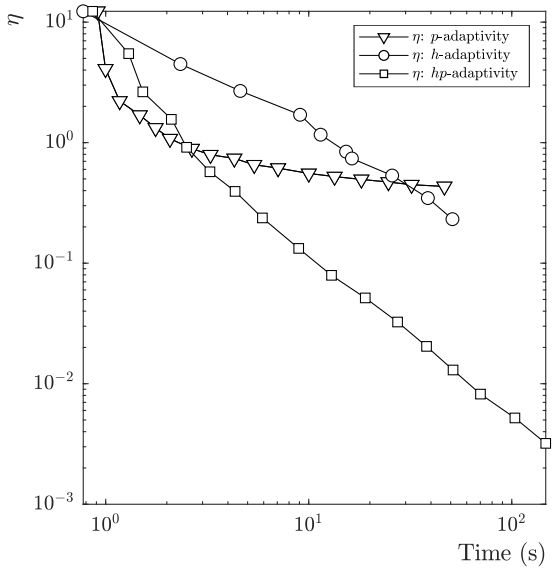

Figure 4.12: *hp*-adaptivity of the smooth problem in a L-shaped domain: A log-log plot of the time taken to run a *h*-, *p*- or *hp*-adaptive step and the associated error estimate value. Run on AMD 4.4Ghz A10-5800k CPU with 16Gb of RAM.

using *p*-adaptivity is less than *hp*-adaptivity, as shown in Figure 4.12. This would give the indication that for this non-smooth problem *p*-adaptivity is a better method for refinement than *hp*-adaptivity. However, Figure 4.10a shows that exponential convergence of η is only maintained using *hp*-adaptivity, conversely the rate at which the *p*-adaptive scheme is converging with respect to $\text{NDOF}^{1/3}$ is slowing. This is also reflected in the time taken for each step in Figure 4.12, the *p*-adaptive strategy is unable to maintain consistent polynomial convergence, whereas *hp*-adaptivity is. The result is that to achieve a highly accurate solution for a problem containing a singularity, *hp*-adaptivity is the better choice, since it maintains consistent exponential convergence in η against $\text{NDOF}^{1/3}$ and consistent polynomial convergence in η against time.

4.5 observations

This chapter was not directly related to modelling fracture problems, but rather it presented a hp-adaptive method driven by an error estimate which is capable of achieving very accurate solutions to problems containing singularities. The techniques presented in this chapter are the ground work to developing a technique which can achieve highly accurate values of the CF for problems containing multiple crack tips, which otherwise would be very computationally expensive when considering only uniform h-refinement. The error estimate was shown numerically to be reliable and efficient for the error in the SIPG norm. Additionally the implementation of the error estimate was demonstrated to be correct for all weakly applied boundary conditions, and the convergence rate of the error estimate, with uniform refinement, was unaffected by the presence of average BCs. The error estimate is useful as it firstly directs the hp-adaptive method presented here, achieving exponential convergence of the SIPG norm error but further, it is shown in the next chapter, via the SIPG norm error, that the error estimate bounds the CF calculation and thus can be used to determine the overall improvement of the CF accuracy with refinement.

Chapter 5

Error estimation of the configuration force

5.1 Introduction

In Chapter 3 the notation of a configurational force (CF) acting a crack tip was introduced to describe the direction a crack will propagate, and when a crack will propagate in terms of the Griffith failure criteria. Two main conclusion were drawn from the chapter. Firstly, the literature presented several different methodologies for calculating the CF. Secondly, if performed in a naive way, obtaining an accurate value of the CF for a problem containing a single crack required significant computational effort. Therefore, in Chapter 4 tools for *hp*-adaptively refining a symmetric interior penalty discontinuous Galerkin (SIPG) mesh were introduced, these tools are used here to achieve exponential convergence of the CF value with respect to $\text{NDOF}^{1/3}$. This should allow the generation of accurate CF values for problems containing multiple crack tips. This chapter is based on, with some further additions, on a recently published paper by Bird [96]. It is tasked with:

1. Using the residual *a posteriori* error estimate to determine the overall improvement of the domain component of the CF domain calculation;

2. Introducing a second error measure to asses the error of the crack edge component of the CF;

3. Providing a robust methodology to determine highly accurate values of the CF for problems containing multiple crack tips; and

4. Generate a set of benchmark solutions of the crack tip CF.

The accurate determination of the CF for fracture mechanics problems is essential in order to obtain realistic predictions of fatigue life [106], as well as determining accurate propagation paths. As discussed in Chapter 3, the power released by a crack is given in a continuous domain is

$$\mathscr{D} = V_i^{\partial\Gamma} \lim_{|C|\to 0} \int_C \Sigma_{ij} n_j \mathrm{d}s = V_i^{\partial\Gamma} g_i, \tag{5.1}$$

which is the inner product of two components: The crack tip CF, g_i, and the propagation velocity of the crack $V_i^{\partial\Gamma}$, also referred to as the configurational velocity. As discussed in Chapter 3, the evaluation of g_i in a discretised domain had several interpretations for its calculation:

- A tip calculation $g_i^{h,t}$. An integral over the interior of elements at the crack tip is performed, [1, 4].
- A domain calculation, $g_i^{h,D}$. An integral over the interior of elements which all within a radius r_d about the crack tip, [60].
- A domain calculation, $g_i^{h,\Gamma}$, over the set of elements and the crack edges, within a radius r_d about the crack tip [64, 98];
- And an alternative edge integral technique, presented by Eischen [2], which is not discussed in this thesis but is equivalent to the techniques of [64, 98].

To the best of the author's knowledge, the most accurate method to determine the CF directly at the crack tip based on nodal CF values is by [60]. In that paper, CF calculations with errors in the region of 0.01% were obtained for problems where only the area integral of the CF was required. In the case where only the CF at the crack tip node is considered, errors of $\approx 3\%$ have been achieved [1, 4]. For a homogeneous isotropic material with no loading on the crack faces, and no body force, both components of the CF at the crack tip can be determined from SIFs [16], the first term of which is the same as the J-integral. Accurate values for the SIFs for homogeneous isotropic materials have been found using the extended boundary element method (XBEM) with the J-integral. With this method errors of $\approx 1 \times 10^{-5}\%$ were achieved by [123, 124]. However the XBEM method is an enrichment method where the enrichment function is dependent on the material type, it is not trivial to determine the stress solution in the proximity of the crack tip for general anisotropic or heterogeneous materials. Alternatively, typical errors of the SIFs produced by using the extended finite element method (XFEM), in conjunction with the interaction integral, are in the region of $< 0.5\%$ [24, 125], with errors of $\approx 0.1\%$ achieved by [126]. If the enrichment functions are correctly determined and implemented for a crack tip problem, uniform h-refinement will regain polynomial convergence on the stress and displacement fields of order p and $p+1$ respectively, where p is the element basis function order. See for example the discussions of the effect of enrichment functions at crack tip singularities on convergence rates in the non-exhaustive list: [33, 127–129], with XFEM convergence studies performed by [130]. Accurate solutions of the SIFs have also been achieved by the fractural-like finite element method [131] and the Petrov-Galerkin natural element method [132]. These techniques all require some knowledge of the stress field at the crack tip *a priori*. One of the most popular ways to determine the CF, and the corresponding SIFs, is through the J-integral [22] in conjunction with the interaction integral [23] which requires a known auxiliary stress field which is dependent on the material type. Alternative methods to determine the SIFs include: the equivalent domain integral method [64], determining both components of the CF directly using the near tip stress solution [2, 106], the virtual crack extension method [133], virtual crack closure technique [134], or by considering the nodal CF at the crack tip in the context of a finite

element CF mechanics [4]. Eischen [2] presented a method to evaluate the second component of the CF by splitting the crack face integral into two separate integrals. The first integral considered the crack faces but did not include a region at the crack tip, the region at the crack tip was evaluated by the second integral. Using the near tip stress solution it was shown that the value of the second integral is a function of the length of the crack face integrated over, the mode II SIF and a stress value [2], also referred to as the T-stress [19]. The second component of the CF can be determined by the method presented by [2]. Alternatively the T-stress component could be calculated using the interaction integral as shown by [135]. When the methodology to determine the T-stress provided by [2] is combined with an enrichment of the near tip stress solution, accurate results for the determination of the CF have been achieved with XBEM [136].

The stress field near a crack tip for brittle materials is inherently singular and therefore difficult to compute accurately using finite element methods [137]. Barsoum [61] presented one of the earliest methods used to capture the stress singularity by making the Jacobian matrix, and therefore the corresponding stresses, of an element singular at the crack tip with the quarter point element. In 1999 Belytschko *et al.* [24] presented an enrichment method for fracture mechanics using finite elements which would later come to be known as the XFEM. Similar methods were also presented by [138] and [139]. The XFEM removed the necessity for the element geometry to conform to the crack edges by including jumps in displacements and stresses within elements. XFEM also improved the representation of the stress field at the crack tip by including singular terms derived from the near tip displacement field [137] to determine stress intensity values. The approach has also been applied directly to determine the CF by Fagerström *et al.* [84, 85]. A discontinuous Galerkin XFEM method capable of achieving optimal convergent results has also been produced by Shen *el al.* [86].

The stress solution, and therefore the evaluation of the J-integral and SIFs, of a problem modelled using finite elements can be improved by using a h-adaptive, p-adaptive or hp-adaptive methods. *A posteriori* error estimates can be used in conjunction with adaptivity techniques to estimate the global errors, or errors of specific features, of a problem. Within the context of fracture mechanics one of the earliest works of using h-adaptivity is presented by [140], here only the global error was improved, the error associated with the J-integral integral at the crack tip was not quantified. More recently, Stein *et al.* [111, 112] made a significant contribution to error driven fracture analysis through the use of a goal-orientated error estimator to provide an estimation of the J-integral accuracy and to flag elements for h-refinement. The adaptivity approach of the analysis was further improved upon by [98]. Using error analysis for fracture problems has also been extended to XFEM by using a global recovery method [141, 142], which quantifies the error between the enriched and non-enriched solution to estimate the error in stress solution about the crack tip. In a similar fashion the Zienkiewicz and Zhu *a posteriori* error estimator [143] has been used to drive h-refinement in fracture problems modelled using the continuous Galerkin finite element method [144, 145]. The most popular technique to improve the accuracy of the stress around the crack for finite elements is to use a goal orientated *a posteriori* error, such as in [146–150] amongst others. A numerical example of using residual based *a posteriori* error estimates to drive h-adaptive algorithms for problems containing cracks

was shown by Cirak *et al.* [151]. However, there were a number of limitations in the analysis: (i) there was no investigation into how the CF improved, (ii) only the first component of the CF was considered, (iii) there was no comparison to an analytical solution, and (iv) only polynomial convergence was achieved. Last, direct evaluation of nodal CF values has also been used to improve the stress solution of crack problems, in *hr*- and *r*-adaptive methods [97].

The papers in this introduction improve the stress solution effectively at the crack tip. However in computing the CF, J-integral or SIFs, knowledge of the stress field is required *a priori*. This chapter has two key contributions:

- Firstly a rigorous *hp a posteriori* error estimator η [65] is combined with a *hp*-adaptive scheme, [118], to achieve very accurate values for both components of the CF for linear elastic homogeneous isotropic problems. The error estimate is shown to bound the error in the CF component acting parallel to the crack edges.

- Secondly the difficulty in modelling stress singularities on the boundaries is discussed. A simple and effective novel method is proposed to evaluate the CF directly on the boundary is developed, which is further improved by using an error measure on the crack edges. No *a priori* knowledge of the stress tip singularity is required. This provides potential for the proposed method to act as a black box with the capability to be applied to a range of materials.

An advantage of the approach considered is that since the error estimate is an *a posteriori* residual based error estimator which is shown to bound from above the error in the CF. Therefore there is no need to solve an adjoint problem for each refinement step, which is expensive and the case for goal-orientated error estimates.

This chapter is split into 6 further sections. Section 5.2 presents a reliable *a posteriori* error estimator for the error in the area integral of the CF calculation. The error estimate for the area integral of the CF makes use of the residual based *a posteriori* error estimate for the SIPG norm presented in Chapter 4, [65]. The error estimate for the CF area integral is validated using the Westergaard problem. The inclined crack problem, originally presented in Chapter 3, was shown to demonstrate domain dependence when only the area integral component of the CF was considered. In this section the argument is continued however, the numerical evidence is significantly more rigorous as the *hp*-adaptive strategy achieves a reduction in the error estimate, and therefore the CF error, of several orders of magnitude. Additionally, the concept of nodal CF values is used to explain why domain independence exists for the crack tip CF calculation when only an area integral is considered. The issue of using a finite element with a polynomial basis to consider line integrals on singularities is explored. The results of which are used to propose a novel method of determining the crack tip CF in Section 5.3. The proposed method contains the area and crack face integral components of the CF calculation, hence a second error estimate for the line integral along the crack faces is introduced. The error estimate for the line integral component of the CF is then validated using the Westergaard problem. In Section 5.5 the complete error estimator for the proposed CF calculation is summarised. This is followed by a numerical examples in Section 5.6 with observations drawn in Section 5.7.

5.2 Reliable error estimation for the configurational force area integral

One of the conclusions drawn from Chapter 3 was that none of the methods in the literature which directly evaluated the CF at the crack tip could consistently produce either an accurate, or domain independent, CF value at the crack tip. For readability the equation for the tip and domain methods to calculate the CF, from [1, 4] and [60] respectively, are reintroduced as

$$\begin{aligned}\mathscr{D} &= -\{\partial V\}^\top \sum_{n\in n_b}\sum_{K\in A}\int_K [B^V]^\top\{\Sigma^h\}\mathrm{d}v \\ &= \{\partial V\}^\top\{g^{h,t}\} \quad \text{for the tip formulation and,} \\ &= \{\partial V\}^\top\{g^{h,D}\} \quad \text{for the domain formulation}\end{aligned} \tag{5.2}$$

and the domain method with the crack edge integral, [64, 98], is

$$\begin{aligned}\mathscr{D} &= -\{\partial V\}^\top\left(\sum_{K\in A}\int_K\{q\}^\top[B^V]^\top\{\Sigma^h\}\ \mathrm{d}v + \sum_{F\in(\Gamma^+\cup\Gamma^-)}\int_F\{q\}^\top[N]^T[n^\Sigma]\{\hat{\psi}\}\mathrm{d}s\right) \\ \mathscr{D} &= \{\partial V\}^\top\{g^{h,\Gamma}\}.\end{aligned} \tag{5.3}$$

$\{\Sigma^h\}$ is vector of the Eshelby stress, $\{\hat{\psi}\}$ is vector of the free energy function, $[N]$ is a matrix of shape functions, $[B^V]$ is a matrix of shape function derivatives, $[n^\Sigma]$ is matrix of normal components on an element edge F, Γ^+ and Γ^- are the crack edges. In (5.3) the coordinate system is to local the crack face such that a tensor index of 1 and 2 refers respectively to the component of a variable acting parallel and perpendicular to the crack face. Addition, $[n^\Sigma]$ and $[B^V]$ are also defined by the local coordinate system. For $\{g^{h,D}\}$, and $\{g^{h,\Gamma}\}$, A is an area about the crack tip defined by the radius r_d. For $\{g^{h,t}\}$ A refers to the set of elements that have a node at the crack tip node. Last, n_b is the set of nodes within A and n is a node of the element K. The variables that exist in $\{g^{h,t}\}$, $\{g^{h,D}\}$ and $\{g^{h,\Gamma}\}$ are given in their full form in Chapter 3. Lastly, it is important to highlight that, as the crack tip CF can be calculated by three methods, a different symbol is given for the CF corresponding to each method:

- $\{g^{h,t}\}$: the *tip* formation (5.2).
- $\{g^{h,D}\}$: the *domain* formation (5.2).
- $\{g^{h,\Gamma}\}$: the *domain and crack edge* formation (5.3).

In this section a proof showing that the residual based *a posteriori* error estimate η (4.8) can be used to construct an error estimate that is reliable for the error in the area integral of $\{g^{h,D}\}$ and $\{g^{h,\Gamma}\}$ is provided. In Chapter 3 the $\{g^{h,D}\}$ was shown to achieve accurate results, albeit with significant computation effort, of the Westergaard mixed mode problem [13]. Here highly accurate results are achieved for the Westergaard problem with the *hp*-adaptive method discussed in Chapter 4. Additionally, the Westergaard mixed mode stress solution is used to show numerically that the error estimate of the CF is reliable for the true CF error. The inclined

crack problem is then used as a platform to discuss why domain dependence exists for $\{g^{h,D}\}$ for the general problem, a proof is also provided. The section concludes with a discussion, and proof, as to why $\{g^{h,\Gamma}\}$ produces inaccurate results for a FE mesh where the basis functions of elements at the crack tip are polynomials.

5.2.1 Reliability of error estimator for the configurational force

In Chapter, 3 η was shown numerically to be reliable and efficient for the error in the SIPG norm. Using this reliability result, η is used to produce an error estimate that is reliable for the area integral in $\{g^{h,D}\}$ and $\{g^{h,\Gamma}\}$. Firstly the L^2 norm error for a variable, $*$, existing in elements $K \in \mathcal{T}$ is defined as,

$$\|\cdot\|_{0,\mathcal{T}} = \left(\sum_{K\in\mathcal{T}} \|\cdot\|^2_{0,K(\mathcal{T})}\right)^{1/2} = \left(\sum_{K\in\mathcal{T}} \int_K |\cdot|^2 \mathrm{d}v\right)^{1/2},$$

and from the definition of infinitesimal strain (2.2)

$$\begin{aligned} \|\varepsilon_{ij}\|_{0,\mathcal{T}} &= \|(\nabla_j u_i + \nabla_i u_j)/2\|_{0,\mathcal{T}} \\ &\leq (\|\nabla_j u_i\|_{0,\mathcal{T}} + \|\nabla_i u_j\|_{0,\mathcal{T}})/2 = \|\nabla_j u_i\|_{0,\mathcal{T}}. \end{aligned} \tag{5.4}$$

For the material stiffness matrix there exist the constant $D_{\max} = \max_{i,j,k,l\in[1,2]}(|D_{ijkl}|)$, such that

$$\begin{aligned} \|\boldsymbol{\sigma}\|_{0,\mathcal{T}} &= \|D_{ijlm}\varepsilon_{lm}\|_{0,\mathcal{T}} \\ &\leq D_{\max}\|\varepsilon_{lm}\|_{0,\mathcal{T}} \\ &\leq D_{\max}\|\nabla_m u_l\|_{0,\mathcal{T}}. \end{aligned} \tag{5.5}$$

Using (5.4) and (5.5) it can be shown that Σ_{ij} is bound by $\nabla_j u_i$, that is

$$\begin{aligned} \|\Sigma_{ij}\|_{0,\mathcal{T}} &= \|\hat{\psi}\delta_{ij} - \nabla_i u_l \sigma_{lj}\|_{0,\mathcal{T}} \\ &\leq \|\hat{\psi}\|_{0,\mathcal{T}} + \|\nabla_i u_l \sigma_{lj}\|_{0,\mathcal{T}} = \|\sigma_{ij}\varepsilon_{ij}\|_{0,\mathcal{T}}/2 + \|\nabla_i u_l \sigma_{lj}\|_{0,\mathcal{T}} \\ &\leq \|\sigma_{ij}\ \|_{0,\mathcal{T}}\|\varepsilon_{ij}\|_{0,\mathcal{T}}/2 + \|\nabla_i u_l\|_{0,\mathcal{T}}\|\sigma_{ij}\|_{0,\mathcal{T}} \\ &\leq 3/2\|\sigma_{ij}\|_{0,\mathcal{T}}\|\nabla_i u_l\|_{0,\mathcal{T}} \\ &\leq 3/2 D_{\max}\|\nabla_i u_l\|^2_{0,\mathcal{T}}. \end{aligned}$$

Since $\|\nabla_j u_i - \nabla_j u_i^h\|_{0,\mathcal{T}}$ is a component of $|||u_i - u_i^h|||_{\mathcal{T}}$, and using the reliability result from [65], $|||u_i - u_i^h|||_{\mathcal{T}} \leq C_\eta \eta$, it is possible to write,

$$\|\Sigma_{ij} - \Sigma_{ij}^h\|_{0,\mathcal{T}} \leq 3/2 D_{\max}\|\nabla_j u_i - \nabla_j u_i^h\|^2_{0,\mathcal{T}} \leq C_\Sigma \eta^2, \tag{5.6}$$

where C_Σ is a positive constant independent of the size and polynomial order of the elements in the mesh and the magnitude of the load applied on the boundary; the superscript h denotes the finite element approximated value of a variable.

Using η, the inequality (5.6) provides a measure of the L^2 norm error of Σ_{ij} in the mesh

$\mathcal{T}$. However the CF area integrals in $\{g^{h,D}\}$ and $\{g^{h,\Gamma}\}$ also include the function $\nabla_j q$, which varies continuous from 1 at the crack tip to 0 on the boundary of the domain size A. (5.6) must therefore be extended further to include $\nabla_j q$, giving

$$\|\nabla_j q \Sigma_{ij} - \nabla_j q \Sigma_{ij}^h\|_{0,\mathcal{T}} \leq \|\nabla_j q\|_{0,\mathcal{T}} \|\Sigma_{ij} - \Sigma_{ij}^h\|_{0,\mathcal{T}} \leq C_\Sigma \|\nabla_j q\|_{0,\mathcal{T}} \eta^2, \tag{5.7}$$

where $\|\nabla_j q\|$ is only dependent on the initial mesh in a series of mesh refinements. η^2 is always known and since (5.7) is true, η^2 can be calculated to show the minimum rate of convergence for the area integral in $g_i^{h,D}$ and $g_i^{h,\Gamma}$.

When considering a problem with a single crack the area A of $\{g^{h,D}\}$ and $\{g^{h,\Gamma}\}$ is considered as the whole domain. However when a problem contains multiple crack tips the area A, for the CF calculation at a crack tip, only considers a subset of the mesh which is defined as $\mathcal{T}_c \subset \mathcal{T}$. Therefore when quantifying the error in the CF calculation for a crack tip, the same subdomain $\mathcal{T}_c$ corresponding to the area A is used to calculate the error estimate of the CF (5.7). The error estimator value computed over the subdomain is denoted η_c and gives a sharper bound to (5.7) for a crack tip, where $\eta_c \in \bar{\eta}_c$ with $\bar{\eta}_c$ as the set of the error estimate values considered on all separate element sets about each crack tip.

5.2.2 Validation of the error estimator for the configurational force area integral

The Westergaard mixed mode crack problem is used here to show numerically the efficacy of using a *hp*-adaptive method driven by an error estimate to achieve very high accuracies of the CF using the domain method $\{g^{h,D}\}$. Further the problem is used to demonstrate the lack of convergence in the CF error when only considering the nodal CF value at the crack tip node $\{g^{h,t}\}$. However, the Westergaard problem is not general since the free energy function $\hat{\psi}$, and all components of Eshelby stress Σ_{ij}, are continuous across the crack edges. As such the analytical solution of $\{g^{h,D}\}$ is equal to $\{g^{h,\Gamma}\}$ as the line integral terms of $\{g^{h,\Gamma}\}$ are zero. For a more general problem the issue of domain dependence of $\{g^{h,D}\}$ is discussed and the necessity, and difficulty, of including the line integral terms in $\{g^{h,\Gamma}\}$ is explored.

The geometry of the truncated domain of the Westergaard mixed mode problem and BCs are defined in Figure 5.1b with $L = 1$ m and the crack length $a = 0.5$ m. The stress solution of the infinite plate is applied as a Neumann BC to the edges of the truncated domain as

$$g_i^N = \left\{ \begin{array}{c} \sigma_{11} n_1 + \sigma_{12} n_2 \\ \sigma_{12} n_1 + \sigma_{22} n_2 \end{array} \right\}, \quad \text{where} \quad \partial\mathscr{B}_N = \partial\mathscr{B} \setminus (\Gamma^+ \cup \Gamma^-), \tag{5.8}$$

where σ_{11}, σ_{22} and σ_{12} are the infinite plate stress solutions from [13]. The normal and shear stress at the infinite boundary are $\sigma_\infty = \tau_\infty = 1$ Pa, the plate acts in plane stress with a Young's modulus of $E_Y = 5/2$ Pa, and a Poisson's ratio $\nu = 0.3$. Since no Dirichlet BCs are applied to this problem, the problem is made determinate by applying average BCs to restrain rigid body motion, (6.20) (6.20) and (6.20). The analytical solution of the CF values for the Westergaard problem is determined from the relationship between the CF at the crack tip and the SIFs for

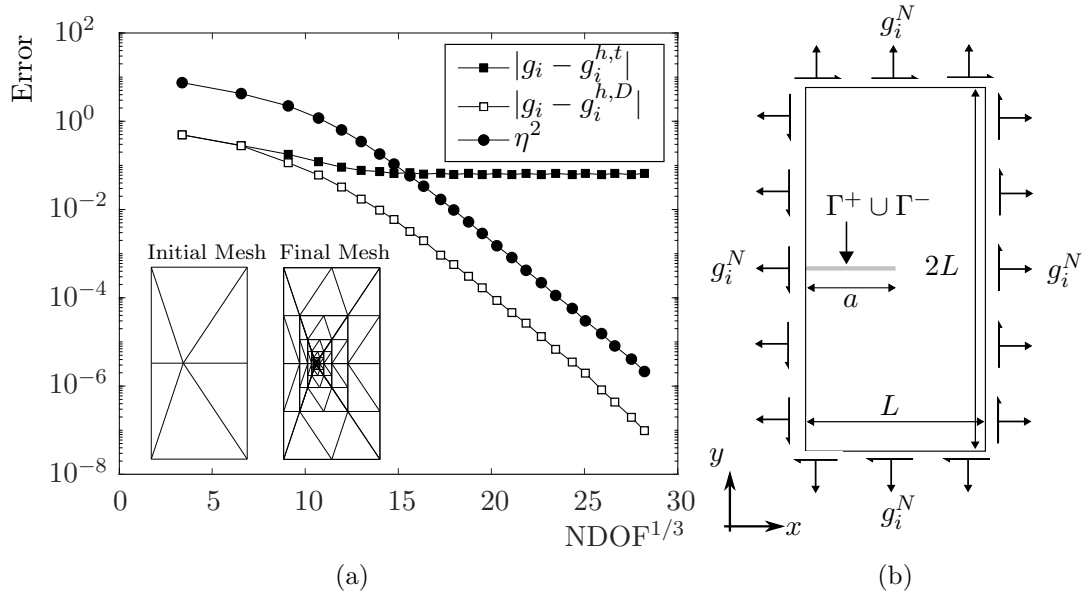

Figure 5.1: Westergaard crack in an infinite plate: (a) CF error for the domain and tip methods (5.2), and the value of error estimate squared against NDOF$^{1/3}$, with the initial mesh before refinement and final mesh after refinement shown by the inset figures. (b) Geometry of the truncated Westergaard problem, with the crack edges shown by the greyed line.

the problem using (3.46), which is repeated here for the sake of readability

$$g_i = \left\{ \begin{array}{c} (K_I^2 + K_{II}^2)/E_Y^* \\ -2(K_I K_{II})/E_Y^* \end{array} \right\} \quad \text{where} \quad E_Y^* = \begin{cases} E_Y * & \text{plane stress} \\ \frac{E_Y *}{1-\nu^2} & \text{plane strain,} \end{cases} \tag{5.9}$$

$K_I = \sigma_\infty \sqrt{\pi a}$ and $K_{II} = \tau_\infty \sqrt{\pi a}$. The initial mesh for the Westergaard problem is shown in Figure 5.1a with $p_K = 3 \ \forall K \in \mathcal{T}$. 25 *hp*-adaptive steps were applied to the mesh with the constants $\delta_2 = 0.3$ and $\delta_1 = 0.07$ for Algorithm 4.1, this produced the final mesh also shown in the inset figures in Figure 5.1a. $\{g\}$ is determined by $\{g^{h,D}\}$ and $\{g^{h,t}\}$, where the domain size of $\{g^{h,D}\}$ is kept constant and is defined by the elements of the initial mesh which share a node at the crack tip, in this case all 6 elements of the mesh.

Figure 5.1a shows that $\{g^{h,D}\}$ converges exponentially with the cubed root of the number of degrees of freedom (NDOF$^{1/3}$) with a *hp*-adaptive scheme driven by an error estimator. After 25 refinement steps an absolute error of 9.716×10^{-8} ($\approx 5.7 \times 10^{-6}$% error) is achieved, at least 4 orders of magnitude greater in accuracy than [60]. $\{g^{h,D}\}$ converges at the same rate as η^2 which is consistent with (5.7).

Although an initial improvement in the calculation of $\{g^{h,t}\}$ is seen in the first $7-8$ adaptivity steps, the solution plateaus to an absolute error of $\approx 10^{-1}$. The initial improvement in error is likely due to the improvement in the stress solution in the entire domain. Only the elements at the crack tip are used to calculate $\{g^{h,t}\}$. Although these elements are refined in p and h the singularity will always reside in the elements at the tip. The approximation of the crack tip singularity in these elements does not improve as a finite element that has an arbitrarily high polynomial basis is unable to describe well a singular function. This error is seen clearly

when calculating $\{g^{h,t}\}$ for the Westergaard problem. $\{g^{h,t}\}$ is domain independent so acts like a normalised stress error of the elements at the crack tip. When calculating $\{g^{h,D}\}$ and performing a *hp*-adaptive refinement the elements which are at the crack tip with each refinement step become exponentially smaller. The result is their contribution to $\{g^{h,D}\}$, and therefore also their associated error, decreases and so continued exponential convergence of $\{g^{h,D}\}$ to the analytical solution of $\{g\}$ is achieved.

5.2.3 Inclined edge crack

An inclined edge crack problem, Figure 5.2a, is presented here to demonstrate the domain dependence of $\{g^{h,D}\}$ (5.2). Specifically the component of $\{g^{h,D}\}$ that acts perpendicular to

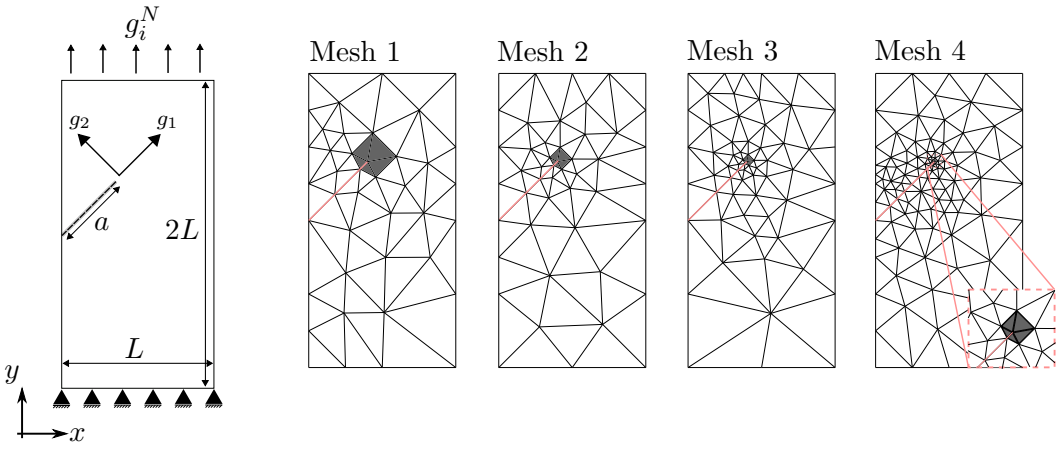

Figure 5.2: Inclined edge crack: (a) geometry of the slanted crack problem with initial meshes 1, 2, 3 and 4 shown in (b).

the crack edges for a straight crack. The plate acts in plane stress with $E_Y = 5/2$ Pa, $\nu = 0.3$, $L = 1$ m, an inclined crack set at 45° to the horizontal with length $a = \sqrt{2}/4$ m, a homogeneous Dirichlet BC is applied on the bottom most edge, a normal traction $g_i^N = [0\ 1]^\top$ Pa on the top edge and a homogeneous Neumann BC on all remaining edges, including the crack edges.

Four initial meshes are consider with $p_K = 3\ \forall K \in \mathcal{T}$, as shown in Figure 5.2b. The domain size for the calculation of $\{g^{h,D}\}$ for each mesh is determined by the elements at the crack tip for each initial mesh, marked by the grey regions in Figure 5.2b. For meshes 1 to 4 the radius of the domain size is approximately 0.0707 m, 0.0354 m, 0.0177 m and 0.0089 m, respectively. Last, 30 *hp*-adaptive steps, from Algorithm 4.1, were applied to the problem with $\delta_2 = 0.3$ and $\delta_1 = 0.07$. The results of the parallel, $g_1^{h,D}$, and perpendicular, $g_2^{h,D}$, components of $\{g^{h,D}\}$ to the crack edges are shown in Figure 5.3a. The parallel components converge to a value invariant of the domain size, whereas the perpendicular components are a function of the domain size.

Similar to the crack tip CF, CFs are also considered to act on element nodes within the mesh.

The nodal CF values for the triangular element K is given by

$$\{G\} = \left\{ \begin{array}{c} G_1 \\ G_2 \end{array} \right\} = \int_K [B^V]^\top \{\Sigma^h\} dv = \left\{ \begin{array}{c} G_1^{v1,K} \\ G_2^{v1,K} \\ G_1^{v2,K} \\ G_2^{v2,K} \\ G_1^{v3,K} \\ G_2^{v3,K} \end{array} \right\}, \tag{5.10}$$

where $G_i = [G_1 \; G_2]^\top$ is a nodal CF value, the superscripts $v1$, $v2$, and $v3$, correspond to the vertex numbers of element K, and the subscripts 1 and 2 correspond respectively to the x and y component of the nodal CF, or if said explicitly the tangential and normal component of G along an edge. The domain dependence is caused by the non-zero nodal CF values on the crack edges which act perpendicular to crack edges, unlike the internal nodal CF values which do tend to zero.

This is expressed clearly in Figure 5.3b. The norm of the nodal CF values acting perpendicular to the crack edge, $|G_2|$ of G_i, for every node along the crack edge (excluding the crack tip node) is plotted against the node's distance away from the crack tip. If the domain calculation $\{g^{h,D}\}$ was domain independent, each nodal value should convergence to zero with *hp*-refinement. For a node, $|G_2|$ is calculated using all elements that contain that node, this includes element either side of the crack edge since the function V_i is continuous across the edges; see Figure 5.4 for the variation of V_i over the crack edges. Figure 5.3b shows that $|G_2|$ has non-zero values at nodes along the crack edge for refinement steps 5, 10 and 15 of mesh 4, increasing the domain size of $\{g^{h,D}\}$ will consider more non-zero nodal CF values along the crack edges, unlike the interior nodes which converge to zero with refinement.

This can be explained in the context of CF mechanics by considering four elements of a mesh $\mathcal{T}_K = \{K_1, K_2, K_3, K_4\} \subset \mathcal{T}$ and their edges $\mathcal{F}_K = \{F_1, F_2, F_3, F_4, F_5, F_6, F_7, F_8\} \subset \mathcal{F}$, as shown in Figure 5.4. The configurational velocity V_i is a test function for the nodal value of G_i on the white filled node in Figure 5.4. V_i varies continuously from 1 on the white filled node to 0 on the black filled node. Two types of edges are present, crack edges marked in grey, $\{F_1, F_2\}$, and internal edges marked in black, $\{F_3, F_4, F_5, F_6, F_7, F_8\}$. The Eshelby stress Σ_{ij} is assumed to vary continuously across the internal edges with jumps in its value only existing between the crack edges, this is assumed to demonstrate that even if Σ is continuous across elements in the mesh, nodal CF values will still exist along the crack edges. Last, since the material is homogeneous $\nabla_j \Sigma_{ij} = 0_i$.

Starting with integration by parts of $\Sigma_{ij}(\nabla_j V_i)$ for an element K

$$\int_K \Sigma_{ij}(\nabla_j V_i) \mathrm{d}v = -\int_K (\nabla_j \Sigma_{ij}) V_i \mathrm{d}v + \int_K \nabla_j (\Sigma_{ij} V_i) \mathrm{d}v, \tag{5.11}$$

and as $\nabla_j \Sigma_{ij} = 0_i$

$$\int_K \Sigma_{ij}(\nabla_j V_i) \mathrm{d}v = \int_K \nabla_j (\Sigma_{ij} V_j) \mathrm{d}v. \tag{5.12}$$

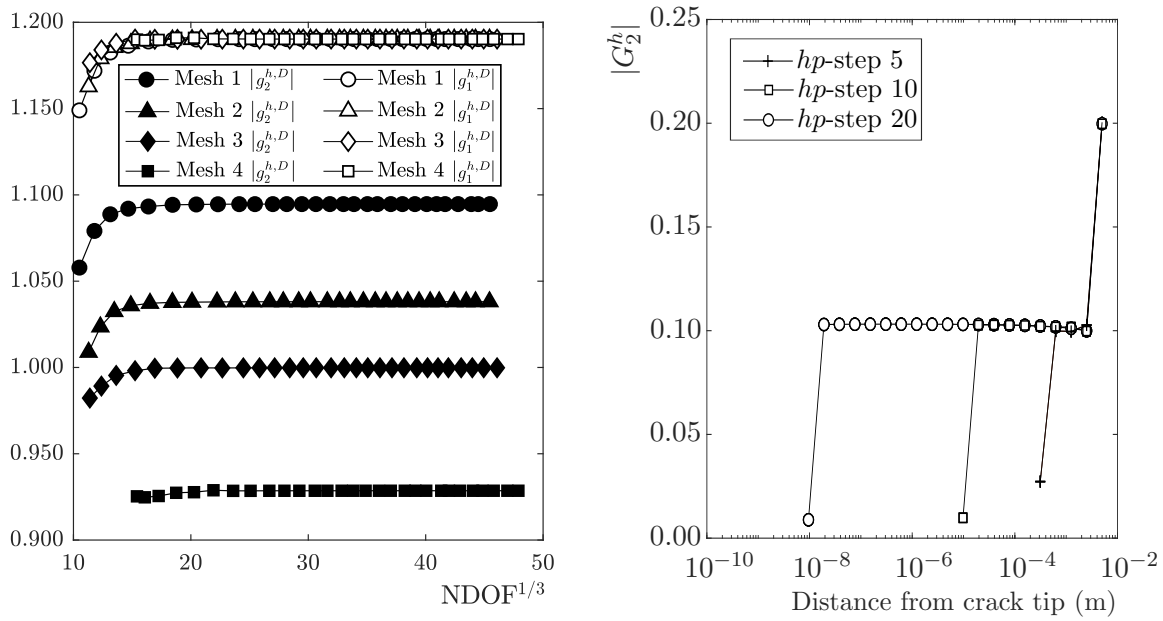

Figure 5.3: Inclined edge crack: (a) $|g_1^{h,D}|$ and $|g_2^{h,D}|$ for the inclined crack problem. (b) The absolute perpendicular value of G_i, $|G_2|$, for each node along the crack edges for mesh 4.

Using the Gauss-Green theorem (5.12) becomes

$$\int_K \Sigma_{ij}(\nabla_j V_i)\mathrm{d}v = \int_{\partial K} n_j(\Sigma_{ij}V_j)\mathrm{d}s, \tag{5.13}$$

and summing together the contribution from all four elements gives

$$\sum_{K\in\mathcal{T}_K}\int_K \Sigma_{ij}(\nabla_j V_i)\mathrm{d}v = \sum_{F\in\mathcal{F}_K}\int_F [\![\Sigma_{ij}V_j]\!]\mathrm{d}s. \tag{5.14}$$

As V_j and Σ_{ij} are continuous across all $F \in \mathcal{F}_K$, but not necessarily across the crack edges, only the line integral along the element edges which coincides with the crack edges is non-zero

$$\sum_{K\in\mathcal{T}_K}\int_K \Sigma_{ij}(\nabla_j V_i)\mathrm{d}v = \int_{F_1\cup F_2} [\![\Sigma_{ij}V_i]\!]\mathrm{d}s. \tag{5.15}$$

V_i and $\nabla_j V_i$ can be written respectively in a vector from for the element K,

$$\{V_i\} = \left\{ \begin{array}{c} V_1 \\ V_2 \end{array} \right\} = [N] \left\{ \begin{array}{c} V_1^{v1,K} \\ V_2^{v1,K} \\ V_1^{v2,K} \\ V_2^{v2,K} \\ V_1^{v3,K} \\ V_2^{v3,K} \end{array} \right\} = [N]\{V^K\}, \tag{5.16}$$

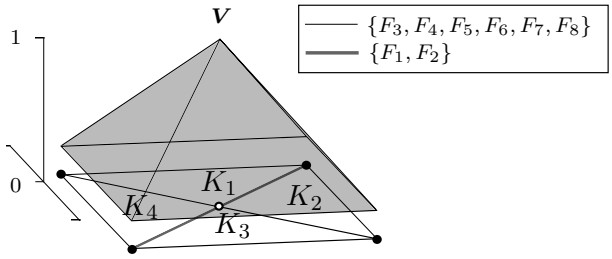

Figure 5.4: A subsection of the mesh $\mathcal{T}_K = \{K_1, K_2, K_3, K_4\} \subset \mathcal{T}$ with the continuous variation of V_i, shown by the grey triangle, from 1 on the white filled node to 0 on the boundary nodes, marked in black.

and

$$\{\nabla_j V_i\} = \begin{Bmatrix} \nabla_1 V_1 \\ \nabla_1 V_2 \\ \nabla_2 V_1 \\ \nabla_2 V_2 \end{Bmatrix} = [B^V]\{V^K\}, \tag{5.17}$$

where $\{V^K\}$ is a vector of nodal constants for V_i over the element K. Given these definitions (5.15) can be rewritten using matrix notation

$$\sum_{K \in \mathcal{T}_K} \int_K \{V^K\}^\top [BV]^\top \{\Sigma_{ij}\} \mathrm{d}v = \int_{F_1} \{V^K\}^\top [N]^\top [n^\Sigma] \{\Sigma_{ij}\} \mathrm{d}s + \int_{F_2} \{V^K\}^\top [N]^\top [n^\Sigma] \{\Sigma_{ij}\} \mathrm{d}s. \tag{5.18}$$

As $\{V^K\}$ is a vector of constants it can be removed from both sides of the equation leaving

$$\{G^{\mathcal{T}_K}\} = \sum_{K \in \mathcal{T}_K} \int_K [BV]^\top \{\Sigma_{ij}\} \mathrm{d}v = \int_{F_1} [N]^\top [n^\Sigma] \{\Sigma_{ij}\} \mathrm{d}s + \int_{F_2} [N]^\top [n^\Sigma] \{\Sigma_{ij}\} \mathrm{d}s, \tag{5.19}$$

where the summation operator sums the elements' DOF together with respect to the *nodal* connectivity. $\{G^{\mathcal{T}_K}\}$ is a vector containing the CF nodal values in x and y for all $K \in \mathcal{T}_K$ which, since Σ_{ij} is not continuous across the crack edges, has non-zero values for all the nodes along the crack edges, agreeing with Figure 5.3b. The result is that the domain integration calculation includes the finite nodal CF at the crack tip, and that by increasing the domain size more non-zero nodal CF values of G_i along the crack edges are included in the calculation of the crack tip $\{g^{h,D}\}$. The CF value at the crack tip will therefore converge to a different value depending on the domain size.

5.2.4 Line integrals near singularities

In order to use the domain independent CF calculation, (5.3), a line integral along the crack edges is required. However as highlighted by [2, 64], amongst others, there are difficulties associated with trying to evaluate the crack edge term in (5.3).

For a crack in an isotropic homogeneous plate it is well known that the displacement field near a crack tip is $u_i \propto r_i^{1/2}$, where r is the distance away from the crack tip, [16]. Investigating the Sobolev space of the displacement field shows that in the interior of the domain $u_i \in [H^{3/2-\epsilon}]^2$

[33], where ϵ is small number. The Sobolev space on the boundary of the domain can be measured using a trace inequality, it is found that the displacement field along a crack edge near the crack tip is in $[H^{1-\epsilon}]^2$ [72]. Therefore since stress is a function of the differential of displacement the stress field on the same boundary is $\sigma_{ij} \in [H^{-\epsilon}]^{3\times 3}$ and therefore not quite in the L^2 norm. The stress field on the boundary next to the crack tip is therefore unable to be modelled by a finite element approximation with a polynomial basis since a polynomial basis can only describe functions which are *at least* in the L^2 norm. Hence integrating along the crack edge to the determine the CF will lead to poor results as the singular part of the stress solution will not be captured by the polynomial basis.

A crack is in the limiting case where the stress field along the crack edges at the crack tip cannot be evaluated using a polynomial basis. However, evaluating stress fields near reentering corners is also difficult, but possible, using a polynomial basis. A diagram of a plate with a reentering corner is shown in Figure 5.5a. If the BCs are smooth the plate has a singular stress field at the point P which behaves like $\sigma_{ij} \propto r_{ij}^{-1/3}$ on the interior of the domain near the crack, meaning $\sigma_{ij} \in [H^{1/6-\epsilon}]^{2\times 2}$ on the domain edges next to the rentrant corner. Therefore the stress field for this problem does exist in the L^2 norm everywhere on the boundary of the domain however, since the stress solution is singular along this edge, it is still difficult to analyse directly, but not impossible.

Consider the problem presented by Figure 5.5a; a L-shaped domain with side length $L = 1$ m. A Neumann BC is applied on the far right edge with $g_i^N = [1 \;\; 1]^\top$ Pa, a homogeneous Dirichlet BC is applied to the bottom most edge and homogeneous Neumann BCs are applied everywhere else. The initial mesh is shown by the inset figure in Figure 5.5b and has $p_K = 3 \; \forall K \in \mathfrak{T}$, the mesh undergoes *hp*-adaptivity with the constants $\delta_2 = 0.3$ and $\delta_1 = 0.07$.

At point P a stress singularity exists with the attached edges having homogeneous Neumann BCs applied. As in [65], the results in Figure 5.5b show that η converges exponentially

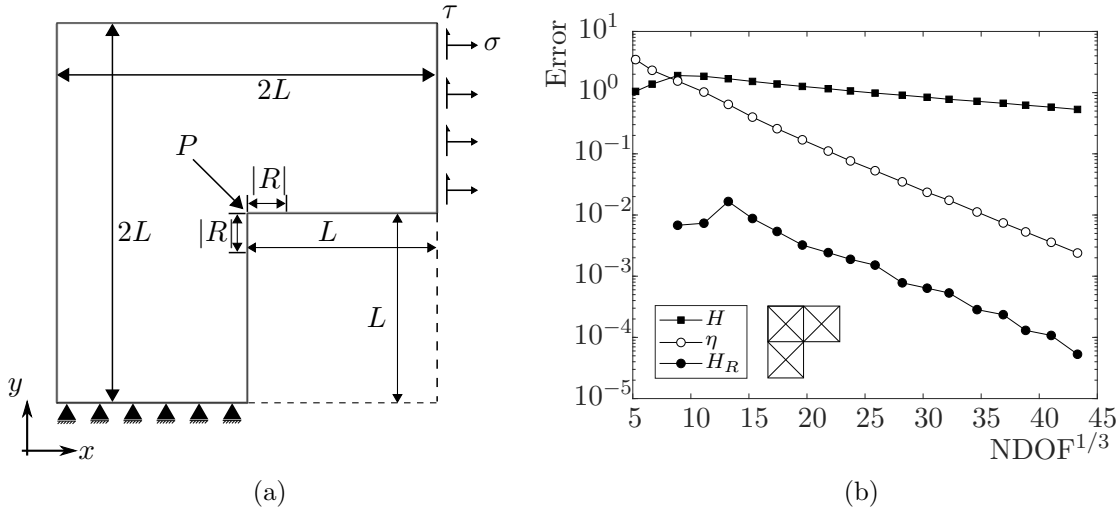

(a) (b)

Figure 5.5: (a) The geometry of the L-shaped. (b) Convergence plots of η, H and H_R with *hp*-adaptive refinement against the NDOF$^{1/3}$ for the L-shaped domain. The initial mesh for the L shaped domain is inset in (b).

with NDOF$^{1/3}$. Figure 5.5b also shows that the error in the L^2 norm of tractions along the

homogeneous Neumann boundary $\partial\Omega_{NO} \subset \partial\Omega_N$

$$H = \sqrt{\int_{\partial\Omega_{N0}} |\sigma_{ij}^h n_j|^2},$$

converges at a rate much slower than η. However if the L^2 norm error calculation is performed along $\partial\mathscr{B}_{NO} \setminus R$, that is excluding the region R of length $|R|$

$$H_R = \sqrt{\int_{\partial\Omega_{N0}\setminus R} |\sigma_{ij}^h n_j|^2},$$

where R is of arbitrary length, but is set as $|R| = 0.05$ and includes the point P, convergence of a rate similar to η is achieved as the singular part of the function is not included in H_R. This idea will be used in the next section to develop a general domain approach to determine the crack tip CF.

5.3 A general domain independent method for the configurational force computation

In Section 5.2.3 the issue of domain dependence was been highlighted for the component of the CF acting perpendicular to the crack faces, $g_2^{h,D}$, for problems where the jump in energy across the crack edges is not zero. In order to compute g_i, whilst not making assumptions of the stress field around the crack tip, a line integral is required along the crack edges. But as shown in Section 5.2.4, the convergence of the error of a stress field along edges is poor when a singularity exists on the edges, therefore a new method to overcome this difficulty is required in which exponential convergence is obtained with *hp*-adaptivity.

The new method considers (5.3) but excludes a region R on the crack edges that contains the crack tip such that $g_i^{h,\Gamma}$ is redefined as

$$\{g_i^{h,\Gamma\setminus R}\} = \underbrace{\sum_{K\in A}\int_K \{q\}^\top [B^V]^\top \{\Sigma_{ij}^h\}\,\mathrm{d}v}_{\text{part1}} + \underbrace{\lim_{R\to 0}\sum_{F\in(\Gamma^+\cup\Gamma^-)\setminus R}\int_F \{q\}^\top [N]^T [n^\Sigma]\{\hat{\psi}\}\mathrm{d}s}_{\text{part2}}. \tag{5.20}$$

where the crack edges, $(\Gamma^+ \cup \Gamma^-)$, consider all of the crack edges up to the node at the crack tip. By excluding an arbitrary region R along a line that contains a singularity, exponential convergence of the error in the stress field along the crack edges should be recovered as this portion of the boundary has a regular stress field. However, for the computation of g_i the region R is by definition 0, and therefore not arbitrary. In order to achieve accurate results the proposed method has to ensure that the stress solution along $\Gamma^+ \cup \Gamma^- \setminus R$ improves and that $|R| \to 0$. The *hp*-adaptive scheme, Algorithm 4.1, improves the stress solution along $\Gamma^+ \cup \Gamma^- \setminus R$. R is reduced such that the number of elements considered with R always increases, h-refinement will normally occur at the crack tip as this is where the highest errors exist. This ensures that in the finite element solution the singularity becomes more localised to the crack tip and the effect of the singularity on the calculation of $\Gamma^+ \cup \Gamma^- \setminus R$ reduces i.e. the regularity of the element in

R which is also adjacent to $\Gamma^+ \cup \Gamma^- \setminus R$ increases and thus the effect of the singularity on the error of the calculation along $\Gamma^+ \cup \Gamma^- \setminus R$ reduces.

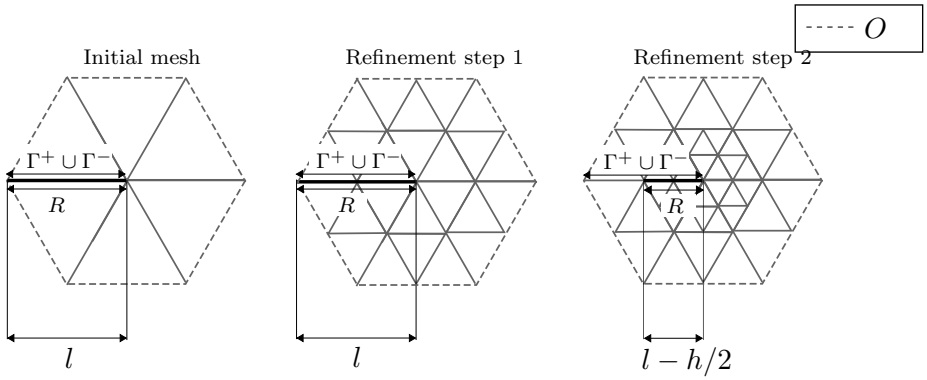

Figure 5.6: The first 2 refinement steps and the corresponding reduction in the excluded length adjacent to the crack tip, R.

Consider Figure 5.6, at refinement step 0 six elements are considered within O, with the region R being the same as region $\Gamma^+ \cup \Gamma^-$. The length of the crack edges excluded by R for the initial mesh is l m. From the initial mesh to refinement step 1 an *hp*-adaptive step has occurred, increasing the number of elements from six to 24. However the region R is not reduced by an element edge length since the number of elements within R will not increase. Only once a second *hp*-refinement step has occurred to produce step 2 does R reduce as the number of element edges considered within R increases from 1 in the initial mesh, to 2 in refinement step 2. This pattern is summarised in Table 5.1. By reducing R in this fashion ensures that the size of R will go to zero. The size of the element edge length at the crack tip is always reducing by half, therefore $|R| \to 0$ is defined by the following series,

$$|R| = l - \sum_{q_{hp}=1}^{\infty} \frac{l}{2q_{hp}} = 0. \tag{5.21}$$

where q_{hp} is a count of every other *hp*-adaptive step (assuming h refinement at the crack). The calculation of $g_i^{h,\Gamma\setminus R}$ can only occur with *hp*-adaptivity, Algorithm 4.1. Therefore, when

Refinement step	Number of edges excluded	Size of R
0	1	l
1	1	l
2	2	$l - l/2$
3	2	$l - l/2$
4	3	$l - l/2 - l/4$
5	3	$l - l/2 - l/4$

Table 5.1: How the number of edges considered inside R and the total corresponding length excluded from (5.20) varies with refinement steps.

referring to the effectiveness of $g_i^{h,\Gamma\setminus R}$, the author is referring to combined effectiveness of the calculation of $g_i^{h,\Gamma\setminus R}$ with Algorithm 4.1.

5.4 Reliable error estimation for the crack face integral of the configurational force

5.4.1 Error in computed crack tip component

In Section 5.2.1 η^2 was shown to bound the error in the area integral component of the CF (5.20). It is also possible to bound the error in the edge integral of the CF and the portion of the CF that is ignored in the integral. A measure of the error for all three components of (5.20) will provided.

An error estimate for the edge integral component of (5.20) can be create by using η, the property of Eshelby stress in a homogeneous material $\nabla_j \Sigma_{ij} = 0_i$, and a trace inequality relating integrals on the interior of an element K to integration a specific face F of an element. The trace inequality is defined as,

$$\|v\|_{0,F} \leq B \frac{h^{1/2}}{|K|^{1/2}} (\|v\|_{0,K} + h\|\nabla_j v\|_{0,K}) \quad \text{for} \quad v \in H^s(K) \quad s \geq 1. \tag{5.22}$$

up to an arbitrary constant B which is independent of v and h. (5.22) is true for any function v, provided that it is sufficiently regular, $s \geq 1$ [72]. This inequality can be applied to the Eshelby stress Σ_{ij},

$$\|\Sigma_{ij}\|_{0,F} \leq B \frac{h^{1/2}}{|K|^{1/2}} (\|\Sigma_{ij}\|_{0,K} + h\|\nabla_j \Sigma_{ij}\|_{0,K}) \quad \Sigma_{ij} \in [H^s(K)]^{2\times 2} \quad s \geq 1 \tag{5.23}$$

and can be subsequently used to determine the error in the Eshelby stress along an element length F.

$$\|\Sigma_{ij} - \Sigma_{ij}^h\|_{0,F} \leq B \frac{h^{1/2}}{|K|^{1/2}} (\|\Sigma_{ij} - \Sigma_{ij}^h\|_{0,K} + h\|\nabla_j \Sigma_{ij} - \nabla_j \Sigma_{ij}^h\|_{0,K}). \tag{5.24}$$

Using the inequality $\|\Sigma_{ij} - \Sigma_{ij}^h\|_{0,K} \lesssim \eta^2$ and $\nabla_j \Sigma_{ij} = 0_i$ allows a computable upper bound to (5.24) to be created for the F,

$$\|\Sigma_{ij} - \Sigma_{ij}^h\|_{0,F} \lesssim \frac{h^{1/2}}{|K|^{1/2}} (\eta_K^2 + h\|\nabla_j \Sigma_{ij}^h\|_{0,K}) \tag{5.25}$$

which can then be expanded further to compute the error the error for all element edges F along the crack faces $(\Gamma^+ \cup \Gamma^-) \setminus R$

$$\sqrt{\sum_{F \in (\Gamma^+ \cup \Gamma^-) \setminus R} \|\Sigma_{ij} - \Sigma_{ij}^h\|_{0,F}^2} \lesssim \sqrt{\sum_{K \in Q} \left(\frac{h^{1/2}}{|K|} (\eta_K^2 + h\|\nabla_j \Sigma_{ij}^h\|_{0,K}) \right)^2}. \tag{5.26}$$

Last with the Cauchy-Schwarz inequality, the norm of the user defined, and therefore known, virtual work function q in (5.20) is included in (5.26) to complete the error estimate for edge

integral component

$$\begin{aligned}\|q(\hat{\psi}-\hat{\psi}^h)\|_{0,Q} &\lesssim \|q\|_{0,Q}\|\hat{\psi}-\hat{\psi}^h\|_{0,Q} \\ &\lesssim \|q\|_{0,Q}\|\Sigma_{ij}-\Sigma^h_{ij}\|_{0,Q} \quad \text{which using the inequality (5.26) becomes} \\ &\lesssim \|q\|_{0,Q}\sqrt{\sum_{K\in Q}\left(\frac{h^{1/2}}{|K|}(\eta_K^2+h\|\nabla_j\Sigma^h_{ij}\|_{0,K})\right)^2} = \eta_\Gamma\end{aligned} \tag{5.27}$$

where $Q = F \in (\Gamma^+ \cup \Gamma^-) \setminus R$, $\|\hat{\psi}\| \lesssim \|\Sigma_{ij}\| \lesssim \|\hat{\psi}\|$, and η_Γ is the error estimate for the error in the line integral component of (5.20).

The RHS of (5.26) has only been shown here to be reliable for the error in the Eshelby stress, and therefore also $\hat{\psi}$, along the faces $F \in (\Gamma^+ \cup \Gamma^-) \setminus R$, it will be shown in the next section, using the Westergaard problem, to be good estimate for how the true error is converging. However, it is important to note that the RHS (5.27) is only an upper bound and so could be a conservative estimate for the true error. (5.27) is also *only* valid for elements that do not have a node at the crack tip, elements at the crack tip have a regularity for $\hat{\psi}$ of $s < 1$ and so the estimate (5.27) becomes invalid.

5.4.2 Error in non-computed crack tip component

All problems considered in thesis are homogeneous, either isotropic or anisotropic with homogeneous Neumann BCs on the crack faces and no body force. The displacement field local to the crack tip, acting along the crack faces, is known for these problems. It is therefore possible to state the convergence in the error for the ignored portion of line integral of (5.20), the line integral over the region R. However for problems with jumps in material properties at the crack tip, heterogeneous Neumann or Dirichlet BCs on the crack faces, or a non-smooth body smooth the local crack tip solution, the local crack tip solution might not be known. Therefore this error measure can only be used in special circumstances however, the method for computing the CF using (5.20) can still be used. But, with no measure of how the error in not including the line integral over the region R is converging. All that can be known is that integral over the R is finite, and thus reducing $|R|$ will also reduce the error.

The displacement near the crack tip acting parallel and on the crack face Γ^+ is u_r^+, can be represented by an infinite series [33],

$$u_r^+ = A^+ r^{1/2} + \sum_{n=1}^{\infty} B_n^+ r^{n+1/2} \tag{5.28}$$

where A^+ and B_n^+ are constants dependent on the loading conditions and shape of the problem domain. A similar expression exists of u_r^- on Γ^-

$$u_r^- = A^- r^{1/2} + \sum_{n=1}^{\infty} B_n^- r^{n+1/2}. \tag{5.29}$$

Differentiating (5.28) with respect to r, the distance away from the crack gives

$$\frac{\partial u_r^+}{\partial r} = \underbrace{C^+ r^{-1/2}}_{\text{singular component}} + \underbrace{\sum_{n=1}^{\infty} D_n^+ r^{(n-1/2)}}_{\text{regular component}}, \tag{5.30}$$

where u_r^+ is the displacement field on Γ^+, $C^+ = -2A^+$ and $D^+ = B_n^+/(n-1/2)$. The energy along crack faces Γ^+ and Γ^- is respectively denoted $\hat{\psi}^+$ and $\hat{\psi}^-$, they are determined by

$$\begin{aligned} \hat{\psi}^+ = D(1,1)\left(\frac{\partial u^+}{\partial r}\right)^2 &= D(1,1)\left(C^+ r^{-1/2} + D_1^+ r^{1/2}\right)^2, \\ &= D(1,1)\left(E^+ r^{-1} + F^+ + G^+ r\right) \end{aligned} \tag{5.31}$$

where $D(1,1)$ is the component of the material stiffness matrix (2.3), and

$$\hat{\psi}^- = D(1,1)\left(E^- r^{-1} + F^- + G^- r\right) \tag{5.32}$$

where E^+, F^+, and G^+ are constants resulting from multiplying out the brackets in (5.31). E^-, F^- and G^- are produce in an equivalent manner when generating $\hat{\psi}^-$. Using (5.31) and (5.32) an expression for the edge integral component not included in (5.20) can be produced,

$$\begin{aligned} \int_0^{|R|} \left(\hat{\psi}^+ - \hat{\psi}^-\right) \, \mathrm{d}r = D_{11}(&E^+ \log(|R|) + F^+ + G^+|R| \\ &-E^- \log(|R|) - F^- - G^-|R|) \end{aligned} \tag{5.33}$$

By inspecting (5.33) several results can be determined. Firstly, for the CF to be finite $E^+ = E^-$, otherwise the CF value becomes infinite. The integral (5.33) can therefore be simplified further to give

$$\int_0^{|R|} \left(\hat{\psi}^+ - \hat{\psi}^-\right) \, \mathrm{d}r = D(1,1)[(F^+ - F^-)|R| + (G^+ - G^-)|R|^2]. \tag{5.34}$$

Secondly when $|R| < 1$ and taken to the limit of 0, the convergence of (5.34) to *zero* is limited by the term $(F^+ - F^-)|R|$, which reduces at the same rate as $|R| \to 0$. This term dictates the rate of convergence, the error in not including the line integral term in (5.20) is therefore given as

$$\eta_{|R|} = |R| \propto D(1,1)(F^+ - F^-)|R| \tag{5.35}$$

where the higher order terms of $|R|$ are ignored since they become smaller faster than $|R| \to 0$, and the constant $(F^+ - F^-)$ is unknown.

5.4.3 Validation of the error estimator for the crack face integral

In Section 5.2.4 it is was shown that the L^2 error in the homogeneous Neumann BC converged at a similar rate to the error estimate if the component along the boundary containing the singularity was ignored. In this section the error estimate for the error of the Eshelby stress on the boundary of a domain, away from a singularity, is validated when Algorithm 4.1 is used to

evaluate the crack face terms in $\{g^{h,\Gamma\setminus R}\}$. This analysis is performed to show that η_Γ is reliable for the error in the crack face terms of $\{g^{h,\Gamma\setminus R}\}$ and that Algorithm 4.1 achieves a reduction in the error of face terms considered in $(\Gamma^+ \cup \Gamma^-) \setminus R$ as $|R| \to 0$.

Although the Eshelby stress solution for the Westergaard problem is continuous across the crack faces the norm of the Eshelby stress is finite and non-zero, excluding the portion of the boundary at the crack tip. The mixed mode Westergaard problem is therefore used to evaluate the reliability of η_Γ for the crack face terms of $\{g^{h,\Gamma\setminus R}\}$. The same material properties, BCs, initial mesh and *hp*-refinement strategy (running for 30 *hp*-refinement steps) as in Section 5.2.2 for the mixed mode Westergaard problem are used.

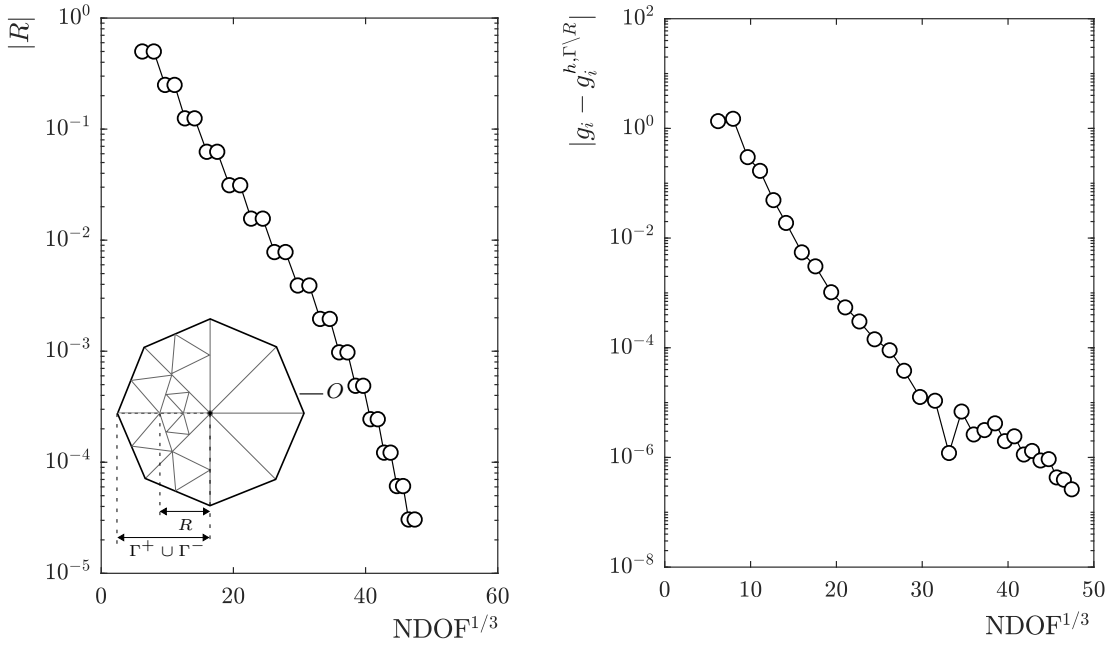

Figure 5.7: Westergaard crack in an infinite plate: (a) excluded length $|R|$ with $\text{NDOF}^{1/3}$ and (b) the error in the CF calculation $|g_i - g_i^{h,\Gamma\setminus R}|$ against $\text{NDOF}^{1/3}$.

Figure 5.7a shows the exponential convergence of $|R| \to 0$ with $\text{NDOF}^{1/3}$, demonstrating that the error in not including the line integral, $\eta_{|R|}$, over the excluded region R will also decrease at the same rate. In Figure 5.7b the error in the value of $\{g^{h,\Gamma\setminus R}\}$ is shown to achieve exponential convergence with respect to $\text{NDOF}^{1/3}$. Further, Figure 5.8a shows that both the L^2 error of the energy solution along $(\Gamma^+ \cup \Gamma^-) \setminus R$, and its associated error estimate η_Γ, achieve exponential convergence when evaluated using Algorithm 4.1. η_Γ and $\|\hat{\psi}_h - \hat{\psi}\|$ also demonstrate a good correspondence in Figure 5.8a, and when plotted in Figure 5.8b as ratio show that η_Γ may be also efficient for $\|\hat{\psi}_h - \hat{\psi}\|$ since the ratio exhibits an oscillatory and random behaviour with *hp*-adaptivity. In conclusion

- η_Γ is validated as an error estimate for $\|\hat{\psi}^h - \hat{\psi}\|_{0,Q}$.
- $|R| \to 0$ exponentially fast with respect to $\text{NDOF}^{1/3}$ with Algorithm 4.1;

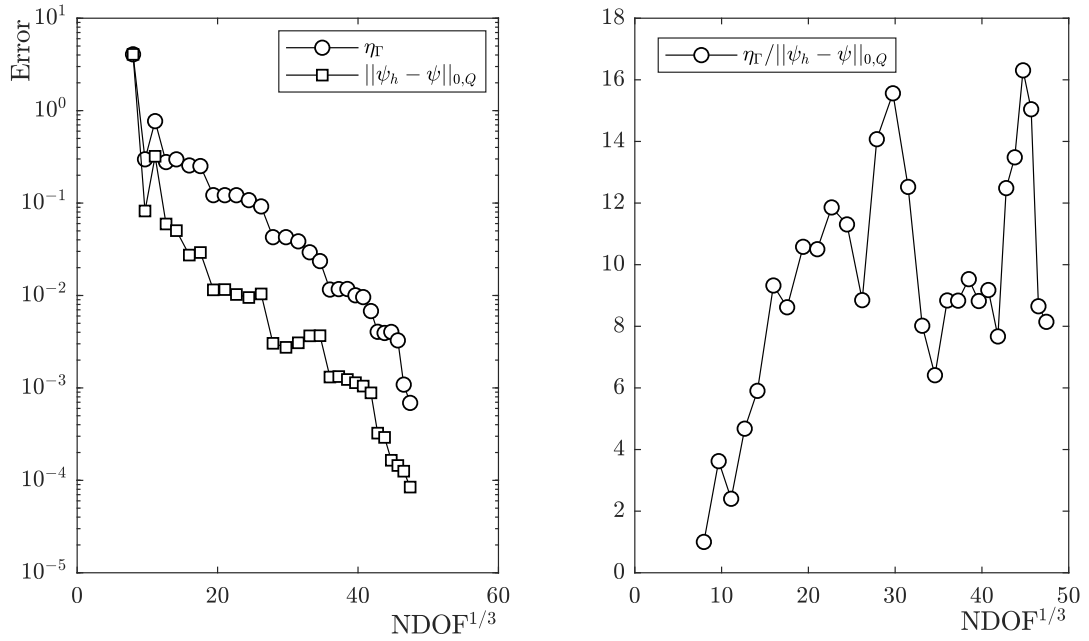

(a) (b)

Figure 5.8: Westergaard crack in an infinite plate: (a) the convergence of the estimated η_Γ and the true error $\|\hat{\psi}_h - \hat{\psi}\|_{0,Q}$, where $Q = (\Gamma^+ \cup \Gamma^-) \setminus R$. (b) the variation of the ratio η_Γ over $\|\hat{\psi}_h - \hat{\psi}\|_{0,Q}$ with *hp*-refinement.

- additionally, $\|\hat{\psi}^h - \hat{\psi}\|_{0,Q} \to 0$ with respect to NDOF$^{1/3}$ with Algorithm 4.1.

In Section 5.6 the robustness of Algorithm 4.1 to achieve exponential convergence of $|R|$ and η_Γ is tested against more complex multi-crack problems where the stress solutions are not known.

5.5 Complete error estimation of the configurational force calculation

In this chapter all components of the (5.20) were shown to be bound by an error estimator. The area integral, part 1 of (5.20), was shown to be bound η^2, (4.8), in Section 5.2.1. The line integral, part 2 of (5.20), was shown to be bound η_Γ, (5.27), in Section 5.2.1. The magnitude of the integral over R which is ignored, was shown to be bound $\eta_{|R|}$, (5.35), in Section 5.4.3. However $\eta_{|R|}$ can only be computed if the strength of the singularity at the crack tip is known. For the general problem the convergence of $\eta_{|R|}$ with R is not known, however the line integral over R is still finite. Therefore, (5.20) is still applicable since as $R \to 0$, the magnitude of the ignored integral will also go to 0, however the rate at which integral will go to 0 with respect to the integral will be unknown.

All three estimates bound their respective components up to a positive arbitrary constant, the value of these constants is unknown. Therefore only the relative changes in η^2, η_Γ and $\eta_{|R|}$ can be used as a measure of the accuracy of $\{g^{h,\Gamma\setminus R}\}$. The results presented in Section 5.6 are performed with assumption that the first mesh produces results of $\{g^{h,\Gamma\setminus R}\}$ which are of a correct order of magnitude with the associated total error being the same order of magnitude.

$\{g_1^{h,\Gamma\setminus R}\}$, the component of the CF acting parallel to the crack face, is only a function of part 1 of (5.20) and therefore the error of $\{g_1^{h,\Gamma\setminus R}\}$ is bound by η^2 up to an arbitrary constant. $\{g_2^{h,\Gamma\setminus R}\}$ is a function of the part 1 and 2 of (5.20) and therefore is dependent on all three error measures. Both components of $\{g^{h,\Gamma\setminus R}\}$ for all problems here are presented here, up to 7 significant figures, with their associated values of η^2, η_Γ and $\eta_{|R|}$. The error of $\{g^{h,\Gamma\setminus R}\}$ is determined using

$$\% \text{ error in CF} = 100 \times \min\left\{\left(\frac{\eta^2_{\text{start}}}{\eta^2_{\text{end}}}\right), \left(\frac{\eta_{\Gamma,\text{start}}}{\eta_{\Gamma,\text{end}}}\right), \left(\frac{\eta_{|R|,\text{start}}}{\eta_{|R|,\text{end}}}\right)\right\} \tag{5.36}$$

where the subscripts start and end correspond to respectively to the first and last value of an error measure in a series of refinements.

5.6 Numerical examples

Combining the error estimate η, Algorithm 4.1, and $\{g^{h,\Gamma\setminus R}\}$, it was shown that very accurate results in comparison to an analytical solution of g_i were possible for the area integral component of $\{g^{h,\Gamma\setminus R}\}$ and the line integral component of $\{g^{h,\Gamma\setminus R}\}$ in Section 5.4.3. All problems in this section are plates acting in plane strain with $E = 1$ Pa, $\nu = 0.3$ with $p_K = 3\ \forall K \in \mathcal{T}$ and with a limit is set on p_K of 15. The limit on p_K was applied to prevent very high order elements appearing the mesh. Although exponential convergence is maintained using continually higher orders with the current *hp* marking scheme, the marking scheme does suffer in this instance from continually marking elements for *p*-refinement even if the error of the element is negligible. The result is the solver time becomes large and with negligible reduction in the size η. By limiting the polynomial order to $p_K = 15$ the solver time is decreased. Finally, all initial meshes were generated using Triangle [99].

5.6.1 Inclined edge crack

The first problem to be investigated is the inclined edge crack problem originally investigated by [2] and visited in Section 3.4.4 of Chapter 3. This problem is used to demonstrate that the convergence of $\{g^{h,\Gamma\setminus R}\}$ is domain independent, the results of $\{g^{h,\Gamma\setminus R}\}$ compare well to the results of [2], and exponential convergence of η_Γ is achieved. For the purpose of readability the problem is redefined as an inclined crack in a finite plate, Figure 5.2a, with a traction of $g_i^N = [0\ \ 1]^\top$ Pa acting on the top boundary and with a roller BC on the bottom edge. The *hp*-adaptivity strategy used $\delta_2 = 0.3$ and $\delta_1 = 0.07$ and ran for 30 adaptive steps. The initial and final meshes are shown in Figures 5.2b and 5.9 respectively.

Four different meshes where used, as shown in Figure 5.2b, each with a different domain size which is highlighted in grey on each initial mesh. The final value of the component acting parallel to the crack face, $g_1^{\Gamma\setminus R}$, and the component acting normal to the crack face, $g_2^{\Gamma\setminus R}$, is shown in Table 5.2. Table 5.2 clearly shows domain independence of $g_2^{\Gamma\setminus R}$, since for all meshes $g_2^{\Gamma\setminus R}$ have the same value up-to 3 significant figures. Further, all four meshes generate results which agree excellently with those achieved by [2].

Overall for the four meshes *h*-refinement occurred at the crack tip, the result being that $|R|$ decreased by a factor of 3.1×10^{-5} for all meshes, hence $\eta_{|R|}$ decreased by the same quantity. In

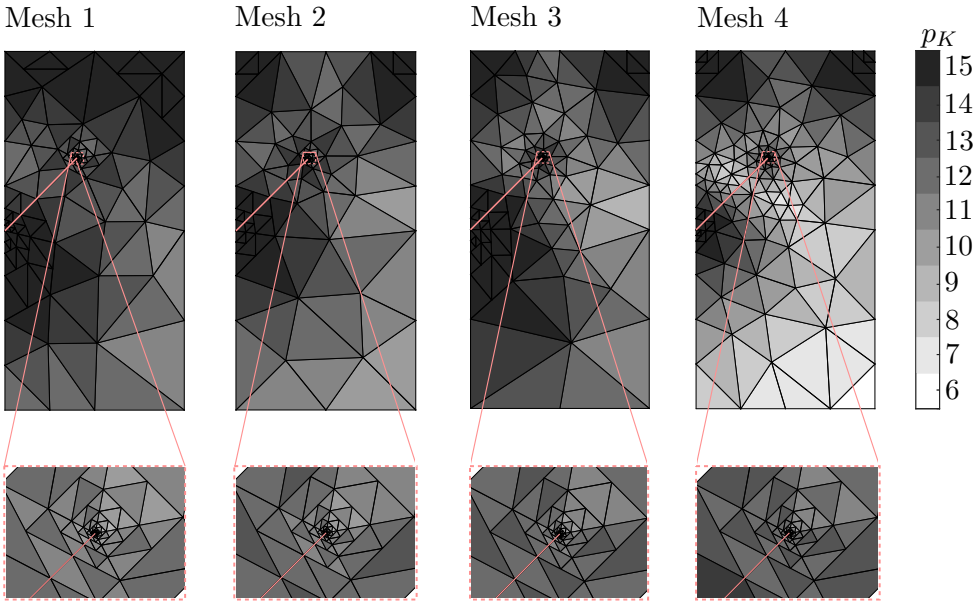

Figure 5.9: Inclined edge crack: The final element and polynomial distribution for meshes 1 to 4 after 30 *hp*-refinement steps with an enlarged view of the elements about the crack tip.

	Mesh 1	Mesh 2	Mesh 3	Mesh 4	Eischen [2]
$g_1^{h,\Gamma\setminus R}$	3.996605	3.996605	3.996605	3.996605	3.997
$g_2^{h,\Gamma\setminus R}$	-2.879464	-2.878902	-2.878504	-2.878223	-2.879

Table 5.2: Inclined edge crack: $g_i^{h,\Gamma\setminus R}$ values acting parallel and perpendicular to the crack edges.

Table 5.3 the ratios of η^2 and η_Γ between their first and last value in a series of refinements is provided. For all four meshes η^2 changed by a magnitude of $\approx 10^{10}$, and as a result $g_1^{h,\Gamma\setminus R}$ for mesh sizes achieves the same value up to at least 7 significant figures as shown in Table 5.2. η_Γ changed by an order of magnitude of $\approx 10^3$. Consistently η_Γ achieved the smallest decrease in its value. Hence, it is concluded in this case the evaluate of the face term on $(\Gamma^+ \cup \Gamma^-) \setminus R$ is the largest cause of error in $g_2^{h,\Gamma\setminus R}$. The change in the value of $|g_i^{h,\Gamma\setminus R}|$ with *hp*-adaptivity is shown in Figure 5.10a, the plot shows a step-like convergence as the length of $|R|$ is decreased and is converging to a final value from above. Inspecting Table 5.2 with the direction of convergence of Figure 5.10a would suggest that the value of g_2 achieved by [2] is a slight overprediction with the true value is slightly below and more similar to those achieved here. Lastly, although the convergence of η_Γ is the slowest out of the three error estimates, it still achieves exponential convergence with *hp*-adaptivity and Algorithm 4.1. This is shown clearly in Figure 5.10b where

	Mesh 1	Mesh 2	Mesh 3	Mesh 4
ratio η^2	4.605455×10^{-10}	3.841525×10^{-10}	4.311791×10^{-10}	3.120268×10^{-10}
ratio η_Γ	8.381845×10^{-3}	5.543627×10^{-3}	6.174230×10^{-3}	9.873442×10^{-3}

Table 5.3: Inclined edge crack: The ratio of η^2 and η_Γ between the first and last refinement step for meshes 1 to 4.

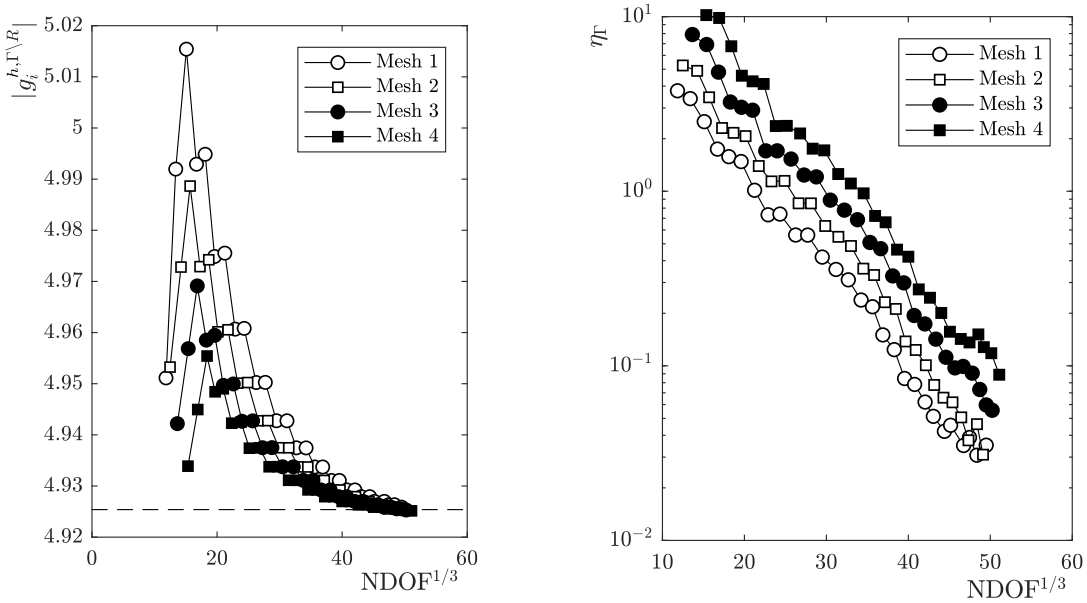

(a) (b)

Figure 5.10: Inclined crack: (a) convergence of $|g_i^{h,\Gamma\setminus R}|$ with respect to the NDOF$^{1/3}$ with *hp*-adaptivity and Algorithm 4.1 and (b), the corresponding convergence of η_Γ.

for all four meshes a similar rate of exponential convergence is achieved.

5.6.2 Split crack

The split crack problem, Figure 5.11a, has been visited in literature by [5, 152], amongst others. In this section a comparison is made between the CF obtained from the SIFs from [5] against the values achieved by $\{g^{h,\Gamma\setminus R}\}$. The SIFs in [5] were obtained using an enrichment function in conjunction with the interaction integral [23] where the crack is straight and where the shape of the stress field at the crack tip has to be known *a priori*. The geometry, and corresponding initial mesh, of the problem is shown in Figures 5.11a and 5.11b respectively. The dimensions and loads applied to the split crack problem are, $H = 16$ m, $W = 20$ m, $a = b = 1$ m, $\theta = 45°$, and $g_i^N = [0\ \ 1]^\top$ Pa applying a uniaxial tension to the plate. As no Dirichlet BCs exist, average BCs are applied for the vertical displacement and rotation to restrict rigid body motion, [75]. The *hp*-adaptive strategy ran for 30 refinement steps using $\delta_2 = 0.3$ and $\delta_1 = 0.07$ with the initial and final mesh shown in Figures 5.11b and 5.14.

	g_1^h [5]	$g_1^{h,\Gamma\setminus R}$	g_2^h [5]	$g_2^{h,\Gamma\setminus R}$
A	2.660	2.682148	0	3.139162×10^{-11}
B	1.230046	1.233918	1.229695	-1.232544
C	1.230046	1.233918	-1.229695	-1.232544

Table 5.4: Split crack: Values of the parallel $g_1^{h,\Gamma\setminus R}$ and perpendicular component $g_2^{h,\Gamma\setminus R}$ acting at crack tips A, B and C in comparison to the corresponding values obtained by [5].

The final values of $\{g^{h,\Gamma\setminus R}\}$ are compare well to those obtained by [5] in Table 5.4. Figures

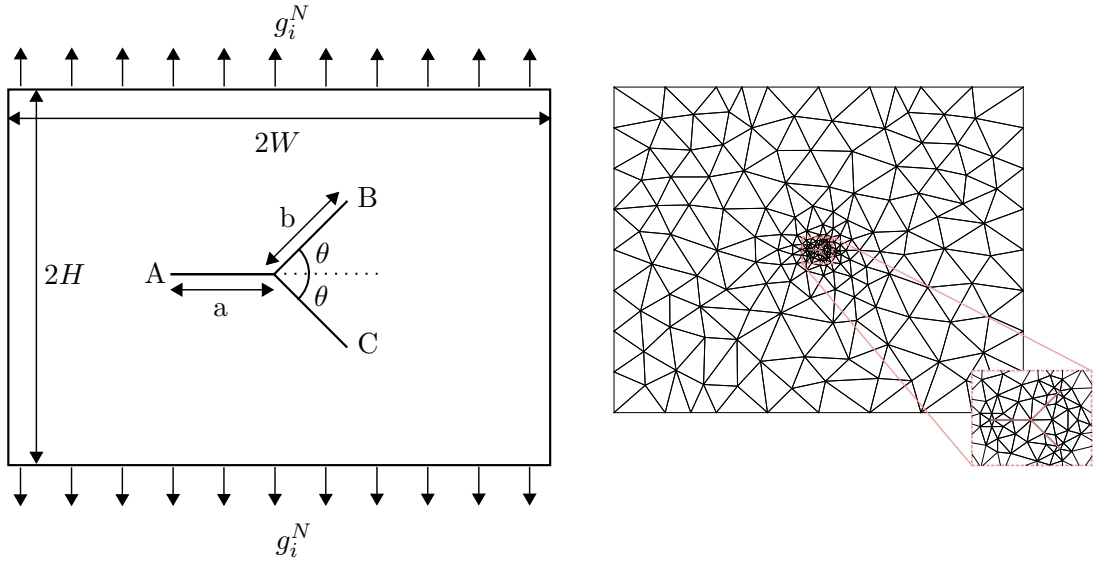

(a) (b)

Figure 5.11: Split crack: (a) the geometry and loading conditions with the initial mesh with $p_K = 3 \forall K \in \mathcal{T}$ shown in (b).

	Crack A	Crack B	Crack C
ratio η^2	4.806251×10^{-10}	4.806251×10^{-10}	4.806251×10^{-10}
ratio η_Γ	8.363981×10^{-3}	4.436014×10^{-3}	4.503948×10^{-3}

Table 5.5: Split crack: The ratio of η^2 and η_Γ between the first and last refinement step for cracks A, B and C.

5.12a and 5.12b show the direction of the convergence of the value of $|g_i^{h,\Gamma\backslash R}|$ for all cracks to be from below, which suggests that the results obtained by [5] slightly underpredicted the value of $g_1^{h,\Gamma\backslash R}$ and $g_2^{h,\Gamma\backslash R}$. Further, all error estimates have a significant change in magnitude. Firstly, for all three cracks h-refinement occurred at refinement step, not only does this demonstrated that $\eta_{|R|}$ reduced by a factor of 3.1×10^{-5}, but also that the hp-adaptive method chosen here is effective at identifying the crack tips. η^2 for the entire mesh reduced by 4.806251×10^{-10} and hence the area integral of $g_i^{h,\Gamma\backslash R}$ for all three cracks reduced by a similar factor. Lastly Table 5.5 shows the change in the value of η_Γ for the calculation of the line component of $g_i^{h,\Gamma\backslash R}$ cracks A, B and C, with the corresponding convergence plot shown in Figure 5.13.

Similar to the inclined crack results, in Section 5.6.1, the value of η_Γ changed by the smallest quantity for all three error estimates and corresponds to causing the largest error in $g_2^{h,\Gamma\backslash R}$. However using (5.36), Table 5.5 shows that for Cracks B and C η_Γ reduced by a factor of at least $\approx 4.4 \times 10^{-4}$ corresponding to an estimated percentage error of $\approx 0.04\%$. The results achieved by [5] for g_2^h are $\approx 0.23\%$ different from those achieved here and outside the estimated percentage accuracy. The estimated percentage accuracy is only an estimate, however the large orders of magnitude for all error estimates and the direction of convergence for $|g_i^{h,\Gamma\backslash R}|$ for all cracks suggests that the results achieved by [5] slightly underpredicted the value of $|g_i^{h,\Gamma\backslash R}|$ for all cracks.

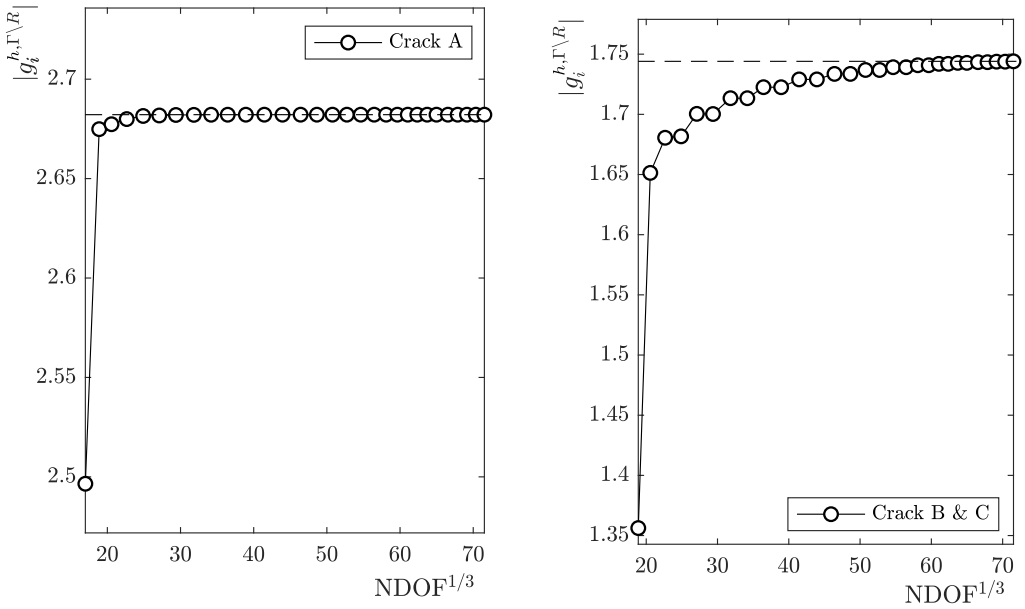

(a) (b)

Figure 5.12: Split crack: (a) $|g_i^{h,\Gamma\setminus R}|$ for crack A and (b) $|g_i^{h,\Gamma\setminus R}|$ for crack B & C. The final converged value for both plots is indicated by the dashed line.

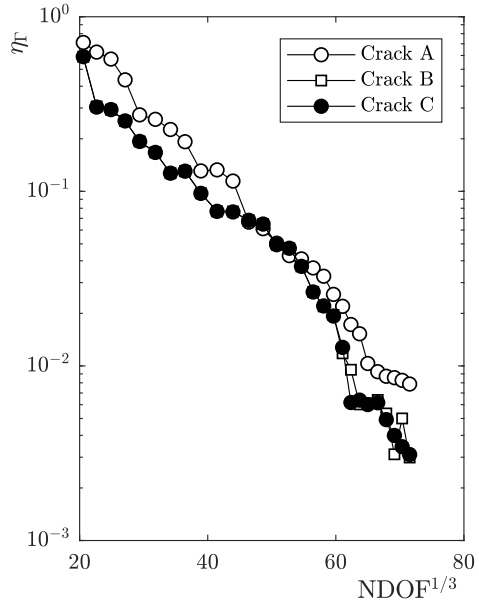

Figure 5.13: Split crack: η_Γ for cracks A, B and C

5.6.3 Tree crack

The final problem considered is the tree-crack problem, previously visited by Ai *et al.* [6]. The geometry and loading conditions are shown in Figure 5.15 with outer dimensions $L = 20$ m and $H = 4$ m. A slight variant of this problem was considered by [6, 153] where the tree crack geometry was contained within a square which had a biaxial tensile load applied. However that

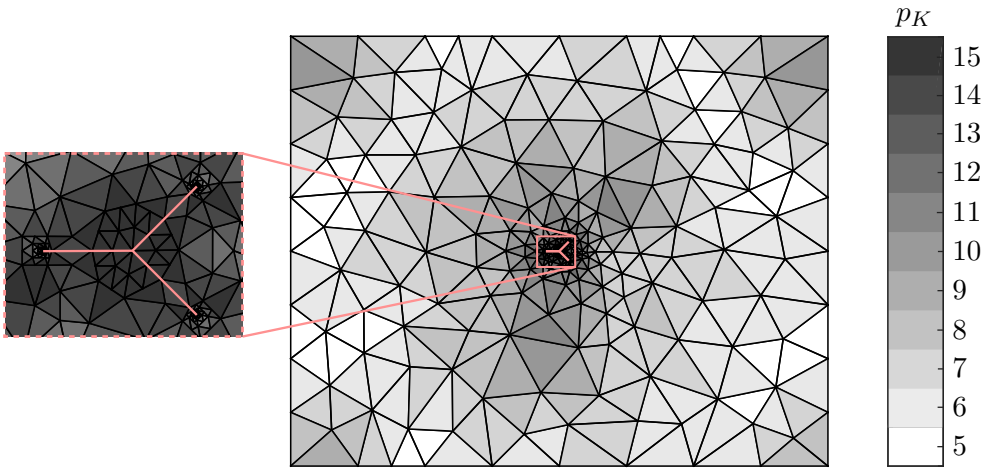

Figure 5.14: A colour plot of the final element distribution and polynomial order after 35 refinement steps.

problem contained closing cracks which neither [6] or [153] consider producing unusable results. The tree crack is marked by the grey lines with dimensions $a = 1$ m, $b = 0.5$ m and $\theta = \pi/4$. A traction of $g_i^N = [0\ \ 1]^\top$ Pa was applied on the left most edge acting to open up the crack edges and a weak homogeneous Dirichlet BC applied on the right most edge. The adaptivity strategy uses $\delta_2 = 0.3$ and $\delta_1 = 0.07$, with a limit set on p_K of 15, and ran for 28 refinement steps with $p_K = 3\ \forall K \in \mathcal{T}$ for the initial mesh, shown in Figure 5.16. The problem contains

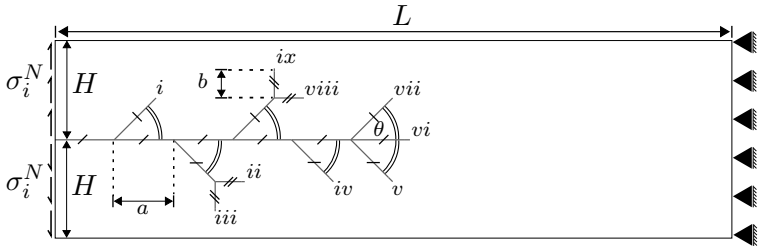

Figure 5.15: Tree crack: geometry, loading conditions and BCs.

9 opening cracks, at each crack tip a singular stress field exists of relatively different strengths. The problem is inherently more difficult to solve than the previous problems due to the number of cracks and the associated singular stress field. The problem therefore tests the robustness of the evaluation of $g_i^{h,\Gamma\backslash R}$ for difficult problems.

The final values of $g_i^{h,\Gamma\backslash R}$ are provided in Table 5.6, with the convergence rate of $g_1^{h,\Gamma\backslash R}$ and $g_2^{h,\Gamma\backslash R}$ with respect to the NDOF$^{1/3}$ shown in Figures 5.18, 5.19 and 5.20. For all convergence plots, $g_2^{h,\Gamma\backslash R}$ displays the step-like convergence patterns as $|R| \to 0$ as seen for the inclined and split crack problems, investigated in the previous sections.

As well as the values converging, the error in the area calculation for each crack tip, η_c^2, converges exponentially. The minimum reduction in magnitude of η_c^2 of all the crack tips was 2.4611×10^{-8}. The reduction in the error of the line integral for each crack tip η_Γ is shown in Table 5.6, the minimum reduction error was achieved by crack ix of 9.69×10^{-4}. However for all

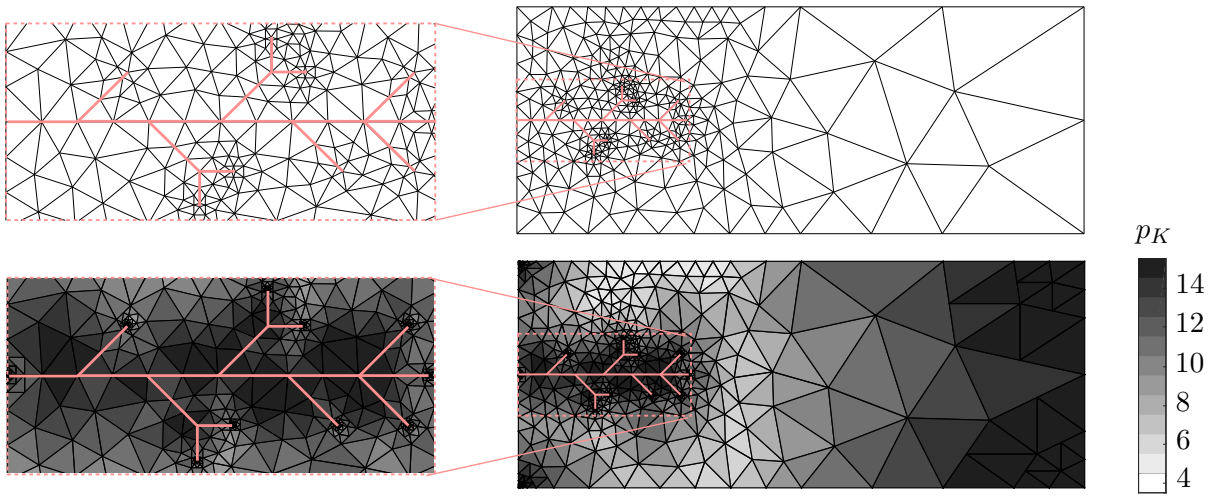

Figure 5.16: Tree crack: top right is the initial mesh of the whole problem, with an expanded view of the mesh about the cracks on the top left. Bottom right is a grey-scale plot of the element polynomial and element distribution of the final mesh after 28 *hp*-adaptive steps with an expanded view of the mesh about the cracks on the bottom left.

9 crack continued exponential convergence was achieved with *hp*-refinement and with Algorithm 4.1, this is demonstrated by Figure 5.17 where for each crack η_Γ is plotted against NDOF$^{1/3}$. Lastly, the error $\eta_{|R|}$ reduces by an order of magnitude of 1.24×10^{-4} for all cracks, since the *hp*-adaptive scheme performed *h*-refinement at each crack tip at every refinement step. Again, similar to the split and inclined crack problem, the smallest change in error was achieved by η_Γ.

Crack number	$g_1^{h,\Gamma\setminus R}$	g_1^h [6]	$g_2^{h,\Gamma\setminus R}$	g_2^h [6]	η_Γ ratio
i	4.959547×10^0	5.67	4.266616×10^0	4.64	4.02×10^{-4}
ii	1.503760×10^0	1.83	$-1.47046e \times 10^0$	-1.65	3.16×10^{-4}
iii	6.318318×10^1	-	1.352840×10^1	-	2.07×10^{-4}
iv	2.369873×10^1	-	2.620001×10^1	-	3.17×10^{-4}
v	5.386360×10^1	-	1.873850×10^2	-	7.72×10^{-4}
vi	8.684274×10^1	80.3	1.173388×10^{-1}	0	8.81×10^{-4}
vii	1.857197×10^2	-	5.355523×10^1	-	7.40×10^{-4}
$viii$	1.616839×10^0	-	1.427027×10^0	-	4.05×10^{-4}
ix	1.113449×10^2	110.7	-1.889263×10^1	-18.8	9.69×10^{-4}

Table 5.6: Tree crack: a comparison between $g_i^{h,\Gamma\setminus R}$ and equivalent g_i values obtained using the SIFs from [6], and the ratio of η_Γ between the first and last refinement step.

The results for the CF acting parallel to the crack tip $g_1^{h,\Gamma\setminus R}$ and perpendicular $g_2^{h,\Gamma\setminus R}$ are in good agreement with those achieved by [6]. Significantly less refinement was performed by [6] and the direction of the convergence was not always clear, it is therefore considered that the results presented here are a new benchmark. The results of the tree crack problem demonstrate even for complex problems the evaluation of $g_i^{h,\Gamma\setminus R}$ is robust. For all cracks exponential convergence of errors associated with $g_i^{h,\Gamma\setminus R}$ was achieved.

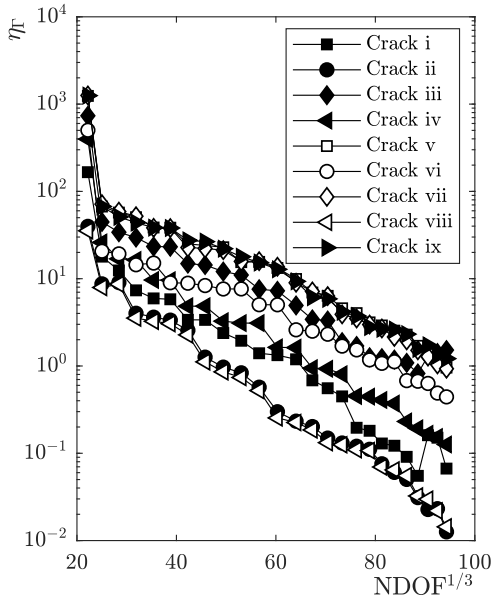

Figure 5.17: Tree crack: η_Γ for cracks i to ix.

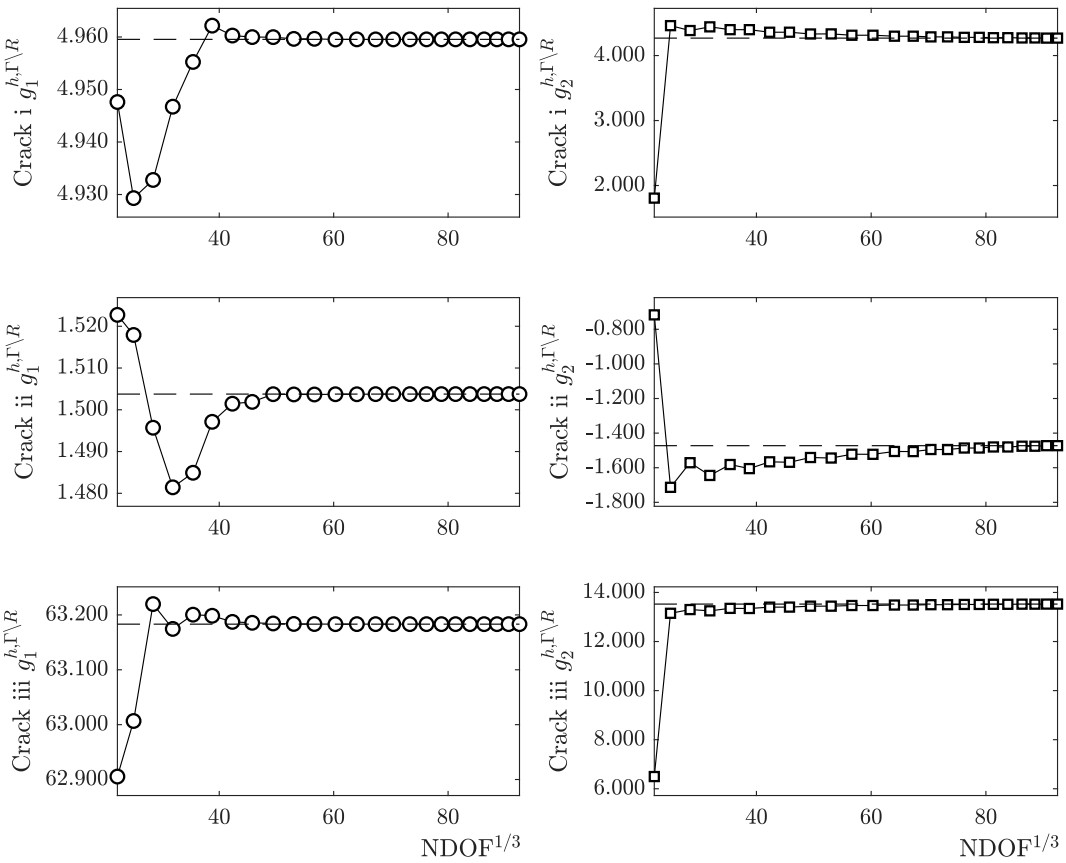

Figure 5.18: Tree crack: $g_1^{h,\Gamma\backslash R}$ and: $g_2^{h,\Gamma\backslash R}$ for cracks i to iii.

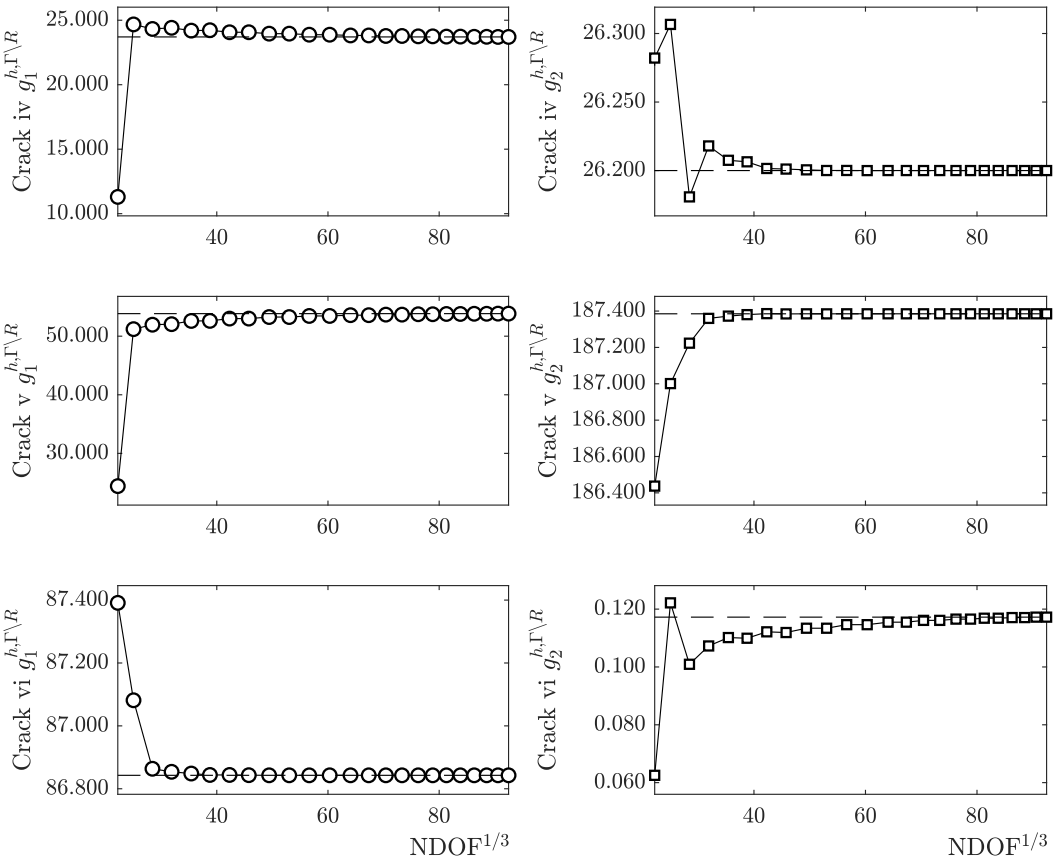

Figure 5.19: Tree crack: $g_1^{h,\Gamma\setminus R}$ and: $g_2^{h,\Gamma\setminus R}$ for cracks *iv* to *vi*.

5.7 Observations

In this chapter it was demonstrated and discussed how considering the nodal CF component at the crack tip will lead to results of poor accuracy, and how domain methods which only consider area integrals to determine the CF at the crack can only be applied to a small range of problems. Hence, this chapter proposed a novel method to determine the CF at the crack tip which does not require knowledge of the stress field about the crack tip to be known *a priori*, $\{g^{h,\Gamma\setminus R}\}$. The main difficulty associated with calculating the crack tip CF is determining the component that acts perpendicular to the crack face. The perpendicular component requires integrals along the crack faces which are cannot be evaluated using a polynomial basis, specifically the elements at the crack tip. Here, the calculation of $\{g^{h,\Gamma\setminus R}\}$ worked on the premise that with *hp*-adaptivity *h*-refinement always occurred at the crack tip. With *hp*-adaptivity this allowed $R \to 0$ by ignoring an increasing larger number of element edges at the crack tip, with the total length of the ignored element edges made increasingly smaller. This meant the calculation of the crack face term along $(\Gamma^+ \cup \Gamma^-) \setminus R$ became more accurate with *hp*-refinement whilst $R \to 0$.

Three error estimates for the components of $\{g^{h,\Gamma\setminus R}\}$ were provided in this chapter to ensure that the calculation of $\{g^{h,\Gamma\setminus R}\}$ become more accurate with *hp*-adaptivity. The area integral component of $\{g^{h,\Gamma\setminus R}\}$ was bound by η^2, the line integral component along $(\Gamma^+ \cup \Gamma^-) \setminus R$ was bound by η_Γ, and the ignored portion of the line integral along R had a magnitude proportional to $|R|$, denoted $\eta_{|R|}$. The value of $\eta_{|R|}$ is only known if the strength of the crack tip singularity

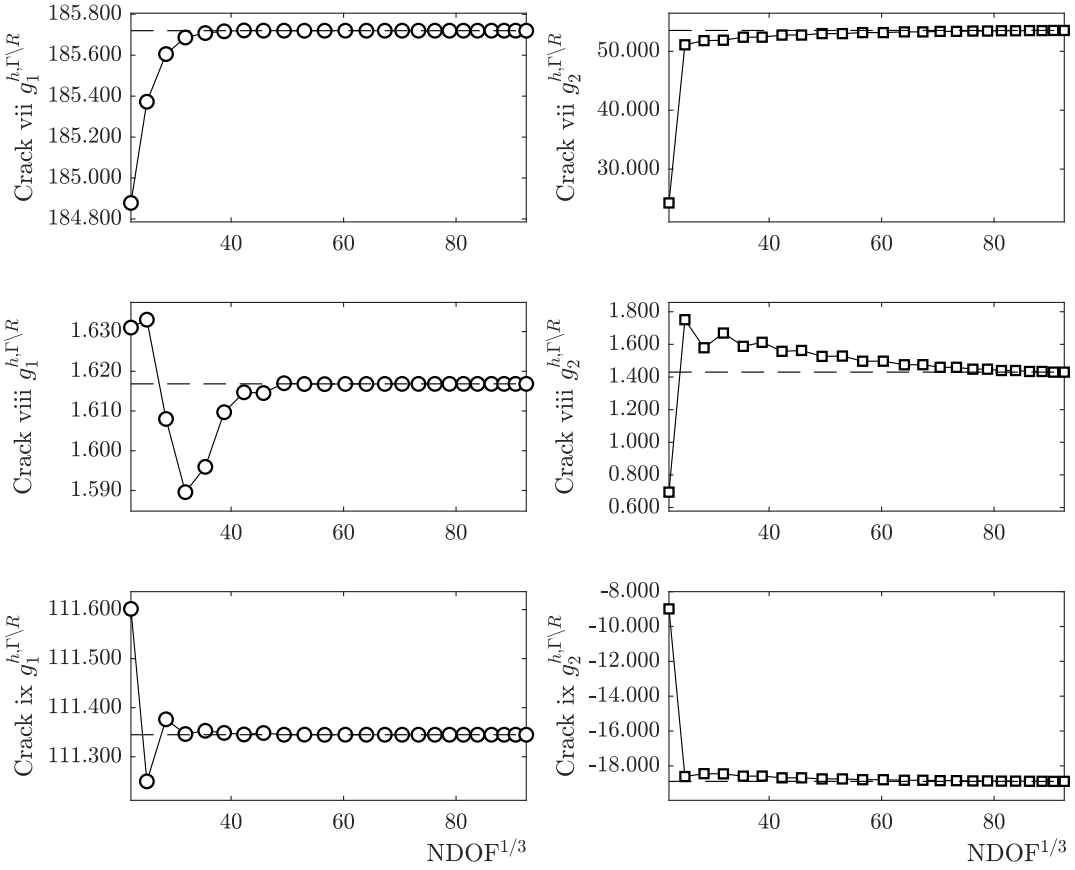

Figure 5.20: Tree crack: $g_1^{h,\Gamma\backslash R}$ and: $g_2^{h,\Gamma\backslash R}$ for cracks *vii* to *ix*.

is known however, $\eta_{|R|}$ is always finite and a function of $|R|$. Therefore the calculation $\{g^{h,\Gamma\backslash R}\}$ does not require knowledge of the crack tip singularity, however if the strength of the singularity is known it is useful in determine the rate at which the error $\eta_{|R|}$ is decreasing as $|R| \to 0$. The method of $|R| \to 0$ is considered slightly naive, and the adaptivity process could be improved. For instance, the *hp*-adaptivity of the mesh is driven by the *a posteriori* residual based error estimate η which is directly linked to the error in the area integral component of $\{g^{h,\Gamma\backslash R}\}$. However η_Γ contains components other than η in its calculation, and η is multiplied by characteristics of the element geometry. A more robust algorithm would be to drive *hp*-adaptivity based on both η and η_Γ, and letting $R \to 0$ based on the value of η_Γ rather than simply reducing $|R|$ by an element length every other refinement step. This being said, the calculation of $\{g^{h,\Gamma\backslash R}\}$ is shown here to be robust, with exponential convergence of all the errors of $\{g^{h,\Gamma\backslash R}\}$ achieved even for the most complex tree crack problem.

The calculation of $\{g^{h,\Gamma\backslash R}\}$ is considered to be a black box for calculating the crack tip CF for any material, besides heterogeneous materials. In the next chapter the methodology in the calculation $\{g^{h,\Gamma\backslash R}\}$ is used to obtain highly accurate results for cracks in general anisotropic materials, with no change in the algorithm to compute $\{g^{h,\Gamma\backslash R}\}$.

Chapter 6

Anisotropic fracture

6.1 Introduction

The aim of this chapter is to investigate the efficacy of the method described in the previous chapter to calculate the crack tip CF for an anisotropic material. This chapter considers fully anisotropic and orthotropic material behaviour. However, the focus of the chapter is on orthotropic materials since this material group is commonly used in engineering in the form of a composite material. Typically composite materials exist as either a thin layer of unidirectional layer of fibres, or a bi-direction weave of fibres; such as uni-or bi-directional carbon fibre weave, and carbon-Kelvar bidirectional weave, amongst others. Composites allow for flexible design since their material stiffness acting to resist a load is highly dependent on the fibre orientation. This facilitates engineers to produce structures with a high stiffness to weight ratio compared to isotropic materials since no redundant stiffness, and therefore material weight, exists to resist loads that the component was not designed for. It is therefore useful, in order to maximise the stiffness to weight ratio, to have a highly anisotropic material. They are commonly used in constructing shell structures in aerospace, performance cars, large scale turbines and satellites [154].

In Chapter 5 a method to compute the crack tip CF which was domain independent and required no knowledge of the stress field local to the crack tip *a priori* was developed. The results were compared to those obtained by other techniques in the literature however, these techniques required *a priori* knowledge of the local crack tip stress field. It was concluded the method was robust for isotropic materials, capable of producing accurate CF values for problems containing numerous mixed mode cracks with all error estimates associated with the calculation converging exponentially with respect to $\text{NDOF}^{1/3}$. The methodology presented in Section 5.3 to analyse the CF at crack tips in isotropic materials is used on a series of composite materials to demonstrate that the technique is robust. If successful, the method will demonstrate it is robust to different linear elastic homogeneous materials, concluding that a single method can be used to consider an arbitrary homogeneous material. It is possible to define the level of anisotropic material behaviour as the ratio between the Young's moduli in the most-to-least stiff direction, [155], however, it is noted that other definitions do exist [3]. The level of anisotropy used in numerical analysis to validate numerical methodologies is typically ≈ 10, [7, 87, 124, 156, 157],

however it has been shown experimentally the level of anisotropy can be of the order 10^2, [158]. In this chapter the ability of the technique to analyse the CF at the crack tip for orthotropic materials is validated using the error estimates defined in Chapter 5 and comparing the final CF values to those obtain in literature. Further, the ability of the method to accurately determine the CF at the crack tip for fully anisotropic materials is determined using the error estimates associated with the CF calculation.

For a general anisotropic material the displacement solution, and associated stress solution, at the crack tip can either be found using Stroh's formulation as in [159], or by writing the near crack tip stress solution in a complex variables form, as in [160, 161]. This is useful for numerical methods where the basis functions at the crack tip are enriched using the local crack tip stress solution, or during post-processing such as the M-integral in conjunction with the J-integral [23], to determine the crack tip CF or the associated SIFs. In the context of BEM this has been approached by: [7] where the SIFs are a variable to be solved for and thus the SIFs are directly evaluated using the XBEM; [38] use quarter point elements at the crack tip to correctly capture the crack tip stress singularity and then extract the SIFs from the displacement field at the crack tip and; [162] apply the Dual BEM to anisotropic analysis of cracks in composite laminates. Modelling anisotropic materials has also been approached in the XFEM framework, the author's of [163] developed enrichment functions for orthotropic materials whilst [159] derived enrichment functions for the stress solution of a fully anisotropic material. A comprehensive review of the history of the implementation of XFEM methods for orthotropic materials can be found in [154]. For anisotropic materials it is also possible to apply the M-integral to determine the SIFs, this is considered by the authors in [87, 157]. Element free Galerkin methods for modelling anisotropic materials also exist [156], as well as fractal FEMs where the SIFs are solved for [162].

For isotropic materials the penalty term, κ, for the *hp*-SIPG method is constant throughout the mesh. However, for anisotropic materials this definition of can over-penalise the SIPG formulation. To prevent over-penalisation, a new definition of the penalty term is required. The penalty term in SIPG weakly enforces continuity for the displacement solution across adjacent element edges and, between element edges and applied BCs. The penalty term has to be high enough to ensure that the SIPG bilinear form is coercive, thus a unique solution can be obtained [69]. For elliptic scalar diffusion problems, which contain anisotropic diffusive behaviour, κ has been shown to be a function of the face orientation, [164–166]; this reduces the value of κ preventing over-penalisation. The new form of κ is the achieved by reevaluating the coercive condition and introducing edge normals into the penalty term forming a sharper bound for the coercive inequality. Currently, this has only been performed for scalar problems [164, 165], the proof is extended here to linear elasticity.

After this introduction, the chapter continues with Section 6.2, an overview of the types of anisotropic materials and their associated material stiffness matrix that exist in a two dimensional setting. This is followed by Section 6.3, where a penalty term is derived for the *hp*-SIPG form for an anisotropic material. In Section 6.4 a method for determining the CF for anisotropic materials from SIFs is presented. This is necessary so that the CFs determined for the numer-

ical examples in Section 6.5 can be compared to equivalent SIFs values found in literature. Observations are drawn in Section 6.7.

6.2 Anisotropic materials

Linear elastic anisotropic materials acting in plane stress are considered in this chapter. As with isotropic materials, stress in tensorial notation double contraction between a fourth order material stiffness matrix and strain. In matrix notation this has the form,

$$\{\sigma\} = [D]\{\varepsilon\} \quad \text{or} \quad \{\varepsilon\} = [C]\{\sigma\}, \tag{6.1}$$

where $[C]$ is the compliance matrix, $[D]$ is the anisotropic material stiffness matrix, $\{\sigma\}$ is the stress the Cauchy stress vector and $\{\varepsilon\}$ is the small engineering strain vector. The change in the material model, from an isotropic to anisotropic material, amounts to an increased number of independent constants that construct the terms in $[D]$. As such, the *hp*-SIPG FE form for anisotropic materials is the same as isotropic materials (2.4). The material stiffness matrix, $[D]$, for isotropic materials acting in two, or three, dimension is dependent only on the Young's modulus E_Y and the Poisson ratio ν of the material. The material stiffness matrix for a general anisotropic material acting in two dimensions, in plane stress or strain, is dependent on six material constants and is given by

$$[D] = \begin{bmatrix} D(1,1) & D(1,2) & D(1,3) \\ D(1,2) & D(2,2) & D(2,3) \\ D(1,3) & D(2,3) & D(3,3) \end{bmatrix}, \tag{6.2}$$

which has the corresponding compliance matrix

$$[D]^{-1} = [C] = \begin{bmatrix} C(1,1) & C(1,2) & C(1,3) \\ C(1,2) & C(2,2) & C(2,3) \\ C(1,3) & C(2,3) & C(3,3) \end{bmatrix}. \tag{6.3}$$

$[D]$ is a symmetric positive definite matrix; from the definition of a hyperelasticity $[D]$ is symmetric and the eigenvalues of $[D]$ are real and positive ensuring only positive strain energy can exist. This is exploited later in Section 6.3.1 to determine a robust penalty parameter κ for anisotropic materials. Three types of anisotropy are considered in this chapter in two dimensions.

Transversely isotropic material behaviour: In three dimensions a transversely isotropic material has a plane which is isotropic, shown by plane A of Figure 6.1a, the material stiffness matrix $[D]$ is invariant to any rotations about the normal to this plane. However, an arbitrary rotation of $[D]$ about any other axis will generate a different material stiffness matrix. Consider the plane B of the transversely isotropic material in Figure 6.1a, an arbitrary plane with its axes parallel and perpendicular to plane A. This plane exhibits orthotropic material behaviour, such that if this plane represented a material acting in plane stress it would have the following

orthotropic compliance matrix

$$[C_{ijkl}] = \begin{bmatrix} 1/E_{Y,1} & -\nu_{12}/E_{Y,1} & 0 \\ -\nu_{21}/E_{Y,2} & 1/E_{Y,2} & 0 \\ 0 & 0 & 1/G_{12} \end{bmatrix}, \tag{6.4}$$

where $E_{Y,1}$ is the Young's modulus acting tangential to the isotropic plane, $E_{Y,2}$ is the Young's modulus acting perpendicular to the isotropic plane, G_{12} is the shear modulus between the tangential and perpendicular directions to the plane, and since the matrix is symmetric $\nu_{12}/E_{Y,1} = \nu_{21}/E_{Y,2}$. ν_{12} is the Poisson's ratio that corresponds to a contraction in direction 2 when an extension is applied in direction 1, with ν_{21} as visa versa. The indices 1 and 2, denote the Young's moduli in the principal directions of the anisotropic material behaviour. Only when the global coordinates system is parallel to the directions 1 and 2 does the compliance matrix for an orthotropic material have the form (6.4).

Orthotropic material behaviour: An Orthotropic material has three mutually orthogonal planes of symmetry, shown by the $x-y$ plane A, $x-z$ plane B and the $y-z$ plane C in Figure 6.1b, such that the material matrix is invariant to a reflection about any one of these planes. However, an arbitrary rotation about an arbitrary direction will result in a new material matrix. The principal axes of the orthotropic material behaviour are considered parallel to the global axes that support the coordinates system (x, y, z) such that, the compliance matrix for the material acting in plane stress on one of these planes, for example A, can be represented by 6.4. Where $E_{Y,1}$ is the Young's modulus acting in the x direction, $E_{Y,2}$ is the Young's modulus acting in y, G_{12} is the shear modulus between the axes x and y. ν_{12} is the Poisson's ratio that corresponds to a contraction in direction y when an extension is applied in direction x, with ν_{21} as visa versa. By analogy, the matrix (6.4) is also the compliance matrix for planes B and C.

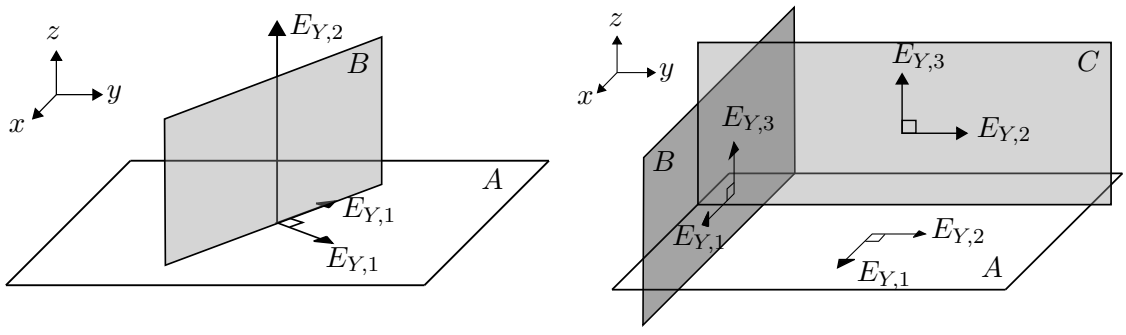

(a) (b)

Figure 6.1: A diagram showing the different planes and principal axes of isotropy and anisotropy for, a transversely isotropic and orthotropic material in (a) and (b) respectively.

General anisotropic material behaviour: No rotation symmetry exists, further there is no plane over which a reflection can occur such the matrix remains unchanged. The material stiffness matrix in two dimensions therefore has the form (6.2), where it is constructed from six material constants. All the material constants are dependent on the orientation of the global coordinates system, corresponding to the coordinate system of $[D]$, in respect to local coordinate

system of the material.

It is therefore necessary to define how $[D_{ijkl}]$ is rotated to represent this change. Following [167], firstly it is necessary to define variables which have a coordinate system parallel to the principal directions of the anisotropic material behaviour, the local stress tensor σ'_{ij} and its corresponding vector form $\{\sigma'_{ij}\}$, and the local strain tensor ε'_{ij} and its corresponding vector form for engineering strain $\{\varepsilon'^{\gamma}_{ij}\}$ and is vector form for tensorial strain $\{\varepsilon'_{ij}\}$. The matrix which maps tensorial strain to engineering strain is defined $[S]$ and has the form

$$\begin{aligned} \{\varepsilon'^{\gamma}_{ij}\} &= [S]\{\varepsilon'_{ij}\} \\ \left\{ \begin{array}{c} \varepsilon'_{11} \\ \varepsilon'_{22} \\ \gamma'_{21} \end{array} \right\} &= \left[\begin{array}{ccc} 1 & 0 & 0 \\ 0 & 1 & 0 \\ 0 & 0 & 2 \end{array} \right] \left\{ \begin{array}{c} \varepsilon'_{11} \\ \varepsilon'_{22} \\ \varepsilon'_{21} \end{array} \right\}. \end{aligned} \tag{6.5}$$

The rotation matrix which rotates a symmetric second order tensor represented in vector form, hence the requirement for the definition of tensorial strain (6.5), from a global to local coordinate system is defined as

$$[R]\{\cdot_{ij}\} = \{\cdot'_{ij}\}, \quad \text{where} \quad [R] = \left[\begin{array}{ccc} \cos^2(\theta) & \sin^2(\theta) & 2\cos(\theta)\sin(\theta) \\ \sin^2(\theta) & \cos^2(\theta) & -2\cos(\theta)\sin(\theta) \\ -\sin(\theta)\cos(\theta) & \sin(\theta)\cos(\theta) & \cos^2(\theta) - \sin^2(\theta) \end{array} \right], \tag{6.6}$$

where $\{\cdot\} \in \mathbb{R}^{3\times 1}$ and θ is the angle of anticlockwise rotation. (6.5) and (6.6) provide the tools deriving an equation for rotating the material stiffness from a local to global coordinate system. In the local coordinate system the relationship between stress and and strain is defined

$$\{\sigma'\} = [D']\{\varepsilon'^{\gamma}_{lm}\},$$

Where $[D']$ is the material stiffness matrix with principal directions parallel to the local coordinate system. Next, the stress is defined in terms of the global coordinate system using (6.6)

$$\begin{aligned} &[R]\{\sigma\} = [D']\{\varepsilon'^{\gamma}\} \\ &\text{and premultiplying by } [R]^{-1} \text{ to give,} \\ &\{\sigma\} = [R]^{-1}[D']\{\varepsilon'^{\gamma}\}, \end{aligned}$$

and the engineering strain is represented as tensorial strain with (6.5),

$$\{\sigma\} = [R]^{-1}[D'][S]\{\varepsilon'\}.$$

The local tensorial strain is then mapped to the global coordinate system

$$\{\sigma\} = [R]^{-1}[D'][S][R]\{\varepsilon\}$$

and finally converted to engineering strain,

$$\{\sigma\} = [R]^{-1}[D'][S][R][S]^{-1}\{\varepsilon^{\gamma}\}$$
$$\{\sigma\} = [R]^{-1}[D']\left([R]^{\top}\right)^{-1}\{\varepsilon^{\gamma}\}, \quad \text{where} \quad \left([R]^{\top}\right)^{-1} = [S][R][S]^{-1},$$

When the principal directions of the anisotropic behaviour are not parallel to the global coordinate system, the global material stiffness matrix is therefore defined as

$$[D] = [R]^{-1}[D']\left([R]^{\top}\right)^{-1}. \tag{6.7}$$

6.2.1 Defining the level of anisotropic material behaviour

There are several ways to define how anisotropic material is. For instance for an orthotropic material it is possible to use the ratio between the Young's moduli that act in the principal material directions [155]. A general definition for all types of anisotropic material behaviour exists, however, it is more complex, [3]. The derivation starts with the small strain compatibility equation with the ultimate aim of finding the roots of biharmonic equation for anisotropic materials,

$$\frac{\partial^2 \varepsilon_{11}}{\partial y^2} + \frac{\partial^2 \varepsilon_{22}}{\partial x^2} + \frac{\partial^2 \gamma_{12}}{\partial x \partial y} = 0. \tag{6.8}$$

The definition of strain, in terms of the compliance matrix and stress (6.1), is then substituted in to give

$$\frac{\partial^2}{\partial y^2}\left(C(1,1)\sigma_{11} + C(1,2)\sigma_{22} + C(1,3)\sigma_{12}\right) + \frac{\partial^2}{\partial x^2}\left(C(1,2)\sigma_{11} + C(2,2)\sigma_{22} + C(2,3)\sigma_{12}\right) +$$
$$\frac{\partial^2}{\partial x \partial y}\left(C(1,3)\sigma_{11} + C(2,3)\sigma_{22} + C(3,3)\sigma_{12}\right) = 0, \tag{6.9}$$

where the components of the compliance matrix are defined in (6.3). Next a stress function, $F(x, y)$, is introduced which satisfies the strong form statement of equilibrium $\nabla_j \sigma_{ij} = 0_i$,

$$\sigma_{11} = \frac{\partial^2 F}{\partial y^2}, \quad \sigma_{22} = \frac{\partial^2 F}{\partial x^2} \quad \text{and} \quad \sigma_{12} = -\frac{\partial^2 F}{\partial x \partial y}. \tag{6.10}$$

Substituting (6.10) into (6.9) gives

$$C(2,2)\frac{\partial^4 F}{\partial x^4} - 2C(1,3)\frac{\partial^4 F}{\partial x^3 \partial y} + (2C(1,2) + C(3,3))\frac{\partial^4 F}{\partial x^2 \partial y^2} - 2C(1,3)\frac{\partial^4 F}{\partial x \partial y^3} + C(1,1)\frac{\partial^4 F}{\partial y^4} = 0, \tag{6.11}$$

a biharmonic equation with roots to be found. The roots of (6.11), defined μ, can be found by considering the solution $F(x, y) = e^{\mu y - x}$ [168], which when substituted into (6.11) gives the characteristic equation,

$$C(2,2) + 2C(2,3)\mu + (2C(1,3) + C(3,3))\mu^2 + 2C(1,3)\mu^3 + C(1,1)\mu^4 = 0. \tag{6.12}$$

Four roots exist, $\{\mu_1, \mu_2, \mu_3, \mu_4\}$ and are in general complex such that $\mu_3 = \bar{\mu_1}$ and $\mu_4 = \bar{\mu_2}$. Using μ_1 and μ_2 it can be stated how anisotropic a material is, since for an isotropic material $\mu_1 = \mu_2$. As such the maximum ratio between the normed values of μ_1 and μ_2 is used to judge the level of anisotropic material behaviour [3]. The larger the ratio, the higher the level of anisotropic material behaviour.

6.3 The penalty term in the SIPG method

The penalty term in Chapter 2 for the SIPG bilinear form (2.9) was defined as the maximum eigenvalue of the material stiffness matrix $[D_{ijlm}]$ multiplied by a factor 10. The purpose of the penalty is to ensure that the SIPG bilinear form is coercive, and thus a unique solution can be obtained. Although the penalty term contains the factor 10 a larger number could also be suitable however, a significantly larger number could cause the stiffness matrix to become over-penalised and ill-conditioned, which would produce inaccurate results. Anisotropic materials are particularly sensitive to the possibility of over-penalisation. This can be explained by considering an orthotropic material, it has a principal axis corresponding to a stiff Young's modulus and a perpendicular axis corresponding to a less-stiff Young's modulus. If an element edge is orientated such that it is perpendicular to the direction of the less-stiff material, using the isotropic form of κ will result in a parameter parameter the same magnitude as the stiffer anisotropic material behaviour. The result is values in the stiffness matrix will be produced by combining terms which are possibly orders of magnitude different, producing round off-errors. However, since the jump in the stress solution is in the direction of the less-stiff material a lower penalty can be used whilst conserving the coercive condition. Over-penalisation increases the condition number and ultimately, this makes the linear solution for a direct solver, which is used here, more sensitive to round off-errors and which produces a less accurate, or potentially destroyed, solution [73].

Investigation into the definition of the SIPG penalty term for modelling anisotropic and heterogeneous convection-diffusion-reaction problems with anisotropic diffusion coefficients is explored in [164], and anisotropic advection-diffusion problems in [165]. The derivation of a more suitable penalty term for an anisotropic linear elastic problem is similar to derivation of the penalty terms in [164, 165] since a linear elastic problem is analogous to a diffusion problem except with a fourth order tensor coefficient matrix rather than a second order tensor matrix. Making the penalty term a function of the isotropic material stiffness was shown numerically to be sufficient in [117], again this is analogous to isotropic diffusion problems where the penalty term is a function of a diffusive coefficient matrix, [166, 169]. A succinct proof for the value of the penalty term for isotropic elliptic problems, where the diffusion coefficient matrix is the identity matrix, can be found in [69]. For the first time, to the best of the author's knowledge, a proof is provided to determine a more suitable penalty term for anisotropic linear elastic materials; the proof combines the methodologies provided in [69, 164, 165].

6.3.1 Penalty term for anisotropic materials

The penalty term for SIPG is derived from the coercive proof. During this proof the constant C is not a specific constant but is used to indicate the product of several hidden constants. The

statement of coercivity for SIPG is,

$$a(u_i, u_i) \geq C\|u_i\|_{\mathfrak{T}}^2 \quad \text{where} \quad u_i \in W_{\bar{p}}(\mathfrak{T}), \tag{6.13}$$

where $a(u_i, u_i)$ is defined in (2.10). However for the purpose of this section it is more conveniently written as a series of norms,

$$a(u_i, u_i) = \sum_{K\in\mathfrak{T}} \|d_{pqij}\varepsilon_{pq}\|_{0,K}^2 + \sum_{F\in\mathcal{F}_I\cup\mathcal{F}_D} \beta_F\|\langle u_i\rangle\|_{0,F}^2 - 2\sum_{F\in\mathcal{F}_I\cup\mathcal{F}_D}\int_F \{n_j D_{ijpq}\varepsilon_{pq}\}\langle u_i\rangle \mathrm{d}s \tag{6.14}$$

with $W_{\bar{p}}(\mathfrak{T})$ defined in (2.8), and C is an unknown positive constant. The material stiffness tensor D_{ijlm} is positive definite and has the symmetries $D_{ijlm} = D_{lmij}$, $D_{ijlm} = D_{jilm}$ and $D_{ijlm} = D_{ijml}$, and since positive definite all eigenvalues are positive real numbers. It is therefore possible to decompose D_{ijlm} into two further fourth order symmetric tensors with positive eigenvalues, $D_{ijkl} = d_{ijmn}d_{klmn}$, where $d_{ijlm} = d_{lmij}$, $d_{ijlm} = d_{jilm}$ and $d_{ijlm} = d_{ijml}$. This allows the DG energy norm, initially defined in [65], to be rewritten as,

$$\|u_i\|_{\mathfrak{T}}^2 = \sum_{K\in\mathfrak{T}} \|d_{ijpq}\varepsilon_{ij}\|_{0,K}^2 + \sum_{F\in\mathcal{F}_I} \beta_F\|\langle u_i\rangle\|_{0,F}^2 + \sum_{F\in\mathcal{F}_D} \beta_F\|u_i\|_{0,F}^2, \tag{6.15}$$

where the operator $\langle u_i\rangle$ is defined as

$$\langle u_i\rangle = \begin{cases} u_i^{K+} - u_i^{K-}, & \text{if on the internal edges,} \quad F = \partial K^+ \cap \partial K^- \in \mathcal{F}_I(\mathfrak{T}), \\ u_i^K, & \text{if on the external edges,} \quad F = \partial K \cap \partial\Omega_\Gamma \in \mathcal{F}_B. \end{cases} \tag{6.16}$$

In order to prove (6.13) a second norm is introduced,

$$\|u_i\|_{\mathrm{DG}}^2 = \|u_i\|_{\mathfrak{T}}^2 + \sum_{F\in\mathcal{F}_D\cup\mathcal{F}_I}\int_F \frac{1}{\beta_F}\{n_j d_{pqij}\varepsilon_{pq}\}^2 \mathrm{d}s, \tag{6.17}$$

where

$$\beta_F = \begin{cases} \kappa_F \frac{\max(p_{K-}^2, p_{K+}^2)}{h_F}, & \text{if on the internal edges,} \quad F = \partial K^+ \cap \partial K^- \in \mathcal{F}_I(\mathfrak{T}), \\ \kappa_F \frac{p_K^2}{h_F} & \text{if on the external edges,} \quad F = \partial K \cap \partial\Omega_\Gamma \in \mathcal{F}_B, \end{cases} \tag{6.18}$$

κ_F is constant to be found for the face F and $\|u_i\|_{\mathrm{DG}}^2 \geq \|u_i\|_{\mathfrak{T}}^2$. Before proving (6.13) and determining the penalty term for anisotropic materials, several inequalities are introduced. Firstly

for $\forall F \in \mathcal{F}_I$

$$\begin{aligned}\int_F \frac{1}{\beta_F}\{n_j d_{pqij}\varepsilon_{pq}\}^2 \mathrm{d}s &= \frac{1}{4}\int_F \frac{1}{\beta_F}(n_j^+ d_{pqij}\varepsilon_{pq}^+ + n_j^- d_{pqij}\varepsilon_{pq}^-)^2 \mathrm{d}s \\ &= \frac{1}{4}\int_F \frac{1}{\beta_F}(n_j^+ d_{pqij}\varepsilon_{pq}^+ - n_j^+ d_{pqij}\varepsilon_{pq}^-)^2 \mathrm{d}s \\ &\leq \frac{C}{\beta_F}\int_F (n_j^+ d_{pqij}\varepsilon_{pq}^+)^2 + (n_j^+ d_{pqij}\varepsilon_{pq}^-)^2 \mathrm{d}s, \\ &\text{since } (a-b)^2 = a^2 + b^2 - 2ab \leq a^2 + b^2 .\text{if } a, b > 0\end{aligned} \tag{6.19}$$

Similarly for $\forall F \in \mathcal{F}_B$

$$\int_F \frac{1}{\beta_F}\{n_j d_{pqij}\varepsilon_{pq}\}^2 \mathrm{d}s \leq \frac{C}{\beta_F}\int_F (n_j d_{pqij}\varepsilon_{pq})^2 \mathrm{d}s, \tag{6.20}$$

where $\{\cdot\}$ is an average operator on arbitrary high order tensor, for example u_i

$$\{u_i\} = \begin{cases} (u_i^{K+} + u_i^{K-})/2, & \text{if on the internal edges,} \quad F = \partial K^+ \cap \partial K^- \in \mathcal{F}_I(\mathcal{T}), \\ u_i^K, & \text{if on the external edges,} \quad F = \partial K \cap \partial\Omega_\Gamma \in \mathcal{F}_B. \end{cases} \tag{6.21}$$

The norms (6.19) and (6.20) are norms over a edge F. Using the trace inequality defined in [69] these norms over the edge can be bound by a norm over the interior of K where $\partial K \cap F \neq \emptyset$,

$$\|d_{pqij}\varepsilon_{ij}\|_{0,F}^2 \leq C\left(\frac{1}{h_K}\|d_{pqij}\varepsilon_{ij}\|_{0,K}^2 + \|d_{pqij}\varepsilon_{ij}\|_{0,K}\|\nabla_q d_{pqij}\varepsilon_{ij}\|_{0,K}\right), \tag{6.22}$$

where h_K is the diameter of circle that intersects all three vertices of the triangular element K. Considering a single term from the right hand side of (6.19) and using (6.22), the following result can therefore be obtained

$$\begin{aligned}\int_F \frac{1}{\beta_F}(n_j d_{pqij}\varepsilon_{pq})^2 \mathrm{d}s &\leq \int_F \frac{1}{\beta_F}(d_{pqij}\varepsilon_{pq})^2 \mathrm{d}s \\ &= \frac{1}{\beta_F}\|d_{pqij}\varepsilon_{pq}\|_{0,F}^2 \\ &\text{which from (6.22) becomes,} \\ &\leq \frac{C}{\beta_F}\left(\frac{1}{h_K}\|d_{pqij}\varepsilon_{pq}\|_{0,K}^2 + \|d_{pqij}\varepsilon_{pq}\|_{0,K}\|\nabla_j d_{pqij}\varepsilon_{pq}\|_{0,K}\right) \\ &\text{and since } C\frac{p_K^2}{h_K}\|d_{pqij}\varepsilon_{pq}\|_{0,K} \leq \|\nabla_j d_{pqij}\varepsilon_{pq}\|_{0,K} \text{ [69]}, \\ &\leq \frac{C}{\beta_F}\left(\frac{1}{h_K} + C\frac{p_K^2}{h_K}\right)\|d_{pqij}\varepsilon_{pq}\|_{0,K}^2 \\ &\leq \frac{C}{\beta_F}\frac{p_K^2}{h_K}\|d_{pqij}\varepsilon_{pq}\|_{0,K}^2.\end{aligned} \tag{6.23}$$

The result of (6.23) can be applied directly to the inequality (6.20) for an internal face $F \in \mathcal{F}_I$, shared by the elements $K^+ \cup K^-$, corresponding to a single element K to give

$$\frac{C}{\beta_F}\int_F (n_j^+ d_{pqij}\varepsilon_{pq}^+)^2 + (n_j^+ d_{pqij}\varepsilon_{pq}^-)^2 \mathrm{d}s \leq \frac{C}{\kappa_F}\|d_{pqij}\varepsilon_{pq}\|^2_{0,K^+\cup K^-}, \tag{6.24}$$

and also to (6.19) for the faces $F \in \mathcal{F}_B$,

$$\frac{C}{\beta_F}\int_F (n_j d_{pqij}\varepsilon_{pq})^2 \mathrm{d}s \leq \frac{C}{\kappa_F}\|d_{pqij}\varepsilon_{pq}\|^2_{0,K}. \tag{6.25}$$

Now that the inequalities (6.24) and (6.25) have been defined it is possible to show (6.13). This achieved by showing that $a(u_i,u_i) - C\|u_i\|^2_{\mathcal{T}} \geq 0$ and so starts with,

$$\begin{aligned} a(u_i,u_i) - C\|u_h\|^2_{\mathrm{DG}} = (1-C)&\sum_{K\in\mathcal{T}} \|d_{pqij}\varepsilon_{pq}\|^2_{0,K} \\ &+ (1-C)\left(\sum_{F\in\mathcal{F}_I\cup\mathcal{F}_D} \beta_F\|\langle u_i\rangle\|^2_{0,F}\right) \\ &- 2\sum_{F\in\mathcal{F}_I\cup\mathcal{F}_D}\int_F \{n_j D_{ijpq}\varepsilon_{pq}\}\langle u_i\rangle \mathrm{d}s \\ &- C\sum_{F\in\mathcal{F}_D\cup\mathcal{F}_I}\int_F \frac{1}{\beta_F}\{n_j d_{pqij}\varepsilon_{pq}\}^2 \mathrm{d}s. \end{aligned} \tag{6.26}$$

To show that (6.26) is greater than 0, it is necessary to transform the last two norms into the form of either $\|d_{ijpq}\varepsilon_{pq}\|^2_{0,K}$ or $\beta_F\|n_j^+\langle u_i\rangle\|^2_{0,F}$. Considering the penultimate integral of (6.26) for an arbitrary face F,

$$\begin{aligned} 2\int_F \{n_j D_{ijpq}\varepsilon_{pq}\}\mathrm{d}s &= 2\int_F \{n_j^+ d_{ijst} d_{pqst}\varepsilon_{pq}\}\langle u_i\rangle \mathrm{d}s \\ &= 2\int_F \{d_{pqst}\varepsilon_{pq}\}\langle n_j^+ d_{ijst} u_i\rangle \mathrm{d}s \\ &\text{and using a Cauchy-Swartz inequality becomes} \\ &\leq 2\left(\int_F \frac{1}{\beta_F}\{d_{sqlm}\varepsilon_{sq}\}^2 \mathrm{d}s\right)^{1/2}\left(\int_F \beta_F\langle n_j^+ d_{ijst}u_i\rangle^2\right)^{1/2}. \end{aligned} \tag{6.27}$$

Applying Young's inequality

$$2ab \leq \frac{a^2}{\epsilon} + \epsilon b^2, \tag{6.28}$$

where $\epsilon > 0$, and a and b are real positive numbers, to (6.27) and using the results (6.19) and (6.23), for an internal face, (6.27) becomes

$$\begin{aligned} 2\left(\int_F \frac{1}{\beta_F}\{d_{sqlm}\varepsilon_{lm}\}^2 \mathrm{d}s\right)^{1/2} & \left(\int_F \beta_F \langle n_j^+ d_{ijst} u_i\rangle^2\right)^{1/2} \\ & \leq \gamma_F \int_F \frac{1}{\beta_F}\{d_{sqlm}\varepsilon_{sq}\}^2 \mathrm{d}s + \frac{1}{\gamma_F}\int_F \beta_F \langle n_j^+ d_{ijst} u_i\rangle^2 \mathrm{d}s \\ & \leq \gamma_F \frac{C}{\kappa_F}\|d_{sqlm}\varepsilon_{sq}\|^2_{0,K^+\cup K^-} + \frac{1}{\gamma_F}|n_j^+ d_{ijst}|_F^2 \beta_F \int_F |\langle u_i\rangle|^2 \mathrm{d}s \end{aligned} \tag{6.29}$$

where $|n_j^+ d_{ijst}|_F^2 = |n_j^+ d_{ijst} n_q^+ d_{pqst}|_F$. Similarly, for an external face

$$\begin{aligned} \left(\int_F \frac{1}{\beta_F}\{d_{pqlm}\varepsilon_{pq}\}^2 \mathrm{d}s\right)^{1/2} & \left(\int_F \beta_F \langle n_j d_{ijst} u_i\rangle^2\right)^{1/2} \\ & \leq \gamma_F \frac{C}{\kappa_F}\|d_{pqlm}\varepsilon_{pq}\|^2_{0,K} + \frac{1}{\gamma_F}|n_j d_{ijst}|_F^2 \beta_F \int_F |\langle u_i\rangle|^2 \mathrm{d}s \end{aligned} \tag{6.30}$$

where $\gamma_F > 0$ is the Young's constant for the face F. Substituting the inequalities (6.24), (6.25) and (6.27) and (6.30) into (6.26) gives,

$$\begin{aligned} a(u_i,u_i) - C\|u_i\|^2_{\mathrm{DG}} \geq & \sum_{K\in\mathcal{T}} \left((1 - C - (C+\gamma_{F_1})\frac{C}{\kappa_{F_1}} - (C+\gamma_{F_2})\frac{C}{\kappa_{F_2}} - (C+\gamma_{F_3})\frac{C}{\kappa_{F_3}})\|d_{pqlm}\varepsilon_{pq}\|^2_{0,K}\right) \\ & + \sum_{F\in(\mathcal{F}_I\cup\mathcal{F}_B)} \left(\left(1 - C - \frac{|n_j d_{ijst}|_F^2}{\gamma_F}\right)\beta_F \|\langle u_i\rangle\|^2_{0,F}\right) \geq 0. \end{aligned} \tag{6.31}$$

Each element K has three edges F_1, F_2, and F_3. Therefore each element K will have three Young's constants γ_{F_1}, γ_{F_2} and γ_{F_3} where each Young's constant corresponds to integrals each edge, and three penalty terms corresponding to each edge κ_1, κ_2 and κ_3. To guarantee (6.31) to be greater than 0 each coefficient for the face F and element K must be greater than 0. The coefficient for the face F is greater than 0 if

$$0 < C \leq 1 - \frac{|n_j d_{ijst}|_F^2}{\gamma_F}, \tag{6.32}$$

with $\gamma_F > |n_j d_{ijst}|_F^2$. Now that $\gamma_F > |n_j d_{ijst}|_F^2$ is defined, it is possible to determine κ_F by ensuring the coefficient for the element K is greater than 0,

$$\begin{aligned} 0 < C &\leq \frac{1 - \gamma_{F_1} C/\kappa_{F_1} - \gamma_{F_2} C/\kappa_{F_2} - \gamma_{F_3} C/\kappa_{F_3}}{1 + C\kappa_{F_1} + C\kappa_{F_2} + C\kappa_{F_3}} \\ &\leq \frac{1 - |n_j d_{ijst}|^2_{F_1} C/\kappa_{F_1} - |n_j d_{ijst}|^2_{F_2} C/\kappa_{F_2} - |n_j d_{ijst}|^2_{F_3} C/\kappa_{F_3}}{1 + C\kappa_{F_1} + C\kappa_{F_2} + C\kappa_{F_3}}, \end{aligned} \tag{6.33}$$

hence

$$0 \leq 1 - |n_j d_{ijsq}|^2_{F_1} C/\kappa_{F_1} - |n_j d_{ijsq}|^2_{F_2} C/\kappa_{F_2} - |n_j d_{ijsq}|^2_{F_3} C/\kappa_{F_3} \tag{6.34}$$

which can be guaranteed if

$$3|n_j d_{ijst}|_F^2 C \leq \kappa_F \quad \forall F \in \{F_1, F_2, F_3\}. \tag{6.35}$$

The coercivity condition (6.13) can be ensured by satisfying (6.35), therefore the penalty parameter κ_F is a function of the material stiffness matrix and the normal to the face F. As d_{ijsq} is a fourth order tensor the full form of $|n_j d_{ijst}|_F^2$ is not particularly clear. A clearer, and therefore more useful, interpretation is achieved by looking at the matrix equivalent form of $|n_j d_{ijsq}|_F^2$,

$$\begin{aligned}
|n_j d_{ijsq}|_F^2 = \Bigg| & \begin{bmatrix} n_x & 0 & n_y \\ 0 & n_y & n_x \end{bmatrix} \begin{bmatrix} d(1,1) & d(1,2) & d(1,3) \\ d(2,1) & d(2,2) & d(2,3) \\ d(3,1) & d(3,2) & d(3,3) \end{bmatrix} \\
& \qquad \begin{bmatrix} d(1,1) & d(2,1) & d(3,1) \\ d(1,2) & d(2,2) & d(3,2) \\ d(1,3) & d(2,4) & d(3,3) \end{bmatrix} \begin{bmatrix} n_x & 0 \\ 0 & n_y \\ n_y & n_x \end{bmatrix} \Bigg|_F \\
= & \left| \begin{bmatrix} n_x & 0 & n_y \\ 0 & n_y & n_x \end{bmatrix} \begin{bmatrix} D(1,1) & D(1,2) & D(1,3) \\ D(2,1) & D(2,2) & D(2,3) \\ D(3,1) & D(3,2) & D(3,3) \end{bmatrix} \begin{bmatrix} n_x & 0 \\ 0 & n_y \\ n_y & n_x \end{bmatrix} \right|_F \\
= & \left| [n]^\top [D_{ijlm}][n] \right|_F ,
\end{aligned} \tag{6.36}$$

where n_x and n_y are the normal components to the face F and $[D_{ijlm}]$ is the material stiffness matrix defined in (2.3). The penalty parameter κ_F for an edge F is therefore defined as

$$\kappa_F = 3C \left| [n]^\top [D_{ijlm}][n] \right|_F , \tag{6.37}$$

where $C = 10$ is assumed to be sufficient [170]. The proof to determine κ_F for edges $F \in \mathcal{F}_B \cup \mathcal{F}_I$ has been provided here, and could be extended to also consider the penalty for edges $F \in \mathcal{F}_T$. However, it is not included here for the sake of readability, and would provide a result similar to that of (6.37) since the roller boundary is a specific case of the Dirichlet BC applied only to the displacement normal to the domain edge.

6.4 Configurational force anisotropic fracture

The methodology used in Section 5.3 to determine the CF at the crack tip for an isotropic material is used here for anisotropic materials. However, in the literature the CF values are more commonly represented as SIFs. Therefore, similarly to isotropic materials 3.46, it is necessary to express the CF as a function as SIFs so that a comparison can be made between the results obtained here and those obtained in literature when expressed as SIFs. The derivation to express the CF as a set of SIFs for anisotropic materials is provided in [161]. Here, the results of [161] are presented to show how the crack tip CF is determine from SIFs for anisotropic materials using the roots μ_1 and μ_2 from (6.12). To determine the first component of the CF the following

terms are generated

$$
\begin{aligned}
C(1,1) &= -\frac{C(2,2)}{2}\mathrm{Im}\left(\frac{\mu_1+\mu_2}{\mu_1\mu_2}\right) \\
C(1,2) &= -\frac{C(2,2)}{2}\mathrm{Im}\left(\frac{1}{\mu_1\mu_2}\right) + \frac{C(1,1)}{2}\mathrm{Im}(\mu_1\mu_2) \\
C(2,2) &= \frac{C(1,1)}{2}\mathrm{Im}(\mu_1+\mu_2).
\end{aligned}
\tag{6.38}
$$

From which the first component, which acts parallel to the crack edges, of the CF can be expressed as,

$$
g_1 = C(1,1)K_I^2 + C(1,2)K_IK_{II} + C(2,2)K_{II}^2 \tag{6.39}
$$

where K_I and K_{II} are the mode I and mode II SIFs respectively. Similarly the second component of the CF, which acts perpendicular to the crack edges, requires the terms

$$
\begin{aligned}
\beta_{11} &= -\frac{1}{2}\mathrm{Im}(\omega_{11}\omega_{21} + \omega_{31}\omega_{41}) \\
\beta_{12} &= -\frac{1}{2}\mathrm{Im}(\omega_{11}\omega_{22} + \omega_{12}\omega_{21} + \omega_{31}\omega_{42} + \omega_{32}\omega_{41}) \\
\beta_{22} &= -\frac{1}{2}\mathrm{Im}(\omega_{12}\omega_{22} + \omega_{32}\omega_{42}).
\end{aligned}
\tag{6.40}
$$

From which the second component of the CF can be expressed as,

$$
g_2 = \beta_{11}K_I^2 + \beta_{12}K_IK_{II} + \beta_{22}K_{II}^2. \tag{6.41}
$$

In a similar fashion to $C(i,j)$ terms of (6.38), the ω terms in (6.40) are determined from the roots of (6.12) and components of the material compliance matrix (6.2)

$$
\begin{array}{ll}
\omega_{11} = \frac{\mu_1\mu_2}{\mu_1-\mu_2}\left(\frac{-\mu_1}{\sqrt{\mu_1}} + \frac{\mu_2}{\sqrt{\mu_2}}\right) & \omega_{12} = \frac{1}{\mu_1-\mu_2}\left(\frac{-\mu_1^2}{\sqrt{\mu_1}} + \frac{\mu_2^2}{\sqrt{\mu_2}}\right) \\
\omega_{21} = \frac{\mu_1\mu_2}{\mu_1-\mu_2}\left(\frac{-p_1}{\sqrt{\mu_1}} + \frac{p_2}{\sqrt{\mu_2}}\right) & \omega_{22} = \frac{1}{\mu_1-\mu_2}\left(\frac{-p_1\mu_1}{\sqrt{\mu_1}} + \frac{p_2\mu_2}{\sqrt{\mu_2}}\right) \\
\omega_{31} = \frac{\mu_1\mu_2}{\mu_1-\mu_2}\left(\frac{1}{\sqrt{\mu_1}} - \frac{1}{\sqrt{\mu_2}}\right) & \omega_{32} = \frac{1}{\mu_1-\mu_2}\left(\frac{\mu_1}{\sqrt{\mu_1}} + \frac{-\mu_2}{\sqrt{\mu_2}}\right) \\
\omega_{41} = \frac{\mu_1\mu_2}{\mu_1-\mu_2}\left(\frac{-q_1}{\sqrt{\mu_1}} + \frac{q_2}{\sqrt{\mu_2}}\right) & \omega_{42} = \frac{1}{\mu_1-\mu_2}\left(\frac{-q_1\mu_1}{\sqrt{\mu_1}} + \frac{q_2\mu_2}{\sqrt{\mu_2}}\right)
\end{array}
\tag{6.42}
$$

where $p_i = C(1,1)\mu_i^2 + C(1,2) - C(1,6)\mu_i$ and $q_i = C(1,2)\mu_i + C(2,2)/\mu_i - C(2,6)$.

6.5 Numerical examples

In this section a series of numerical examples are considered. Firstly the penalty parameter presented in Section 6.3.1 is numerical verified for high and low levels of anisotropic material behaviour. This is achieved by demonstrating by obtaining convergence rates consistent with the *a priori* error estimate for the SIPG norm (4.7), and the *a posteriori* error estimate η (4.8). The second set of numerical examples consider a number mixed mode crack problems. The overall purpose of considering multiple crack problems is to:

1. Validate that the calculation of $g_i^{h,\Gamma\backslash R}$ agrees well with the results obtained in literature for anisotropic material behaviour.

2. Validate that $g_i^{h,\Gamma\backslash R}$ is robust to high levels of anisotropic material behaviour, up to the standards presented in literature.

3. Validate $g_i^{h,\Gamma\backslash R}$ for mixed mode multiple crack problems for general anisotropic and orthotropic material behaviour.

4. Verify that convergence is achieved for all the error estimates associated with $g_i^{h,\Gamma\backslash R}$.

In order to investigate the above points, four problems considering cracks are considered in order as in Table 6.1. For each problem the angle of the principal axes of the anisotropic material

Problem	Type of anisotropy	$(E_{\max}/E_{\min})$	$\lvert\mu_1 - \mu_2\rvert$	Number of cracks
Tensile crack	Orthotropic	12.4	2.75	1
Shear crack	Orthotropic	12.4	2.75	1
Inclined double ended crack	Orthotropic	2.8	1.75	2
Split crack	Anisotropic	n/a	1.78	3

Table 6.1: An outline of the crack problems considered in Section 6.5.

behaviour is also rotated; the effect this has the on the convergence of $g_i^{h,\Gamma\backslash R}$ and its associated error estimates is investigated.

6.5.1 SIPG validation for anisotropic materials

Before analysing CF's at crack tips, it is necessary to numerically verify the convergence rate in the error of the SIPG norm, and the corresponding *a posteriori* error estimate η (4.8), is consistent with the *a priori* statement of convergence (4.7). This ensures the implementation of the anisotropic stiffness matrix, with the corresponding rotation (6.7), is correct. Further, it will verify that the new penalty term derived for anisotropic materials in Section 6.3.1 is suitable for very high levels of anisotropic behaviour. The problem considered here exists in the unit square $(x, y) \in \Omega_\Gamma = (0, 1)^2$. The manufactured displacement solution is smooth, $u_i \in [H(\Omega_\Gamma)^\infty]^2$, and is defined as

$$u_i = \begin{Bmatrix} \sin(\frac{15}{2}\pi x)\sin(\frac{15}{2}\pi y) \\ \sin(\frac{15}{2}\pi x)\sin(\frac{15}{2}\pi y) \end{Bmatrix}, \tag{6.43}$$

with homogeneous Dirichlet BCs applied on $x = 0$ m, heterogeneous Dirichlet BCs on $x = 1$ m, and heterogeneous Neumann BCs on $y = 0$ m and $y = 1$ m. No average boundary conditions are applied since Dirichlet boundary conditions are present in the x and y directions. A body force, f_i, is applied to the interior of the domain and is determined from (6.43) using the strong form set of equations which define linear elasticity, 2.1. The material considered here is orthotropic hence, the inverse of the compliance matrix shown in (6.4) is used as the material stiffness matrix, with $E_{Y,1} = M \times 1$ Pa, $E_{Y,2} = G_{12} = 1$ Pa and $\nu_{12} = 0.3$, where M is scale factor which can either decrease or increase the level of anisotropy. A rotation of 37° is also applied to the material stiffness matrix using (6.7). The rotation ensures that the principal axes of the orthotropic material behaviour are not parallel to the domain's boundaries, and thus the application of a weakly applied Neumann or Dirichlet BC is a combination of all material stiffness matrix terms. Further, the rotation makes it unlikely that internal edges of the mesh, and therefore the weak interaction of adjacent elements, are also not parallel to the principal axes of the orthotropic

material behaviour. This decreases the likelihood of possible false positive result obtained by the either the BCs or internal edges in terms of: the definition of the new penalty; the effect of the penalty parameter on the condition number and the implementation of the anisotropic material behaviour when generating the global stiffness matrix.

Two values of M are considered, $M = 1$ and $M = 10^8$. Showing that the correct convergence rate is achieved with $M = 1$ will demonstrate that the SIPG formulation is suitable for anisotropic materials typically used in composite manufacture, as discussed in Section 6.1. Choosing $M = 10^8$ is necessary to show that the SIPG formulation, with the anisotropic penalty, is robust for very high levels of anisotropy. Although unlikely that such a material exists, verifying that the SIPG formulation, and corresponding error estimate η, is sufficiently robust for this level of anisotropy demonstrates the efficacy of the formation. Additionally, if it is found that there are issues with convergence of a problem further on in the section, showing that correct convergence is achieved for this level of anisotropy will demonstrate it is not the formulation causing an issue. Rather, a combination of anisotropy material behaviour and a particular set of loading conditions which could be creating a difficult, or impossible, problem to solve.

The initial mesh used to demonstrate convergence is shown as an inset figure in Figure 6.2a. The mesh is unstructured to further ensure no element edges are coincident with the anisotropic material behaviour. The polynomial order of the mesh is homogeneous such that $p_K = p \, \forall K \in \mathcal{T}$, where p has a value in the range $[1, 9]$. For a mesh of a homogeneous polynomial order p, the mesh is uniformly refined three times. The value of error in the SIPG norm and η, and the corresponding NDOF, are recorded for each mesh with the convergence respectively shown in Figures 6.2a and 6.2b. When the mesh is uniformly refined in element size, h-refinement, the convergence rate of the error in the SIPG norm and η with respect to the $\text{NDOF}^{1/2}$ should be p, as shown by the *a priori* error estimate (4.1).

p_K	1	2	3	4	5	6	7	8	9
$M = 1$	0.951	1.98	2.96	4.02	5.04	5.97	6.92	8.01	8.95
$M = 10^8$	0.986	1.94	3.09	3.98	5.06	5.92	6.97	7.93	8.96

Table 6.2: A square domain with heterogeneous and homogeneous Dirichlet BCs and heterogeneous Neumann BCs: convergence rate for all polynomials in the range $[1, 9]$ for $M = 1$ and $M = 10^8$.

Figures 6.2a and 6.2b demonstrate the correct convergence of the error in the SIPG norm and η for meshes of homogeneous polynomial order 1, 2, 4, 6 and 8 for both $M = 1$ and $M = 10^9$. Table 6.2 gives the rate of convergence between the finest two discretisation for all meshes with a uniform polynomial order in the range $[1, 9]$. For all polynomial orders the convergence rate is similar to the value defined by the *a priori* error estimate. The table demonstrates that the SIPG formulation with Dirichlet and Neumann BCs, and with the anisotropic penalty term (6.35), is robust since for modelling low and high levels of anisotropic material behaviour since the correct order of convergence is achieved for all polynomial orders.

Both the error in the SIPG norm and η are $\approx 10^8$ times higher for $M = 10^8$ compared to

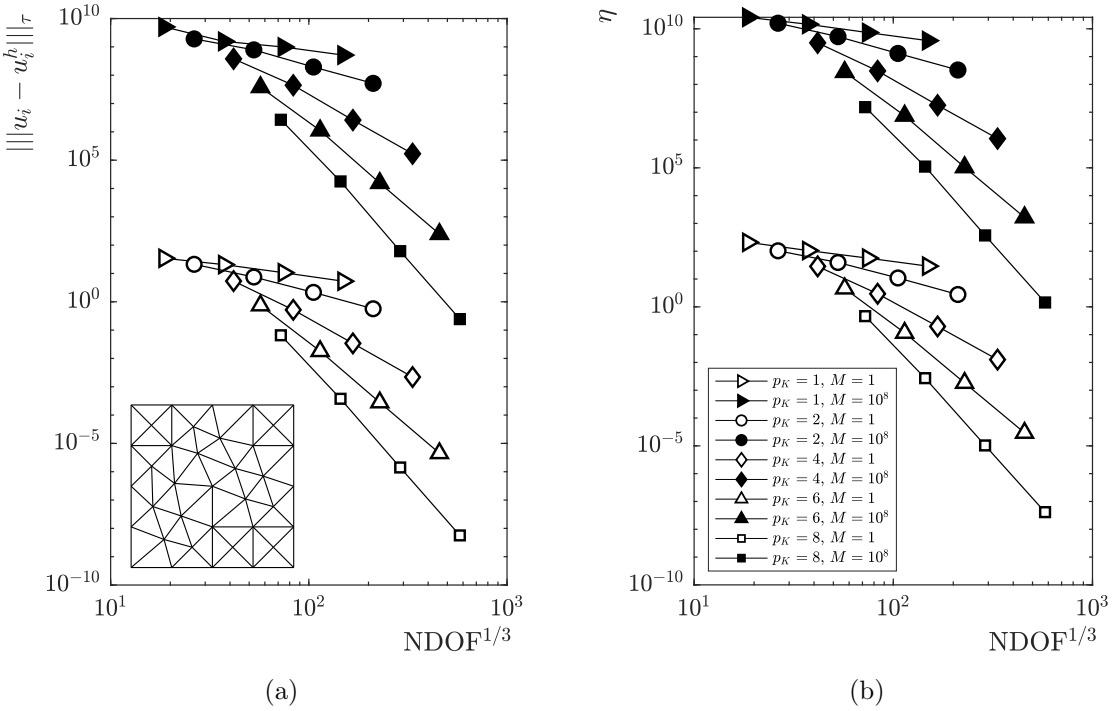

(a) (b)

Figure 6.2: A square domain with heterogeneous and homogeneous Dirichlet BCs and heterogeneous Neumann BCs: (a) convergence of the error in the SIPG norm for meshes of homogeneous polynomial order being uniformly refined, and (b) the corresponding value of η for each mesh. The initial mesh is provided as inset figure in (a) with the legend for both plots provided in (b).

$M = 1$. The reason is the error in the gradient of displacement $\|\nabla_j u_i - \nabla_j u_i^h\|_{0,\mathcal{T}}$ is similar for both values of M for all meshes. Since the error in norm of stress is bound by $\|\sigma_{ij} - \sigma_{ij}^h\|_{0,\mathcal{T}} \lesssim |D_{ijkl}|\|\nabla_j u_i - \nabla_j u_i^h\|_{0,\mathcal{T}}$, it follows that the error in the stress norm is bound by a value that is proportional to M. The error in the SIPG norm is a function in the error norm of stress, and η is reliable and efficient for the error in the SIPG norm invariant with respect to the value of $|D_{ijkl}|$, hence both values show a dependence on the value of M.

6.5.2 Uniaxial tensile crack

A single mixed mode crack in an orthotropic plate acting in plane stress is considered in this section. The material properties of the plate are provided by Table 6.3. A schematic of the problem's geometry and BCs are shown in Figure 6.3a, with outer dimensions $H = W = 1$ m and crack length $a = 0.5$ m. The load applied is applied to the top and bottom edge by a Neumann boundary condition with values $g_i^N = [0\ 1]^\top$ Pa and $g_i^N = [0\ -1]^\top$ Pa respectively. Since no Dirichlet BCs exist, the average displacement and rotation BCs are applied, (2.52), (2.53) and (2.54) respectively. The principal axes of the orthotropic material are rotated by angle θ, see Figure 6.3a, with respect to the global coordinate system. 10 θ values, in steps of $10°$ are considered in the range $[0°, 90°]$ for this problem.

The high level of anisotropy presents multiple new challenges for the *hp*-adaptive scheme and the algorithm for computing $g_i^{h,\Gamma\backslash R}$:

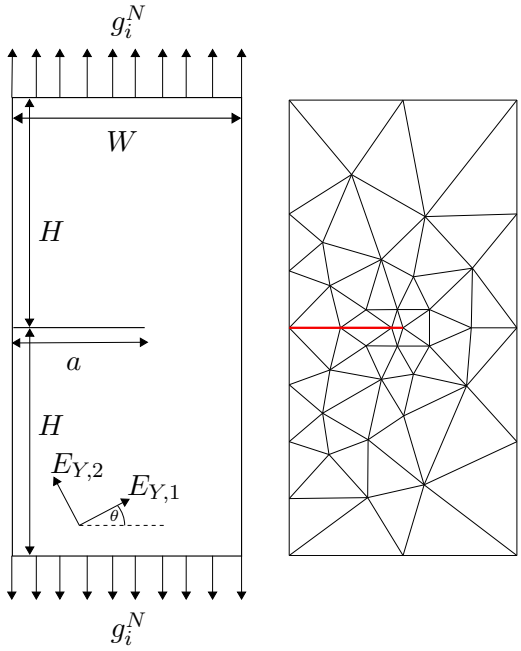

(a) (b)

Figure 6.3: Uniaxial tensile crack: plate dimensions, crack position and BCs and, the initial mesh with the crack edges highlighted in red.

$E_{Y,1}$ (Pa)	$E_{Y,2}$ (Pa)	G_{12} (Pa)	ν_{12}
144.8	11.7	9.66	0.21

Table 6.3: Orthotropic material properties used for the tension and shear crack problems.

- It is necessary for continued h-refinement to occur at the crack tip to ensure $R \to 0$ in a pragmatic manner with respect to the number of hp-adaptive steps.
- It is not desirable for elements on the crack edge to undergo consistent refinement in h, other than the elements at the crack tip, as this will reduce the speed of $R \to 0$.
- Refining appropriately in h, or p, the regions of the problem that have large errors associated with the anisotropic material behaviour as well as the errors associated the crack tip stress field such that $\eta \to 0$ exponentially with respect to the NDOF$^{1/3}$.
- Last, refining sufficiently along the crack faces such that the error in the crack face term of the CF calculation, η_Γ, reduces sufficiently that increasing the length of the crack edge integral corresponds overall to a reduction in η_Γ.

The initial mesh, for all values of θ, is provided by Figure 6.3b with an associated polynomial order of $p_K = 2\ \forall K \in \mathcal{T}$. 35 hp-refinement steps were performed on the mesh with $\delta_2 = 0.01$ and $\delta_1 = 0.001$. These values are significantly lower than those expressed in previous sections, respectively 0.3 and 0.07. Changing the values of δ_2 and δ_1 to lower values does not affect the convergence of η. However, it does cause more h-refinement to occur at the crack faces which slows down the rate at which $R \to 0$. This is necessary since at higher values of δ_2 and δ_1

the rate of $R \to 0$ is too fast such that the error associated with the crack edge integral η_Γ increases. By decreasing δ_2 and δ_1 convergence is achieved for all error estimate components - this discussion is continued at the end of the section. Further, for this problem the length of $|R|$ is reduced every third step, rather than every second step as in the previous chapter, to further decrease the rate which at $|R| \to 0$.

The results for the final values of $g_1^{h,\Gamma\setminus R}$ and $g_2^{h,\Gamma\setminus R}$, with a comparison to results obtained in the literature, for a range of θ values are shown respectively in Figures 6.4a and Figures 6.4b; Table 6.4 provides the corresponding values. Inspecting Figures 6.4a and 6.4b, and Table 6.4, shows that good agreement is obtained for $g_1^{h,\Gamma\setminus R}$, whilst comparatively poorer agreement is obtained for $g_2^{h,\Gamma\setminus R}$ against the results obtained in [3] for the full range of θ values.

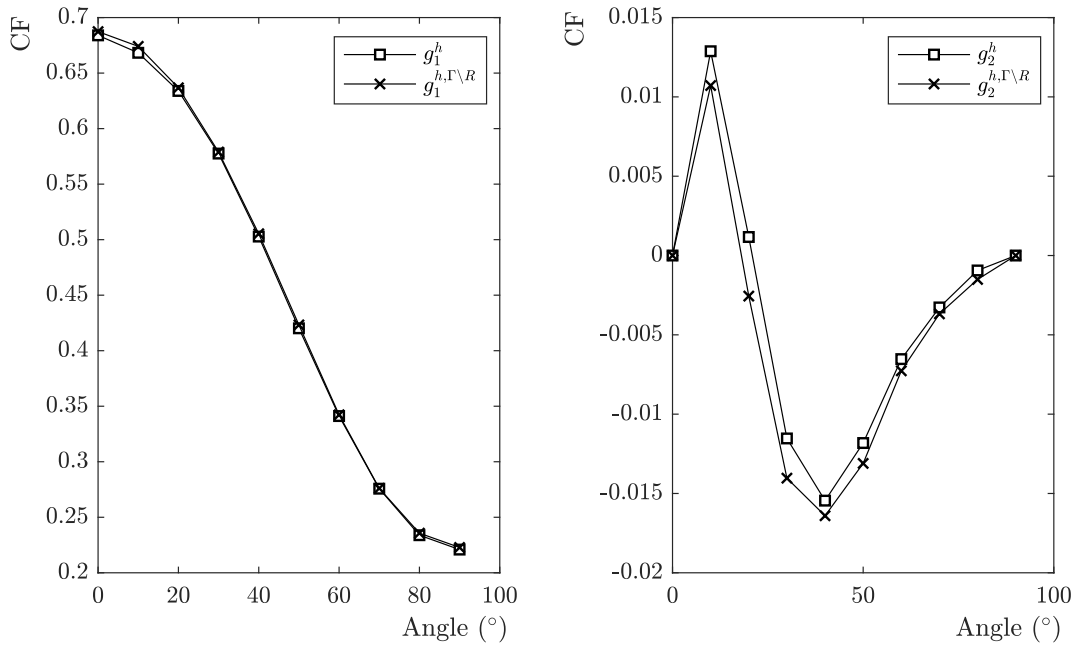

(a) (b)

Figure 6.4: Uniaxial tensile crack: final values $g_1^{h,\Gamma\setminus R}$ and $g_2^{h,\Gamma\setminus R}$ for a range of rotations of the principal directions of orthotropic material behaviour, with a respective comparison to g_1^h and g_2^h obtained from [3].

An advantage of having an error estimate for each component of the calculation of $g_2^{h,\Gamma\setminus R}$ is that a basis is provided to investigate the validity of the results. The first error estimate to consider is η^2 which corresponds to the area integral component of $g_2^{h,\Gamma\setminus R}$. Table 6.5 shows for all angles of anisotropic material behaviour that the ratio of η^2 between the last and first value is less than 0.0047%. η^2 bounds the error in the area integral component of $g_2^{h,\Gamma\setminus R}$ from above, it is therefore likely that the error associated with this component of the calculation has decreased by a similar order of magnitude. It is concluded that the error of the area integral component is orders of magnitude smaller than the error presented in the final column of Table 6.4, therefore the error in the area integral of $g_2^{h,\Gamma\setminus R}$ is a not the source of discrepancy.

The second error to be considered is $\eta_{|R|}$, shown in Table 6.5, which is proportional to the

θ (°)	$g_1^{h,\Gamma\setminus R}$	g_1^h	$\frac{\lvert g_1^{h,\Gamma\setminus R} - g_1^h \rvert}{\lvert g_1^{h,\Gamma\setminus R} \rvert} \times 100$	$g_2^{h,\Gamma\setminus R}$	g_2^h	$\frac{\lvert g_2^{h,\Gamma\setminus R} - g_2^h \rvert}{\lvert g_2^{h,\Gamma\setminus R} \rvert} \times 100$
0	0.6874	0.6839	0.51	-2.4720×10^{-10}	-4.2027×10^{-17}	–
10	0.6741	0.6682	0.88	1.0715×10^{-2}	-1.2878×10^{-2}	220.18
20	0.6368	0.6339	0.46	-2.5573×10^{-3}	-1.1675×10^{-3}	54.34
30	0.5789	0.5775	0.24	-1.4034×10^{-2}	-1.1531×10^{-2}	17.83
40	0.5053	0.5027	0.51	-1.6404×10^{-2}	-1.5451×10^{-2}	5.80
50	0.4232	0.4201	0.73	-1.3104×10^{-2}	-1.1820×10^{-2}	9.79
60	0.3423	0.3411	0.35	-7.2701×10^{-3}	-6.5293×10^{-3}	10.18
70	0.2760	0.2757	0.11	-3.6783×10^{-3}	-3.2723×10^{-3}	11.03
80	0.2357	0.2338	0.81	-1.5076×10^{-3}	-9.4133×10^{-4}	37.56
90	0.2228	0.2208	0.90	-6.6012×10^{-12}	1.1937×10^{-17}	–

Table 6.4: Uniaxial tensile crack: final values $g_1^{h,\Gamma\setminus R}$ and $g_2^{h,\Gamma\setminus R}$ for a range of rotations of the principal directions of orthotropic material behaviour, with a respective comparison to g_1^h and g_2^h obtained by [3] and the corresponding % difference in their values.

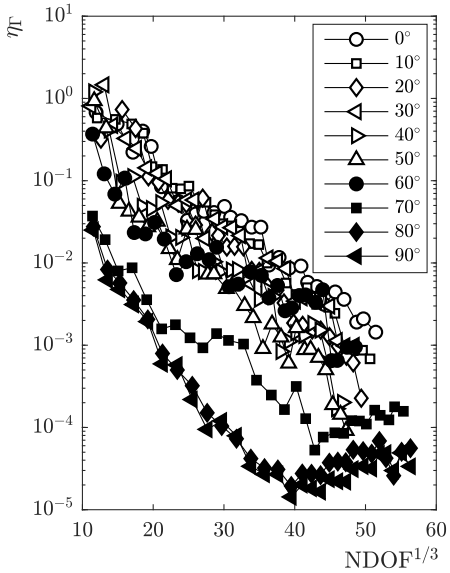

Figure 6.5: Uniaxial tensile crack: convergence of η_Γ with respect to the NDOF$^{1/3}$ for all angles of rotation of the principal directions of the orthotropic material behaviour.

	Error ratio (%)		
θ (°)	$\eta^2 \times 10^{-6}$	$\eta_{\lvert R \rvert}$	η_Γ
0	0.1936	2.3438	0.2129
10	0.1849	1.1719	0.4397
20	0.1936	2.3438	0.5351
30	0.2209	2.3438	0.1225
40	0.1764	2.3438	0.0168
50	0.1681	0.7812	0.0098
60	0.2601	0.0977	0.2580
70	0.0676	0.0977	0.4231
80	0.0784	0.0977	0.2029
90	0.0900	0.0977	0.1341

Table 6.5: Uniaxial tensile crack: ratio between the first and last values of the error estimates η^2, η_Γ and $\eta_{\lvert R \rvert}$ for all angles of orthotropic material behaviour.

excluded region of the CF edge integral. For angles of anisotropic material behaviour in the range $\theta \in [50°, 90°]$ errors less than 0.79% were observed, whilst in the range $\theta \in [0°, 40°]$ the errors were less than 2.5%. For all problems considered the reduction in the length of $|R|$ results in a step in the convergence of $g_2^{h,\Gamma\setminus h}$, this is particularly noticeable for θ values 40°, 50° and 60° of Figures 6.6a and 6.6b. Making the assumption that the initial error by not including any face term is less than 100% of the initial value of $g_2^{h,\Gamma\setminus R}$, the percentage error in not including the face term is bound by above by the values in Table 6.5. This is the case for all values of $g_2^{h,\Gamma\setminus h}$ apart from 10°, where the ratio between the initial to final value is in the order of $\approx 150\%$. However, the percentage difference for $\theta = 10°$ is 220.18%, two orders of magnitude larger than

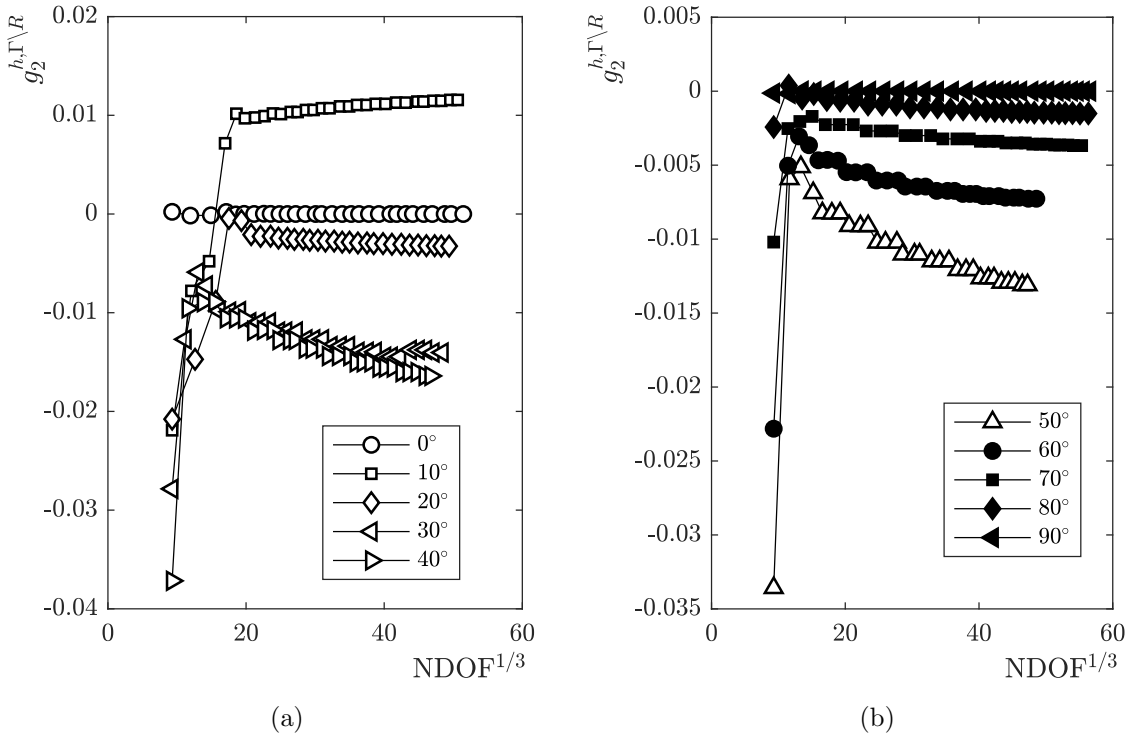

Figure 6.6: Uniaxial tensile crack: $g_2^{h,\Gamma\setminus R}$ for each *hp*-refinement step, plotted against the corresponding NDOF$^{1/3}$ for a range of orthotropic principal directions.

the estimated error of 1.1719%. The errors of $g_2^{h,\Gamma\setminus R}$ in Table 6.4 are significantly larger than the predicted contribution of the error term $\eta_{|R|}$. It is therefore concluded that the error in $\eta_{|R|}$ is not the cause of the large percentage difference in Table 6.4.

The last error term to be considered is η_Γ, with the ratio of between the first and last value given in Table 6.5. The convergence of η_Γ is provided by Figure 6.5. The maximum percentage error obtained for $g_2^{h,\Gamma\setminus R}$ using η_Γ, assuming that the initial error is less than or equal to the entire value of $g_2^{h,\Gamma\setminus R}$, is less than 0.54%. Consistent convergence of η_Γ is also observed for all values, except for angles in the range $\theta \in [70°, 90°]$. For these values of θ, the reduction in R is too fast in respect to added the contribution to η_Γ from the new elements for the final steps of the *hp*-adaptive strategy. Overall, the error values η_Γ are orders of magnitude smaller than the percentage difference between the results obtained here and in [3], it is therefore considered that the error associated with the edge integral of $g_2^{h,\Gamma\setminus h}$ is also not the source of the error.

The last source of error is possibly from the literature itself. This problem was first approached in 1990 by Chu *et al.* [161], however the paper is not clear on the values of $E_{Y,1}$, $E_{Y,2}$, G_{12} and ν_{12} were used. This confusion is brought by about by Chu *et al.* considering two types of *"Glass epoxy"*, but when stating the experimental setup up it is not clear what material was considered. The results from Su *et al.* [3] are compared to [161], and apparent good agreement for all SIFs was achieved. Su *et al.* [3] do state clearly what material they used, however using their proposed material here produced poorer comparative results, even for $g_1^{h,\Gamma\setminus R}$. Further, a comparison of the general trend for the components of $g_i^{h,\Gamma\setminus R}$ with θ was not agreeable. Only

by considering the first set of material properties stated in [161] for a different set of problems, contrary to the material properties stated in [161] for the tensile crack results, is an agreeable trend produced for the tensile crack problem. This problem has also been approached by numerous other authors such as [156, 163, 171] however, fewer θ values were considered, the level of anisotropy was lower as $E_{Y,1}$ was 114.8 Pa and further, disagreement was also observed between the SIFs in this set of literature.

As stated in the numerical setup to this section, δ_1 and δ_2 were reduced substantial from previous values considered in Chapter 5. The result is that for every *hp*-refinement step, *h*-refinement occurred at the crack tip, but also for the first time *h*-refinement occurred along the crack edges. A test case is considered to explain why a reduction in the values of δ_1 and δ_2 is necessary and also, why the length R was chosen to be reduced every third refinement step rather than every second. In order to explain this results it is necessary to define the cumulative error for the crack edge integral,

$$\eta^2_{\Gamma,L} = \sum_{K\in L}\left(\left[\frac{h}{|K|}\right]^{1/2}(\eta^2_K + h\|\nabla_j \Sigma^h_{ij}\|_{0,K})\right), \tag{6.44}$$

where L is a portion of the cracked edges that excludes, a region of the crack edges that contains the crack tip $\partial\Gamma$, see Figure 6.7.

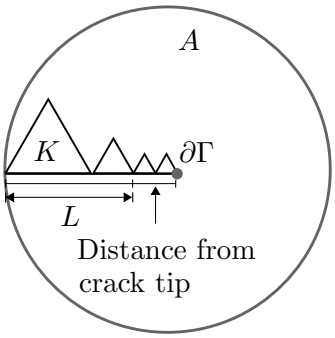

Figure 6.7: A diagram showing how the variables in (6.44) correspond to the geometry and elements of the crack.

Two sets of δ values, with different rates of reducing $|R|$ to zero, are considered. The first set has $\delta_2 = 0.3$, $\delta_1 = 0.07$ with $|R|$ reduced ever second *hp*-refinement step; the associated results are plotting in Figure 6.8a. The second set has $\delta_2 = 0.01$, $\delta_1 = 0.001$ with $|R|$ reducing every third *hp*-refinement step. Each line on Figures 6.8a and 6.8b corresponds to a *hp*-adaptive step. Each point corresponds to a different integrated length L along the crack face, the distance of a point from the crack tip is defined as $|R_L| = |(\Gamma^+ \cup \Gamma) \setminus L|$. For a *hp*-adaptive step, the point which has the smallest distance from the crack tip is η^2_Γ; the value of η_Γ for the crack edge integral for the chosen δ values and rate of reducing $|R| \to 0$. The two simulations performed ran for 35 refinement steps, the latter corresponds to the results presented in Table 6.5.

The green line in Figure 6.8a is the value of η^2_Γ when the values $\delta_2 = 0.3$, $\delta_1 = 0.07$ are used with $|R|$ reduced every second step; the line demonstrates that convergence for this set of refinement parameters is unobtainable. However, Figure 6.8a demonstrates it could be possible

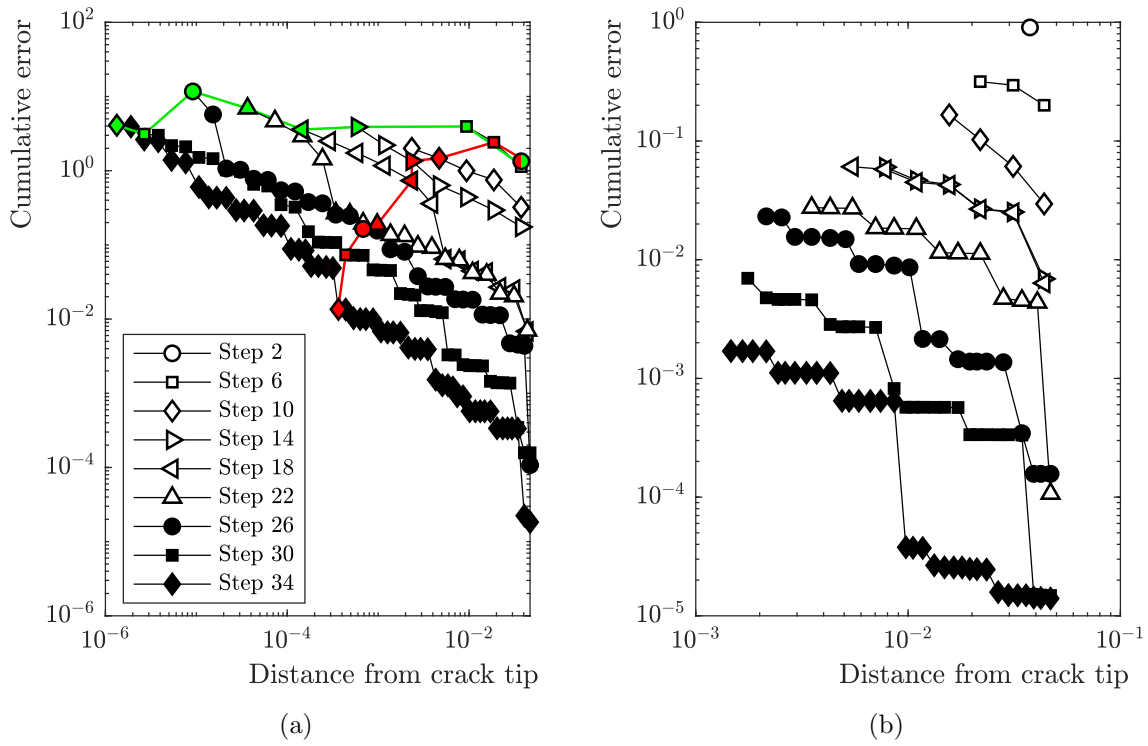

Figure 6.8: Uniaxial tensile crack: estimated cumulative error of the crack edge integral varies for different δ values and rates of reducing $|R|$, for different numbers of hp-refinement steps. (a) considers $\delta_2 = 0.3$, $\delta_1 = 0.07$ with $|R|$ reduced every second refinement step whilst (b) considers $\delta_2 = 0.01$, $\delta_1 = 0.001$ with $|R|$ reduced every third refinement step. The legend for both figures is provided in (a).

to choose a slower rate of reducing $|R| \to 0$ such that η_Γ does tend to zero. This is demonstrated by the red line on Figure 6.8a which presents itself as alternative rate for reducing $|R|$ such that the value η_Γ^2 does decrease for $\delta_2 = 0.3$ and $\delta_1 = 0.07$. Whereas $\delta_2 = 0.01$, $\delta_1 = 0.001$ with $|R|$ reduced every third step will achieve convergence, as shown by Figure 6.8b. It is therefore concluded that the choice of δ_2 and δ_1 is not critical to the convergence of both $\eta_{|R|}$ and η_Γ, but rather the rate at which $|R| \to 0$ is important. Thus if the rate at which $|R|$ went to zero was adaptively controlled, driven by the information provided the error estimate η_Γ, the method would be robust to changes in δ_2 and δ_1.

6.5.3 Shear crack

The second problem considered in this chapter is a single crack in a plate undergoing shear load, as shown in Figure 6.9. The plate is constructed from an orthotropic material with the material properties defined in Table 6.3. The plate has outer dimensions $H = W = 1$ m with the crack having a length $a = 0.5$ m. On the bottom most face a homogeneous Dirichlet BC is applied with a heterogeneous Neumann BC applied on the top surface with a value $g_i^N = [1\ 0]^\top$ Pa. Since the plate is restrained in all directions no average boundary conditions are applied. The initial mesh of the problem is the same as single crack tensile problem, shown in Figure 6.3b with $p_K = 2\ \forall K \in \mathcal{T}$.

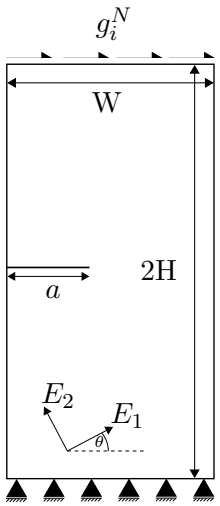

Figure 6.9: Shear crack: plate dimensions, crack position and BCs.

θ (°)	δ_2	δ_1
-90	0.100	0.005
-80	0.100	0.005
-70	0.100	0.005
-60	0.100	0.005
-50	0.100	0.005
-40	0.100	0.005
-30	0.050	0.001
-20	0.050	0.001
-10	0.020	0.001
0	0.010	0.001
10	0.010	0.001
20	0.030	0.001
30	0.050	0.001
40	0.050	0.001
50	0.050	0.001
60	0.100	0.001
70	0.100	0.005
80	0.100	0.005
90	0.100	0.005

Table 6.6: Shear crack: the δ values for each rotation of the orthotropic material behaviour, θ.

This problem faces the same challenges as the tensile crack problem considered in the previous section. However, here a homogeneous Dirichlet BC is also considered. Now both the anisotropic material behaviour and the BCs will contribute to the crack acting in mixed mode fashion. The result is the two components of $g_i^{h,\Gamma\backslash R}$ will be more comparable, specifically the edge integral component of $g_2^{h,\Gamma\backslash R}$ is now effected by the anisotropic material behaviour and the BCs. A series of orthotropic material orientations, θ, is considered in the range $\theta \in [-90°, 90°]$, in divisions of $10°$.

For each value of θ, 35 hp-refinement steps occurred. In order to prevent $|R|$ reducing too quickly and resulting in a non-convergent result for η_Γ the values of δ_2 and δ_1 had to be lowered

Angle (°)	$\frac{\lvert g_1^{h,\Gamma\setminus R} - g_1^h \rvert}{\lvert g_1^{h,\Gamma\setminus R} \rvert} \times 100$	$\frac{\lvert g_2^{h,\Gamma\setminus R} - g_2^h \rvert}{\lvert g_2^{h,\Gamma\setminus R} \rvert} \times 100$
-60	0.14	10.38
-30	0.13	5.58
-20	0.18	0.22
-10	0.77	0.79
0	0.55	0.81
30	0.34	2.81
60	0.46	0.73
90	0.77	0.61

Table 6.7: Shear crack: the % difference between the results obtained here and in [3] for a range of material behaviour.

significantly when compared to the isotropic crack problems presented in Chapter 5, as explained for the tensile crack problem. The δ_2 and δ_1 values for all θ values considered is shown in Table 6.6. However, unlike the tensile crack problem R could be reduced every second refinement step since for all θ values. This was because firstly, the lower δ_2 and δ_1 values caused h-refinement to occur on the crack edges and so $|R|$ reduced at a slower rate than if no-refinement occurred on the edges. Secondly, it was not necessary to reduce $|R|$ every third step, or greater, as the error value η_Γ able to converge with the chosen set of refinement parameters and rate of $|R| \to 0$.

Table 6.7 provides the % differences between the values obtained here and in [3]. Good agreement is achieved between all values, apart from values for $g_2^{h,\Gamma\setminus R}$ for $\theta = -60°$ and $\theta = -30°$. A plot of the change in $g_1^{h,\Gamma\setminus R}$ and $g_2^{h,\Gamma\setminus R}$ with respect to the angle of the principal axis is shown respectively in Figures 6.10a and 6.10b. The ratio in the error estimates η^2, η_Γ and $\eta_{|R|}$ obtained for all rotations is shown in Table 6.8, all error contributions are considered to be less than 1%, part from η_Γ for $\theta \in [70°, 80°]$. In particular for the values of $g_2^{h,\Gamma\setminus R}$ that achieved the largest difference between those obtained in [3], $\theta \in [-60°, -30°]$, all error values are considered to be less than 0.3%. Further, the convergence of $g_1^{h,\Gamma\setminus R}$ and $g_2^{h,\Gamma\setminus R}$ with respect to hp-adaptive steps is consistent, see respectively Figures 6.11a and 6.11b. Figure 6.11b shows that for $\theta \in [-60°, -30°]$ the values are converging towards a smaller negative value and therefore away from the values obtained by [3]. It is therefore suggested, with the support of the error estimate values and the direction of convergence that the results obtained here for $\theta \in [-60°, -30°]$ are more accurate than the results obtained by [3].

Although good agreement is obtained between the results here and those in [3] it is necessary to highlight that the algorithm for reducing $R \to 0$, with hp-refinement may not be robust for materials with a higher level of anisotropic material behaviour. In particular the convergence results for $\theta \in \{-90°, -80°, -70°, 70°, 80°, 90°\}$ for η_Γ, shown in Figures 6.12a and 6.12b, potentially highlights this issue. For all other values of θ the final value of $g_2^{h,\Gamma\setminus R}$ was obtained at the 35^{th} refinement step. However, for $\theta \in \{-90°, -80°, -70°\}$ $g_2^{h,\Gamma\setminus R}$ was considered at the 24^{th} refinement step and for the values $\theta \in \{70°, 80°, 90°\}$ and $g_2^{h,\Gamma\setminus R}$ was obtained at the 30^{th} refinement step. For clarity the hp-step at which the values for $g_2^{h,\Gamma\setminus R}$ is quoted are highlighted by a red marker in 6.12a and 6.12b. After the respective hp-adaptive steps the value η_Γ starts to

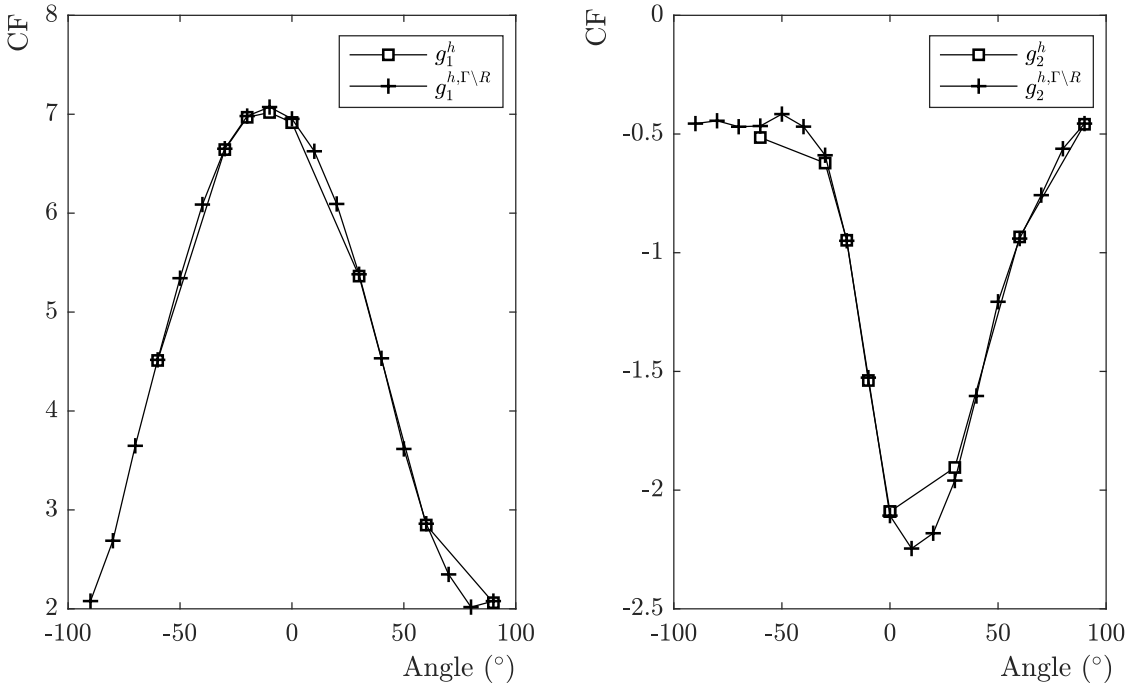

Figure 6.10: Shear crack: (a) and (b) respectively show the values of $g_1^{h,\Gamma\setminus R}$ and $g_2^{h,\Gamma\setminus R}$ for a range in the angles of the principal orthotropic material behaviour. Where possible, (a) and (b) also contain the values of $g_1^{h,\Gamma\setminus R}$ and $g_2^{h,\Gamma\setminus R}$ obtained by [3].

increase. The error added by including new elements edges to the calculation of $g_2^{h,\Gamma\setminus R}$ was substantial with respect to the reduction in the error along the crack face. Even with *hp*-refinement the reduction in the along the crack face was insufficient compared to the added error contribution from the new elements. The value of $g_2^{h,\Gamma\setminus R}$ that corresponds to the lowest value of η_Γ was chosen. For $\theta \in \{-90°, -80°, -70°, 70°, 80°, 90°\}$ the dominant error was η_Γ. If $|R|$ was reduced more, η_Γ would increase further making it likely that the error in the value of $g_2^{\Gamma\setminus R}$ would also increase. The word *likely* is used as it is unknown how the size of these error estimates correspond to the actual error in $g_2^{h,\Gamma\setminus R}$, the error estimates only give an indication of how the error is converging. Therefore, if η_Γ is increasing whilst $\eta_{|R|}$ is decreasing the convergence of $g_2^{\Gamma\setminus R}$ is either slowing down or diverging from the true solution. Hence, the safest option is to choose the last value of $g_2^{\Gamma\setminus R}$ when all error estimates are converging. The remaining convergence of η_Γ for all other values of θ with *hp*-refinement are shown in respectively in Figures 6.13a, 6.13c and 6.13b, in which consistent convergence was obtained.

θ (°)	$g_1^{h,\Gamma\setminus R}$	g_1^h	$g_2^{h,\Gamma\setminus R}$	g_2^h	η^2 (%)	η_Γ (%)	$\eta_{\lvert R\rvert}$ (%)
-90 *	2.0782	n/a	-0.4561	n/a	1.0236×10^{-6}	4.2960×10^{-1}	1.5259×10^{-3}
-80 *	2.6886	n/a	-0.4442	n/a	9.2408×10^{-7}	6.5249×10^{-1}	1.5259×10^{-3}
-70 *	3.6482	n/a	-0.4692	n/a	7.7864×10^{-7}	9.4067×10^{-1}	1.5259×10^{-3}
-60	4.5170	4.5109	-0.4664	-0.5148	1.3760×10^{-8}	2.9194×10^{-1}	4.8828×10^{-2}
-50	5.3426	n/a	-0.4160	n/a	1.2615×10^{-8}	3.3523×10^{-2}	1.9531×10^{-1}
-40	6.0871	n/a	-0.4689	n/a	1.4337×10^{-8}	9.0310×10^{-2}	3.9063×10^{-1}
-30	6.6514	6.6427	-0.5894	-0.6223	1.0954×10^{-8}	2.2343×10^{-1}	3.9063×10^{-1}
-20	6.9816	6.9692	-0.9497	-0.9476	1.0462×10^{-8}	1.8086×10^{0}	2.9297×10^{-1}
-10	7.0726	7.0180	-1.5262	-1.5382	9.6442×10^{-9}	6.2362×10^{-1}	2.9297×10^{-1}
0	6.9533	6.9152	-2.1074	-2.0904	1.0650×10^{-8}	2.0611×10^{-1}	2.9297×10^{-1}
10	6.6256	n/a	-2.2460	n/a	1.1168×10^{-8}	5.3616×10^{-1}	3.9063×10^{-1}
20	6.0931	n/a	-2.1816	n/a	1.1171×10^{-8}	5.7683×10^{-1}	2.9297×10^{-1}
30	5.3821	5.3637	-1.9597	-1.9047	1.3506×10^{-8}	5.0583×10^{-1}	2.9297×10^{-1}
40	4.5326	n/a	-1.6035	n/a	1.0798×10^{-8}	9.3272×10^{-2}	3.9063×10^{-1}
50	3.6163	n/a	-1.2066	n/a	7.9531×10^{-9}	6.0048×10^{-2}	3.9063×10^{-1}
60	2.8603	2.8470	-0.9404	-0.9335	4.2842×10^{-9}	5.5248×10^{-1}	4.8828×10^{-2}
70 †	2.3479	n/a	-0.7575	n/a	3.0215×10^{-7}	1.2436×10^{0}	1.5259×10^{-3}
80 †	2.0176	n/a	-0.5620	n/a	2.7596×10^{-7}	1.5521×10^{0}	1.5259×10^{-3}
90 †	2.0782	2.0621	-0.4561	-0.4589	2.8329×10^{-7}	7.3830×10^{-1}	1.5259×10^{-3}

* corresponds to the variables for the angle taken at the 26^{th} refinement step and †corresponds to variables for the angle taken at the 30^{th} refinement step. All other variables correspond to the 35^{th} refinement step.

Table 6.8: Shear crack: the final values of $g_1^{h,\Gamma\setminus R}$ and $g_2^{h,\Gamma\setminus R}$ for rotations of the anisotropic material behaviour in the range $\theta \in [-90°, 90°]$ with the corresponding values of g_1^h and g_2^h obtained by [3].

6.5.4 Double ended inclined crack with rotating anisotropy

The problem considered in this section is an inclined double ended crack centred in a plate acting in plane stress. The schematic of the plate and crack dimensions with the loading conditions are shown in Figure 6.14a. The plate has dimensions $H = 2$ m, $W = 1$ m, $a = 0.2$ m such that domain is defined as $(x, y) \in \Omega = (0, 2) \times (0, 4)$ m with homogeneous Neumann BCs on $x = 0$ m and $x = 2$ m, and heterogeneous Neumann BCs on $y = 0$ m and $y = 4$ m. The inclined crack is found at the centre of the plate and is angled at 45°. The heterogeneous Neumann BC applied to the boundary is $g_i^N = [0, 1]^\top$ Pa on the edge, $y = 4$, m and $g_i^N = [0, -1]^\top$ Pa on the edge, $y = 0$ m. Since no Dirichlet BCs exist, the average displacement and rotation BCs are applied, (2.52), (2.53) and (2.54) respectively. The material considered is orthotropic and acts in plane stress, the principal material properties are $E_1 = 48.26$ Pa, $E_2 = 17.24$ Pa, $G_{12} = 6.89$ Pa and $\nu = 0.29$.

This problem is chosen to validate the computation of $g_i^{h,\Gamma\setminus R}$ at a crack tip for anisotropic materials since it has been approached by numerous authors, such as those found in the non-exhaustive list [3, 156, 157, 161] and the references therein. As well as having multiple sources to validate results, the problem itself is interesting as the results consider a mixed mode doubled ended crack in an orthotropic material where the orientation of the material's principal axes are rotated by an angle θ, see Figure 6.14a. The problem can therefore also be used to validate the efficacy of calculating $g_i^{h,\Gamma\setminus R}$ for a range of anisotropic material behaviour for a multiple crack

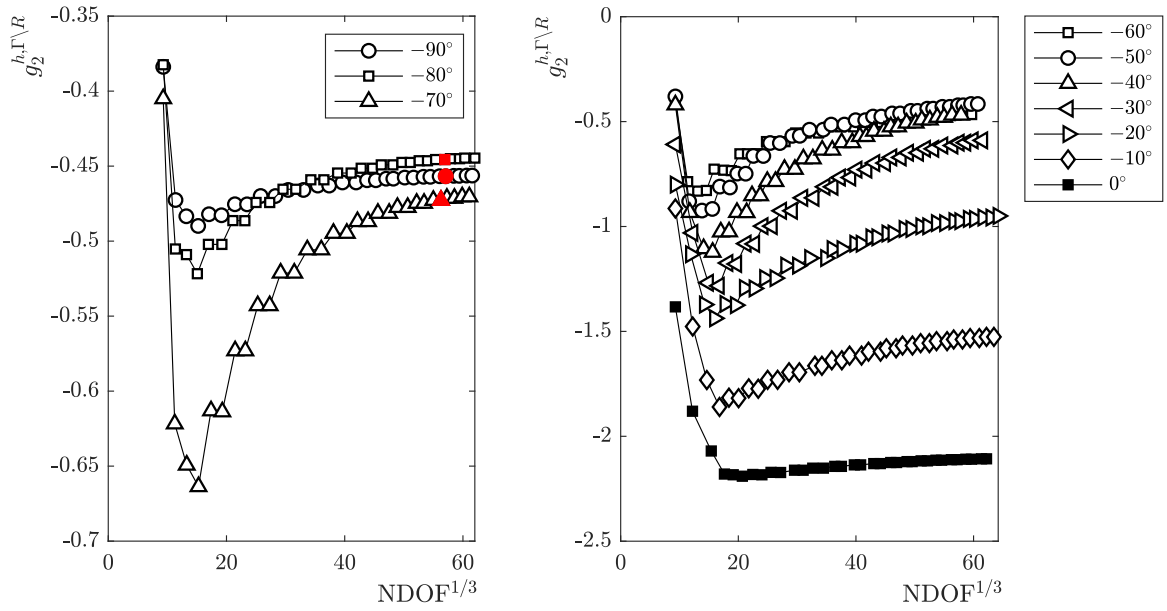

Figure 6.11: Shear crack: $g_2^{h,\Gamma\setminus R}$ against NDOF$^{1/3}$ for each *hp*-adaptive step for angles in the set $\theta \in \{-90, -80, -70\}$ shown in (a), with the red marker corresponding to the * values in Table 6.8. Convergence of η_Γ in the for angles in the range $\theta \in [-60, 0]$ shown in (b).

problem. Further, the effect of the range of the anisotropic behaviour on η^2 and η_Γ and be investigated, if the errors have reduced significantly a new benchmark crack tip CF values for this problem can be set. The current crack tip CF benchmark for this problem was obtained in [7]. The authors use an enriched BEM formulation to determine the SIF directly, it is one of the most recent papers to consider this problem.

For all orientations of anisotropy the initial mesh for this problem is shown in Figure 6.14b with $p_K = 2\ \forall K \in \mathcal{T}$. The initial mesh undergoes 30 *hp*-adaptive steps with, $\delta_2 = 0.3$ and $\delta_1 = 0.07$. For each refinement step the value of $g_i^{h,\Gamma\setminus R}$, η^2, η_Γ and $\eta_{|R|}$ are recorded. The rotation of anisotropy considered $\theta \in \{0°, 20°, 45°, 60°, 90°, 105°, 120°, 135°\}$ and the values of $g_i^{h,\Gamma\setminus R}$ are compared, where available, to the CF values obtained using the SIFs in [7]. The convergence of $|g_i^{h,\Gamma\setminus R}|$ for each θ value is plotted against the NDOF$^{1/3}$ in Figure 6.15. As an example the final mesh element and element polynomial order distribution for $\theta = 0°$ is shown in Figure 6.14c. Similar to the isotropic convergence results for $|g_i^{h,\Gamma\setminus R}|$ found in Chapter 5, a jump in the value of $|g_i^{h,\Gamma\setminus R}|$ is observed each time the length of the region R is reduced. For all 7 orientations of anisotropic material behaviour Figure 6.15 demonstrates convergence of $|g_i^{h,\Gamma\setminus R}|$, this is supported with excellent agreement for both components of the CF in comparison to the results generated [7], see Table 6.9. Additionally all three error estimates achieved good convergence results. First, the error corresponding to the decrease in the length of the region R $\eta_{|R|}$ (5.35), decreased by a factor of 3.1×10^{-5} for all angles of anisotropy as the region was decreased every other *hp*-adaptive step. Second, for all cases considered η^2 decreased by a factor of the order 10^{-10}, see Table 6.9 for the precise values for each anisotropic value. The value

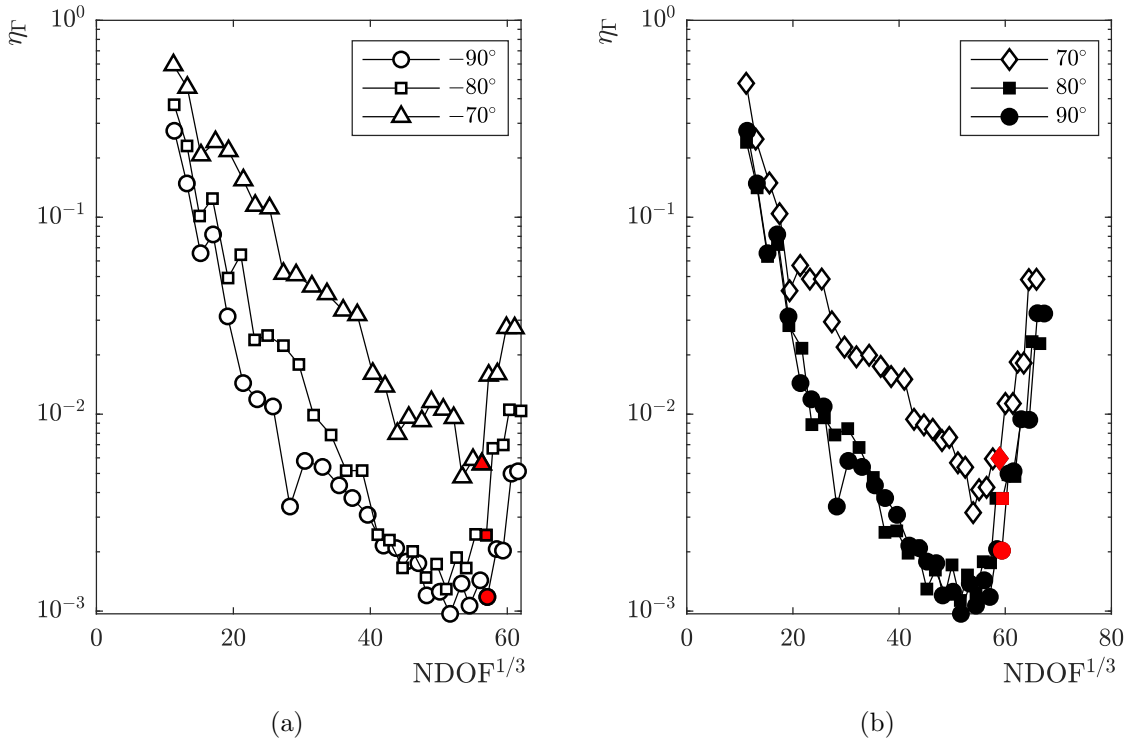

Figure 6.12: Shear crack: convergence of η_Γ against NDOF$^{1/3}$ for each *hp*-adaptive step for angles in the set $\theta \in \{-90, -80, -70\}$ shown in (a). Convergence of η_Γ for angles in the set $\theta \in \{70, 80, 90\}$ are shown in (b). The red marker corresponding to the †and * values in Table 6.8.

of η_Γ achieved consistently the poorest convergence for each value of θ, however as shown in Figures 6.16a and 6.16b the convergence is consistently exponential. The change in η_Γ for each angle of anisotropy is also shown in Table 6.9.

		Angle (θ)							
		0°	20°	45°	60°	90°	105°	120°	135°
$g_1^{h,\Gamma\setminus R}$	($\times 10^{-2}$)	1.8072	1.7390	1.4642	1.2674	1.0630	1.1062	1.2382	1.4224
g_1^h	($\times 10^{-2}$)	1.8012	n/a	1.4166	n/a	1.0582	1.1085	1.2716	1.4973
$g_2^{h,\Gamma\setminus R}$	($\times 10^{-2}$)	-1.418	-1.455	-1.108	-9.637	-1.199	-1.469	-1.784	-1.767
g_2^h	($\times 10^{-2}$)	-1.4117	n/a	-1.0628	n/a	-1.1950	-1.4749	-1.8309	-1.8552
ratio η^2	($\times 10^{-10}$)	3.90	3.23	4.46	6.10	4.32	5.66	4.38	3.15
ratio η_Γ	($\times 10^{-3}$)	5.81	3.13	2.09	2.24	4.34	7.90	13.4	14.2
$\lvert g_1^h - g_1^{h,\Gamma\setminus R}\rvert / \lvert g_1^h\rvert$		0.33%	n/a	3.4%	n/a	0.45%	0.20%	2.6%	5.0%
$\lvert g_2^h - g_2^{h,\Gamma\setminus R}\rvert / \lvert g_2^h\rvert$		0.44%	n/a	4.3%	n/a	0.33%	0.28%	2.6%	4.8%

Table 6.9: A double ended inclined crack centred in a plate: $g_i^{h,\Gamma\setminus R}$, and g_i^h from [7], for a range of θ values. The ratio in error estimates, η^2 and η_Γ, between the first and last refinement steps for each value of θ are also presented alongside the percentage difference in the CF components obtained here and in [7].

Table 6.9 shows that for values of θ, the percentage difference between the results obtained here and from [7] are of the same order of magnitude for both components of the CF. For the

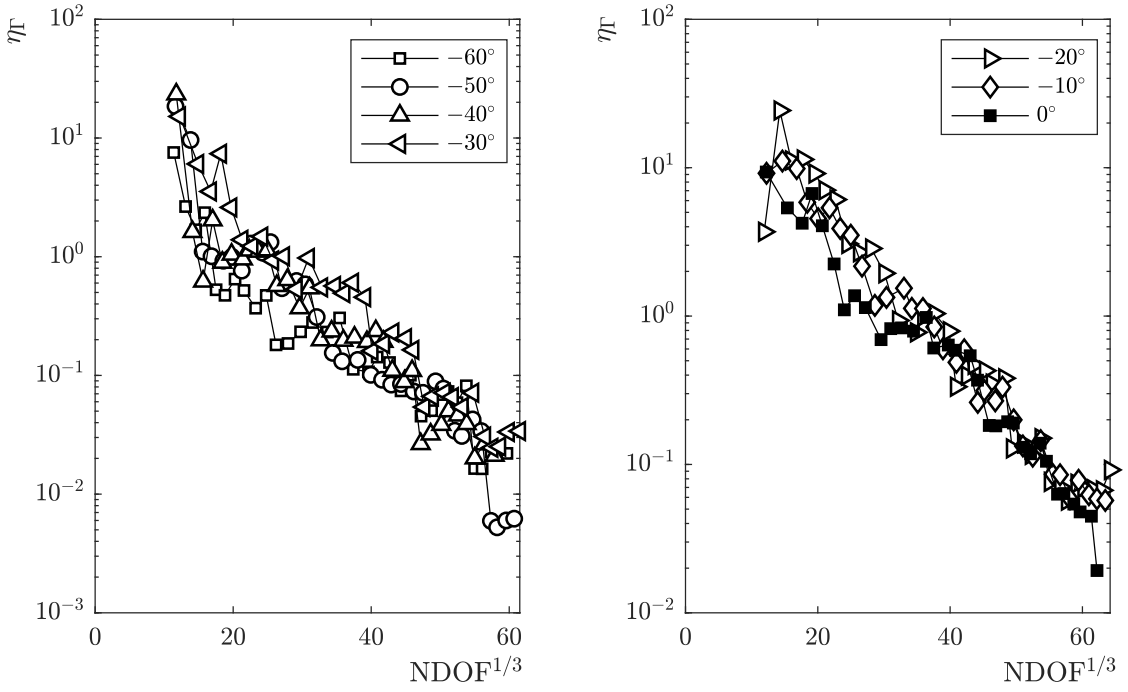

Figure 6.13: Shear crack: convergence of η_Γ against NDOF$^{1/3}$ for each hp-adaptive step for angles in the sets $\theta \in \{-60, -50, -40, -30\}$ in (a), $\theta \in \{-20, -10, 0\}$ in (b) and for angles in the range $\theta \in [10, 60]$ shown in (c).

range of θ values considered, neither component of the CF has a consistently higher or lower percentage difference. The error associated with the first component of $g_i^{h,\Gamma\setminus R}$ decreases by a

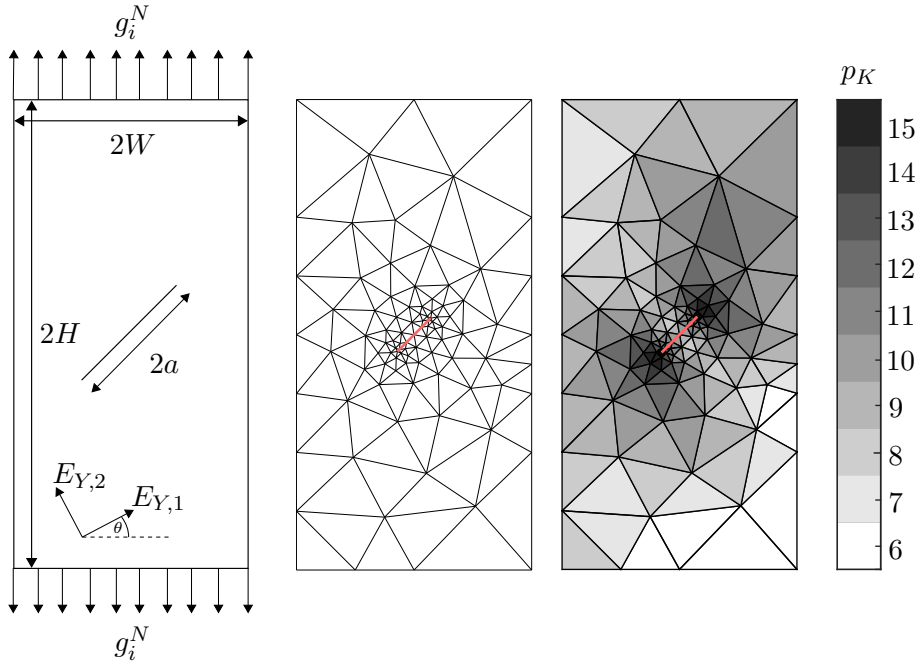

Figure 6.14: A double ended inclined crack centred in a plate: (a) the geometry and boundary conditions of the problem (b) the initial mesh with $p_K = 2\ \forall K \in \mathcal{T}$ and (c) the final mesh after 30 *hp*-refinement steps with $\theta = 0°$.

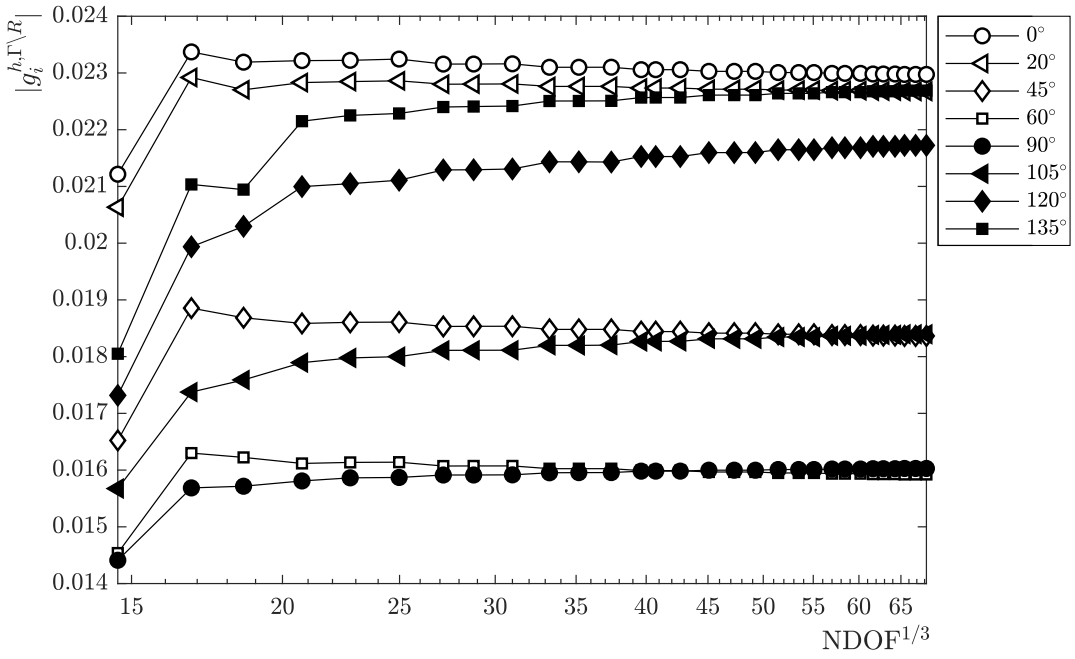

Figure 6.15: A double ended inclined crack centred in a plate: $|g_i^{h,\Gamma\backslash R}|$ with respect to NDOF$^{1/3}$ for a range of anisotropic material orientations.

ratio of approximately 10^{-10} times for all anisotropic material orientations. Figure 6.15 shows that $|g_i^{h,\Gamma\backslash R}|$ does not change by an order of magnitude. It is therefore concluded that the initial

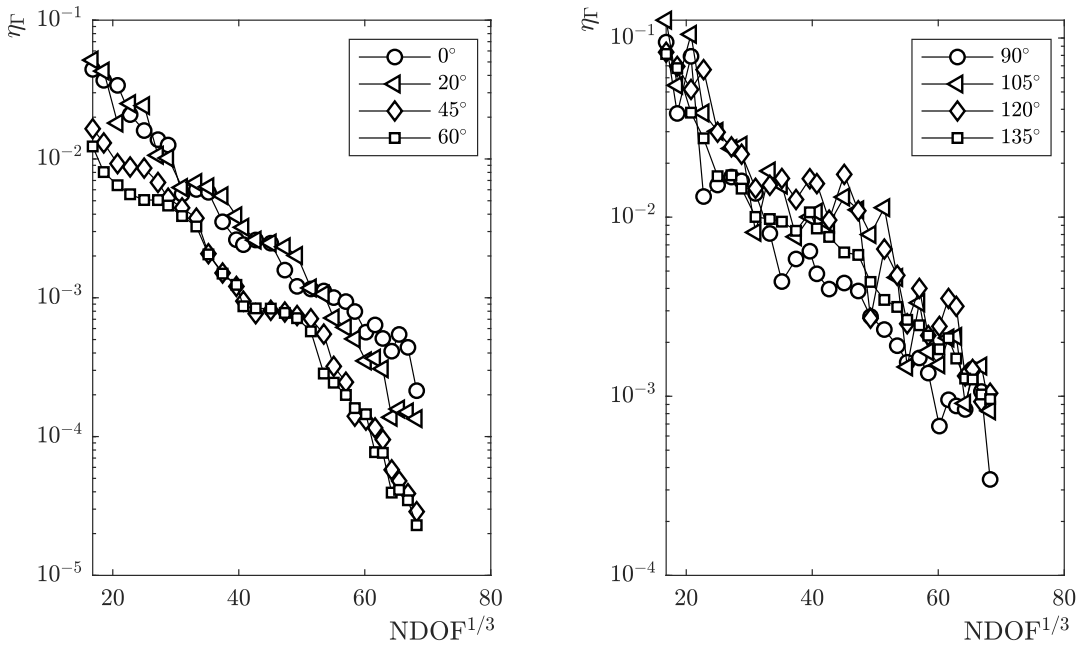

Figure 6.16: A double ended inclined crack centred in a plate: convergence of the error estimate η_Γ, which corresponds to the edge integral component of $g_i^{h,\Gamma\backslash R}$ for θ values $[0, 20, 45, 60]$ in (a) and $[90, 105, 120, 135]$ values in (b).

error is less than 100% of the total value, hence the maximum percentage error associated with the first component is approximately less than 10^{-8}%. Additionally, the percentage error of the second component of the CF can also be stated. For the range of anisotropic orientations considered, inspecting Table 6.9 shows the percentage error to be less than a minimum of 0.209% and maximum of 1.42% for $g_2^{h,\Gamma\backslash R}$. The estimated error associated with the first component of the CF is significantly smaller than the percentage difference for the first component of the CF. This would suggest that results achieved here are more accurate than those in [7]. The estimated error for the second component of the CF is of a similar magnitude to the associated percentage difference. However, since the percentage difference is of a similar magnitude for both components of the CF it is suggested that the actual error of the second component of the CF is smaller than the estimated error. Therefore, since the actual error is considered smaller than the estimated error, the results obtained for the second component of the CF are also considered to be more accurate than those obtained by [7].

6.6 Anisotropic split crack

The last problem to be considered in this chapter is the split crack problem visited in Chapter 5. The geometry of the problem is described with Figure 6.17a with the initial mesh shown in Figure 6.17b with $H = 16$ m, $W = 20$ m, $\theta = 45°$ and $a = b = 1$ m, and with three cracks labelled A, B and C. A Neumann BC is applied on the top and bottom edge with the respective values $g_i^N = [0\ 1]^\top$ Pa and $g_i^N = [0\ -1]^\top$ Pa. The compliance matrix this problem is, in terms

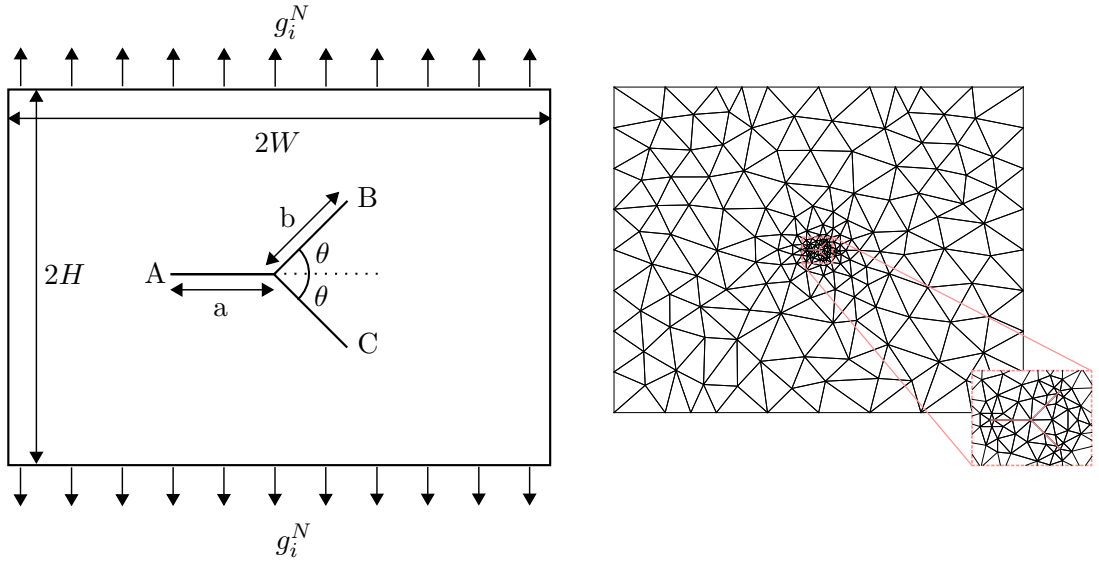

Figure 6.17: Split crack: (a) the geometry and loading conditions and initial mesh (b).

of the local coordinate system, is

$$[C'_{ijkl}] = \begin{bmatrix} 1/E_{Y,1} & -\nu_{12}/E_{Y,1} & \text{-}1/40 \\ -\nu_{12}/E_{Y,1} & 1/E_{Y,2} & \text{-}1/20 \\ \text{-}1/40 & \text{-}1/20 & 1/G_{12}. \end{bmatrix} \tag{6.45}$$

with $E_{Y,1} = 44.8$ Pa, $E_{Y,2} = 11.7$ Pa, $G_{12} = 9.66$ Pa and $\nu_{12} = 0.21$. The principal directions of the material properties, 1 and 2, parallel with the x and y axes respectively, Figure 6.17a. Four rotations of anisotropic material behaviour are considered $C \in \{-90°, -45°, 0°, 45°\}$. The initial

	Angle θ			
	$-90°$	$-45°$	$0°$	$45°$
Crack A	3	2	2	3
Crack B	3	3	2	3
Crack C	2	2	3	3

Table 6.10: Split crack: the number of *hp*-refinement steps that occur between each reduction in the length of R.

mesh is shown in Figure 6.17b with $p_K = 3 \forall K \in \mathcal{T}$. 35 *hp*-refinement steps were performed with the adaptive parameters having the values $\delta_2 = 0.02$ and $\delta_1 = 0.001$. The last parameter to be chosen is how $|R|$ is reduced to 0, for this problem the length of R was reduced either every second or third *hp*-refinement step. The rate R was reduced was dependent on the crack and the orientation of the anisotropic material properties, see Table 6.10. The split crack problem was initially run with $|R|$ reducing every third refinement step, then if possible the rate at which $|R|$ decreased was raised to every second step if convergence was maintained for all error estimate values. As no Dirichlet BCs are applied all three average boundary conditions are applied, (2.52), (2.53) and (2.54).

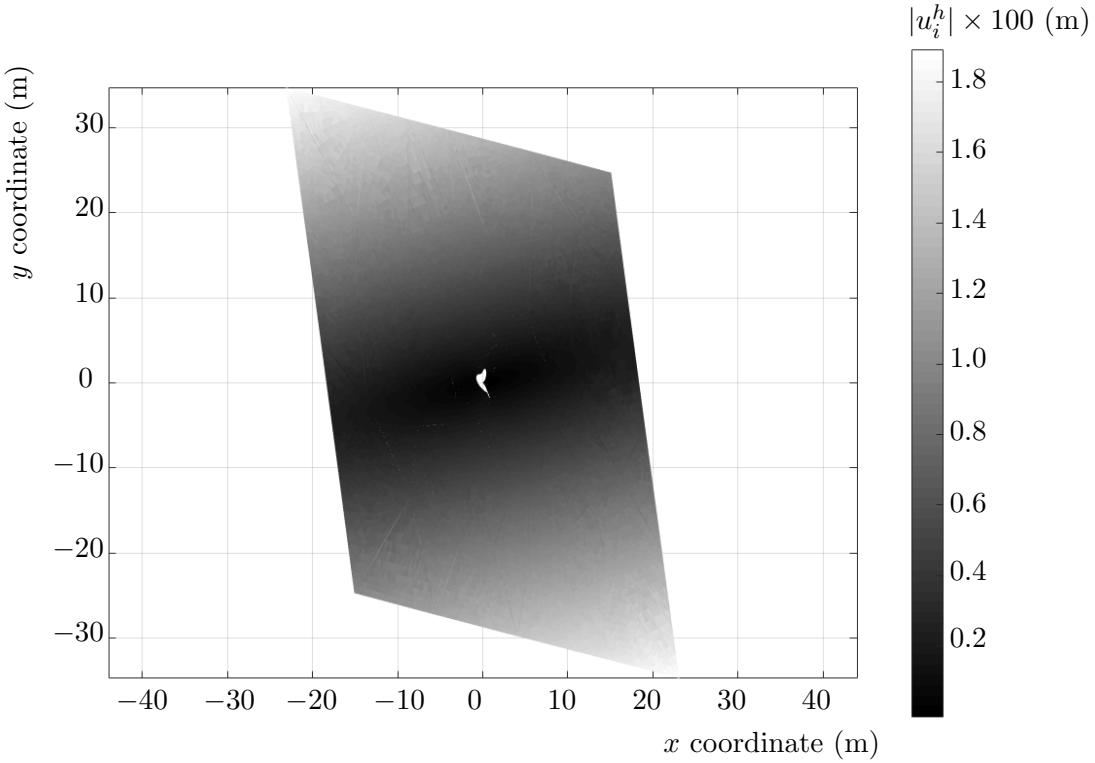

Figure 6.18: Split crack: the displaced shape, scaled by a factor of 100, with a greyscale colour plot overlaid showing the displacement magnitude for $C = 0°$.

The first observation for this problem is the displacement plot for $C = 0°$ shown in Figure 6.18 for the most refined mesh. As only a uniaxial tensile load is applied to the specimen it is unusual, especially given the symmetry of the problem, that a shear like deformation is observed. However the compliance matrix for this material, (6.45), couples normal, and shear, stresses and strains. This coupling exist because of the terms existing in positions $(1,3)$, $(2,3)$, $(3,1)$ and $(3,2)$ of the compliance matrix (6.45). All cracks for all values of C are mixed mode, this observed by the opening and shear action occurring for all cracks in Figure 6.18 and in Table 6.11 it is observed for all three cracks and all values of C that $g_1^{h,\Gamma\backslash R}$ and $g_2^{h,\Gamma\backslash R}$ are of similar orders of magnitude. For crack A the mixed mode behaviour is caused by the anisotropic material behaviour, whereas for cracks B and C the orientation of the cracks and material causes the cracks to act in mixed mode. Further, since the anisotropic material induces shear strains from an applied plane stress, the problem is no longer symmetric. The result is that the same value of $g_1^{h,\Gamma\backslash R}$ is not observed for cracks B and C, and $g_2^{h,\Gamma\backslash R}$ is no longer opposite and equal, as in the isotropic case.

The results for $g_i^{h,\Gamma\backslash R}$, and the corresponding error measures, for all three cracks and C values are shown in Table 6.11. For all cracks and C values a good convergence of all error estimate components is achieved; all error estimate ratios are of less the 1% except for η_Γ for crack B when $C = 45°$ which has a value of 3%. Similar to the Tension crack and the Shear crack problems, by lowering the δ values and the reducing the rate at which $|R| \to 0$ ensured that both η_Γ and

	Angle C	$-90°$	$-45°$	$0°$	$45°$
	ratio η^2 %	8.2563×10^{-9}	5.0387×10^{-9}	8.9763×10^{-9}	3.7814×10^{-9}
Crack A	$g_1^{h,\Gamma\setminus R}$	7.8974×10^{-2}	1.7505×10^{-1}	1.5932×10^{-1}	6.2220×10^{-2}
	$g_2^{h,\Gamma\setminus R}$	-1.8999×10^{-2}	-6.8559×10^{-2}	7.1562×10^{-2}	1.1542×10^{-2}
	ratio η_Γ %	6.1921×10^{-1}	8.1749×10^{-2}	2.5368×10^{-2}	5.6245×10^{-1}
	ratio $\eta_{\lvert R\rvert}$ %	4.8828×10^{-2}	5.8594×10^{-1}	7.8125×10^{-1}	2.4414×10^{-2}
Crack B	$g_1^{h,\Gamma\setminus R}$	3.4558×10^{-2}	8.4144×10^{-2}	6.5172×10^{-2}	2.3059×10^{-2}
	$g_2^{h,\Gamma\setminus R}$	-2.8257×10^{-2}	-2.0276×10^{-2}	-4.3919×10^{-2}	-2.7811×10^{-2}
	ratio η_Γ %	2.6853×10^{-1}	1.1127×10^{0}	1.7446×10^{-1}	3.0483×10^{0}
	ratio $\eta_{\lvert R\rvert}$ %	4.8797×10^{-2}	2.4383×10^{-2}	1.4645×10^{-1}	2.4383×10^{-2}
Crack C	$g_1^{h,\Gamma\setminus R}$	2.9915×10^{-2}	7.6700×10^{-2}	7.6745×10^{-2}	2.7452×10^{-2}
	$g_2^{h,\Gamma\setminus R}$	3.9210×10^{-2}	4.0636×10^{-2}	1.5644×10^{-2}	2.5314×10^{-2}
	ratio η_Γ %	6.5498×10^{-1}	1.6337×10^{-2}	2.0347×10^{-1}	8.7104×10^{-1}
	ratio $\eta_{\lvert R\rvert}$ %	9.7625×10^{-2}	9.7625×10^{-2}	4.8797×10^{-2}	2.4383×10^{-2}

Table 6.11: Split crack: $g_i^{h,\Gamma\setminus R}$ for a range of C values. The ratio in error estimates, η^2, η_Γ and $\eta_{|R|}$ for each crack and value of C is also shown.

$\eta_{|R|}$ converged consistently. Consistent convergence of η_Γ is demonstrated for cracks A, B and C in Figures 6.19a, 6.19b and 6.19c respectively. The convergence of $g_2^{h,\Gamma\setminus R}$ is also observed

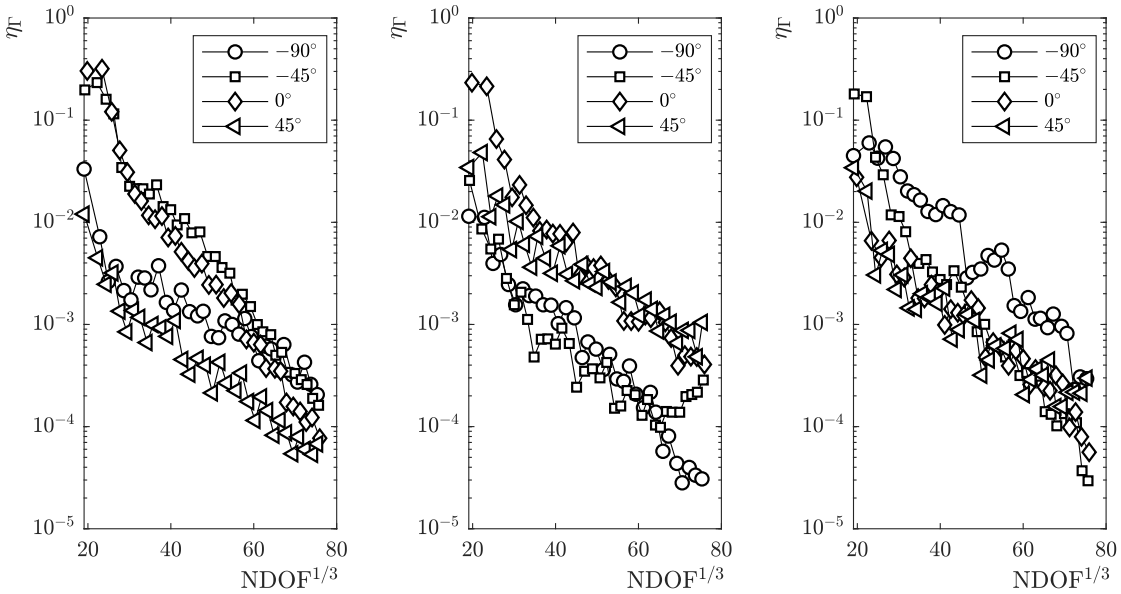

Figure 6.19: Split crack: convergence of $\eta_{|R|}$ against the NDOF$^{1/3}$ for cracks A, B and C, for all values of C, shown respectively in (a), (b) and (c).

for cracks A, B and C in Figures 6.20a, 6.20b and 6.20c respectively. Several observations can be drawn from this problem for the algorithm that calculates of $g_i^{h,\Gamma\setminus R}$. Firstly, it is robust to fully anisotropic problems, with all associated error estimate values displaying convergence. Secondly this problem is considered more complex that the previous problems presented in this chapter since it contains three cracks. The problem supports the claim of the other problems. Convergence is achieved here by lower the values of δ and reducing the rate at which R tends to

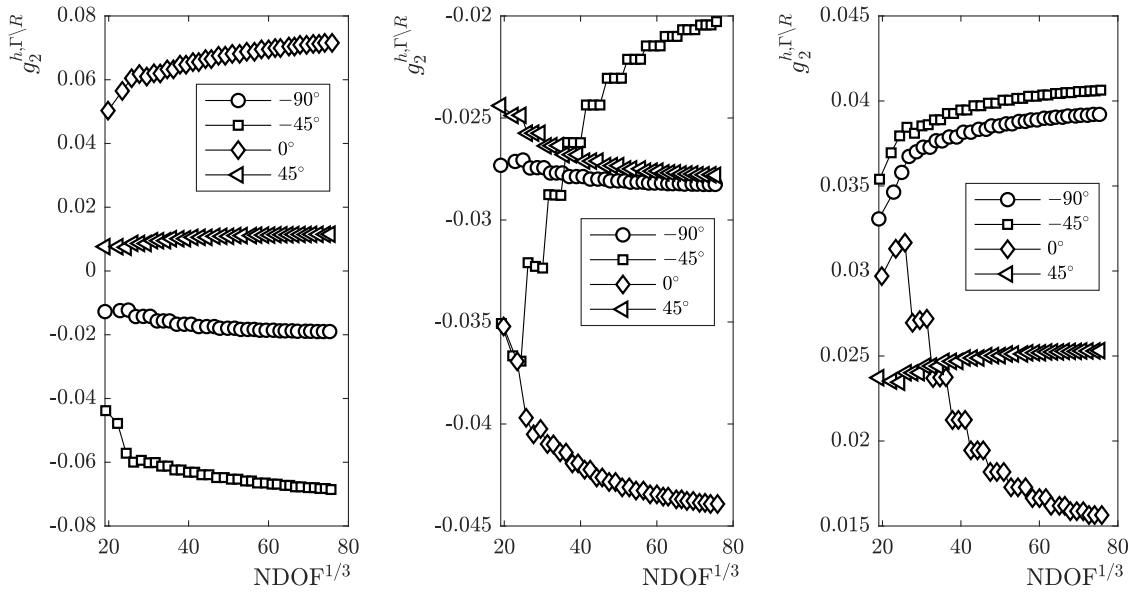

Figure 6.20: Split crack: convergence of $g_2^{h,\Gamma\setminus R}$ against the NDOF$^{1/3}$ for cracks A, B and C, for all values of C, shown respectively in (a), (b) and (c).

zero however, an algorithm which could choose the rate at which $R \to 0$ dependent on the error estimate values, η_Γ and $\eta_{|R|}$, would be more robust to the values of δ. Ultimately, an automated algorithm could achieve faster convergence for a set of δ values than define beforehand the rate at which $|R| \to 0$.

6.7 Observations

The first objective to this chapter was deriving a robust penalty term for the *hp*-SIPG method when modelling anisotropic materials. It was first necessary to consider proofs from elliptic scalar diffusion problems where the diffusion coefficient matrix was anisotropic and isotropic. Using techniques from the literature a robust penalty parameter, κ_F, for a face F was derived. By considering a smooth problem with an analytical solution the penalty parameter was shown numerically to be robust to high levels of anisotropic material behaviour for the error in the SIPG norm and the residual based *a posteriori* error estimate η. It was therefore concluded that if there were issues with convergence with with either error this was therefore more likely due to the shape of the domain considered and the applied boundary conditions, and not the *hp*-SIPG formulation.

Four mixed mode problems were considered in this chapter: a single crack tensile crack, a single crack shear, a double ended crack and lastly a split crack problem. A range in the level, orientation and type of anisotropic behaviour was considered to fully explore how robust the technique $g_i^{h,\Gamma\setminus R}$ was to calculate the crack tip CF. The efficacy of $g_i^{h,\Gamma\setminus R}$ for these problems was measured by comparing the most accurate value obtained against the CFs obtained in literature. Further the convergence of the error estimators for the components of $g_i^{h,\Gamma\setminus R}$ was

used to validate the technique for anisotropic materials. Having error estimates for $g_i^{h,\Gamma\setminus R}$ was particularly useful for the anisotropic problems. Firstly, it enabled the *hp*-adaptive parameters δ_2 and δ_1, and the rate at which $|R| \to 0$, to be tuned to maximum the convergence of the error estimates η_Γ and $\eta_{|R|}$. Secondly, the error estimates were used to support the accuracy of $g_i^{h,\Gamma\setminus R}$. This particularly useful for the tensile crack problem where significant difference in the value of $g_2^{h,\Gamma\setminus R}$ and equivalent values in the literature were obtained. Without the error estimates it would not be possible to justify that the values obtained here are accurate, and that discrepancies are arising from confusion in the literature. The error estimates converged for all cracks of all problems exponentially, this demonstrated that with *hp*-refinement $g_i^{h,\Gamma\setminus R}$ was converging to the correct value. However, as the choice of how $|R|$ reduced was predefined rather than adapting to the values of the estimates, towards the final set of refinement steps for some problems it was observed that it was possible for the error estimates to increase.

In general, very good agreement was obtained between the results here and those in the literature. However, investigating anisotropic materials also presented ways in which the algorithm for determining $g_i^{h,\Gamma\setminus R}$ could be improved. This was discussed thoroughly for the tensile crack problem where it was concluded that a more robust method to obtaining an accurate value of $g_i^{h,\Gamma\setminus R}$, with respect to the refinement parameters δ_2 and δ_1, could be obtained by using the error estimates $\eta_{|R|}$ and η_Γ to control how $|R|$ is reduced with *hp*-adaptivity. However, it must also be noted that these conclusions were only possible due to the error estimates $\eta_{|R|}$ and η_Γ.

Chapter 7

Crack propagation

7.1 Introduction

This chapter is tasked with developing efficient and accurate algorithms for propagating a crack in two dimensions using the configurational force (CF). The chapter two algorithms. The first algorithm is denoted the *rp*-adaptive method and is considered a cheaper and less accurate method to determine the crack path using the domain and tip CF calculation, $\{g^{h,t}\}$ and $\{g^{h,D}\}$ respectively. The second method is the *hpr*-adaptive method which uses the method proposed in this thesis to propagate the crack, $\{g^{h,\Gamma\setminus R}\}$. The *hpr*-adaptive method is more expensive than the *rp*-adaptive method, due to *hp*-adaptivity occurring between each propagation step, but, it will be shown in this chapter to be orders of magnitude more precise for a given crack propagation length.

The work of Eshelby [17, 172] is fundamental to describing how a crack will propagate in a continuous domain using a CF. The local variational formulations in [77, 79, 80, 173–176] use a CF acting at a crack tip to describe the propagation of a crack. Using the CF to describe a moving fracture front was initially attempted by Mueller and Maugin [83] within the conventional finite-element context and Larsson and Fagerström [84, 85] in XFEM, with an optimally convergent DG-XFEM achieved by [86]. Later a robust *r*-adaptive technique was defined by Miehe and co workers [1, 4, 89] for propagating cracks which was also taken to three dimensions by [90]. Furthermore, the framework has recently been applied to materials with non-linear behaviour, see for example the works of Runesson *et al.* [91] and Tillberg and Larsson [92] on elasto-plasticity and Näser *et al.* [93, 94] on time-dependent materials and the review by Özenç *et al.* [95].

An alternative to CF crack propagation is the path independent J-integral [22]. Ishikawa *et al.* [177] demonstrated the J-integral is the sum of its mode I and mode II counterparts, in other words the J-integral is the sum of the mode I and mode II contribution to the crack growth. The SIFs are evaluated separately by decomposing the stress and displacement field about the crack tip, [178]. One method to determine the crack propagation direction is the maximal principal stress criterion [179]. The crack path can be analysed using the 'Gθ method', see [180], in conjunction with the maximum strain energy release rate criterion (MSERRC) [181]. The Gθ can also be used in conjunction with the maximum circumferential stress criterion

(MCSC) [179] or the minimum strain energy density criterion (MSEDC) [182]. The virtual crack extension method can also be used to determine the crack propagation direction for mixed mode problems. The virtual crack extension method was introduced independently by deLorenzi, [183] and [133, 184–187]. Within the context of XFEM, [188] presented in 2D, and 3D, a fixed-length crack extension algorithm to model stable, unstable and partially stable fracture fronts. Last, for homogeneous anisotropic materials Saomua *et al.* [189] extended the maximum circumferential tensile stress criteria from isotropic to anisotropic materials as method for determining the direction of crack propagation. Critically, this included a reformulation of the toughness criteria into a function that varies continuously with angle around the crack tip.

Hansbo and Hansbo [190, 191] present a crack propagation method, for linear and non-linear elasticity, using DG methods. However, similar to Heintz [192], the crack propagation techniques proposed in these papers do not exploit the edge communication at element interfaces that exist in DG methods. This is similar to several continuous Galerkin methods where the elements are split internally. Arranz *et al.* [193] very briefly outlined the advantages of using weak element edge terms to propagate a crack however they do not provide any algorithm to do so. []

The hybrid DG method exploits element interfaces and element specific degrees of freedom to propagate a crack using a cohesive zone, initial works include [194, 195]. However, this method is strongly mesh dependent as the failure criterion is defined across element interfaces rather than nodes at the crack tip. Cracks can therefore only exist at the initialised boundaries of elements of the original mesh, unlike the r-adaptive method provided by [1] where the element interfaces adapt and align with the predicted crack direction. Accurate solutions for crack propagation paths using the hybrid DG method can only be obtained with very refined meshes [196]. Hybrid DG methods have also been explored by [196–199], amongst others. Within the context of cohesive law fracture h- and hp-adaptive schemes, respectively [200] and [201], have been produced for space-time DG methods. Additionally a review of the cohesive laws which drive the traction-separation is provided by [29].

In this chapter the mesh independent r-adaptive CF crack propagation method provided by [1] with a DG formulation, as performed by the author in [75], this is denoted the rp-method and takes advantage of the element specific degrees of freedom along element interfaces to propagate a crack in a mesh independent fashion. A second method, the hpr-method is also described in this chapter based on the hp-adaptive CF computation described in Chapter 5. These two methods allow for efficient brittle crack propagation in two dimensions. The cracks are propagated in discrete steps, with a staggered algorithm, along element interfaces which align themselves with the predicted crack propagation direction. Two algorithms for crack propagation are presented in this chapter

1. A less accurate but computationally cheap rp-adaptive propagation scheme which is driven by Miehe's *et al.* [1, 4] discrete CF formulation. The formulation was presented in Chapter 3. The r-adaptive component for this method ensures that no new degrees of freedom are added to the data structure during propagation, with p-adaptivity driven by the problem's geometry rather than an error estimator.

2. A more accurate and computationally expensive hpr-adaptive propagation scheme. The

error estimators η^2, η_Γ and $\eta_{|R|}$ used to determine whether the CF calculation is sufficiently accurate for propagation. For this scheme the CF is calculated using $g_i^{h,\Gamma\backslash R}$, initially presented in Chapter 5.

For both schemes, cracks are propagated using a Griffith failure criteria. The direction of propagation is determined by the CF vector at the crack tip. For both methods, the cracks are propagated in a load release r-adaptive quasi-static fashion with the results validated against those obtained in literature to demonstrate the predictive capabilities of the various methods. A comparison of the methods is also presented.

After this introduction the chapter is split into 5 further sections. In Section 7.2 the continuous time formulation of the CF is discretised, based on the work of [1, 4, 89]. In Sections 7.3 and 7.4 the *rp*-adaptive and *hpr*-adaptive propagation schemes are respectively described. In Section 7.5 *rp*-adaptive and *hpr*-adaptive methods for a series of problems are validated and compared. Observations drawn in Section 7.6.

7.2 Configurational force fracture propagation

This section provides the key equations for the small strain description of the CF approach to modelling brittle fracture based on the work of Miehe *et al.* [1]. This is followed by Sections 7.3 and 7.4 where the *rp*- and *hpr*-adaptive crack propagation schemes are described. However, it is first necessary to continue with the derivation of the dissipation of power when a crack propagates from Section 3.2. In the continuous form the dissipation of power by a crack propagating is,

$$\mathscr{D} = \partial V_i \left(\lim_{|C|\to 0} \int_C \Sigma_{ij} n_j \mathrm{d}s \right), \tag{7.1}$$

where ∂V_i is the crack tip material velocity with the crack tip CF defined as,

$$g_i = \lim_{|C|\to 0} \int_C \Sigma_{ij} n_j \mathrm{d}s. \tag{7.2}$$

As discussed in Chapter 3 several methods in the literature have been presented to calculate the discretised form of g_i. Due to the varying complexity of calculating the forms of the discrete CF, a different form is used for the *rp*-adaptive and the *hpr*-adaptive crack propagation methods, as shown in Table 7.1. The variables used in the CF equations in Table 7.1 can be found in their

Propagation Method	CF equation	Thesis Location	Original Source
rp-adaptivity	$\{g^{h,t}\} = \sum_{n\in n_t} \sum_{K\in A} \int_K [BV]^\top \{\Sigma^h\} \mathrm{d}v \geq 0$	Section 3.3	[1, 4]
	$\{g^{h,D}\} = \sum_{n\in n_b} \sum_{K\in A} \int_K \{q\}^\top [BV]^\top \{\Sigma^h_{ij}\} \, \mathrm{d}v$	Section 3.3	[60]
hpr-adaptivity	$\{g_i^{h,\Gamma\backslash R}\} = \sum_{K\in A} \int_K \{q\}^\top [BV]^\top \{\Sigma^h_{ij}\} \, \mathrm{d}v$ $+\lim_{R\to 0} \sum_{F\in(\Gamma^+\cup\Gamma^-)\backslash R} \int_F \{q\}^\top [N]^T [n^\Sigma] \{\hat{\psi}\} \mathrm{d}s$	Section 5.3	[96]

Table 7.1: The discretised CF equations used for the *rp*-adaptive and *hpr*-adaptive methods.

respective sections; however each CF equation has the following correspond name that is used to describe it:

- $\{g^{h,t}\}$ - *CF tip method*
- $\{g^{h,G}\}$ - *CF domain method*
- $\{g^{h,\Gamma\backslash R}\}$ - *CF domain with edges method*

The final step is determining how the crack will propagate. Here a quasi-static crack propagation framework is employed as presented in [1, 4]. First it is necessary to integrate the discrete dissipation power at the crack, (7.1), over the time period $[t^n, t^{n+1}]$

$$\Delta\mathscr{D}^h = \int_{t^n}^{t^{n+1}} \mathscr{D}^h \mathrm{d}t \approx \Delta o_i g_i, \tag{7.3}$$

where $\mathscr{D}^h$ is the discretised form of $\mathscr{D}$ in the spacial domain, the power dissipated by a propagating crack; it has the form

$$\mathscr{D}^h = V_i^{\partial\Gamma} g_i,$$

where g_i is determined in the discretised domain using one of the three methods presented in Table 7.1. (7.3) gives an incremental constant increase in the crack surface length, Δo_i, over the time period $[t^n, t^{n+1}]$. It has the form,

$$\Delta o_i = \Delta\gamma_I \frac{g_i}{|g_i|} \quad \text{where} \quad \Delta\gamma_I = \begin{cases} h_o & \text{for } |g_i| \geq g_c \\ 0 & \text{otherwise} \end{cases} \tag{7.4}$$

where g_c is a Griffith material failure criteria. h_o is the increase in crack length which is defined separately for the *rp*-adaptive and *hpr*-adaptive crack propagation methods. $\Delta\gamma_I$ is subject to the Karush-Kuhn-Tucker conditions

$$\Delta\gamma_I \geqslant 0, \quad (|g_i| - g_c) \leqslant 0 \quad \text{and} \quad \Delta\gamma_I(|g_i| - g_c) = 0. \tag{7.5}$$

Motion of nodes can be permitted in the material configuration except motion that would change the shape of the boundary[1]. It is recognised that is possible to dissipate power by moving nodes in the material configuration other than those at the crack tip, [97, 202], and thus achieve a minimal energy solution to the problem. However this is a highly non-linear problem and therefore computationally expensive. It is therefore not solved for here, consistent with the works of [1, 4, 89, 98, 190, 191, 193] and many others, but instead recognise it could potentially improve the solutions. Here, only power dissipation in the form of surface generation, or crack propagation, when the Griffith failure criterion $|g_i| > g_c$, is satisfied at a crack tip.

The key equations for modelling brittle fracture propagation based on CF have now been outlined. The crack tip CF value, for all crack tips, is calculated in a post-processing procedure

[1]The material configuration is the domain through which material changes occur, such as an advancing crack tip. The material domain is introduced and described in Chapter 3.

once the linear elastic system for small strain problems has been solved. It should also be stated that it is possible to simultaneously solve for the CF and material velocity as in [90], based on the works of [203]. However, this makes the problem non-linear and inherently more difficult and expensive to solve.

7.3 *rp*-adaptivity algorithm

The benefit to using symmetric interior penalty discontinuous Galerkin (SIPG) method is the flexibility available to switch off edge interactions between elements by removing the SIPG edge stiffness terms from the global stiffness matrix. This creates new surfaces, and is used to propagate a crack. No degrees of freedom (DOF) are added to the data structure to propagate a crack whilst only minimal manipulation is required to enable a *p*-adaptive scheme. The data structure is arranged such that all the DOF corresponding to first order components of all elements are numbered first. The labelling of all these DOF is unchanged throughout a simulation, as this is the minimum requirement for a finite element discretisation to exist. All subsequent higher order DOF are numbered greater than their first order counterparts. An example of the data structure is shown in Figure 7.1.

In a crack propagation scheme the CF, g_i, is evaluated at each crack tip using either the tip or domain method, see Table 7.1. If $|g_i| \geq g_c$, then the crack will propagate in the direction g_i and the *rp*-adaptivity method will be applied as given in Algorithm 7.1.

An example of a crack propagating through a mesh, using Algorithm 7.1, with its corresponding changing global stiffness matrix is shown in Figure 7.1. The mesh is constructed from 6 elements. For the simplicity of this example only elements sharing a node at the crack tip having a polynomial order, p_K, greater than 1. It is possible to have a group of elements with $p_K > 1$ about the crack tip, these element reside within the radius r_p. An element is considered inside r_p if at least one of its nodes are inside r_p. To propagate a crack, first the linear elastic system is solved producing a stress field. g_i is then calculated from the stress field in the material domain, then following Figure 7.1:

- Step 1: the element edge most aligned with g_i is reorientated about the crack tip to be coincident with g_i. The reorientated edge length has size $h_o = \frac{g_i}{|g_i|} m_i |F_c|$, where F_c is the most aligned element edge with $\frac{g_i}{|g_i|}$ and m_i is the normal tangent vector of the edge.
- Step 2: the SIPG edge stiffness terms associated with the reorientated edge are removed from the global stiffness matrix. This propagates the crack. Their values reside at the positions highlighted by the black 'X's in the second global stiffness matrix.

This is equivalent to applying homogeneous Neumann boundary conditions on the new crack surfaces. Furthermore the SIPG edge stiffness matrix calculations for this edge are also removed from any further calculations to prevent any edge interaction reappearing. This removes any direct interaction between elements along the edge creating a new surface, which extends the boundary of the domain, and propagating the crack.

- Step 3: as only elements on the crack tip have a polynomial order greater than 1, and the crack has moved, all rows and columns of the global stiffness matrix associated with the

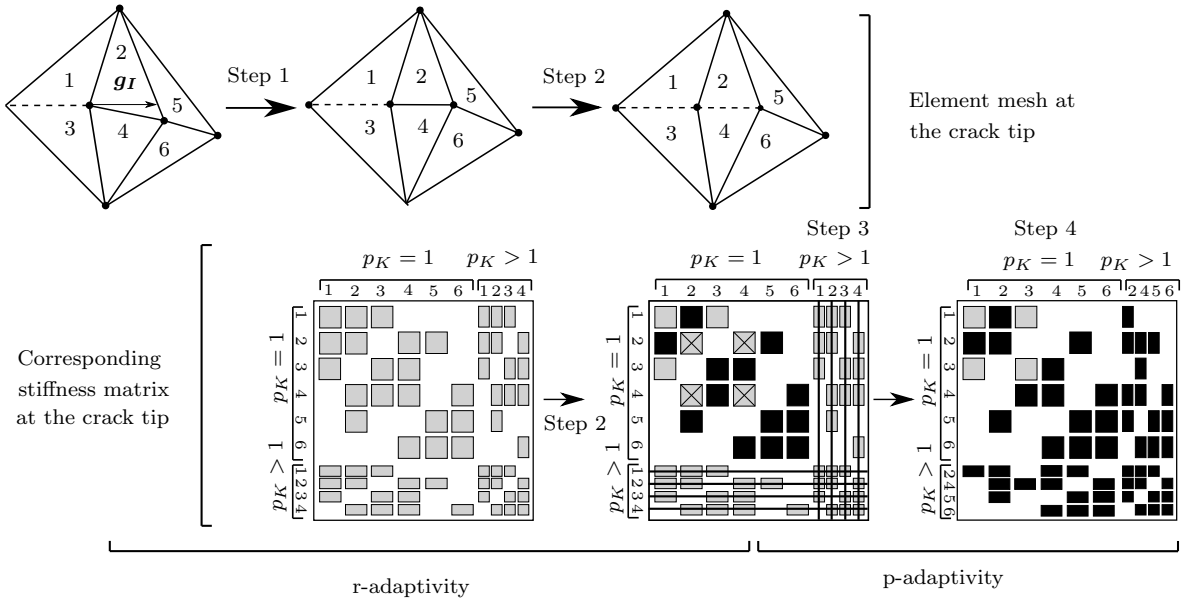

Figure 7.1: *rp*-adaptivity for a 6 element mesh at a crack tip, with high order elements at the tip and the corresponding sparsity matrix. The numbers on the rows and columns of the matrices correspond to element numbers in the mesh.

higher order DOF of elements no longer at the crack tip are removed.

This is highlighted by the black lines through the final rows and columns of the second stiffness matrix. Additionally, as the geometry of elements which share a node with the new crack tip have also changed, all values associated with these elements' local stiffness are removed. This is represented by the solid black blocks in the second matrix.

- Step 4: the updated local stiffness matrix components of elements are added back into the matrix. This corresponds to element with a changed geometry or increase in polynomial order. All new values are highlighted with black boxes in the third matrix in Figure 7.1.

The specific detail of the *rp*-adaptive method which Figure 7.1 follows is provided in Algorithm 7.1. The last stage of Algorithm 7.1 is recalculating the SIPG area and surface local stiffness matrices for $\mathfrak{T}_r$ and $\mathfrak{T}_p$ and adding these matrices back into the global stiffness matrix.

7.4 *hpr*-adaptivity algorithm with error estimation

The *hpr*-adaptive algorithm, presented in Algorithm 7.2, is more complex than the *rp*-adaptive algorithm presented in the previous section. Unlike the *rp*-adaptive algorithm, the step size is not defined by the element edge length but rather a predefined constant $\varkappa$. This makes aligning element edges with the direction of the configuration force more complex. Further, this propagation scheme increases the possibility of elements becoming distorted, or even potentially inverted therefore, an element quality check is also incorporated into the propagation scheme.

The propagation scheme uses the accurate calculation of g_i by considering $g_i^{h,\Gamma\backslash R}$. In order to obtain an accurate value of $g_i^{h,\Gamma\backslash R}$ a number of *hp*-refinement steps need to occur on the mesh, this creates more new elements when compared to the *rp*-adaptive method. However,

Algorithm 7.1 *rp*-adaptivity

Phase 1 – r-adaptivity

1: Find interior nodes of the space A about $\partial\Gamma$ and label n_b.
2: Perform (3.25) or (3.27) to obtain g_i.
3: Use (7.4) to get Δo_i.
4: Create a set of edges connected to crack node $\partial\Gamma$ with corresponding unit vectors away from crack tip m_i.
5: Identify the most aligned edge F_c with o_i by comparing all m_i with Δo_i. Label the most aligned unit vector m_i as m_i^c, and the corresponding edge length : $F_c = \arg\{\max_{d\in F}(\Delta o_i m_i^d)\}$, [4].
6: Reorientate m_i^c such that $m_j^c \Delta o_k \epsilon_{ijk} = 0_i$, where ϵ_{ijk} is the Levi-Civita tensor, [4]. Make the reorientated edge length $h_o = \frac{g_i}{|g_i|}|F_c|$.

Phase 2 – Creating a new surface

7: Identify new crack node n_c at the end of edge F_c.
8: Remove any further DG edge stiffness calculations associated with F_c and delete its values from the global stiffness matrix.
9: Identify all elements with changed vertex coordinates $\rightarrow E_r$.
10: Remove all values in rows and columns, in the global stiffness matrix, for all DOF associated with $\mathcal{T}_r$.

Phase 3 – p-adaptivity

11: About n_c find nodes within $r_p \rightarrow n_p$.
12: Remove all rows and columns associated with an order $p_K > 1$ for elements not within r_p.
13: Identify elements with $p_k = 1$ which contain nodes n_p and label E_p.

Phase 4 – Computation

14: Compute local area and surface stiffness matrices for all DOF in set E_r.
15: Compute components of the local area and surface stiffness matrices components associated with a polynomial order > 1 for elements in $\mathcal{T}_p$.
16: Add the newly computed local stiffness matrices components, for $\mathcal{T}_r \cup \mathcal{T}_p$, to the global stiffness matrix.

this set of new elements are not necessary for defining the crack propagation path and are also not necessary to calculate g_i at the next propagation step. The results is that significantly fewer elements are needed to modelled the crack path compared to the *rp*-adaptive method, the elements created to determine $g_i^{h,\Gamma\backslash R}$ are disregarded each time time the crack propagates. The mesh through which a crack propagates is defined $\mathcal{T}$ and the mesh used to calculate $g_i^{h,\Gamma\backslash R}$ is defined $\mathcal{T}_\Gamma$. The values of $g_i^{h,\Gamma\backslash R}$ are only to propagate a crack when its calculation is considered to be sufficiently accurate. The % accuracy of $g_i^{h,\Gamma\backslash R}$ is defined using (5.36). When the accuracy is higher than a predefined acceptable accuracy T%, $g_i^{h,\Gamma\backslash R}$ can be used to propagate a crack.

Figure 7.1 provides an example of a crack propagating through a mesh using Algorithm 7.2. Figure 7.1 has the following steps:

- Step 1: a crack tip $\partial\Gamma$ exists in the mesh $\mathcal{T}$ with a corresponding node n_c. The mesh $\mathcal{T}_\Gamma = \mathcal{T}$ is then defined.

The mesh $\mathcal{T}$ is used to propagate the crack however, in order to know the direction the crack should propagate in the CF at the crack tip needs to be calculated using $g_i^{h,\Gamma\backslash R}$. To calculate $g_i^{h,\Gamma\backslash R}$ *hp*-refinement needs to occur, however this level of mesh fidelity is not necessary for tracking where the crack is propagating. Hence, the mesh $\mathcal{T}_\Gamma = \mathcal{T}$ is defined, which contains the most up to date crack path and tip location.

- Step 2: *hp*-refinement occurs on the mesh $\mathcal{T}_\Gamma$ on which $g_i^{h,\Gamma\backslash R}$ is calculated for the node n_c, using the algorithm described in Section 5.3.

- Step 3: once an accuracy of $g_i^{h,\Gamma\backslash R}$ greater than $T\%$ has been obtained, measured using (5.36), $g_i^{h,\Gamma\backslash R}$ is considered sufficiently accurate to propagate a crack.

Once the crack propagates, the mesh $\mathcal{T}_\Gamma$ used to calculate $g_i^{h,\Gamma\backslash R}$ is redundant as this mesh, and corresponding accuracy, is bespoke for this crack position step. The crack tip CF value, $g_i^{h,\Gamma\backslash R}$, is therefore transferred to the crack propagation mesh $\mathcal{T}$, such that $g_i = g_i^{h,\Gamma\backslash R}$.

- Step 4: since the node n_c exist in the mesh $\mathcal{T}$ and $\mathcal{T}_\Gamma$, the value for g_i, obtained using $g_i^{h,\Gamma\backslash R}$, is used to predicted the direction of crack growth on the mesh $\mathcal{T}$. Now that the propagation path direction has been obtained, the crack edges along which fracture will occur have to be identified. Depending on how the element edges are orientated with respect to the crack path will cause the algorithm to either progress with *step 5.1* only, or, *step 5.1* then *step 5.2*.

- Step 5.1: the coordinates of the current crack tip position for the node n_c are defined X_i^c. The new crack tip position is determined using

$$x_i^c = X_i^c + \frac{g_i}{|g_i|}\varkappa \tag{7.6}$$

  where $\varkappa$ is the user defined length of propagation. Now the location of the new crack tip position n_c' with coordinates x_i^c is known. Before r-adaptivity is performed on the mesh the current crack tip node, n_c, is relabelled n_a. The mesh can now undergo r-adaptivity with three sub-steps:

  r-adaptivity sub-step 1: The set of all nodes connected to n_a via a single edge is defined $n_e \in N^E$, with each node having the corresponding coordinate x_i^e. Then, the edge most aligned with the unit vector $g_i/|g_i|$ from the node n_a is found by considering,

$$F_c = arg\left\{\max_{n_e \in N^E}\left(\frac{g_i}{|g_i|}\frac{(x_i^e - x_i^a)}{|x_i^e - x_i^a|}\right)\right\}. \tag{7.7}$$

r-**adaptivity sub-step 2**: once the edge F_c has been found the coordinate n^e is repositioned such that it has the new location $x_i^{e\prime}$

$$x_i^{e\prime} = x_i^e + \underbrace{|x_i^e - x_i^a|}_{|F_c|} \frac{g_i}{|g_i|}, \tag{7.8}$$

the element interaction along this edge is subsequently removed, causing the crack to propagate.

r-**adaptivity sub-step 3**: the node n^e is then relabelled n_a. A set of elements is created $\mathcal{T}_a \subset \mathcal{T}$. If the new crack position x_i^c resides in elements $K \in \mathcal{T}_a$, the element is labelled K_a. The nearest node in K_a to x_i^c is labelled n_m and has coordinates x_i^m. n_m is moved to the coordinate position x_i^c and subsequently relabelled n_c'. If $\mathcal{T}_a$ is empty the algorithm repeats by starting again at *r*-**adaptivity step 1**.

- Step 5.2: the element set $\mathcal{T}_a$ is checked to ensure that the creation of the crack tip node position x_i^c has not caused significant distortion. Distortion is measured as,

$$|x_i^m - x_i^c|/h_F > d_l \tag{7.9}$$

where d_l is a fraction that controls the quality of the element and h_F is the smallest edge length of K_a before any nodal coordinate changes. Distortion for a coarse mesh is important however with *hp*-adaptivity the error associated with distorted elements can be reduced significantly with refinement. The distortion parameter is introduced in this algorithm to prevent element inversion, such that an element becomes negative, from occurring. If (7.9) is true, significant distortion has occurred, the *r*-adaptivity performed in step 5.1 is undone, the elements in the set $\mathcal{T}_a$ are uniformly refined in h and step 5.1 is repeated. If (7.9) is not true the algorithm progresses with Step 6.

- Step 6: the mesh $\mathcal{T}'$ and the crack tip node n_c' are then subsequently defined respectively $\mathcal{T}$ and n_c. The algorithm then repeats itself going back to Step 1 in order for further crack propagation to occur.

- Stopping criteria, the algorithm is halted once a user-defined stopping criteria has been reached. This could be either: a maximum number of crack steps have occurred, a maximum crack length have been reached, or the crack intersects the problem's boundary domain.

7.5 Numerical validation

In this section a series of examples are used to compare, contrast and validate the *rp*-adaptive method and the *hpr*-adaptive method for crack propagation. The two methods are compared against each and against results obtained in the literature. Single and mixed mode cracks are considered for single and multiple crack problems for both methods to show that the methods are robust. The first problem considered contains a single mode I crack, since it is the sim-

Algorithm 7.2 *hpr*-adaptivity

1: Define the the length for each crack propagation steps $\varkappa$ m.
2: Define a stopping criteria to stop propagation.
3: Define the accuracy measure $T\%$ for the calculation of $g_i^{h,\Gamma\setminus R}$.
4: Create the mesh $\mathcal{T}$ through which the cracks are propagated, and identify the current crack node n_c and corresponding position X_i^c.
5: **while** Stopping criteria is not met **do**
6: Create the mesh $\mathcal{T}_\Gamma$, such that $\mathcal{T}_\Gamma = \mathcal{T}$.
7: On the mesh $\mathcal{T}_\Gamma$ find $g_i^{h,\Gamma\setminus R}$ for the node n_c to a sufficient accuracy $T\%$.
8: On $\mathcal{T}$ set $g_i = g_i^{h,\Gamma\setminus R}$.
9: Define the $n_a = n_c$.
10: Using g_i and $\varkappa$, determine the location of the new crack tip position x_i^c using (7.6).
11: **while** exit==0 **do**
12: Find the set of all nodes connected to n_a via a single edge. Define the nodes $n_e \in N_E$ with corresponding coordinates x_i^e.
13: Using (7.7) determine the edge F_c, that contains the node n_a, that is most aligned to the unit vector $g_i/|g_i|$.
14: Determine the node n^e, and corresponding coordinate position x_i^e, that shares the edge F_c with node n_a.
15: Reposition n^e to $x_i^{e\prime}$ using (7.8). Remove the element interaction along edge F_c.
16: Relabel n^e as n_a
17: Create the set of elements which each contain the node n_a, $\mathcal{T}_a \subset \mathcal{T}$.
18: **if** If the new crack position x_i^c resides in an element $K \in \mathcal{T}_a$ **then**
19: Label the element that contains the coordinate x_i^c K_a.
20: Determine the nearest node in K_a to x_i^c and label n_m
21: n_m is moved to the coordinate position x_i^c and subsequently relabelled n_c'.
22: Using (7.9) calculate the level of distortion that has occurred for the elements $K \in \mathcal{T}_a$.
23: **if** If the excess distortion has occurred **then**
24: Undo *all* changes to the mesh which occurred on lines 11-17.
25: Uniformly refine the elements $K \in \mathcal{T}_a$
26: **else**
27: Since element edges have be been reorientated and split a new mesh has been generated and is defined $\mathcal{T}'$.
28: set exit=0 to complete crack propagation for this step.
29: **end if**
30: **end if**
31: **end while**
32: Set $\mathcal{T} = \mathcal{T}'$ and $n_c = n_c'$ for the next crack propagation loop.
33: **end while**

plest problem it is as an example to demonstrate how the more complex *hpr*-adaptive method functions.

7.5.1 Single edge notched quasi-static crack propagation test

A single edge notched (SEN) quasi-static crack propagation test is performed in this section, the geometry and loading conditions are presented in Figure 7.3a with $H = 1$ m, $W = 0.5$ m, $a = 0.1$ with a heterogeneous Dirichlet boundary condition applied with a displacement of 0.01 m at the

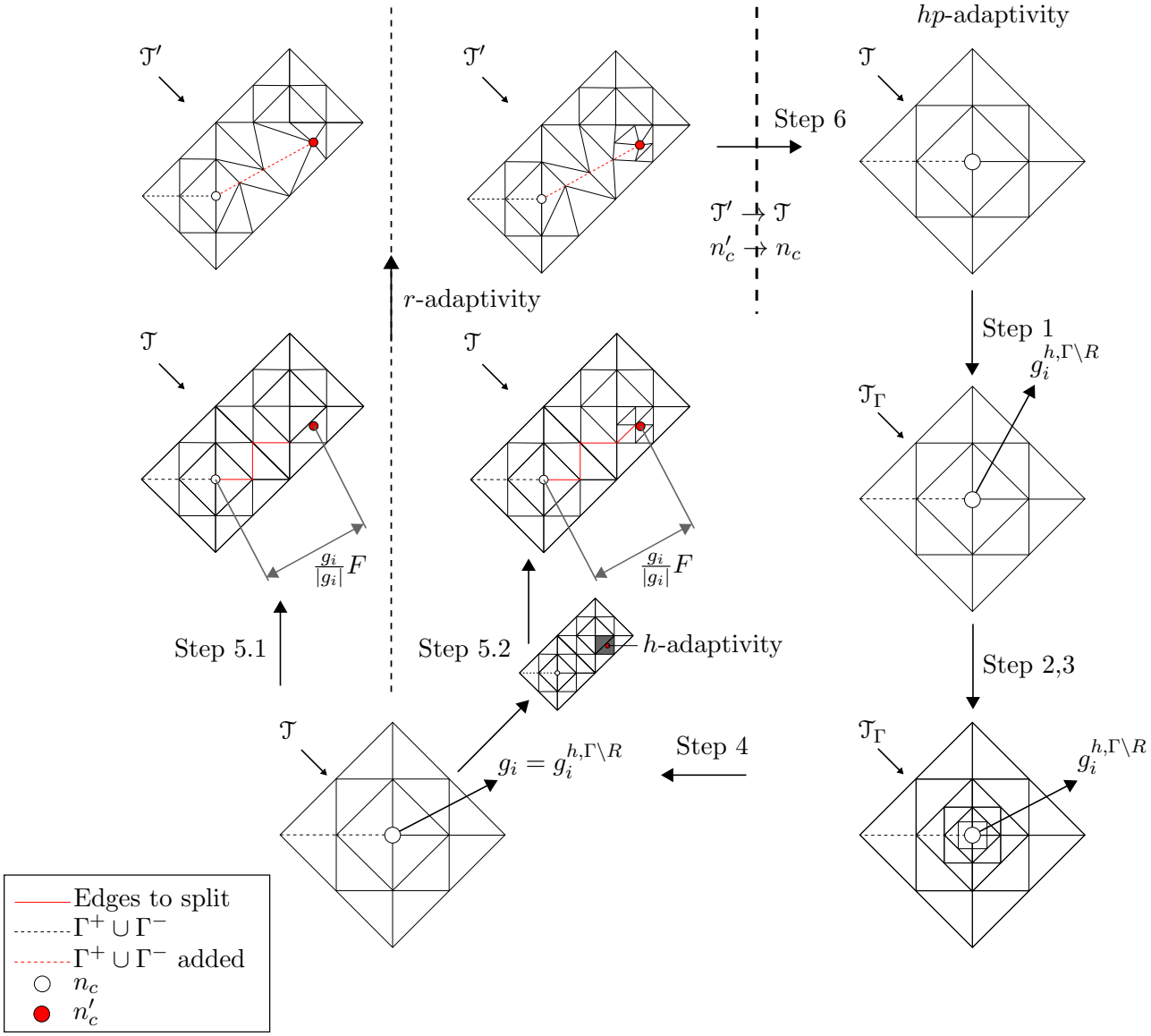

Figure 7.2: A schematic of the *hpr*-adaptive algorithm with the steps corresponding to the description of the *hpr*-algorithmic description in Section 7.4.

top and bottom of the plate. The plate acts in plane strain with $\mu = 8$ GPa, Poisson's ratio $\nu = 0.3$ and a Griffith failure criterion of $g_c = 1000$ N/m. The *rp*-adaptive and *hpr*-adaptive methods are used to propagate the crack. For the *rp*-adaptive method the mesh is shown in Figure 7.3d, with an element length graded from $h_{cF} = 0.04$ m around the expected crack path to 0.35 m with $r_p = 0.08$ m, the radius about the crack tip which has a higher polynomial order, and $r_d = 0.1$ m, the domain radius for the $\{g^{h,D}\}$ calculation. For the *hpr*-adaptive method the refinement parameters are set to $\delta_2 = 0.7$ and $\delta_1 = 0.03$ with propagation only occurring when the error $T\%$ for the computation of $\{g^{h,\Gamma\backslash R}\}$ is less than 1%. The initial mesh, and subsequent meshes during propagation, is shown in Figure 7.4.

The results for the instantaneous CF deviation from the expected crack direction, of 0°, are shown in Figures 7.3b and 7.3c. Each figure shows a total of 8 element edge separations. The result is crack that propagates in a near mode I fashion across the plate giving a total crack path

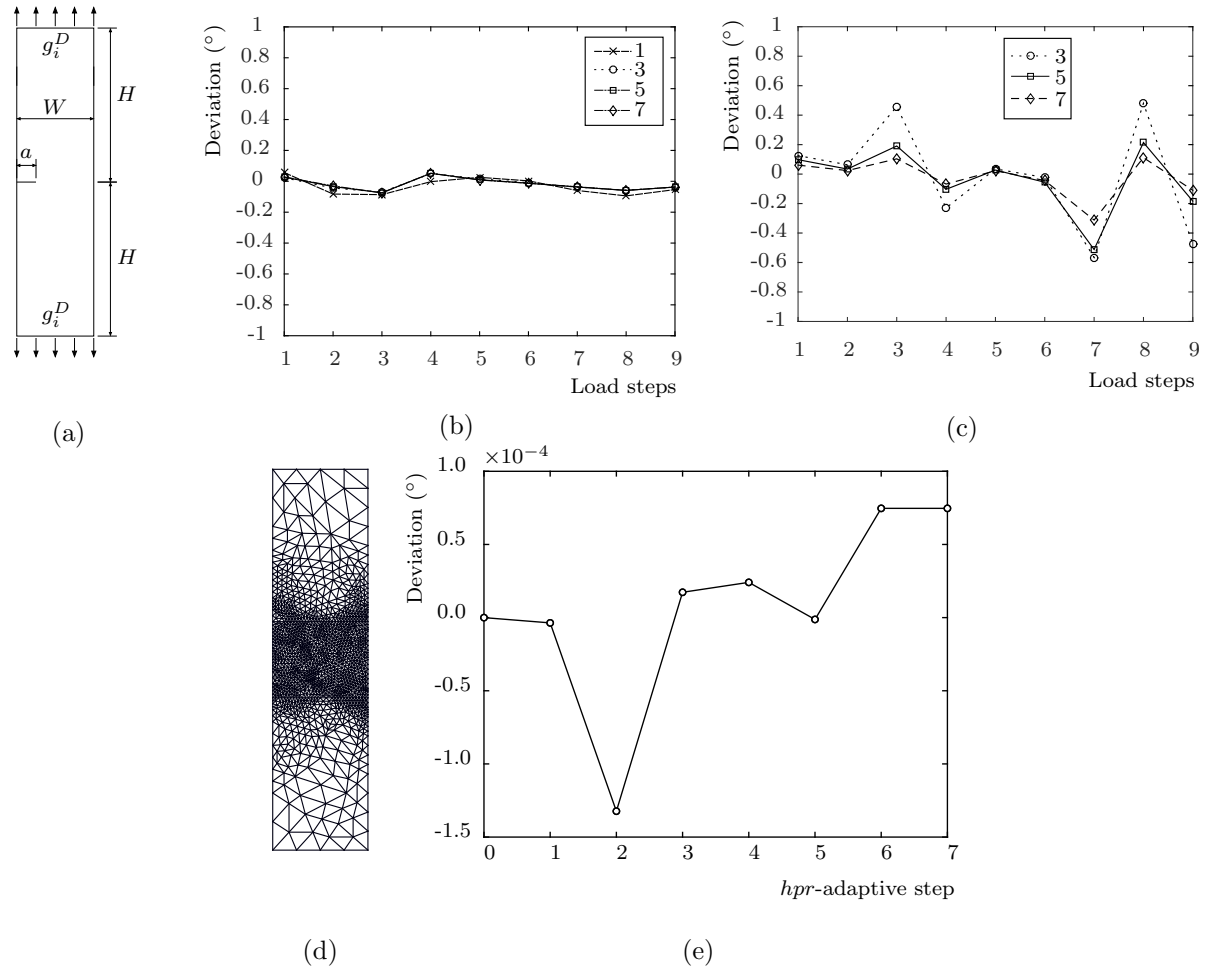

Figure 7.3: SEN crack: The problem geometry and boundary conditions are shown in (a). The resultant deviation of the crack path away from the planar direction using *rp*-adaptive method with $\{g^{h,D}\}$ is shown in (b) and using $\{g^{h,t}\}$ shown in (c) with (d) the initial mesh used for both (a) and (b). The deviation using $\{g^{h,\Gamma\backslash R}\}$ is shown in (e) with the mesh for each *hpr*-adaptive step shown in Figure 7.4. The legends in (b) and (c) refer to the order of the high polynomial order elements within the radius r_p about the crack tip.

length across the plate of 0.31 m and 0.30 m, for Figures 7.3b and 7.3c respectively. The figures demonstrate the improvements gained by using the domain approach. The paths generated by $\{g^{h,t}\}$ and $\{g^{h,D}\}$ both deviate from the expected planar fashion across the plate. $\{g^{h,D}\}$ obtained a maximum difference, from 0°, of 0.09° compared to calculation $\{g^{h,t}\}$ which achieved 0.55°. The figures show how the path direction is governed by integration scheme more than the polynomial order of elements around the tip. The average difference between $p_K = 1$ and $p_K = 7$ for the domain approach was 0.029°, and for the tip approach was 1.86°.

The *hpr*-adaptive method performs better than the *rp*-adaptive method in terms of deviation angle from the expected planar direction of the crack propagation path. Figure 7.3e shows that the maximum deviation from the crack path is -1.3×10^{-4}° despite the mesh being non-symmetric. The meshes of the 7 crack propagation steps are shown in Figure 7.4, the crack tip progression is shown by the red marker. Between each *r*-adaptive step a *hp*-adaptive step occurs,

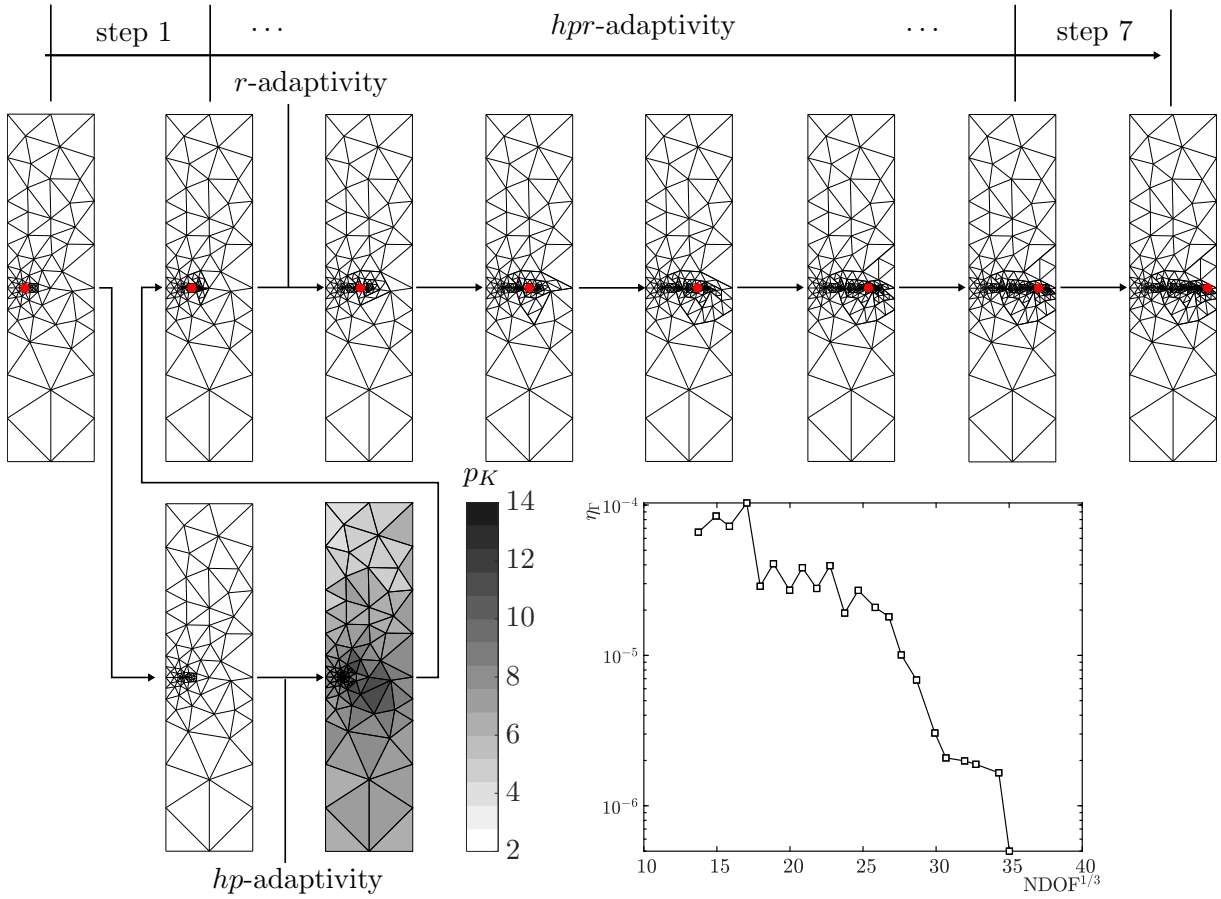

Figure 7.4: SEN crack: The development of the problem mesh with 7 *hpr*-adaptive steps. The figure includes for step 1 the first and last mesh during the *hp*-adaptive step to determine $\{g^{h,\Gamma\backslash R}\}$ with the corresponding convergence of η_Γ shown by the inset graph.

as an example the initial and final mesh generated during *hp*-adaptivity is shown for the first *r*-adaptive step; the corresponding convergence of the error η_Γ is shown in the inset graph of Figure 7.4. For achieving an accurate results for the crack path and efficiently crack the progression of the crack tip the *hpr*-adaptive is more efficient than the *r*-adaptive method, significantly fewer elements are used for the *hpr*-adaptive method, as shown in Figure 7.4, compared to the *r*-adaptive method shown in Figure 7.3d. However, due to the *hp*-refinement steps necessary to determine $\{g^{h,\Gamma\backslash R}\}$ the overall time for the *hpr*-adaptive method was slower than the *r*-adaptive method.

7.5.2 Double notched two holed quasi-static crack propagation test

This benchmark is taken from [181]. It is a tension test of a double edge notched specimen with two holes, the geometry and loading conditions are shown in Figure 7.5a. The test is necessary to show firstly that the *rp*-adaptivity method for SIPG produces results that are comparable to those obtained in the literature using the CG method with CF based fracture. Further, the problem will demonstrate the accuracy improvements when using the *hpr*-adaptive method. The plate acts in plane strain and has a shear modulus $\mu = 8$ GPa, Poisson's ratio $\nu = 0.3$ and a Griffith failure criterion of $g_c = 1000$ N/m. In Figure 7.5b the mesh is refined around the crack

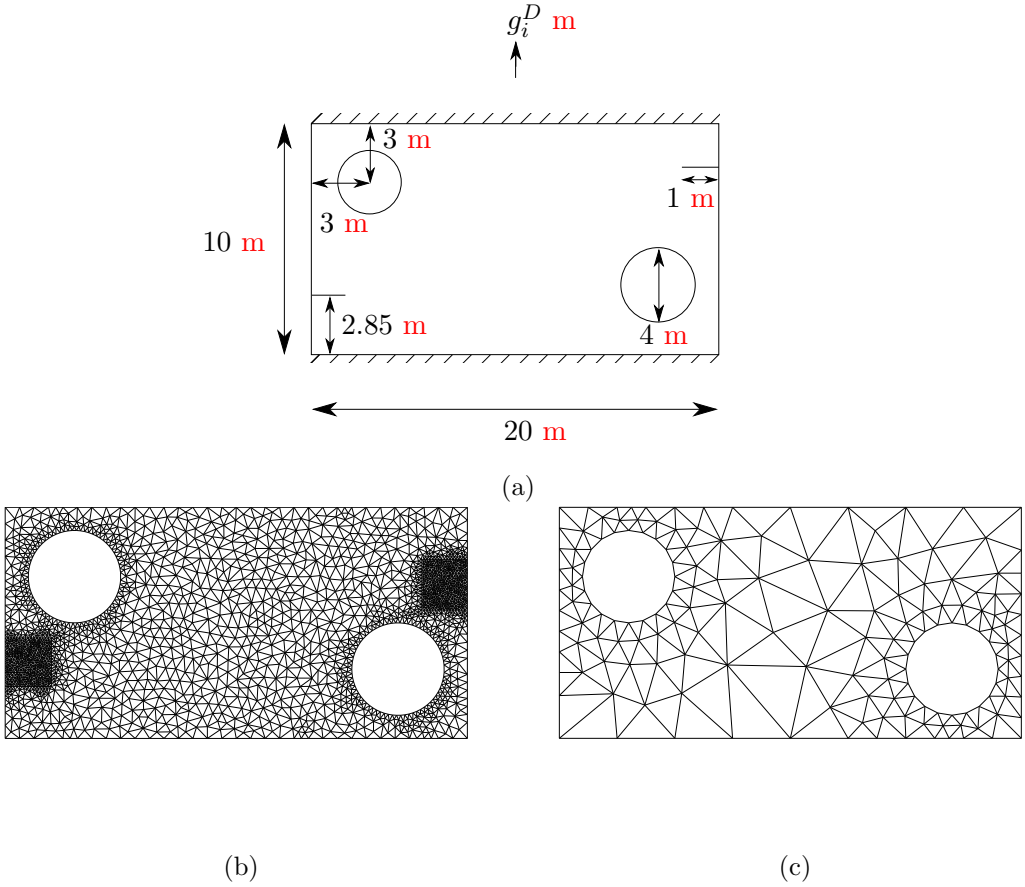

Figure 7.5: Double crack and hole example: (a) geometry for the two holed quasi-static crack propagation test and (b) starting mesh with element length of 0.3 m refined to 0.015 m at the crack tips for the *rp*-adaptive method and (c) the initial mesh for the *hpr*-adaptive method.

tips as in [4], this is to ensure a more valid comparison. A heterogeneous Dirichlet BC is applied to the top of the plate with $g_i^D = [0\ 0.1]$ m and a homogeneous Dirichlet BC is applied to the bottom of the plate.

For the *rp*-adaptive method the radius of elements about the crack tip which had a higher polynomial order was $r_p = 0.1$ m, with elements of polynomial order of 3 within r_p and 1 elsewhere. The CF domain method, $\{g^{h,D}\}$, with $r_d = 0.2$ m was employed to evaluate this mixed mode problem. For the *hpr*-adaptive method the CF was calculated using $\{g^{h,\Gamma\backslash R}\}$ with $\delta_2 = 0.7$ and $\delta_1 = 0.01$, with the initial domain size set as the area of the elements on the initial mesh before *hp*-adaptivity. $T\%$ was set to 1%, only once all measures values had decreased by a magnitude of 0.01 does propagation occur. The crack propagation size was set to 0.6 m. For both methods the two cracks propagate simultaneously in the same load step. The deformed mesh for the *rp*-adaptive and *hpr*-adaptive methods are respectively shown in Figures 7.6b and 7.6c. Figure 7.6c is the final *hp*-adaptive mesh.

Figure 7.6a is a comparison between the crack propagation path obtained here using the *rp*-adaptive method and that by Miehe *et al.* [4]. The Figure shows good agreement between the two crack paths however, the problem is antisymmetric and so the relative crack paths about the crack tip should be the same. To investigate the variance of the two crack paths and their

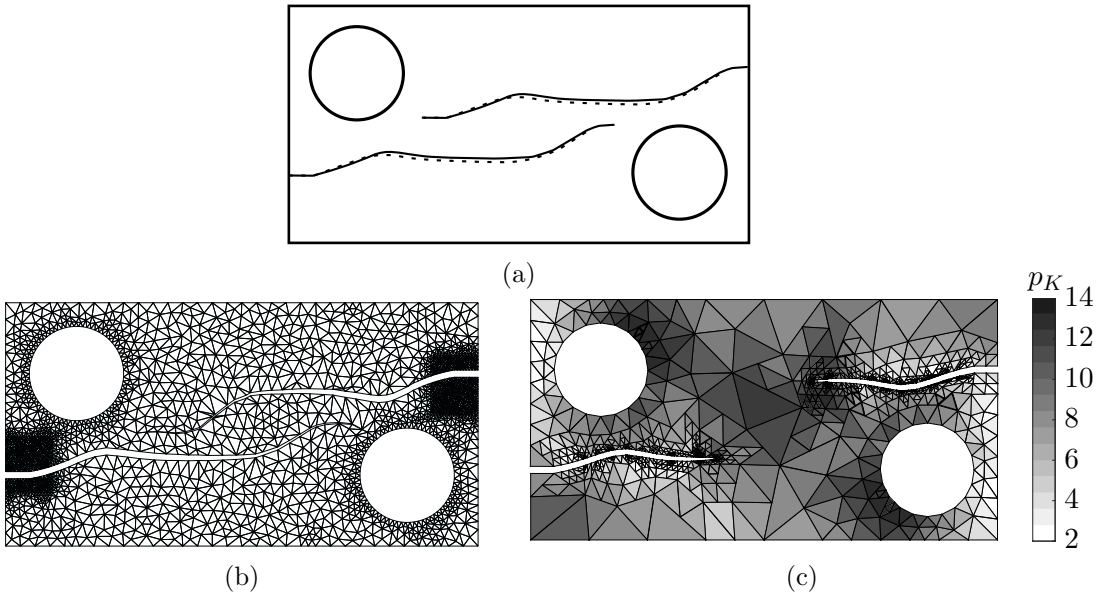

Figure 7.6: Double crack and hole example: (a) a comparison of paths between those obtained in Figure 7.6b (solid line) using the *rp*-adaptive method and the path obtained by [4] (dashed line). (b) is a snapshot of the *rp*-adaptive mesh during propagation and (c) is a snapshot of the *hpr*-adaptive mesh at the end of an *hp*-adaptive step to determine $\{g^{h,\Gamma\setminus R}\}$. The displacements for (b) and (c) have been magnified by a factor of 10.

dependency on the mesh for the *rp*-adaptive method, a fine and a course mesh are considered as shown in Figure 7.10c. The cracks were propagated with the relative crack paths shown in Figure 7.6b with the difference in the crack paths acting as a measure of precision. The precision was measured as the maximum percentage difference from the mean of the two crack paths for a mesh. The coarser mesh, element length of 0.25 m, obtained a precision of 20%. The refined mesh, element length of 0.123 m, achieved a precision of 2%. The lack of precision is caused by two features. First, for a coarse unstructured mesh, the stress field is poorly represented. This means on the first load step the configuration force is unlikely to be the same at both crack tips and so the two cracks will propagate in slightly different directions. Secondly, as the increase in crack length Δo_i, is larger for the coarse mesh the error in crack path is magnified. This results in a diverging crack path, Figure 7.7a, and different stress fields at the tips, Figure 7.8b. The locations of the new crack tips and the stress fields, Figure 7.8a, now contrast more than if a finer mesh was used, Figure 7.7a. Ultimately the difference between the stress fields and the error in crack path compounds the inaccuracy as the crack propagates through the specimen. However, the *hpr*-adaptive method exhibits almost no dependency on the mesh size with Figure 7.7a showing the crack paths to be nearly identical with a precision of 0.0093%. Further, refinement in crack propagation size for the *hpr*-adaptive method will also lead to a more accurate crack path. The *hpr*-adaptive method should therefore be able to achieve a precise and accurate crack path.

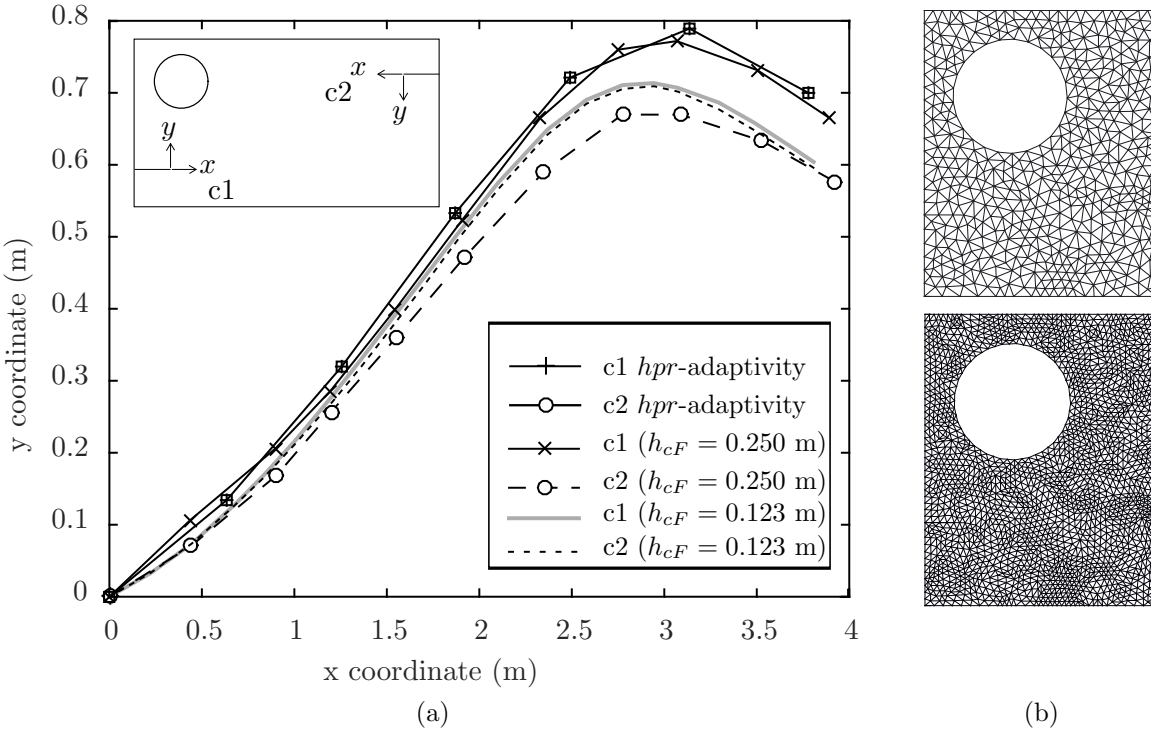

Figure 7.7: Double crack and hole example: (a) the crack propagation paths for the two different mesh refinements in (b) using the *rp*-adaptive method and the propagation path using the *hpr*-adaptive method. (b) shows the two meshes used for the *rp*-adaptivity method with $h_{cF} = 0.250$ m (top right), and $h_{cF} = 0.123$ m (bottom right).

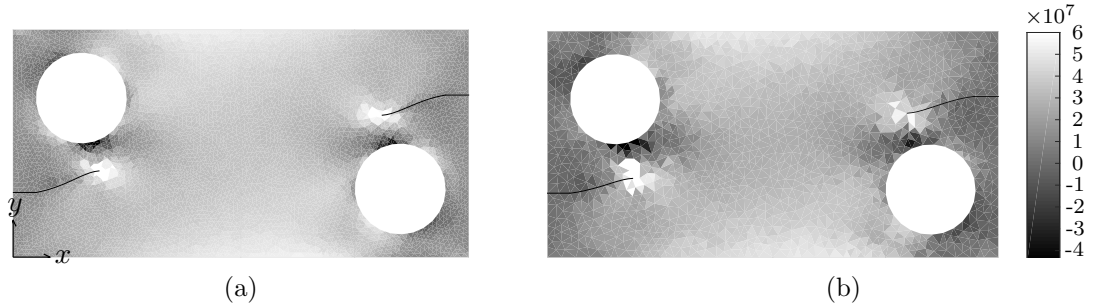

Figure 7.8: Double crack and hole example: plot of σ_{xx} (Pa) for (a) $h_{cF} = 0.123$ m and (b) $h_{cF} = 0.250$ m.

7.5.3 Split crack problem

The most complex problem considered in this chapter is the split crack problem, it contains three crack tips, two of which are mixed mode as shown in Chapter 5. A few authors [4, 55, 90], claimed from their numerical experiments that a CF based crack propagation scheme is unable to model kinked cracks unlike the maximum circumferential stress criterion; this section will demonstrate the CF approach can. This problem also has no Dirichlet BCs, it will therefore test, for multiple crack propagation steps, the relative precision between the two cracks when using all the average BCs.

The problem dimensions, crack dimensions and boundary conditions are shown in Figure 7.9a with $H = 16$ m, $W = 20$ m, $a = b = 1$ m, $\theta = 45°$ and three crack tips A, B and C.

The Neumann BCs $g_i^N = [0\ 100]$ MPa and $g_i^N = [0\ -100]$ MPa are applied on the top and

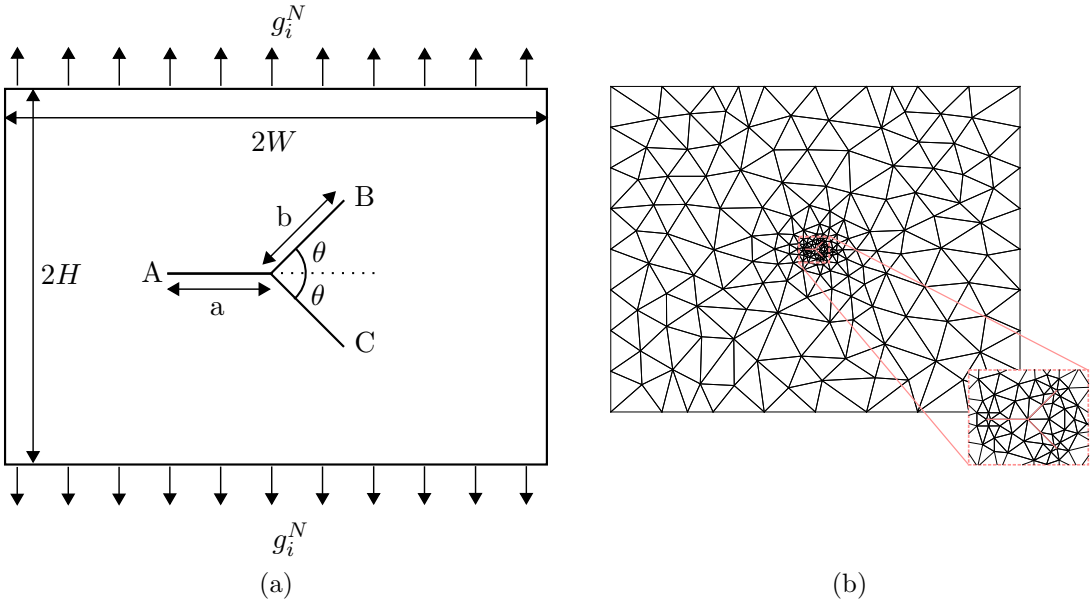

Figure 7.9: Split crack: (a) the geometry and loading conditions with the initial mesh with $p_K = 2 \forall K \in \mathcal{T}$ shown in (b).

bottom edge respectively. The problem acts in plane strain with a shear modulus of $\mu = 8$ GPa, Poisson's ratio $\nu = 0.3$ and a Griffith failure criterion of $g_c = 1000$ N/m. The initial mesh is shown in Figure 7.9b with $p_K = 2 \forall K \in \mathcal{T}$. The crack tip CF was calculated using the *hpr*-adaptive method with $\{g^{h,\Gamma \backslash R}\}$ with the refinement parameters $\delta_2 = 0.7$ and $\delta_1 = 0.01$, the crack propagation criteria, T was set to 1% with the crack propagation step length set to 1 m. 13 crack propagation steps were applied to the problem. The relative cracks paths for all crack tips is shown in Figure 7.10a with the final *hp*-refinement mesh for the 13^{th} propagation step shown in Figure 7.10b. Since the problem and boundary conditions are symmetric about the crack edges of A, crack A is a pure mode I problem and should propagate in a planar fashion which it does as shown in Figures 7.10a and 7.10b. The maximum deviation of the crack A from $y = 0$ m was 0.0011 m, the maximum instantaneous crack propagation angle away from $y = 0$ m for a crack propagation step was 0.0327°. The second observation is that the crack paths for cracks B and C are almost identical as shown in Figure 7.10a, despite the mesh not being symmetric about the axial load, see Figure 7.10b for the non-symmetric mesh. The percentage precision of the relative two crack paths away from their average position was 0.0134%, demonstrating despite the increase in complexity of the problem compared to the double hole problem the precision of the crack paths is high and nearly of the same order of magnitude. Although the crack paths are precise the accuracy of the crack path could be investigated by reducing the crack propagation length. The last point to address is that that initial crack propagation path is kinked, despite the claims in the literature that the CF method for propagation a crack results only smooth crack paths. The initial propagation angle away from the crack edges for crack B is 45.4°.

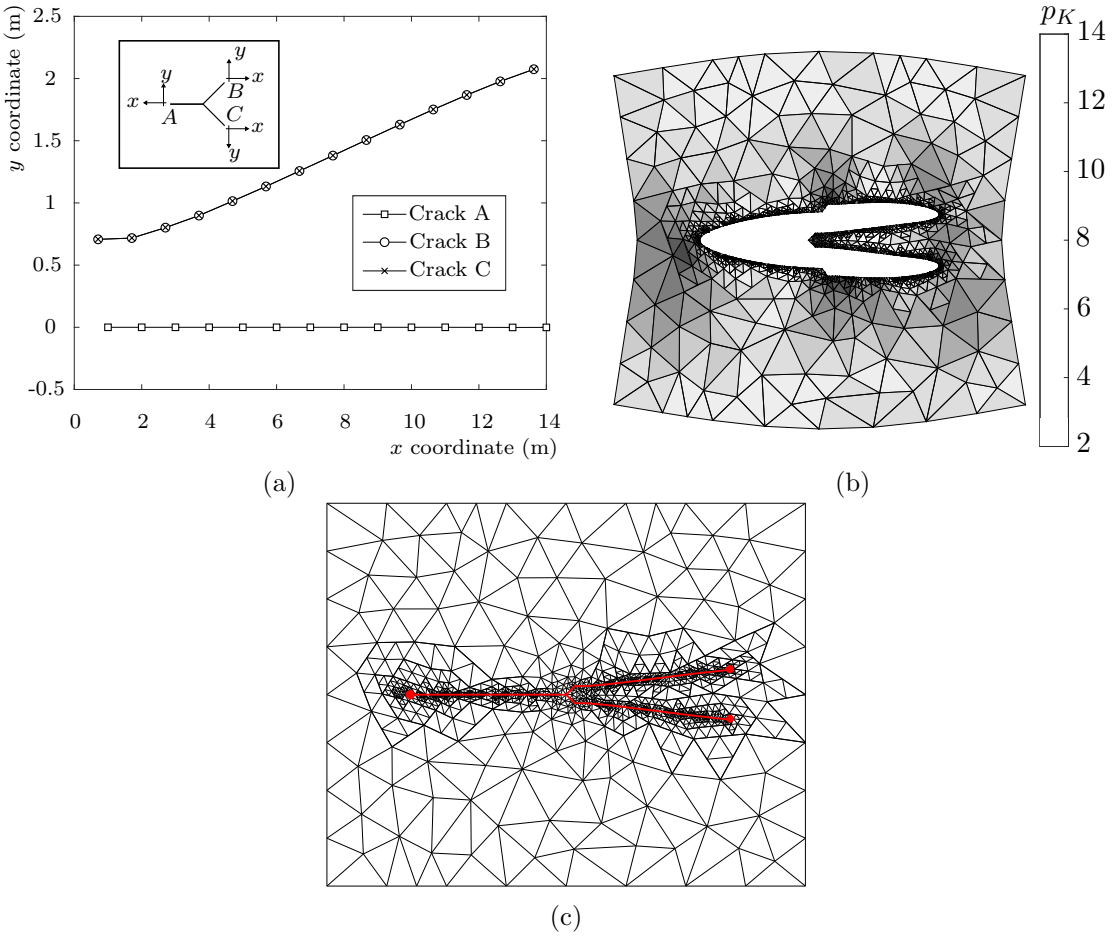

Figure 7.10: Split crack: (a) the relative crack propagation paths with the final *hp*-adaptive mesh for the 13$^{\text{th}}$ *hpr*-adaptive step with the displacement magnified by a factor of 10^2 in (b). The final undeformed mesh is shown in (c) before any further *hp*-refinement occur.

7.5.4 Shear crack

The last problem to be considered in this section is the shear crack problem. This problem is a particularly interesting single crack problem as the resultant crack path is highly mesh dependent, it is therefore able to test how robust the computation of $\{g^{h,\Gamma\setminus R}\}$ with respect to the initial problem mesh. This problem has been visited by several authors from a numerical setting [1, 204], amongst others, and is based on the experimental results from [179]. The boundary conditions and dimensions are given in Figure 7.11a, with $H = W = 1$ m, $a = 0.5$ m with a homogeneous Dirichlet BC applied on the bottom edge of the square and heterogeneous BC applied on the top edge with $g_i^D = [0.2\ 0]$ m. The plate acts in plane stress with $\mu = 8.0$ GPa, $\nu = 0.3$ with a Griffith failure criterion of $g_c = 1000$ N/m. The initial mesh of the problem is given in Figure 7.11b. The crack is propagated using the *hpr*-adaptive method with the crack propagation length set to $\varkappa = 0.05$ m. Two values of the accuracy parameter $T\%$ are considered, a coarse value of 50% and a fine value of 1%, the respective crack propagation paths are shown in Figures 7.11c and 7.11d. The final crack path is provided by the red line with the final crack tip position given by the red marker in Figures 7.11c and 7.11d.

The first observation is that the two cracks paths are very different, the coarse evaluation

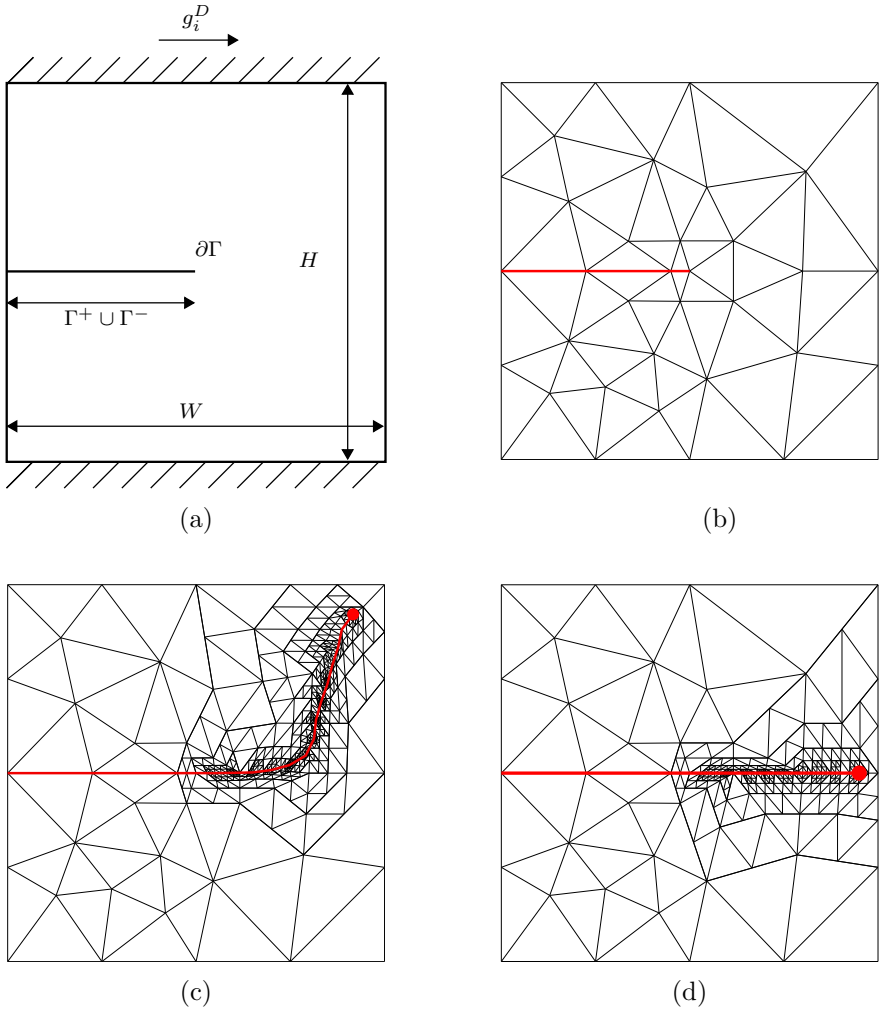

Figure 7.11: Shear crack: (a) the problem geometry with the initial mesh shown in (b). The final mesh when $T = 50\%$ and $T = 1\%$ using the *hpr*-adaptive method. The crack edges are marked in red with the crack tip given by the red marker.

exhibits mixed mode propagation whilst the fine evaluation is nearly pure mode II. Further, the coarse crack path is an unrealistic results as the crack edges overlap where there should be contact. Nevertheless, the crack behaviour for the coarse problem is similar to the results obtained in [1, 204], except the crack path for these problems goes down rather than up. The problem represents a bifurcation, either the crack will propagate in a purely mode II fashion or, as soon as the crack deviates a little from the mode II path, the mixed mode behaviour becomes larger. When $T = 1\%$ the crack propagates in a nearly pure planar fashion, with the maximum deviation from the pure mode II crack path of 8.6×10^{-5} m. This value corresponds to the final crack tip position shown in Figure 7.11d. This demonstrates the computation of $\{g^{h,\Gamma\backslash R}\}$ is robust to the mesh since, even though the mesh is non-symmetric and the problem is very sensitive to any deviation from the pure mode II path, the predicted crack path almost exactly planar.

The results obtained in [1, 204] are obtained on non-symmetric meshes using the crack tip CF, with a level of 'perturbation' applied to the background mesh or particles. With perturbation

the results agree, with refinement in crack step size, to the experimental results obtained by [179]. Clearly, as shown in Figure 7.11c, the crack path is dependent on the perturbation and can lead to an unrealistic result. The author considers this generally to be a concern. When the laboratory solution to the problem is known a researcher with numerical experience can give results which agree with experimental data. This is problematic because if the solution is not known, how much faith can be given to these numerical methods to give the correct predicted result? Indeed, given how sensitive the numerical result is to the mesh it is more likely that for this problem the BCs do not match those of the experiment in [179].

7.6 Observations

In this chapter the thermodynamically consistent framework, presented by Miehe and co-workers [1, 4, 89], has been used to model brittle fracture for small strain problems in a SIPG finite element method. The proposed *rp*-adaptive propagation method exploits the element specific degrees of freedom and the weak interaction between elements, and existing as stiffness terms in the global stiffness matrix to propagate a crack in a fashion that is independent of the original element interface orientation. The crack tip CF for this method is calculated using $\{g^{h,D}\}$. These benefits were first realised in the author's paper [75]. The crack is propagated through: (i) moving an element edge in line with the CF, (ii) removing the DG edge stiffness values, in the global stiffness matrix corresponding to the reorientated edge, (iii) recalculating the local stiffness matrices of elements with changed geometry or polynomial order, and, (iv) updating the values global stiffness matrix.

The *hpr*-adaptive propagation method is more computation expensive that the *rp*-adaptive method however, it is orders of magnitude more precise, the crack propagation step is predefined, quality of the elements is ensured and the crack tip CF is calculated highly accurately using $\{g^{h,\Gamma\backslash R}\}$ to a user defined estimated accuracy. The *hpr*-adaptive method is able to achieve highly precise crack propagation results for problems contain multiple mixed mode cracks however, a thorough investigation into how the crack propagation length affects the accuracy of the crack path is required.

Chapter 8

Conclusion

8.1 Conclusions

This thesis was concerned with the accurate numerical determination of the crack tip configurational force (CF) and methodologies for propagating a crack in a finite element (FE) mesh. All chapters provide novel material which was directly, or indirectly, associated with accurately determining the crack tip CF, except Chapter 1. Chapter 1 was an introduction to the thesis and provides: a historic introduction to the subject of fracture mechanics, an overview of the fracture mechanics techniques for evaluating the energy released when a crack propagates, and a discussion of the available numerical techniques used for fracture analysis. Chapter 2 introduces the symmetric interior penalty discontinuous Galerkin (SIPG) finite element method (FEM) and, for the first time, average BCs necessary for problems where Dirichlet BCs in either the x or y direction were not included in the formulation. This was followed by Chapter 3, the CF calculation was cast within the SIPG FEM and discrete crack tip CF formulations were investigated. The issues of the current CF calculations in the literature were highlighted and discussed. In Chapter 4 a residual based *a posteriori* error estimator was introduced with a *hp*-adaptive scheme. In Chapter 5 the *hp*-adaptive scheme and the error estimator was used to develop a novel method for computing the crack tip CF, with error estimates derived for all components of the CF calculation. The method was then shown to be robust for anisotropic materials in Chapter 6 however, the anisotropic material analysis highlighted ways in which the method presented in Chapter 5 could be improved further. Last, in Chapter 7 two methods were proposed for fracture propagation: i) a fast and simple *rp*-adaptive method, *ii*) a slower but accurate and precise *hpr*-adaptive method.

8.2 Recommendations for future work and discussions

The research performed in this thesis could be extended in the following directions:

- The computation of the crack tip CF in a range of anisotropic materials in Chapter 6.1 highlighted potential improvements to the algorithm proposed in Chapter 5, $g_i^{h,\Gamma\backslash R}$. As discussed in Section 6.1, the improvements would make the calculation of $g_i^{h,\Gamma\backslash R}$ more robust to *hp*-adaptive parameters δ_2 and δ_1. Specifically when δ_2 and δ_1 were poorly chosen it was possible for not all the error estimators for the edge components of $g_i^{h,\Gamma\backslash R}$, $\eta_{|R|}$ and

η_Γ, to converge. This was primarily driven by the naive algorithm to reduce the length of the ignored region R, of $g_i^{h,\Gamma\backslash R}$, with *hp*-adaptivity, in $g_i^{h,\Gamma\backslash R}$. The rate to reduce R was predefined beforehand and as such it could reduce too quickly with *hp*-refinement causing the error term η_Γ to increase. However, it would be possible to produce an algorithm where the reduction in $|R|$, and the associated error estimate $\eta_{|R|}$, was driven by the error estimates $\eta_{|R|}$ and η_Γ such that regardless of the choice of δ_2 and δ_1 convergence of $\eta_{|R|}$ and η_Γ is always achieved with *hp*-adaptivity.

- The computation of $g_i^{h,\Gamma\backslash R}$ could be extended to discontinuous and functionally graded heterogeneous materials. Firstly, functionally graded heterogeneous materials only requires a slight modification to the domain formulation (3.35) which has the form,

$$\mathscr{D} = -V_i^{\partial\Gamma}\left(\int_A (\nabla_j q)\Sigma_{ij}\mathrm{d}v - \int_{\Gamma^+\cup\Gamma^-} q\Sigma_{ij}n_j\mathrm{d}s\right). \tag{8.1}$$

  but, as shown by [87], (8.1) for a functionally graded material can be rewritten as

$$\mathscr{D} = -V_i^{\partial\Gamma}\left(\int_A (\nabla_j q)\Sigma_{ij}\mathrm{d}v + \underbrace{\frac{1}{2}\int_A (\nabla_i D_{pjkl})\varepsilon_{kl}\varepsilon_{pj}\mathrm{d}v}_{\text{Integral 1}} - \int_{\Gamma^+\cup\Gamma^-} q\Sigma_{ij}n_j\mathrm{d}s\right). \tag{8.2}$$

  Where integral 1 of (8.2) can be bound by the residual based *a posteriori* error estimator. The continuous formulation of the CF calculation for a material with a discontinuous material heterogeneity has the form [205],

$$\mathscr{D} = -V_i^{\partial\Gamma}\left(\int_A (\nabla_j q)\Sigma_{ij}\mathrm{d}v - \int_{\Gamma^+\cup\Gamma^-} q\Sigma_{ij}n_j\mathrm{d}s - \underbrace{\int_l q\Sigma_{ij}n_j\mathrm{d}s}_{\text{Integral 1}}\right). \tag{8.3}$$

  where l is a set that contains both edges of any line of material discontinuity that intersects with the crack tip, analogous to the integral along the crack edges in (8.3). The same methodology to compute the crack edge terms could be applied to integral term 1 of (8.3); term (8.3) accounts for the discontinuity material heterogeneity intersection with the crack tip.

- With little modification the algorithm to compute $g_i^{h,\Gamma\backslash R}$, and the associated error estimators, could be applied to calculating the CF along a crack front in three-dimensions. For a three-dimensional problem space the crack front CF is defined $g_i \in \mathbb{R}^{3\times 1}$. If the CF is orientated with respect to the crack front reference frame, as in Figure 8.1, only g_2 requires an area integral along the crack faces; g_3 has the same integral form as g_1. Therefore, no new error estimators are required for the computation of g_2 hence, an analogous method to computing $g_2^{h,\Gamma\backslash R}$ with the error estimates $\eta_{|R|}$ and η_Γ in two-dimensions could be used to compute g_2 in three dimensions. The most significant issue would be the scalability of

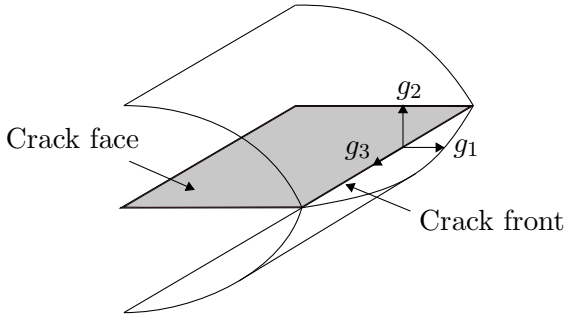

Figure 8.1: A sketch of three-dimensional crack face and crack edge with the CF $g_i \in \mathbb{R}^{3\times1}$ orientated with the local coordinate system of the crack front.

the algorithm and whether in three-dimensions the *hp*-adaptive algorithm would simply be too computationally expensive to make it a viable option to other three-dimensional, but less accurate, CF algorithms [1, 89, 90].

- This thesis used a residual based *a posteriori* error estimator that was reliable and efficient for the error in the SIPG norm. The error estimator was then used to estimate the error of the proposed CF calculation. However, alternative *a posteriori* error estimates do exists with their own advantages and disadvantages. The residual based *a posteriori* error estimate is simple to calculate, and is calculated using the displacement solution from the linear elastic problem being solved. Therefore only the solution from the linear elastic problem is required to determine its corresponding error estimator. A possible alternative is a goal-orientated error estimate which directly evaluates a feature of the solution which is useful to user, for instance the CF calculation. It is more expensive however since, it requires the dual problem of the linear elastic problem to be solved on a more refined mesh, however it is suggested that the goal error estimate can be very close to the actual error of CF [111, 112, 206].

- In general it would be interesting to use error estimation and *hp*-adaptivity for geometrically non-linear problems. Further, investigating whether it would be possible to apply the method to determine $g_i^{R\setminus\Gamma}$ to a geometrically non-linear problem and perhaps going even further and combining material non-linearity with geometric non-linearity.

Appendix A

SIPG basis function matrices

This appendix presents the full form of the basis function matrices used in Chapter 2 for the approximation of the displacement $u_i^{h,K} \in \mathbb{R}^2$, test function $w_i^{h,K} \in \mathbb{R}^2$, stress $\sigma_{ij}^{h,K} \in \mathbb{R}^{2\times 2}$ and stress test function $\sigma_{ij}^{h,K} \in \mathbb{R}^{2\times 2}$ over the element K. The superscript h refers to a variable being approximated by a polynomial basis with K referring to the element in which the basis exists; $i, j \in \{1, 2\}$ are tensor indices. Each function has an equivalent vector form which is respectively given as

$$\{u^{h,K}\} = \left\{ \begin{array}{c} u_1^{h,K} \\ u_2^{h,K} \end{array} \right\}, \quad \{w^{h,K}\} = \left\{ \begin{array}{c} w_1^{h,K} \\ w_2^{h,K} \end{array} \right\},$$

$$\{\sigma^{h,K}\} = \left\{ \begin{array}{c} \sigma_{11}^{h,K} \\ \sigma_{22}^{h,K} \\ \sigma_{12}^{h,K} \end{array} \right\} \quad \text{and} \quad \{\sigma^{h,K}\} = \left\{ \begin{array}{c} \tilde{\sigma}_{11}^{h,K} \\ \tilde{\sigma}_{22}^{h,K} \\ \tilde{\sigma}_{12}^{h,K} \end{array} \right\}.$$

All elements considered in this thesis are triangles with the basis constructed from three different types of function, depending on the polynomial order of the element p_K. Each triangle has three vertices labeled $v1$, $v2$ and $v2$ and three edges $e1$, $e2$ and $e3$, the respective positioning of the vertices and edges is provided by Figure 2.3. The three types of function are:

- Vertex shape functions exist in all elements, $\psi^{v1}, \psi^{v2}, \psi^{v3}$.
- Edge functions which exist for element with a polynomial order $p_K > 1$, $\psi_{p_e}^{e1}, \psi_{p_e}^{e2}$, and $\psi_{p_e}^{e3}$, with the edge polynomial order $p_e \in [2, p_K]$.
- Bubble functions which exist for element with a polynomial order $p_K > 2$, $\psi_{p_B}^{B}$, with the bubble function polynomial order $p_B \in [3, p_K]$.

The vertex, edge and bubble functions are respectively defined for the local element $\widehat{K}$ in (2.14), (2.15) and (2.16). The vector form of the displacement function is calculated using

$$\{u^{h,K}\} = [N^K]\{U^K\} \tag{A.0.1}$$

where $[N^K]$ is a matrix of shape the functions for an element K and $\{U^K\}$ is a vector of the basis functions coefficients which are solved for using the SIPG FE calculation in (2.23). The

full matrix form of (A.0.3) is

$$\{u^{h,K}\} = [N^K]\{U^K\}$$

$$\{u^{h,K}\} = \begin{bmatrix} \psi^{v1} & 0 \\ 0 & \psi^{v1} \\ \psi^{v2} & 0 \\ 0 & \psi^{v2} \\ \psi^{v3} & 0 \\ 0 & \psi^{v3} \\ \psi_2^{e1} & 0 \\ 0 & \psi_2^{e1} \\ \vdots & \vdots \\ \psi_{p_K}^{e1} & 0 \\ 0 & \psi_{p_K}^{e1} \\ \psi_2^{e2} & 0 \\ 0 & \psi_2^{e2} \\ \vdots & \vdots \\ \psi_{p_K}^{e2} & 0 \\ 0 & \psi_{p_K}^{e2} \\ \psi_2^{e3} & 0 \\ 0 & \psi_2^{e3} \\ \vdots & \vdots \\ \psi_{p_K}^{e3} & 0 \\ 0 & \psi_{p_K}^{e3} \\ \psi_3^{B} & 0 \\ 0 & \psi_3^{B} \\ \vdots & \vdots \\ \psi_{p_K}^{B} & 0 \\ 0 & \psi_{p_K}^{B} \end{bmatrix}^\top \begin{pmatrix} U_1^{v1,K} \\ U_2^{v1,K} \\ U_1^{v2,K} \\ U_2^{v2,K} \\ U_1^{v3,K} \\ U_2^{v3,K} \\ U_{2,1}^{e1,K} \\ U_{2,2}^{e1,K} \\ \vdots \\ U_{p_K,1}^{e1,K} \\ U_{p_K,2}^{e1,K} \\ U_{2,1}^{e2,K} \\ U_{2,2}^{e2,K} \\ \vdots \\ U_{p_K,1}^{e2,K} \\ U_{p_K,2}^{e2,K} \\ U_{2,1}^{e3,K} \\ U_{2,2}^{e3,K} \\ \vdots \\ U_{p_K,1}^{e3,K} \\ U_{p_K,2}^{e3,K} \\ U_{3,1}^{B,K} \\ U_{3,2}^{B,K} \\ \vdots \\ U_{p_K,1}^{B,K} \\ U_{p_K,2}^{B,K} \end{pmatrix} \begin{matrix} \left.\vphantom{\begin{matrix} a \\ a \\ a \\ a \\ a \\ a \end{matrix}}\right] \\ \text{Vertex functions} \\ \left.\vphantom{\begin{matrix} a \\ a \\ a \\ a \\ a \\ a \\ a \\ a \\ a \\ a \\ a \\ a \end{matrix}}\right] \\ \text{Edge functions} \\ \left.\vphantom{\begin{matrix} a \\ a \\ a \\ a \\ a \\ a \\ a \\ a \\ a \\ a \\ a \\ a \end{matrix}}\right] \\ \text{Bubble functions} \\ \left.\vphantom{\begin{matrix} a \\ a \\ a \\ a \\ a \\ a \end{matrix}}\right] \end{matrix} \tag{A.0.2}$$

The coefficients for the vertex shape functions are defined $U_i^{v,K}$, where $i \in \{1, 2\}$ corresponds to the x and y direction respectively and $v \in \{v1, v2, v3\}$. For the edge functions the coefficient is $U_{p_e,i}^{e,K}$ where the edge the coefficient belongs to is $e \in e1, e2, e3$ and the polynomial order of the corresponding function is $p_e \in [2, p_K]$. Last $U_{i,p_B}^{B,K}$ is the coefficient for the set of element bubble functions where the polynomial order is $p_B \in [3, p_K]$ and B refers to the coefficient being a bubble type.

Next, very similarly to (A.0.2), the vector form of the test function is

$$\{w^{h,K}\} = [N^K]\{W^K\} \tag{A.0.3}$$

with its full form as

$$\{w^{h,K}\} = [N^K]\{W^K\}$$

$$\{w^{h,K}\} = \begin{bmatrix} \psi^{v1} & 0 \\ 0 & \psi^{v1} \\ \psi^{v2} & 0 \\ 0 & \psi^{v2} \\ \psi^{v3} & 0 \\ 0 & \psi^{v3} \\ \psi_2^{e1} & 0 \\ 0 & \psi_2^{e1} \\ \vdots & \vdots \\ \psi_{p_K}^{e1} & 0 \\ 0 & \psi_{p_K}^{e1} \\ \psi_2^{e2} & 0 \\ 0 & \psi_2^{e2} \\ \vdots & \vdots \\ \psi_{p_K}^{e2} & 0 \\ 0 & \psi_{p_K}^{e2} \\ \psi_2^{e3} & 0 \\ 0 & \psi_2^{e3} \\ \vdots & \vdots \\ \psi_{p_K}^{e3} & 0 \\ 0 & \psi_{p_K}^{e3} \\ \psi_3^{B} & 0 \\ 0 & \psi_3^{B} \\ \vdots & \vdots \\ \psi_{p_K}^{B} & 0 \\ 0 & \psi_{p_K}^{B} \end{bmatrix}^\top \begin{pmatrix} W_1^{v1,K} \\ W_2^{v1,K} \\ W_1^{v2,K} \\ W_2^{v2,K} \\ W_1^{v3,K} \\ W_2^{v3,K} \\ W_{2,1}^{e1,K} \\ W_{2,2}^{e1,K} \\ \vdots \\ W_{p_K,1}^{e1,K} \\ W_{p_K,2}^{e1,K} \\ W_{2,1}^{e2,K} \\ W_{2,2}^{e2,K} \\ \vdots \\ W_{p_K,1}^{e2,K} \\ W_{p_K,2}^{e2,K} \\ W_{2,1}^{e3,K} \\ W_{2,2}^{e3,K} \\ \vdots \\ W_{p_K,1}^{e3,K} \\ W_{p_K,2}^{e3,K} \\ W_{3,1}^{B,K} \\ W_{3,2}^{B,K} \\ \vdots \\ W_{p_K,1}^{B,K} \\ W_{p_K,2}^{B,K} \end{pmatrix} \begin{matrix} \\ \end{matrix} \begin{matrix} \text{Vertex functions} \\ \\ \\ \\ \\ \\ \\ \\ \\ \\ \\ \\ \\ \\ \text{Edge functions} \\ \\ \\ \\ \\ \\ \\ \\ \\ \\ \\ \\ \\ \\ \text{Bubble functions} \\ \\ \\ \\ \\ \\ \\ \end{matrix} \tag{A.0.4}$$

Where the forms $W_i^{v,K}$, $W_{p_e,i}^{e,K}$ and $W_{i,p_B}^{B,K}$ and directly analogous to $U_i^{v,K}$, $U_{p_e,i}^{e,K}$ and $U_{i,p_B}^{B,K}$.

The stress approximation over an element K is calculated using

$$\{\sigma^{h,K}\} = [D][B^K]\{U^K\} \tag{A.0.5}$$

where $[D]$ is the material stiffness matrix, described in (2.3) and $[B^K]$ is a matrix of the basis functions derivatives, which have an initial polynomial order up to p_K. The expanded form of

(A.0.5) is

$$\{\sigma^{h,K}\} = [D][B^K]\{U^K\}$$

$$\{\sigma^{h,K}\} = [D] \begin{bmatrix}
\nabla_1\psi^{v1} & 0 & \nabla_2\psi^{v1} \\
0 & \nabla_2\psi^{v1} & \nabla_1\psi^{v1} \\
\nabla_1\psi^{v2} & 0 & \nabla_2\psi^{v2} \\
0 & \nabla_2\psi^{v2} & \nabla_1\psi^{v2} \\
\nabla_1\psi^{v3} & 0 & \nabla_2\psi^{v3} \\
0 & \nabla_2\psi^{v3} & \nabla_1\psi^{v3} \\
\nabla_1\psi_2^{e1} & 0 & \nabla_2\psi_2^{e1} \\
0 & \nabla_2\psi_2^{e1} & \nabla_1\psi_2^{e1} \\
\vdots & \vdots & \vdots \\
\nabla_1\psi_{p_K}^{e1} & 0 & \nabla_2\psi_{p_K}^{e1} \\
0 & \nabla_2\psi_{p_K}^{e1} & \nabla_1\psi_{p_K}^{e1} \\
\nabla_1\psi_2^{e2} & 0 & \nabla_2\psi_2^{e2} \\
0 & \nabla_2\psi_2^{e2} & \nabla_1\psi_2^{e2} \\
\vdots & \vdots & \vdots \\
\nabla_1\psi_{p_K}^{e2} & 0 & \nabla_2\psi_{p_K}^{e2} \\
0 & \nabla_2\psi_{p_K}^{e2} & \nabla_1\psi_{p_K}^{e2} \\
\nabla_1\psi_2^{e3} & 0 & \nabla_2\psi_2^{e3} \\
0 & \nabla_2\psi_2^{e3} & \nabla_1\psi_2^{e3} \\
\vdots & \vdots & \vdots \\
\nabla_1\psi_{p_K}^{e3} & 0 & \nabla_2\psi_{p_K}^{e3} \\
0 & \nabla_2\psi_{p_K}^{e3} & \nabla_1\psi_{p_K}^{e3} \\
\nabla_1\psi_3^{B} & 0 & \nabla_2\psi_3^{B} \\
0 & \nabla_2\psi_3^{B} & \nabla_1\psi_3^{B} \\
\vdots & \vdots & \vdots \\
\nabla_1\psi_{p_K}^{B} & 0 & \nabla_2\psi_{p_K}^{B} \\
0 & \nabla_2\psi_{p_K}^{B} & \nabla_1\psi_{p_K}^{B}
\end{bmatrix}^{\top}
\left\{ \begin{array}{c}
U_1^{v1,K} \\ U_2^{v1,K} \\ U_1^{v2,K} \\ U_2^{v2,K} \\ U_1^{v3,K} \\ U_2^{v3,K} \\
U_{2,1}^{e1,K} \\ U_{2,2}^{e1,K} \\ \vdots \\ U_{p_K,1}^{e1,K} \\ U_{p_K,2}^{e1,K} \\
U_{2,1}^{e2,K} \\ U_{2,2}^{e2,K} \\ \vdots \\ U_{p_K,1}^{e2,K} \\ U_{p_K,2}^{e2,K} \\
U_{2,1}^{e3,K} \\ U_{2,2}^{e3,K} \\ \vdots \\ U_{p_K,1}^{e3,K} \\ U_{p_K,2}^{e3,K} \\
U_{3,1}^{B,K} \\ U_{3,2}^{B,K} \\ \vdots \\ U_{p_K,1}^{B,K} \\ U_{p_K,2}^{B,K}
\end{array} \right\}
\begin{array}{l}
\left.\vphantom{\begin{array}{c}U_1^{v1,K}\\U_2^{v1,K}\\U_1^{v2,K}\\U_2^{v2,K}\\U_1^{v3,K}\\U_2^{v3,K}\end{array}}\right] \text{Vertex functions} \\
\left.\vphantom{\begin{array}{c}U_{2,1}^{e1,K}\\U\\ \vdots\\U_{p_K,1}\\U_{p_K,2}\\U\\U\\ \vdots\\U_{p_K,1}\\U_{p_K,2}\\U\\U\\ \vdots\\U_{p_K,1}\\U_{p_K,2}^{e3,K}\end{array}}\right] \text{Edge functions} \\
\left.\vphantom{\begin{array}{c}U_{3,1}^{B,K}\\U_{3,2}^{B,K}\\ \vdots\\U_{p_K,1}^{B,K}\\U_{p_K,2}^{B,K}\end{array}}\right] \text{Bubble functions}
\end{array}
\tag{A.0.6}$$

The form of $\{U^K\}$ is the same as in (A.0.2). ∇_i is a differential operator, with $i = 1$ corresponding to a differential in x and $i = 2$ corresponding to a differential in y. Last the stress test function is calculated with

$$\{\sigma^{h,K}\} = [D][B^K]\{W^K\} \tag{A.0.7}$$

where $\{W^K\}$ and $[B^K]$ are respectively defined in (A.0.3) and (A.0.6).

Appendix B

Average boundary conditions

The average BCs enforce are defined in Chapter 2 with (2.52), (2.53) and (2.54). For the sake of readability the average displacement in x y and the average rotation condition are repeated here as

$$0 = \int_{\Omega_\Gamma} u_1 \ \mathrm{d}v \approx \sum_{K\in\mathcal{T}} \int_K [{N_u}^K]\{U^K\}\mathrm{d}v = \sum_{K\in\mathcal{T}} \int_K [{N_u}^K]\mathrm{d}v\{U^\mathcal{T}\}, \tag{B.0.1}$$

$$0 = \int_{\Omega_\Gamma} u_2 \ \mathrm{d}v \approx \sum_{K\in\mathcal{T}} \int_K [{N_v}^K]\{U^K\}\mathrm{d}v = \sum_{K\in\mathcal{T}} \int_K [{N_v}^K]\mathrm{d}v\{U^\mathcal{T}\} \tag{B.0.2}$$

and

$$0 = \int_{\Omega_\Gamma} \left(\frac{\partial u_2}{v} - \frac{\partial u_1}{\partial y}\right) \mathrm{d}v \approx \sum_{\Omega_\Gamma} \int_K [C^K]\{U^K\}\mathrm{d}v = \sum_{\Omega_\Gamma} \int_K [C^K]\mathrm{d}v\{U^\mathcal{T}\}. \tag{B.0.3}$$

Where $\{U^K\}$ has the form in (A.0.2) and, $[N_u^K]$, $[N_v^K]$ and $[C^K]$ are expressed in their full vector and matrix form as

$$[N_v^K] = \begin{Bmatrix} 0 \\ \psi^{v1} \\ 0 \\ \psi^{v2} \\ 0 \\ \psi^{v3} \\ \psi_2^{e1} \\ 0 \\ \vdots \\ \psi_{p_K}^{e1} \\ 0 \\ \psi_2^{e2} \\ 0 \\ \vdots \\ \psi_{p_K}^{e2} \\ 0 \\ \psi_2^{e3} \\ 0 \\ \vdots \\ \psi_{p_K}^{e3} \\ 0 \\ \psi_3^{B} \\ 0 \\ \vdots \\ \psi_{p_K}^{B} \\ 0 \end{Bmatrix}^\top \quad (\text{B.0.4}) \qquad [N_u^K] = \begin{Bmatrix} \psi^{v1} \\ 0 \\ \psi^{v2} \\ 0 \\ \psi^{v3} \\ 0 \\ \psi_2^{e1} \\ 0 \\ \vdots \\ \psi_{p_K}^{e1} \\ 0 \\ \psi_2^{e2} \\ 0 \\ \vdots \\ \psi_{p_K}^{e2} \\ 0 \\ \psi_2^{e3} \\ 0 \\ \vdots \\ \psi_{p_K}^{e3} \\ 0 \\ \psi_3^{B} \\ 0 \\ \vdots \\ \psi_{p_K}^{B} \\ 0 \end{Bmatrix}^\top \quad (\text{B.0.5})$$

$$[C^K] = \begin{bmatrix} -\nabla_2\psi^{v1} \\ \nabla_1\psi^{v1} \\ -\nabla_2\psi^{v2} \\ \nabla_1\psi^{v2} \\ -\nabla_2\psi^{v3} \\ \nabla_1\psi^{v3} \end{bmatrix}^\top \begin{matrix} \\ \\ \\ \\ \\ \\ \end{matrix} \text{Vertex functions}$$

$$\begin{bmatrix} -\nabla_2\psi_2^{e1} \\ \nabla_1\psi_2^{e1} \\ \vdots \\ -\nabla_2\psi_{p_K}^{e1} \\ \nabla_1\psi_{p_K}^{e1} \\ -\nabla_2\psi_2^{e2} \\ \nabla_1\psi_2^{e2} \\ \vdots \\ -\nabla_2\psi_{p_K}^{e2} \\ \nabla_1\psi_{p_K}^{e2} \\ -\nabla_2\psi_2^{e3} \\ \nabla_1\psi_2^{e3} \\ \vdots \\ -\nabla_2\psi_{p_K}^{e3} \\ \nabla_1\psi_{p_K}^{e3} \end{bmatrix} \text{Edge functions}$$

$$\begin{bmatrix} -\nabla_2\psi_3^{B} \\ \nabla_1\psi_3^{B} \\ \vdots \\ -\nabla_2\psi_{p_K}^{B} \\ \nabla_1\psi_{p_K}^{B} \end{bmatrix} \text{Bubble functions} \quad (\text{B.0.6})$$

Appendix C

Eshelby Stress term

A term of the Eshelby stress calculation requires $h_{ij}^{h,K} = \nabla_j u_i^{h,K}$, see (3.7) for the definition of Eshelby stress. However, it is convenient to calculate the terms of $h_{ij}^{h,K}$ for K in vector form since the coefficients to the basis of determine $u_i^{h,K}$ are already expressed in vector form,

$$\{h^{h,K}\} = \left[\frac{u_1^{h,K}}{\partial x} \; \frac{u_2^{h,K}}{\partial x} \; \frac{u_1^{h,K}}{\partial y} \; \frac{u_2^{h,K}}{\partial y}\right]^\top = [H^K]\{U^K\} \tag{C.0.1}$$

where

$$
\{h\} = \begin{bmatrix}
\nabla_1\psi^{v1} & 0 & \nabla_2\psi^{v1} & 0 \\
0 & \nabla_2\psi^{v1} & 0 & \nabla_1\psi^{v1} \\
\nabla_1\psi^{v2} & 0 & \nabla_2\psi^{v2} & 0 \\
0 & \nabla_2\psi^{v2} & 0 & \nabla_1\psi^{v2} \\
\nabla_1\psi^{v3} & 0 & \nabla_2\psi^{v3} & 0 \\
0 & \nabla_2\psi^{v3} & 0 & \nabla_1\psi^{v3} \\
\nabla_1\psi_2^{e1} & 0 & \nabla_2\psi_2^{e1} & 0 \\
0 & \nabla_2\psi_2^{e1} & 0 & \nabla_1\psi_2^{e1} \\
\vdots & \vdots & \vdots & \vdots \\
\nabla_1\psi_{p_K}^{e1} & 0 & \nabla_2\psi_{p_K}^{e1} & 0 \\
0 & \nabla_2\psi_{p_K}^{e1} & 0 & \nabla_1\psi_{p_K}^{e1} \\
\nabla_1\psi_2^{e2} & 0 & \nabla_2\psi_2^{e2} & 0 \\
0 & \nabla_2\psi_2^{e2} & 0 & \nabla_1\psi_2^{e2} \\
\vdots & \vdots & \vdots & \vdots \\
\nabla_1\psi_{p_K}^{e2} & 0 & \nabla_2\psi_{p_K}^{e2} & 0 \\
0 & \nabla_2\psi_{p_K}^{e2} & 0 & \nabla_1\psi_{p_K}^{e2} \\
\nabla_1\psi_2^{e3} & 0 & \nabla_2\psi_2^{e3} & 0 \\
0 & \nabla_2\psi_2^{e3} & 0 & \nabla_1\psi_2^{e3} \\
\vdots & \vdots & \vdots & \vdots \\
\nabla_1\psi_{p_K}^{e3} & 0 & \nabla_2\psi_{p_K}^{e3} & 0 \\
0 & \nabla_2\psi_{p_K}^{e3} & 0 & \nabla_1\psi_{p_K}^{e3} \\
\nabla_1\psi_3^{B} & 0 & \nabla_2\psi_3^{B} & 0 \\
0 & \nabla_2\psi_3^{B} & 0 & \nabla_1\psi_3^{B} \\
\vdots & \vdots & \vdots & \vdots \\
\nabla_1\psi_{p_K}^{B} & 0 & \nabla_2\psi_{p_K}^{B} & 0 \\
0 & \nabla_2\psi_{p_K}^{B} & 0 & \nabla_1\psi_{p_K}^{B}
\end{bmatrix}^\top
\left\{\begin{matrix}
U_1^{v1,K} \\
U_2^{v1,K} \\
U_1^{v2,K} \\
U_2^{v2,K} \\
U_1^{v3,K} \\
U_2^{v3,K} \\
U_{2,1}^{e1,K} \\
U_{2,2}^{e1,K} \\
\vdots \\
U_{p_K,1}^{e1,K} \\
U_{p_K,2}^{e1,K} \\
U_{2,1}^{e2,K} \\
U_{2,2}^{e2,K} \\
\vdots \\
U_{p_K,1}^{e2,K} \\
U_{p_K,2}^{e2,K} \\
U_{2,1}^{e3,K} \\
U_{2,2}^{e3,K} \\
\vdots \\
U_{p_K,1}^{e3,K} \\
U_{p_K,2}^{e3,K} \\
U_{3,1}^{B,K} \\
U_{3,2}^{B,K} \\
\vdots \\
U_{p_K,1}^{B,K} \\
U_{p_K,2}^{B,K}
\end{matrix}\right\}
\begin{matrix}
\left.\vphantom{\begin{matrix}U\\U\\U\\U\\U\\U\end{matrix}}\right]\text{Vertex functions} \\
\left.\vphantom{\begin{matrix}U\\U\\U\\U\\U\\U\\U\\U\\U\\U\\U\\U\\U\\U\\U\end{matrix}}\right]\text{Edge functions} \\
\left.\vphantom{\begin{matrix}U\\U\\U\\U\\U\end{matrix}}\right]\text{Bubble functions}
\end{matrix}
\tag{C.0.2}
$$

Appendix D

Error estimator terms

The determine the residual based *a posteriori* error estimator η, it is necessary to find the divergence of $\sigma_{ij}^{h,K}$ at Gauss points on the interior of an element K. The divergence of stress is used in (4.31) and has the vector form

$$\{\nabla\sigma^{h,K}\} = \left\{ \begin{array}{c} \frac{\partial\sigma_{11}^{h,K}}{\partial x} + \frac{\partial\sigma_{12}^{h,K}}{\partial y} \\ \frac{\partial\sigma_{21}^{h,K}}{\partial x} + \frac{\partial\sigma_{22}^{h,K}}{\partial y} \end{array} \right\} = [D_2][BB^K]\{U^K\} \tag{D.0.1}$$

where the form of $\{U^K\}$ is given in (A.0.3) and $[D_2]$ is the matrix

$$D_2 = \left[\begin{array}{cccccccc} D(1,1) & D(1,3) & D(3,1) & D(3,3) & D(1,3) & D(1,2) & D(3,3) & D(3,2) \\ D(3,1) & D(3,3) & D(2,1) & D(2,3) & D(3,3) & D(3,2) & D(2,3) & D(2,2) \end{array} \right]. \tag{D.0.2}$$

The entries (i,j) of the entries in $[D_2]$ correspond to position of entries in the material stiffness matrix $[D]$ defined in (2.3). $[BB^K]$ is a matrix of basis functions, up to an initial polynomial order p_K, with a second order derivative applied. The full form of $[BB^K]$ is

$$
[BB^K] = \begin{bmatrix}
\nabla_1\nabla_1\psi_2^{e1} & 0 & \nabla_1\nabla_2\psi_2^{e1} & 0 & \nabla_1\nabla_2\psi_2^{e1} & 0 & \nabla_2\nabla_2\psi_2^{e1} & 0 \\
0 & \nabla_1\nabla_1\psi_2^{e1} & 0 & \nabla_1\nabla_2\psi_2^{e1} & 0 & \nabla_1\nabla_2\psi_2^{e1} & 0 & \nabla_2\nabla_2\psi_2^{e1} \\
\vdots & \vdots & \vdots & \vdots & \vdots & \vdots & \vdots & \vdots \\
\nabla_1\nabla_1\psi_{p_K}^{e1} & 0 & \nabla_1\nabla_2\psi_{p_K}^{e1} & 0 & \nabla_1\nabla_2\psi_{p_K}^{e1} & 0 & \nabla_2\nabla_2\psi_{p_K}^{e1} & 0 \\
0 & \nabla_1\nabla_1\psi_{p_K}^{e1} & 0 & \nabla_1\nabla_2\psi_{p_K}^{e1} & 0 & \nabla_1\nabla_2\psi_{p_K}^{e1} & 0 & \nabla_2\nabla_2\psi_{p_K}^{e1} \\
\nabla_1\nabla_1\psi_2^{e2} & 0 & \nabla_1\nabla_2\psi_2^{e2} & 0 & \nabla_1\nabla_2\psi_2^{e2} & 0 & \nabla_2\nabla_2\psi_2^{e2} & 0 \\
0 & \nabla_1\nabla_1\psi_2^{e2} & 0 & \nabla_1\nabla_2\psi_2^{e2} & 0 & \nabla_1\nabla_2\psi_2^{e2} & 0 & \nabla_2\nabla_2\psi_2^{e2} \\
\vdots & \vdots & \vdots & \vdots & \vdots & \vdots & \vdots & \vdots \\
\nabla_1\nabla_1\psi_{p_K}^{e2} & 0 & \nabla_1\nabla_2\psi_{p_K}^{e2} & 0 & \nabla_1\nabla_2\psi_{p_K}^{e2} & 0 & \nabla_2\nabla_2\psi_{p_K}^{e2} & 0 \\
0 & \nabla_1\nabla_1\psi_{p_K}^{e2} & 0 & \nabla_1\nabla_2\psi_{p_K}^{e2} & 0 & \nabla_1\nabla_2\psi_{p_K}^{e2} & 0 & \nabla_2\nabla_2\psi_{p_K}^{e2} \\
\nabla_1\nabla_1\psi_2^{e3} & 0 & \nabla_1\nabla_2\psi_2^{e3} & 0 & \nabla_1\nabla_2\psi_2^{e3} & 0 & \nabla_2\nabla_2\psi_2^{e3} & 0 \\
0 & \nabla_1\nabla_1\psi_2^{e3} & 0 & \nabla_1\nabla_2\psi_2^{e3} & 0 & \nabla_1\nabla_2\psi_2^{e3} & 0 & \nabla_2\nabla_2\psi_2^{e3} \\
\vdots & \vdots & \vdots & \vdots & \vdots & \vdots & \vdots & \vdots \\
\nabla_1\nabla_1\psi_{p_K}^{e3} & 0 & \nabla_1\nabla_2\psi_{p_K}^{e3} & 0 & \nabla_1\nabla_2\psi_{p_K}^{e3} & 0 & \nabla_2\nabla_2\psi_{p_K}^{e3} & 0 \\
0 & \nabla_1\nabla_1\psi_{p_K}^{e3} & 0 & \nabla_1\nabla_2\psi_{p_K}^{e3} & 0 & \nabla_1\nabla_2\psi_{p_K}^{e3} & 0 & \nabla_2\nabla_2\psi_{p_K}^{e3} \\
\nabla_1\nabla_1\psi_3^{B} & 0 & \nabla_1\nabla_2\psi_3^{B} & 0 & \nabla_1\nabla_2\psi_3^{B} & 0 & \nabla_2\nabla_2\psi_3^{B} & 0 \\
0 & \nabla_1\nabla_1\psi_3^{B} & 0 & \nabla_1\nabla_2\psi_3^{B} & 0 & \nabla_1\nabla_2\psi_3^{B} & 0 & \nabla_2\nabla_2\psi_3^{B} \\
\vdots & \vdots & \vdots & \vdots & \vdots & \vdots & \vdots & \vdots \\
\nabla_1\nabla_1\psi_{p_K}^{B} & 0 & \nabla_1\nabla_2\psi_{p_K}^{B} & 0 & \nabla_1\nabla_2\psi_{p_K}^{B} & 0 & \nabla_2\nabla_2\psi_{p_K}^{B} & 0 \\
0 & \nabla_1\nabla_1\psi_{p_K}^{B} & 0 & \nabla_1\nabla_2\psi_{p_K}^{B} & 0 & \nabla_1\nabla_2\psi_{p_K}^{B} & 0 & \nabla_2\nabla_2\psi_{p_K}^{B}
\end{bmatrix}^\top
$$

Vertex functions

Edge functions

Bubble functions

(D.0.3)

References

[1] C. Miehe, E. Gürses, and M. Birkle, "A computational framework of configurational-force-driven brittle fracture based on incremental energy minimization," *International Journal of Fracture*, vol. 145, no. 4, pp. 245–259, 2007.

[2] J. Eischen, "An improved method for computing the J2 integral," *Engineering Fracture Mechanics*, vol. 26, no. 5, pp. 691 – 700, 1987.

[3] R. Su and H. Sun, "Numerical solutions of two-dimensional anisotropic crack problems," *International Journal of Solids and Structures*, vol. 40, no. 18, pp. 4615–4635, 2003.

[4] C. Miehe and E. Gürses, "A robust algorithm for configurational-force-driven brittle crack propagation with r-adaptive mesh alignment," *International Journal for Numerical Methods in Engineering*, vol. 72, no. 2, pp. 127–155, 2007.

[5] N. Sukumar and T. Belytschko, "Arbitrary branched and intersecting cracks with the extended finite element method," *International Journal for Numerical Methods in Engineering*, vol. 48, no. 12, pp. 1741–1760, 2000.

[6] W. Ai and C. Augarde, "A multi-cracked particle method for complex fracture problems in 2D," *Mathematics and Computers in Simulation*, vol. 150, pp. 1 – 24, 2018.

[7] G. Hattori, I. A. Alatawi, and J. Trevelyan, "An extended boundary element method formulation for the direct calculation of the stress intensity factors in fully anisotropic materials," *International Journal for Numerical Methods in Engineering*, vol. 109, no. 7, pp. 965–981, 2017.

[8] P. Thompson, "How much did the liberty shipbuilders learn? new evidence for an old case study," *Journal of Political Economy*, vol. 109, no. 1, pp. 103–137, 2001.

[9] P. Withey, "Fatigue failure of the de havilland comet I," *Engineering failure analysis*, vol. 4, no. 2, pp. 147–154, 1997.

[10] Norway Justise Police Departement, "The alexander l. kielland-accident : from a commission appointed by royal decree of 28th march," *Ministry of Justice and Police*, 1981. Translation of "Alexander L. Kielland"-ulykken.

[11] "Hunterston B nuclear reactor to restart after 'cracks' closure." https://www.bbc.co.uk/news/uk-scotland-49410625. Accessed: 2019-08-24.

[12] "Nuclear regulator permits restarting of reactor 4 at hunterson B." https://www.theguardian.com/business/2019/aug/20/edf-nuclear-reactor-restarting-hunterston-b. Accessed: 2019-08-24.

[13] H. Westergaard, "Bearing pressures and cracks," *Journal of Applied Mechanics*, vol. 6, no. 2, pp. A49–A53, 1939.

[14] N. Muskhelishvili, *Some basic problems of the mathematical theory of elasticity*, vol. 17404. Noordhoff, Groningen,, 1953.

[15] M. Williams, "Stress singularities resulting from various boundary conditions in angular corners of plates in extension," *Journal of Applied Mechanics*, vol. 19, no. 4, pp. 526–528, 1952.

[16] G. Irwin, "Analysis of stresses and strains near the end of a crack traversing a plate," *SPIE Milestone Series MS*, vol. 137, pp. 167–170, 1957.

[17] J. D. Eshelby, "The force on an elastic singularity," *Philosophical Transactions of the Royal Society A*, vol. 224, no. 877, pp. 87–112, 1951.

[18] J. Eshelby, "The determination of the elastic field of an ellipsoidal inclusion, and related problems," *The Royal Society*, vol. 241, no. 1226, pp. 376–396, 1957.

[19] J. Rice, "Limitations to the small scale yielding approximation for crack tip plasticity," *Journal of the Mechanics and Physics of Solids*, vol. 22, no. 1, pp. 17 – 26, 1974.

[20] A. Griffith, "VI.The phenomena of rupture and flow in solids," *Philosophical Transactions of the Royal Society of London A: Mathematical, Physical and Engineering Sciences*, vol. 221, no. 582-593, pp. 163–198, 1921.

[21] P. Paris, "A rational analytic theory of fatigue," *Trends in Engineering*, vol. 13, pp. 9–14, 1961.

[22] J. Rice, "A path independent integral and the approximate analysis of strain concentration by notches and cracks," *Journal of Applied Mechanics*, vol. 35, no. 2, pp. 379–386, 1968.

[23] J. Yau, S. Wang, and H. Corten, "A mixed-mode crack analysis of isotropic solids using conservation laws of elasticity," *Journal of Applied Mechanics*, vol. 47, no. 2, pp. 335–341, 1980.

[24] T. Belytschko and T. Black, "Elastic crack growth in finite elements with minimal remeshing," *International journal for numerical methods in engineering*, vol. 45, no. 5, pp. 601–620, 1999.

[25] G. Barenblatt, "The Mathematical Theory of Equilibrium Cracks in Brittle Fracture," *Advances in Applied Mechanics*, vol. 7, pp. 55 – 129, 1962.

[26] D. Dugdale, "Yielding of steel sheets containing slits," *Journal of the Mechanics and Physics of Solids*, vol. 8, no. 2, pp. 100 – 104, 1960.

[27] A. Hillerborg, M. Modéer, and P.-E. Petersson, "Analysis of crack formation and crack growth in concrete by means of fracture mechanics and finite elements," *Cement and concrete research*, vol. 6, no. 6, pp. 773–781, 1976.

[28] J. Planas and M. Elices, "Asymptotic analysis of a cohesive crack: 1. theoretical background," *International Journal of Fracture*, vol. 55, no. 2, pp. 153–177, 1992.

[29] K. Park and G. Paulino, "Cohesive zone models: a critical review of traction-separation relationships across fracture surfaces," *Applied Mechanics Reviews*, vol. 64, no. 6, p. 060802(20), 2011.

[30] M. Elices, G. Guinea, J. Gomez, and J. Planas, "The cohesive zone model: advantages, limitations and challenges," *Engineering fracture mechanics*, vol. 69, no. 2, pp. 137–163, 2002.

[31] H. Tada, P. Paris, and G. Irwin, "The stress analysis of cracks," *Del Research Corp, Hellertown PA*, 1973.

[32] G. Hattori, J. Trevelyan, C. E. Augarde, W. M. Coombs, and A. C. Aplin, "Numerical simulation of fracking in shale rocks: current state and future approaches," *Archives of Computational Methods in Engineering*, vol. 24, no. 2, pp. 281–317, 2017.

[33] G. Strang and G. Fix, *An analysis of the finite element method*, vol. 212. Prentice-hall Englewood Cliffs, NJ, 1973.

[34] M. Lan, H. Waisman, and I. Harari, "A direct analytical method to extract mixed-mode components of strain energy release rates from Irwin's integral using extended finite element method," *International Journal for Numerical Methods in Engineering*, vol. 95, no. 12, pp. 1033–1052, 2013.

[35] T. Fries and T. Belytschko, "The extended/generalized finite element method: an overview of the method and its applications," *International journal for numerical methods in engineering*, vol. 84, no. 3, pp. 253–304, 2010.

[36] C. Brebbia and J. Dominguez, "Boundary element methods for potential problems," *Applied Mathematical Modelling*, vol. 1, no. 7, pp. 372–378, 1977.

[37] V. Rokhlin, "Rapid solution of integral equations of classical potential theory," *Journal of computational physics*, vol. 60, no. 2, pp. 187–207, 1985.

[38] F. García, A. Sáez, and J. Domínguez, "Traction boundary elements for cracks in anisotropic solids," *Engineering analysis with boundary elements*, vol. 28, no. 6, pp. 667–676, 2004.

[39] M. Guiggiani, G. Krishnasamy, T. J. Rudolphi, and F. Rizzo, "A general algorithm for the numerical solution of hypersingular boundary integral equations," *Journal of applied mechanics*, vol. 59, p. 604, 1992.

[40] T. A. Cruse, "BIE fracture mechanics analysis: 25 years of developments," *Computational Mechanics*, vol. 18, no. 1, pp. 1–11, 1996.

[41] A. Portela, M. Aliabadi, and D. Rooke, "The dual boundary element method: effective implementation for crack problems," *International Journal for Numerical Methods in Engineering*, vol. 33, no. 6, pp. 1269–1287, 1992.

[42] R. Simpson and J. Trevelyan, "A partition of unity enriched dual boundary element method for accurate computations in fracture mechanics," *Computer Methods in Applied Mechanics and Engineering*, vol. 200, no. 1-4, pp. 1–10, 2011.

[43] R. Simpson, *Enrichment of the boundary element method through the partition of unity method for fracture analysis using local and global formulations*. PhD thesis, Durham University, 2010.

[44] B. Bourdin, G. Francfort, and J. Marigo, "Numerical experiments in revisited brittle fracture," *Journal of the Mechanics and Physics of Solids*, vol. 48, no. 4, pp. 797 – 826, 2000.

[45] M. Ambati, T. Gerasimov, and L. De Lorenzis, "A review on phase-field models of brittle fracture and a new fast hybrid formulation," *Computational Mechanics*, vol. 55, pp. 383–405, Feb 2015.

[46] C. Miehe, M. Hofacker, and F. Welschinger, "A phase field model for rate-independent crack propagation: Robust algorithmic implementation based on operator splits," *Computer Methods in Applied Mechanics and Engineering*, vol. 199, no. 45, pp. 2765 – 2778, 2010.

[47] C. Miehe, F. Welschinger, and M. Hofacker, "Thermodynamically consistent phase-field models of fracture: Variational principles and multi-field FE implementations," *International Journal for Numerical Methods in Engineering*, vol. 83, no. 10, pp. 1273–1311, 2010.

[48] P. Kerfriden, J.-C. Passieux, and S. P.-A. Bordas, "Local/global model order reduction strategy for the simulation of quasi-brittle fracture," *International Journal for Numerical Methods in Engineering*, vol. 89, no. 2, pp. 154–179, 2012.

[49] M. Strobl and T. Seelig, "Restrictions in phase field modeling of brittle fracture," *PAMM*, vol. 18, no. 1, p. e201800157, 2018.

[50] T. Belytschko, Y. Y. Lu, and L. Gu, "Element-free Galerkin methods," *International Journal for Numerical Methods in Engineering*, vol. 37, no. 2, pp. 229–256, 1994.

[51] T. Belytschko, L. Gu, and Y. Lu, "Fracture and crack growth by element free Galerkin methods," *Modelling and Simulation in Materials Science and Engineering*, vol. 2, no. 3A, p. 519, 1994.

[52] D. Organ, M. Fleming, T. Terry, and T. Belytschko, "Continuous meshless approximations for nonconvex bodies by diffraction and transparency," *Computational Mechanics*, vol. 18, pp. 225–235, Jul 1996.

[53] M. Fleming, Y. Chu, B. Moran, and T. Belytschko, "Enriched element-free Galerkin methods for crack tip fields," *International Journal for Numerical Methods in Engineering*, vol. 40, no. 8, pp. 1483–1504, 1997.

[54] X. Zhuang, *Meshless methods: theory and application in 3D fracture modelling with level sets*. PhD thesis, Durham University, 2010.

[55] W. Ai, *Computational fracture modelling by an adaptive cracking particle method*. PhD thesis, Durham University, 2018.

[56] V. P. Nguyen, T. Rabczuk, S. Bordas, and M. Duflot, "Meshless methods: a review and computer implementation aspects," *Mathematics and Computers in Simulation*, vol. 79, no. 3, pp. 763–813, 2008.

[57] T. Belytschko, Y. Krongauz, D. Organ, M. Fleming, and P. Krysl, "Meshless methods: an overview and recent developments," *Computer Methods in Applied Mechanics and Engineering*, vol. 139, no. 1-4, pp. 3–47, 1996.

[58] S. A. Silling, "Reformulation of elasticity theory for discontinuities and long-range forces," *Journal of the Mechanics and Physics of Solids*, vol. 48, no. 1, pp. 175–209, 2000.

[59] G. Hattori, J. Trevelyan, and W. M. Coombs, "A non-ordinary state-based peridynamics framework for anisotropic materials," *Computer Methods in Applied Mechanics and Engineering*, vol. 339, pp. 416–442, 2018.

[60] R. Denzer, F. J. Barth, and P. Steinmann, "Studies in elastic fracture mechanics based on the material force method," *International Journal for Numerical Methods in Engineering*, vol. 58, no. 12, pp. 1817–1835, 2003.

[61] R. Barsoum, "Triangular quarter-point elements as elastic and perfectly-plastic crack tip elements," *International Journal for numerical Methods in engineering*, vol. 11, no. 1, pp. 85–98, 1977.

[62] F. Li, C. Shih, and A. Needleman, "A comparison of methods for calculating energy release rates," *Engineering Fracture Mechanics*, vol. 21, no. 2, pp. 405–421, 1985.

[63] C. Shih, B. Moran, and T. Nakamura, "Energy release rate along a three-dimensional crack front in a thermally stressed body," *International Journal of Fracture*, vol. 30, no. 2, pp. 79–102, 1986.

[64] I. Raju and K. Shivakumar, "An equivalent domain integral method in the two-dimensional analysis of mixed mode crack problems," *Engineering Fracture Mechanics*, vol. 37, no. 4, pp. 707 – 725, 1990.

[65] R. Bird, W. Coombs, and S. Giani, "A posteriori discontinuous Galerkin error estimator for linear elasticity," *Applied Mathematics and Computation*, vol. Awaiting publication, no. 344, pp. 78–96, 2019.

[66] N. S. Ottosen and H. Petersson, *Introduction to the Finite Element Method*. Prentice-Hall, 1992.

[67] D. Arnold, F. Brezzi, B. Cockburn, and D. Marini, "Unified analysis of discontinuous Galerkin methods for elliptic problems," *SIAM Journal on Numerical Analysis*, vol. 39, no. 5, pp. 1749–1779, 2002.

[68] V. P. Nguyen, P. Kerfriden, M. Brino, S. P. Bordas, and E. Bonisoli, "Nitsche's method for two and three dimensional nurbs patch coupling," *Computational Mechanics*, vol. 53, no. 6, pp. 1163–1182, 2014.

[69] S. Prudhomme, F. Pascal, J. Oden, and A. Romkes, "Review of a priori error estimation for discontinuous Galerkin methods," tech. rep., 2000.

[70] B. Ayuso de Dios, F. Brezzi, L. D. Marini, J. Xu, and L. Zikatanov, "A simple preconditioner for a discontinuous Galerkin method for the stokes problem," *Journal of Scientific Computing*, vol. 58, pp. 517–547, Mar 2014.

[71] J. Nitsche, "Über ein variationsprinzip zur lösung von dirichlet-problemen bei verwendung von teilräumen, die keinen randbedingungen unterworfen sind," in *Abhandlungen aus dem mathematischen Seminar der Universität Hamburg*, vol. 36, pp. 9–15, 1971.

[72] B. Riviere, *Discontinuous Galerkin methods for solving elliptic and parabolic equations: theory and implementation*. SIAM, 2008.

[73] P. Solin, K. Segeth, and I. Dolezel, *Higher-order finite element methods*. CRC Press, 2003.

[74] G. H. Golub and J. H. Welsch, "Calculation of Gauss quadrature rules," *Mathematics of Computation*, vol. 23, no. 106, pp. 221–230, 1969.

[75] R. Bird, W. Coombs, and S. Giani, "A quasi-static discontinuous Galerkin configurational force crack propagation method for brittle materials," *International Journal for Numerical Methods in Engineering*, vol. 113, no. 7, pp. 1061–1080, 2017.

[76] J. Eshelby, "The elastic energy-momentum tensor," *Journal of elasticity*, vol. 5, no. 3-4, pp. 321–335, 1975.

[77] G. Maugin and C. Trimarco, "Pseudomomentum and material forces in nonlinear elastic: Variational formulations and applications to brittle fracture," *Acta Mechanica*, vol. 94, pp. 1–28, 1992.

[78] G. A. Maugin, *Material inhomogeneities in elasticity*, vol. 3. CRC Press, 1993.

[79] M. Gurtin and P. Podio-Guidugli, "Configurational forces and the basic laws for crack propagation," *Journal of the Mechanics and Physics of Solids*, vol. 44, pp. 905–927, 1996.

[80] M. Gurtin, *Configurational forces as basic concepts of continuum physiscs*. Springer-Verlag, New York, 2000.

[81] P. Steinmann, "Application of material forces to hyperelastostatic fracture mechanics. I. Continuum mechanical setting," *International Journal of Solids and Structures*, vol. 37, no. 48-50, pp. 7371–7391, 2000.

[82] P. Steinmann, D. Ackermann, and F. J. Barth, "Application of material forces to hyperelastostatic fracture mechanics. II. Computational setting," *International Journal of Solids and Structures*, vol. 38, pp. 5509–5526, 2001.

[83] R. Mueller and G. Maugin, "On material forces and finite element discretizations," *Computational Mechanics*, vol. 29, no. 1, pp. 52–60, 2002.

[84] R. Larsson and M. Fagerström, "A framework for fracture modelling based on the material forces concept with XFEM kinematics," *International Journal for Numerical Methods in Engineering*, vol. 62, no. 13, pp. 1763–1788, 2005.

[85] M. Fagerström and R. Larsson, "Theory and numerics for finite deformation fracture modelling using strong discontinuities," *International Journal for Numerical Methods in Engineering*, vol. 66, no. 6, pp. 911–948, 2006.

[86] Y. Shen and A. Lew, "An optimally convergent discontinuous Galerkin-based extended finite element method for fracture mechanics," *International Journal for Numerical Methods in Engineering*, vol. 82, no. 6, pp. 716–755, 2010.

[87] J. Kim and G. H. Paulino, "The interaction integral for fracture of orthotropic functionally graded materials: evaluation of stress intensity factors," *International Journal of Solids and Structures*, vol. 40, no. 15, pp. 3967–4001, 2003.

[88] R. E. Smelser and M. E. Gurtin, "On the J-integral for bi-material bodies," *International Journal of Fracture*, vol. 13, no. 3, pp. 382–384, 1977.

[89] E. Gürses and C. Miehe, "A computational framework of three-dimensional configurational-force-driven brittle crack propagation," *Computer Methods in Applied Mechanics and Engineering*, vol. 198, no. 15, pp. 1413–1428, 2009.

[90] Ł. Kaczmarczyk, M. Nezhad, and C. Pearce, "Three-dimensional brittle fracture: configurational-force-driven crack propagation," *International Journal for Numerical Methods in Engineering*, vol. 97, no. 7, pp. 531–550, 2014.

[91] K. Runesson, F. Larsson, and P. Steinmann, "On energetic changes due to configurational motion of standard continua," *International Journal of Solids and Structures*, vol. 46, no. 6, pp. 1464–1475, 2009.

[92] J. Tillberg, F. Larsson, and K. Runesson, "On the role of material dissipation for the crack-driving force," *International Journal of Plasticity*, vol. 26, no. 7, pp. 992–1012, 2010.

[93] B. Näser, M. Kaliske, and R. Müller, "Material forces for inelastic models at large strains: application to fracture mechanics," *Computational Mechanics*, vol. 40, no. 6, pp. 1005–1013, 2007.

[94] B. Näser, M. Kaliske, H. Dal, and C. Netzker, "Fracture mechanical behaviour of visco-elastic materials: application to the so-called dwell-effect," *ZAMM-Journal of Applied Mathematics and Mechanics/Zeitschrift für Angewandte Mathematik und Mechanik*, vol. 89, no. 8, pp. 677–686, 2009.

[95] K. Özenç, M. Kaliske, G. Lin, and G. Bhashyam, "Evaluation of energy contributions in elasto-plastic fracture: a review of the configurational force approach," *Engineering Fracture Mechanics*, vol. 115, pp. 137–153, 2014.

[96] R. Bird, W. Coombs, and S. Giani, "On the accurate determination of the configurational force for brittle fracture," *Engineering Fracture Mechanics*, vol. 216, p. 106370, 2019.

[97] P. Thoutireddy and M. Ortiz, "A variational r-adaption and shape-optimization method for finite-deformation elasticity," *International Journal for Numerical Methods in Engineering*, vol. 61, no. 1, pp. 1–21, 2004.

[98] P. Heintz, F. Larsson, P. Hansbo, and K. Runesson, "Adaptive strategies and error control for computing material forces in fracture mechanics," *International Journal for Numerical Methods in Engineering*, vol. 60, no. 7, pp. 1287–1299, 2004.

[99] R. Jonathan, "Adaptive precision floating-point arithmetic and fast robust geometric predicates," *Discrete & Computational Geometry*, vol. 18, pp. 305–363, Oct. 1997.

[100] R. Denzer and A. Menzel, "Configurational forces for quasi-incompressible large strain electro-viscoelasticity – application to fracture mechanics," *European Journal of Mechanics - A/Solids*, vol. 48, pp. 3 – 15, 2014. Frontiers in Finite-Deformation Electromechanics.

[101] E. Kuhl, R. Denzer, F. Barth, and P. Denzer, "Application of the material force method to thermo-hyperelasticity," *Computer Methods in Applied Mechanics and Engineering*, vol. 193, no. 30–32, pp. 3303 – 3325, 2004. Computational Failure Mechanics.

[102] W. Ochensberger and O. Kolednik, "A new basis for the application of the J -integral for cyclically loaded cracks in elastic–plastic materials," *International Journal of Fracture*, vol. 189, no. 1, pp. 77–101, 2014.

[103] A. Menzel, R. Denzer, and P. Steinmann, "Material forces in computational single-slip crystal-plasticity," *Computational Materials Science*, vol. 32, no. 3–4, pp. 446 – 454, 2005.

[104] T. Pin and T. Pian, "On the convergence of the finite element method for problems with singularity," *International Journal of solids and Structures*, vol. 9, no. 3, pp. 313–321, 1973.

[105] C. Schwab, *p-and hp-finite element methods: Theory and applications in solid and fluid mechanics*. Oxford University Press, 1998.

[106] R. Simpson, *Enrichment of the boundary element method through the partition of unity method for fracture analysis using local and global formulations*. PhD thesis, Durham University, 2010.

[107] C. Sun and Z.-H. Jin, "Chapter 3 - the elastic stress field around a crack tip," in *Fracture Mechanics* (C. Sun and Z.-H. Jin, eds.), pp. 25 – 75, Boston: Academic Press, 2012.

[108] P. Heintz and K. Samuelsson, "On adaptive strategies and error control in fracture mechanics," *Computers & structures*, vol. 82, no. 6, pp. 485–497, 2004.

[109] M. Ainsworth and J. T. Oden, *A posteriori error estimation in finite element analysis*, vol. 37. John Wiley & Sons, 2011.

[110] P. Houston, E. Süli, and T. P. Wihler, "A posteriori error analysis of hp-version discontinuous Galerkin finite-element methods for second-order quasi-linear elliptic pdes," *IMA journal of Numerical Analysis*, vol. 28, no. 2, pp. 245–273, 2008.

[111] M. Rüter and E. Stein, "Goal-oriented a posteriori error estimates in elastic fracture mechanics," in *Fifth World Congress on Computational mechanics, Vienna, Austria*, 2002.

[112] M. Rüter and E. Stein, "Goal-oriented a posteriori error estimates in linear elastic fracture mechanics," *Computer methods in applied mechanics and engineering*, vol. 195, no. 4-6, pp. 251–278, 2006.

[113] R. Verfürth, "Adaptive finite element methods," *Lecture Notes Winter Term*, vol. 8, 2007.

[114] O. A. González-Estrada, J. J. Ródenas, S. P. A. Bordas, M. Duflot, P. Kerfriden, and E. Giner, "On the role of enrichment and statical admissibility of recovered fields in a posteriori error estimation for enriched finite element methods," *Engineering Computations*, 2012.

[115] S. Giani and E. Hall, "An a posteriori error estimator for hp-adaptive discontinuous Galerkin methods for elliptic eigenvalue problems," *Mathematical Models and Methods in Applied Sciences*, vol. 22, no. 10, p. 1250030, 2012.

[116] S. Giani, "hp-adaptive celatus enriched discontinuous galerkin method for second-order elliptic source problems," *SIAM Journal on Scientific Computing*, vol. 40, no. 5, pp. B1391–B1418, 2018.

[117] P. Hansbo and M. Larson, "Energy norm a posteriori error estimates for discontinuous Galerkin approximations of the linear elasticity problem," *Computer Methods in Applied Mechanics and Engineering*, vol. 200, no. 45, pp. 3026–3030, 2011.

[118] T. Eibner and J. Melenk, "An adaptive strategy for hp-FEM based on testing for analyticity," *Computational Mechanics*, vol. 39, no. 5, pp. 575–595, 2007.

[119] M. Heuer, N. Mellado and E. Stephan, "*hp*-adaptive two-level methods for boundary integral equations on curves," *Computing*, vol. 67, no. 4, pp. 305–334, 2001.

[120] P. Houston and E. Süli, "A note on the design of hp-adaptive finite element methods for elliptic partial differential equations," *Computer Methods in Applied Mechanics and Engineering*, vol. 194, no. 2, pp. 229–243, 2005.

[121] P. Houston, B. Senior, and E. Süli, "Sobolev regularity estimation for hp-adaptive finite element methods," in *Numerical Mathematics and Advanced Applications* (F. Brezzi, A. Buffa, S. Corsaro, and A. Murli, eds.), pp. 631–656, 2003.

[122] B. Guo and I. Babuška, "The hp version of the finite element method," *Computational Mechanics*, vol. 1, no. 1, pp. 21–41, 1986.

[123] I. Alatawi and J. Trevelyan, "A direct evaluation of stress intensity factors using the extended dual boundary element method," *Engineering Analysis with Boundary Elements*, vol. 52, pp. 56 – 63, 2015.

[124] G. Hattori, I. A. Alatawi, and J. Trevelyan, "An extended boundary element method formulation for the direct calculation of the stress intensity factors in fully anisotropic materials," *International Journal for Numerical Methods in Engineering*, vol. 109, no. 7, pp. 965–981, 2017.

[125] X. Liu, Q. Xiao, and B. Karihaloo, "XFEM for direct evaluation of mixed mode SIFs in homogeneous and bi-materials," *International Journal for Numerical Methods in Engineering*, vol. 59, no. 8, pp. 1103–1118, 2004.

[126] Y. Wang, C. Cerigato, H. Waisman, and E. Benvenuti, "XFEM with high-order material-dependent enrichment functions for stress intensity factors calculation of interface cracks using irwin's crack closure integral," *Engineering Fracture Mechanics*, vol. 178, pp. 148 – 168, 2017.

[127] A. Fawkes, D. Owen, and A. Luxmoore, "An assessment of crack tip singularity models for use with isoparametric elements," *Engineering Fracture Mechanics*, vol. 11, no. 1, pp. 143–159, 1979.

[128] H. Liebowitz, J. Sandhu, J. Lee, and F. Menandro, "Computational fracture mechanics: research and application," *Engineering fracture mechanics*, vol. 50, no. 5-6, pp. 653–670, 1995.

[129] H. Liebowitz and E. Moyer Jr, "Finite element methods in fracture mechanics," *Computers & Structures*, vol. 31, no. 1, pp. 1–9, 1989.

[130] G. Legrain, N. Moës, and E. Verron, "Robust and direct evaluation of J2 in linear elastic fracture mechanics with the X-FEM," *International Journal for Numerical Methods in Engineering*, vol. 76, no. 10, pp. 1471–1488, 2008.

[131] M. Treifi and S. Oyadiji, "Bi-material V-notch stress intensity factors by the fractal-like finite element method," *Engineering Fracture Mechanics*, vol. 105, pp. 221–237, 2013.

[132] J. Cho and H. Lee, "Calculation of stress intensity factors in 2-D linear fracture mechanics by Petrov-Galerkin natural element method," *International Journal for Numerical Methods in Engineering*, vol. 98, no. 11, pp. 819–839, 2014.

[133] T. Hellen, "On the method of virtual crack extensions," *International Journal for Numerical Methods in Engineering*, vol. 9, no. 1, pp. 187–207, 1975.

[134] K. Ronald, "Virtual crack closure technique: history, approach, and applications," *Applied Mechanics Reviews*, vol. 57, no. 2, pp. 109–143, 2004.

[135] J. Sladek and V. Sladek, "Evaluation of T-stresses and stress intensity factors in stationary thermoelasticity by the coservation integral method," *International journal of fracture*, vol. 86, no. 3, pp. 199–219, 1997.

[136] R. Simpson and J. Trevelyan, "Evaluation of J1 and J2 integrals for curved cracks using an enriched boundary element method," *Engineering Fracture Mechanics*, vol. 78, no. 4, pp. 623 – 637, 2011.

[137] G. Irwin, "Linear fracture mechanics, fracture transition, and fracture control," *Engineering Fracture Mechanics*, vol. 1, no. 2, pp. 241–257, 1968.

[138] N. Moës, J. Dolbow, and T. Belytschko, "A finite element method for crack growth without remeshing," *International Journal for Numerical Methods in Engineering*, vol. 46, no. 1, pp. 131–150, 1999.

[139] G. N. Wells and L. J. Sluys, "A new method for modelling cohesive cracks using finite elements," *International Journal for Numerical Methods in Engineering*, vol. 50, no. 12, pp. 2667–2682, 2001.

[140] J. Min, J. Bass, and L. Spradley, "Adaptive finite element methods for two-dimensional problems in computational fracture mechanics," *Computers & structures*, vol. 50, no. 3, pp. 433–445, 1994.

[141] S. Bordas and M. Duflot, "Derivative recovery and a posteriori error estimate for extended finite elements," *Computer Methods in Applied Mechanics and Engineering*, vol. 196, no. 35, pp. 3381 – 3399, 2007.

[142] M. Duflot and S. Bordas, "A posteriori error estimation for extended finite elements by an extended global recovery," *International Journal for Numerical Methods in Engineering*, vol. 76, no. 8, pp. 1123–1138, 2008.

[143] O. Zienkiewicz and J. Zhu, "The superconvergent patch recovery and a posteriori error estimates. part 1: The recovery technique," *International Journal for Numerical Methods in Engineering*, vol. 33, no. 7, pp. 1331–1364, 1992.

[144] K. S. R. K. Murthy and M. Mukhopadhyay, "Adaptive finite element analysis of mixed-mode crack problems with automatic mesh generator," *International Journal for Numerical Methods in Engineering*, vol. 49, no. 8, pp. 1087–1100, 2000.

[145] A. Khoei, H. Azadi, and H. Moslemi, "Modeling of crack propagation via an automatic adaptive mesh refinement based on modified superconvergent patch recovery technique," *Engineering Fracture Mechanics*, vol. 75, no. 10, pp. 2921–2945, 2008.

[146] M. Rüter and E. Stein, "Adaptive finite element analysis of crack propagation in elastic fracture mechanics based on averaging techniques," *Computational Materials Science*, vol. 31, no. 3, pp. 247 – 257, 2004.

[147] P. Ladevèze, F. Pled, and L. Chamoin, "New bounding techniques for goal-oriented error estimation applied to linear problems," *International Journal for Numerical Methods in Engineering*, vol. 93, no. 13, pp. 1345–1380, 2013.

[148] M. Stein, E. Rüter and S. Ohnimus, "Adaptive finite element analysis and modelling of solids and structures. findings, problems and trends," *International Journal for Numerical Methods in Engineering*, vol. 60, no. 1, pp. 103–138, 2004.

[149] F. Pled, L. Chamoin, and P. Ladevèze, "An enhanced method with local energy minimization for the robust a posteriori construction of equilibrated stress fields in finite element analyses," *Computational Mechanics*, vol. 49, no. 3, pp. 357–378, 2012.

[150] O. González-Estrada, E. Nadal, J. Ródenas, P. Kerfriden, S. Bordas, and F. Fuenmayor, "Mesh adaptivity driven by goal-oriented locally equilibrated superconvergent patch recovery," *Computational Mechanics*, vol. 53, no. 5, pp. 957–976, 2014.

[151] F. Cirak and R. Ekkehard, "A posteriori error estimation and adaptivity for linear elasticity using the reciprocal theorem," *Computer Methods in Applied Mechanics and Engineering*, vol. 156, no. 1, pp. 351 – 362, 1998.

[152] Y. Chen and H. N., "New integration scheme for the branch crack problem," *Engineering Fracture Mechanics*, vol. 52, no. 5, pp. 791 – 801, 1995.

[153] G. W. Ma, X. M. An, H. H. Zhang, and L. X. Li, "Modeling complex crack problems using the numerical manifold method," *International Journal of Fracture*, vol. 156, pp. 21–35, Mar 2009.

[154] S. Mohammadi, *XFEM fracture analysis of composites*. John Wiley & Sons Incorporated, 2012.

[155] B. Hutchinson, "Critical assessment 16: Anisotropy in metals," *Materials Science and Technology*, vol. 31, no. 12, pp. 1393–1401, 2015.

[156] S. S. Ghorashi, S. Mohammadi, and S.-R. Sabbagh-Yazdi, "Orthotropic enriched element free Galerkin method for fracture analysis of composites," *Engineering Fracture Mechanics*, vol. 78, no. 9, pp. 1906–1927, 2011.

[157] L. Cahill, S. Natarajan, S. P. A. Bordas, R. M. O'Higgins, and C. T. McCarthy, "An experimental/numerical investigation into the main driving force for crack propagation in uni-directional fibre-reinforced composite laminae," *Composite Structures*, vol. 107, pp. 119–130, 2014.

[158] Z. A.D. Lethbridge, R. I. Walton, A. Marmier, C. Smith, and K. E. Evans, "Elastic anisotropy and extreme poisson's ratios in single crystals," *Acta Materialia*, vol. 58, pp. 6444–6451, 11 2010.

[159] G. Hattori, R. Rojas-Díaz, A. Sáez, N. Sukumar, and F. García-Sánchez, "New anisotropic crack-tip enrichment functions for the extended finite element method," *Computational Mechanics*, vol. 50, no. 5, pp. 591–601, 2012.

[160] G. C. Sih, P. Paris, and G. R. Irwin, "On cracks in rectilinearly anisotropic bodies," *International Journal of Fracture Mechanics*, vol. 1, no. 3, pp. 189–203, 1965.

[161] S. Chu and C. Hong, "Application of the Jk integral to mixed mode crack problems for anisotropic composite laminates," *Engineering Fracture Mechanics*, vol. 35, no. 6, pp. 1093 – 1103, 1990.

[162] P. Sollero and M. Aliabadi, "Anisotropic analysis of cracks in composite laminates using the dual boundary element method," *Composite structures*, vol. 31, no. 3, pp. 229–233, 1995.

[163] A. Asadpoure and S. Mohammadi, "Developing new enrichment functions for crack simulation in orthotropic media by the extended finite element method," *International Journal for Numerical Methods in Engineering*, vol. 69, no. 10, pp. 2150–2172, 2007.

[164] A. Ern, A. F. Stephansen, and M. Vohralik, "Guaranteed and robust discontinuous Galerkin a posteriori error estimates for convection-diffusion-reaction problems," *Journal of computational and applied mathematics*, vol. 234, no. 1, pp. 114–130, 2010.

[165] A. Ern, A. F. Stephansen, and P. Zunino, "A discontinuous Galerkin method with weighted averages for advection-diffusion equations with locally small and anisotropic diffusivity," *IMA Journal of Numerical Analysis*, vol. 29, no. 2, pp. 235–256, 2009.

[166] Y. Epshteyn and B. Rivière, "Estimation of penalty parameters for symmetric interior penalty galerkin methods," *Journal of Computational and Applied Mathematics*, vol. 206, no. 2, pp. 843–872, 2007.

[167] A. J. M. Spencer, *Continuum mechanics*. Courier Corporation, 2004.

[168] I. Choi and C. Horgan, "Saint-Venant's principle and end effects in anisotropic elasticity," *Journal of Applied Mechanics*, vol. 44, no. 3, pp. 424–430, 1977.

[169] M. Drosson and K. Hillewaert, "On the stability of the symmetric interior penalty method for the Spalart–Allmaras turbulence model," *Journal of Computational and Applied Mathematics*, vol. 246, pp. 122–135, July 2013.

[170] P. Houston, J. Robson, and E. Süli, "Discontinuous Galerkin finite element approximation of quasilinear elliptic boundary value problems I: The scalar case," *IMA Journal of Numerical Analysis*, vol. 25, no. 4, pp. 726–749, 2005.

[171] M. Aliabadi and P. Sollero, "Crack growth analysis in homogeneous orthotropic laminates," *Composites Science and Technology*, vol. 58, no. 10, pp. 1697 – 1703, 1998.

[172] J. Eshelby, "Energy relations and the energy-momentum tensor in continuum mechanics," in *Fundamental Contributions to the Continuum Theory of Evolving Phase Interfaces in Solids: A Collection of Reprints of 14 Seminal Papers*, pp. 82–119, Berlin, Heidelberg: Springer Berlin Heidelberg, 1999.

[173] G. Maugin, "Material force: concepts and applications," *Applied Mechanics Reviews*, vol. 23, pp. 213–245, 1995.

[174] R. Kienzler and G. Herrmann, *Mechanics in material space with applications to defect and fracture mechanics*. Springer-Verlag, New York, 2000.

[175] P. Steinmann and G. Maugin, eds., *Mechanics of material forces*. Springer-Verlag, 2005.

[176] H. Stumpf and K. C. Le, "Variational principles of nonlinear fracture mechanics," *Acta Mechanica*, vol. 83, pp. 25–37, 1990.

[177] H. Ishikawa, H. Kitagawa, and H. Okamura, "J-integral of a mixed mode crack and its application," *Mechanical Behaviour of Materials*, pp. 447–455, 1980.

[178] A. Yan and H. Nguyen-Dang, "Multiple-cracked fatigue crack growth by BEM," *Computational Mechanics*, vol. 16, no. 5, pp. 273–280, 1995.

[179] F. Erdogan and G. Sih, "On the crack extension in plates under plane loading and transverse shear," *Journal of Basic Engineering*, vol. 85, no. 4, pp. 519–525, 1963.

[180] P. Destuynder, M. Djaoua, and S. Lescure, "Quelques remarques sur la mécanique de la rupture élastique," *Journal de Mécanique Théorique et Appliquée*, vol. 2, no. 1, pp. 113–135, 1983.

[181] P.-O. Bouchard, F. Bay, and Y. Chastel, "Numerical modelling of crack propagation: automatic remeshing and comparison of different criteria," *Computer Methods in Applied Mechanics and Engineering*, vol. 192, no. 35, pp. 3887–3908, 2003.

[182] G. Sih and B. Macdonald, "Fracture mechanics applied to engineering problems-strain energy density fracture criterion," *Engineering Fracture Mechanics*, vol. 6, no. 2, pp. 361–386, 1974.

[183] H. deLorenzi, "On the energy release rate and the J-integral for 3-D crack configurations," *International Journal of Fracture*, vol. 19, pp. 183–193, 1982.

[184] D. Parks, "The virtual crack extension method for nonlinear material behavior," *Computer Methods in Applied Mechanics and Engineering*, vol. 12, no. 3, pp. 353–364, 1977.

[185] D. Parks, "A stiffness derivative finite element technique for determination of crack tip stress intensity factors," *International Journal of Fracture*, vol. 10, no. 4, pp. 487–502, 1974.

[186] D. Parks, "Virtual crack extension-A general finite element technique for J-integral evaluation," *Numerical Methods in Fracture Mechanics*, pp. 464–478, 1978.

[187] T. Hellen and W. Blackburn, "The calculation of stress intensity factors for combined tensile and shear loading," *International Journal of Fracture*, vol. 11, no. 4, pp. 605–617, 1975.

[188] D. Sutula, P. Kerfriden, T. Van Dam, and S. P. Bordas, "Minimum energy multiple crack propagation. part-ii: Discrete solution with xfem," *Engineering Fracture Mechanics*, vol. 191, pp. 225–256, 2018.

[189] V. E. Saouma, M. L. Ayari, and D. A. Leavell, "Mixed mode crack propagation in homogeneous anisotropic solids," *Engineering Fracture Mechanics*, vol. 27, no. 2, pp. 171 – 184, 1987.

[190] A. Hansbo and P. Hansbo, "An unfitted finite element method, based on Nitsche's method, for elliptic interface problems," *Computer Methods in Applied Mechanics and Engineering*, vol. 191, no. 47, pp. 5537–5552, 2002.

[191] A. Hansbo and P. Hansbo, "A finite element method for the simulation of strong and weak discontinuities in solid mechanics," *Computer Methods in Applied Mechanics and Engineering*, vol. 193, no. 33, pp. 3523–3540, 2004.

[192] P. Heintz, "On the numerical modelling of quasi-static crack growth in linear elastic fracture mechanics," *International Journal for Numerical Methods in Engineering*, vol. 65, no. 2, pp. 174–189, 2006.

[193] A. Arranz, N. Petrinic, and E. Süli, "Discontinuous element approximation for dynamic fracture," in *Computational Plasticity: Fundamentals and Applications-Proceedings of the*

8th International Conference on Computational Plasticity, COMPLAS VIII, no. PART 1, pp. 545–548, 2005.

[194] J. Mergheim, E. Kuhl, and P. Steinmann, "A hybrid discontinuous Galerkin/interface method for the computational modelling of failure," *Communications in numerical methods in engineering*, vol. 20, no. 7, pp. 511–519, 2004.

[195] H. Huang and F. Costanzo, "On the use of space-time finite elements in the solution of elasto-dynamic fracture problems," *International Journal of Fracture*, vol. 127, no. 2, pp. 119–146, 2004.

[196] R. Radovitzky, A. Seagraves, M. Tupek, and L. Noels, "A scalable 3D fracture and fragmentation algorithm based on a hybrid, discontinuous Galerkin, cohesive element method," *Computer Methods in Applied Mechanics and Engineering*, vol. 200, no. 1, pp. 326–344, 2011.

[197] V. P. Nguyen, "Discontinuous Galerkin/extrinsic cohesive zone modeling: Implementation caveats and applications in computational fracture mechanics," *Engineering Fracture Mechanics*, vol. 128, pp. 37–68, 2014.

[198] L. Wu, G. Becker, and L. Noels, "Elastic damage to crack transition in a coupled non-local implicit discontinuous Galerkin/extrinsic cohesive law framework," *Computer Methods in Applied Mechanics and Engineering*, vol. 279, pp. 379–409, 2014.

[199] M. Prechtel, P. Ronda, R. Janisch, A. Hartmaier, G. Leugering, P. Steinmann, and M. Stingl, "Simulation of fracture in heterogeneous elastic materials with cohesive zone models," *International Journal of Fracture*, vol. 168, no. 1, pp. 15–29, 2011.

[200] R. Abedi, M. Hawker, R. Haber, and K. Matouš, "An adaptive spacetime discontinuous Galerkin method for cohesive models of elastodynamic fracture," *International Journal for Numerical Methods in Engineering*, vol. 81, no. 10, pp. 1207–1241, 2010.

[201] J. Tago, V. M. Cruz-Atienza, J. Virieux, V. Etienne, and F. J. Sánchez-Sesma, "A 3D hp-adaptive discontinuous Galerkin method for modeling earthquake dynamics," *Journal of Geophysical Research: Solid Earth*, vol. 117, no. B9, 2012.

[202] M. Scherer, R. Denzer, and P. Steinmann, "On a solution strategy for energy-based mesh optimization in finite hyperelastostatics," *Computer Methods in Applied Mechanics and Engineering*, vol. 197, no. 6, pp. 609–622, 2008.

[203] E. Kuhl, H. Askes, and P. Steinmann, "An ALE formulation based on spatial and material settings of continuum mechanics. Part 1: Generic hyperelastic formulation," *Computer Methods in Applied Mechanics and Engineering*, vol. 193, no. 39, pp. 4207–4222, 2004.

[204] W. Ai, R. E. Bird, W. M. Coombs, and C. E. Augarde, "A configurational force driven cracking particle method for modelling crack propagation in 2d," *Engineering Analysis with Boundary Elements*, vol. 104, pp. 197 – 208, 2019.

[205] R. E. Smelser and M. E. Gurtin, "On the J-integral for bi-material bodies," *International Journal of Fracture*, vol. 13, no. 3, pp. 382–384, 1977.

[206] M. Stein, E. Rüter and S. Ohnimus, "Error-controlled adaptive goal-oriented modeling and finite element approximations in elasticity," *Computer Methods in Applied Mechanics and Engineering*, vol. 196, pp. 3598–3613, Aug. 2007.